

# IRE Transactions



on Microwave Theory and Techniques

UNIVERSITY OF HAWAII LIBRARY

Volume MTT-7

APRIL, 1959

Number 2

## In This Issue

- Breaking Through the Mental Barrier
- Reflection of a Pyramidally Tapered Rectangular Waveguide
- Cascade Directional Filter
- Propagation in a Dielectric-Loaded Parallel Plane Waveguide
- Electromagnetic Backscattering Measurements
- Network Representations of Obstacles in Waveguides
- Reflectors for a Microwave Fabry-Perot Interferometer
- Precise Control of Ferrite Phase Shifters
- Tables for Cascaded Homogeneous Quarter-Wave Transformers
- The Synthesis of Symmetrical Waveguide Circulators
- Delay Distortion in Crystal Mixers
- The Efficiency of Excitation of a Surface Wave on a Dielectric Cylinder
- Tunable Millimeter Wave Molecular Oscillator and Amplifier
- High-Speed Microwave Switching of Semiconductors—II
- A Logarithmic Transmission Line Chart
- Far Fields Excited by a Point Source
- Analysis of a Negative Conductance Amplifier
- 1959 National Symposium Program

TK 7800  
I23

PUBLISHED BY THE

Professional Group on Microwave Theory and Techniques



## IRE PROFESSIONAL GROUP ON MICROWAVE THEORY AND TECHNIQUES

The Professional Group on Microwave Theory and Techniques is an association of IRE members with professional interest in the field of Microwave Theory and Techniques. All IRE members are eligible for membership and will receive all Group publications upon payment of the prescribed annual fee of \$3.00. Members of the American Physical Society and the Institution of Electrical Engineers of Great Britain may become affiliated with PGMTT and receive all Group publications upon payment of the Affiliate fee of \$7.50 per year.

### Administrative Committee

#### Chairman

T. S. SAAD

#### Vice-Chairman

A. A. OLINER

#### Secretary-Treasurer

S. W. ROSENTHAL

T. N. ANDERSON	H. F. ENGELMANN	GUSTAVE SHAPIRO
R. E. BEAM	HENRY MAGNUSKI	GEORGE SINCLAIR
A. C. BECK	W. W. MUMFORD	P. D. STRUM
A. G. CLAVIER	W. L. PRITCHARD	M. C. THOMPSON, JR.
S. B. COHN	S. D. ROBERTSON	K. TOMIYASU
C. W. CURTIS	R. F. SCHWARTZ	R. D. WENGENROTH

#### Editor

DONALD D. KING

### PGMTT Chapters

Albuquerque-Los Alamos	R. E. Glass	Northern New Jersey	P. R. Wickliffe
Baltimore	E. B. Cole	Omaha-Lincoln	C. M. Hyde
Boston	I. Goldstein	Philadelphia	D. R. Crosby
Buffalo-Niagara	Robert E. Kell	San Diego	B. I. Small, Jr.
Chicago	John Del Vento	San Francisco	Peter D. Lacy
Denver	M. C. Thompson, Jr.	Schenectady	G. J. Griffin
Long Island	K. S. Packard	Syracuse	David K. Cheng
Los Angeles	R. S. Jamison	Tokyo	K. Morita
New York	A. N. Sonnenschein	Washington	Edward A. Wolff

### IRE TRANSACTIONS®

#### on Microwave Theory and Techniques

Published by the Institute of Radio Engineers, Inc., for the Professional Group on Microwave Theory and Techniques, at 1 East 79th Street, New York 21, New York. Responsibility for the contents rests upon the authors, and not upon the IRE, the Group, or its members. Price per copy: IRE PGMTT members, \$2.20; IRE members, \$3.30, nonmembers, \$6.60. Annual subscription price: IRE members, \$8.50; colleges and public libraries, \$12.75; nonmembers, \$17.00.

Address all manuscripts to Donald D. King, PGMTT Editor, Electronic Communications, Inc., 1830 York Road, Timonium, Md. Submission of three copies of manuscripts, including figures, will expedite the review.

COPYRIGHT ©1959—THE INSTITUTE OF RADIO ENGINEERS, INC.

Printed in U.S.A.

All rights, including translations, are reserved by the IRE. Requests for republication privileges should be addressed to the Institute of Radio Engineers, 1 E. 79th St., New York 21, N.Y.



# IRE Transactions

## on

# Microwave Theory and Techniques

### EDITORIAL BOARD

#### Editor

Donald D. King

#### Advertising Editor

Tore N. Anderson

H. M. Altschuler  
D. J. Angelakos  
W. P. Ayres  
R. W. Beatty  
J. C. Cacheris  
S. B. Cohn  
R. E. Collin  
W. A. Edson  
E. J. Feldman  
I. Goldstein  
R. C. Hansen  
H. Heffner  
E. M. T. Jones  
D. D. King  
P. D. Lacy  
Patricia A. Loth  
R. V. Lowman  
H. F. Mathis  
E. W. Matthews, Jr.  
Theodore Moreno  
M. C. Pease  
J. Reed  
H. J. Riblet  
J. M. Richardson  
S. D. Robertson  
R. F. Schwartz  
W. Sichak  
D. C. Stinson  
P. D. Strum  
E. Strumwasser  
L. Swern  
P. H. Vartanian, Jr.  
E. Wantuch  
M. T. Weiss  
G. J. Wheeler  
R. F. Whitmer  
F. K. Willenbrock

Volume MTT-7

APRIL, 1959

Number 2

### TABLE OF CONTENTS

Message from the Editor.....	188
Frontispiece.....	<i>Seymour B. Cohn</i> 189
Breaking Through the Mental Barrier.....	<i>Seymour B. Cohn</i> 190

### CONTRIBUTIONS

Reflection of a Pyramidally Tapered Rectangular Waveguide.....	<i>Katsu Matsumaru</i> 192
Cascade Directional Filter.....	<i>Omar Wing</i> 197
Propagation in a Dielectric-Loaded Parallel Plane Waveguide.....	<i>Marvin Cohn</i> 202
Electromagnetic Backscattering Measurements by a Time-Separation Method.....	<i>Charles C. H. Tang</i> 209
On Network Representations of Certain Obstacles in Waveguide Regions.....	<i>H. M. Altschuler and L. O. Goldstone</i> 213
Reflectors for a Microwave Fabry-Perot Interferometer.....	<i>W. Culshaw</i> 221
Precise Control of Ferrite Phase Shifters.....	<i>D. D. King, C. M. Barrack, and C. M. Johnson</i> 229
Tables for Cascaded Homogeneous Quarter-Wave Transformers.....	<i>Leo Young</i> 233
The Synthesis of Symmetrical Waveguide Circulators.....	<i>B. A. Auld</i> 238
Delay Distortion in Crystal Mixers.....	<i>T. Kawahashi and T. Uchida</i> 247
The Efficiency of Excitation of a Surface Wave on a Dielectric Cylinder.....	<i>J. W. Duncan</i> 257
Proposal for a Tunable Millimeter Wave Molecular Oscillator and Amplifier.....	<i>J. R. Singer</i> 268
High-Speed Microwave Switching of Semiconductors—II.....	<i>Robert V. Garver</i> 272
A Logarithmic Transmission Line Chart.....	<i>A. C. Hudson</i> 277
The Far Fields Excited by a Point Source in a Passive Dissipationless Anisotropic Uniform Waveguide.....	<i>A. D. Bresler</i> 282
Analysis of a Negative Conductance Amplifier Operated with a Nonideal Circulator..	<i>E. W. Sard</i> 288

### CORRESPONDENCE

Propagation Constants in Rectangular Waveguide Partially Filled with Dielectric...	<i>W. L. Weeks</i> 294
A Short Rugged Ferrite Half-Wave Plate for a Single-Sideband Modulator.....	<i>H. I. Glass</i> 295
A Technique for Minimizing Hysteresis in a 35-DB Ferrite Variable Attenuator.....	<i>H. I. Glass</i> 295
Quarter-Wave Compensation of Resonant Discontinuities.....	<i>C. E. Muehe</i> 296
Comments on Ozaki's Comments.....	<i>Henry J. Riblet</i> 297
Vector Formulations for the Field Equations in Anisotropic Waveguides.....	<i>A. D. Bresler</i> 298
An Extension of the Reflection Coefficient Chart to Include Active Networks.....	<i>L. J. Kaplan and D. J. R. Stock</i> 298
Characteristics of a Ferrite-Loaded Rectangular Waveguide Twist.....	<i>A. E. Barrington</i> 299
Contributors.....	300
1959 National Symposium Program.....	303



## Message from the Editor

SINCE the editorship of TRANSACTIONS is a group responsibility which should be rotated among its members, I have asked to be replaced after serving for two years. I deeply appreciate having had this opportunity for it has been interesting, enjoyable, and rewarding. This issue of TRANSACTIONS is the last one under my editorship and the next following issue, July, 1959, will be the first one under the new editor, Dr. Donald D. King.

In order to provide an adequate medium for publishing the important papers on microwaves it became necessary during 1957 and 1958 to publish larger issues of these TRANSACTIONS and to increase the number of Editorial Board members from 12 to 38. During the same two-year period 220 papers were submitted, and each paper was carefully reviewed by three members of the Editorial Board

listed on the Table of Contents page. A strong vote of thanks is due to these Board members who have made a major contribution to PGMTT by their excellent and prompt reviews. At the IRE in New York thanks are due to Mrs. Gene B. Duffy, Mrs. Helene Frischauer, Associate Editor, and, in particular, to Managing Editor Elwood K. Gannett, for their fine cooperation and assistance in publishing these TRANSACTIONS. Thanks are also due to the many authors whose excellent and timely papers have added much to the quality of TRANSACTIONS.

Finally I am indebted to the PGMTT Administrative Committee for providing encouragement and policy guidance, and to T. S. Saad, former editor and present chairman of the PGMTT Administrative Committee, for his enthusiastic interest and valuable comments.

K. TOMIYASU, *Editor*





## Seymour B. Cohn

Seymour B. Cohn (S'41-A'44-M'46-SM'51-F'59) was born in Stamford, Conn., on October 21, 1920. After receiving the B.E. degree in electrical engineering from Yale University, New Haven, Conn., in 1942, he worked for the Radio Research Laboratory of Harvard University, Cambridge, Mass., specializing in UHF and microwave receivers, circuits, and filters. In 1944 he represented the Radio Research Laboratory as a technical observer with the U. S. Air Force in the Mediterranean Theater of Operations. Following the disbanding of the Radio Research Laboratory at the end of 1945, he enrolled as a graduate student at Harvard University and was awarded the M.S. degree in communication engineering in 1946, and the Ph.D. degree in engineering science and applied physics in 1948.

From 1948 to 1953, he was on the staff of the Sperry Gyroscope Company, where he advanced to the position of research engineer. His activities there included studies on waveguide components,

lens antennas, and measurement equipment.

In 1953 he joined the Stanford Research Institute, Menlo Park, Calif., as head of the microwave group, and in 1957 was advanced to manager of the Electromagnetics Laboratory. At Stanford Research Institute he has been continuing his work on many phases of microwave research. His current interests center mainly in microwave filters, parametric amplifiers, and antennas.

Dr. Cohn is the author of several chapters on UHF and microwave filters in the book "Very High Frequency Techniques," written by members of the Radio Research Laboratory and published by the McGraw-Hill Book Co., Inc. He has also contributed a chapter on lens antennas for the "Antenna Engineering Handbook," to be published by McGraw-Hill this year. In 1954 the Yale Engineering Association presented him with their Annual Award for Advancement of Basic and Applied Science.

He is a member of Sigma Xi and Tau Beta Pi.



# Breaking Through the Mental Barrier

SEYMOUR B. COHN†

ANY of us whose work requires thinking will realize that the brain was not really meant for scientific effort. As to whether it is better suited to its more basic functions of guiding the individual is another fascinating subject that I will not consider here. Instead, I choose to pinpoint and attack a major inadequacy of the mind that interferes with our professional labors, and hope thereby, in some degree, to assist progress in our field.

We all know that for routine tasks an electronic computer is often far superior to the human mind. However, as a generator of new ideas the mind despite its inefficiency will probably never be replaced. Our best hope for scientific advance is to improve our use of the mind by understanding its built-in faults and by struggling constantly against them.

One does not have to be a psychologist to know that the mind tends to form easy paths of thought, with access to new ideas blocked by over-generalized beliefs and over-extended assumptions. Scientific principles, whether called laws, rules, theorems, or common knowledge, are invaluable aids when properly used, but when blindly accepted they can guide us to error and wall us from discovery. In effect, misused principles are barriers to creative thought. To break through these barriers we must completely understand the range of validity of each principle, and realize that outside this range any principle may be as unreliable and treacherous as prejudice and superstition.

The history of science is rich in examples of knowledge that served us well, but eventually proved to be barriers to further advance. Around the end of the last century many physical "certainties" were impeding progress until they were suddenly broken through, permitting entry into our current era of "modern" physics. Thus Newton's laws, believed for several hundred years to be the absolute regulators of the motion of matter, were found inadequate for particles approaching the velocity of light. Similarly, energy and mass were each considered to be constants in any given system, until an accumulation of perverse data made necessary the bold step of linking energy and mass together in a composite law of energy-mass conservation.

We can cite in our own field of microwaves many cases of beliefs proved wrong. It was once common knowledge that the transmission of electricity must require at least two conductors. Then in the 1930's several audacious men showed how to send high-frequency electrical waves with almost no loss down hollow conducting

tubes. It still remained common knowledge that a wave could not be transmitted on the outside of a single conductor without radiation loss. Then, about a decade ago, a dielectric-coated wire was made to serve as an efficient transmission line. "Everyone" knew that passive microwave circuits had to obey the law of reciprocity, until it was shown how to circumvent this law by converting RF energy into kinetic energy of precessional motion of electrons spinning in a magnetized ferrite medium. Crystal mixers were known to introduce conversion loss until someone used nonlinear capacitance as the mixing agent, rather than nonlinear resistance, thereby obtaining conversion gain from a supposedly passive element.

I could easily continue with other examples of principles and beliefs found wrong, and important fields thereby created. However, this editorial would serve a more useful purpose if I could succeed in pointing out possible loopholes in our common knowledge through which future discoveries may be made. The best example would be the revelation of a new major breakthrough, which obviously won't be found here. Nonetheless, I will suggest a few weak points in microwave knowledge, and will hope that some far-seeing person will be able to exploit at least one of these into a practical application.

We have all proved as students that a generator emits its full available energy only when the load impedance is the conjugate of the generator impedance. I will now show how one of the postulates in the proof may be evaded in a practical way to allow a generator to put forth its complete available power into any impedance. In Fig. 1, a magnetron with internal impedance  $Z_g = R_g$  is connected to a waveguide of characteristic impedance  $Z_0 = R_g$  and input impedance  $Z_{in} \neq R_g$ . If the magnetron produces a pulsed signal of duration  $\tau = 2l/v_g$  (where  $l$  is the waveguide length and  $v_g$  is the group velocity) the entire available energy will enter the waveguide. Before the reflected wave can return, the magnetron will have become inactive. Thus there will be no pulling effect on the magnetron. Also, the reflected wave will be re-reflected by the magnetron, since  $Z_g$  will have changed from a resistance into a reactance. Of course this scheme would have disadvantages in a practical system, but it illustrates, nevertheless, that the conjugate-match principle is valid only when steady-state conditions hold, and may be evaded easily when time-varying signals and elements are considered.

Power-breakdown ratings on waveguides and components have been arrived at experimentally and confirmed generally by theory. I will now suggest how the power-breakdown point may be increased by a few orders of magnitude. The theory of high-power break-

† Stanford Res. Inst., Menlo Park, Calif.



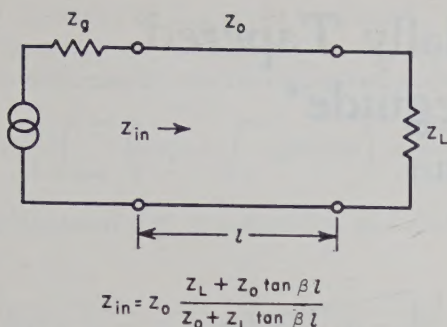


Fig. 1—Microwave circuit.

down assumes free electrons to be present in the strong-field region. Without free electrons, the breakdown process could not start until the electric field became so high as to tear electrons loose from air molecules or surrounding surfaces. I will leave to the reader the practical details of how to prevent formation of free electrons by shielding the microwave circuit from natural radiation, or of how to eliminate free electrons by sweeping them away or instantly trapping them in molecules of some yet unknown gas.

We have in the past decade become familiar with several ways of making nonreciprocal passive components. The major methods utilize spinning electrons in a ferrimagnetic medium placed in a dc magnetic field. Other methods employ a plasma medium with free electrons spiralling around a dc magnetic field. From these examples we are likely to assume that both rotational motion and a static magnetic field are necessary ingredients for passive nonreciprocal performance. But this is not true, as may be seen from the simple device sketched in Fig. 2. Microwave tube designers know that two types of space-charge waves can propagate on an electron beam. One type, used in traveling-wave amplifiers, travels slower than the beam and yields energy to the surrounding RF circuit as the wave grows in amplitude. The other space-charge wave travels faster than the beam and absorbs energy from the RF circuit as it grows. This fast wave is incapable of power amplification (unless pumped at a higher frequency in the para-

metric-amplifier mode of operation), but it can serve nicely as the energy storage element in a passive component. Thus in Fig. 2, the electrical energy of the input signal is transferred into energy of the fast wave by the input helix coupler, and is transferred back into very nearly the original quantity of electrical energy by the output helix coupler. If the generator and load are interchanged, however, the insertion loss will be very high since the fast wave travels only in the direction of the electrons. The exact equality of input signal power to output plus dissipated signal power justifies my calling the component "passive," and distinguishes it from "active" components, such as traveling-wave amplifier tubes and parametric amplifiers, within which signal power is created from nonsignal power. The device adds virtually no noise to the signal, since the input helix serves not only to couple the input signal onto the beam, but also removes the original fast-wave noise from the beam. Perhaps this component may be of practical value below 1000 mc, where ferrite and garnet isolators are relatively poor. In any event, the example will still serve its purpose if it encourages readers to look beyond magnets and whirling particles in seeking new schemes for nonreciprocal passive components.

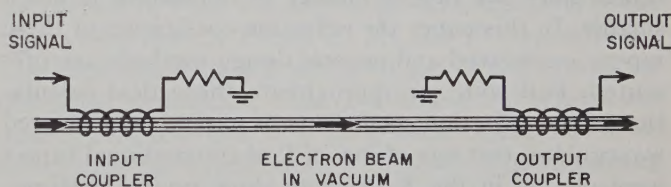


Fig. 2—Nonreciprocal device using fast space-charge wave.

It will now be obvious that I hope through this discussion to foster a critical attitude toward entrenched knowledge. Let us never forget that our most trusted beliefs may, outside their ranges of validity, be mental barriers to productive thinking. Let us arm ourselves with skepticism, combined with a firm grasp of fundamentals, and break through these mental barriers.



# Reflection of a Pyramidally Tapered Rectangular Waveguide\*

KATSU MATSUMARU†

**Summary**—The reflection coefficient  $\Gamma$  of a pyramidally tapered rectangular waveguide is derived by assuming that the taper impedance is proportional to the height and guide wavelength and inversely proportional to the width of the taper cross section. It is shown that the loci of  $\Gamma$ , plotted in the  $K$  plane as a function of taper length for some conventional tapers, do not pass through the center of the chart at multiples of a half-guide wavelength as for an exponential line, but instead they converge almost concentrically. The frequency characteristic of the pyramidally tapered waveguide is compared with other types of tapers. Typical 7-kmc experimental results for several tapers differing in length are presented.

## INTRODUCTION

IN microwave systems, a pyramidal taper is often needed to connect rectangular waveguides whose ratios of width to height are equal for both the input and output terminals. The reflection coefficients of these tapers are smaller than that of either  $E$ - or  $H$ -plane tapers since the rate of change of impedance is much smaller. In this paper the reflection coefficients of these tapers are derived and general design methods are presented. Following an approximate theoretical calculation of the reflection coefficients of pyramidally tapered waveguides, two sets of loci of  $\Gamma$  of conventional tapers were plotted in the  $K$  plane to show typical performances. To confirm the formulas, a set of tapers was made to connect WR-229 and WR-159 waveguides. The calculated locus of  $\Gamma$  of these tapers agreed very well with the measured locus at 7.05 kmc. By using these formulas, it is fairly easy to design properly pyramidally tapered waveguides.

## CALCULATION OF REFLECTION COEFFICIENTS OF PYRAMIDALLY TAPERED WAVEGUIDE

As stated in Schelkunoff's text, the reflection coefficient of pyramidally tapered rectangular waveguide for the dominant mode is quite small compared to those of  $E$ - or  $H$ -plane tapers.<sup>1</sup> First, the formula of reflection coefficient of these tapered waveguides will be derived. In Fig. 1 are shown the cross sections of a tapered waveguide and the coordinate system. The width and the height of the large waveguide are  $a$  and  $b$ , respectively, and the length of the taper is  $h$ . The longitudinal length of the taper to the projected vertex is  $z_0$ . The acute angles at the vertex in the  $xz$  and  $yz$  planes are

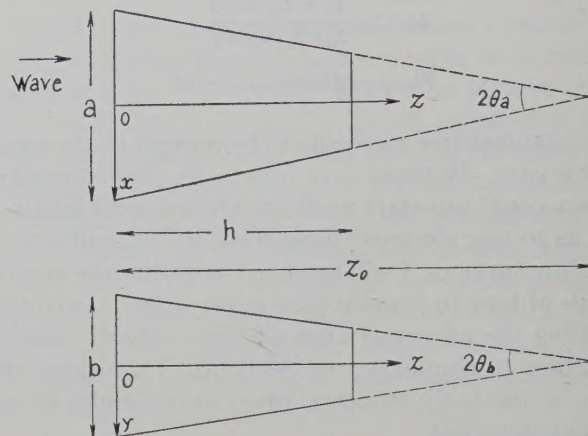


Fig. 1—Illustration of the cross sections and the coordinate system in a taper.

$2\theta_a$  and  $2\theta_b$ , respectively, as shown in Fig. 1. It is assumed that the electromagnetic wave propagates from left to right, and the dielectric constant of the medium within the waveguide is unity. The intrinsic impedance  $K_z$  of a rectangular waveguide is expressed by the following:<sup>2</sup>

$$K_z = \frac{\eta}{\sqrt{1 - (\lambda_0/\lambda_c(z))^2}}, \quad (1)$$

where  $\eta$  is a constant,  $\lambda_0$  is the free space wavelength, and  $\lambda_c(z)$  is the cutoff wavelength at a sectional plane  $z=z$ . By substituting the following relations

$$\frac{\lambda_c(z)}{2a} \equiv \frac{z_0 - z}{z_0}, \quad \text{and} \quad P = \left( \frac{z_0 \lambda_0}{2a} \right)^2 \quad (2)$$

in (1),  $K_z$  can be expressed as a function of  $z$ :

$$K_z = \frac{\eta}{\sqrt{1 - P/(z_0 - z)^2}}. \quad (3)$$

Following Schelkunoff's definition, the integrated impedance  $K_{wv}$  of a rectangular waveguide is assumed to be proportional to its height and inversely proportional to its width.<sup>3</sup> By using (3),  $K_{wv}$  can be expressed as a function of  $z$  as follows:

$$K_{wv} = \frac{2\eta}{\sqrt{1 - P/(z_0 - z)^2}} \cdot \frac{b - 2z \tan \theta_b}{a - 2z \tan \theta_a}. \quad (4)$$

\* Manuscript received by the PGMTT, March 18, 1958; revised manuscript received, December 23, 1958.

† Elec. Communication Lab., Nippon Telegraph and Telephone Public Corp., Tokyo, Japan.

<sup>1</sup> S. A. Schelkunoff, "Electromagnetic Waves," D. Van Nostrand Co. Inc., New York, N. Y., pp. 316-320; 1943.

<sup>2</sup> *Ibid.*, p. 317. See (21)-(11).

<sup>3</sup> *Ibid.*, p. 319. See (21)-(21).



If the rate of change of  $K_{wv}$  in the longitudinal direction is small, the reflection coefficient  $\Gamma$  of the taper, shown in Fig. 1, is obtained by the following integration:

$$\Gamma = \frac{1}{2} \int_{z=0}^{z=h} \left( \exp - \int_0^z 2j\beta(z)dz \right) \times \frac{dK_{wv}}{K_{wv}}. \quad (5)$$

The phase constant  $\beta(z)$  is a function of  $z$  and is given by

$$\begin{aligned} \beta(z) &= \frac{2\pi}{\lambda_0(z)} = \frac{2\pi}{\lambda_0} \sqrt{1 - P/(z_0 - z)^2} \\ &\doteq \frac{2\pi}{\lambda_0} \left( 1 - \frac{P}{2} \frac{1}{(z_0 - z)^2} \right). \end{aligned}$$

By using this approximation, the exponent in (5) is given by

$$- \int_0^z 2j\beta(z)dz \doteq -j \frac{4\pi}{\lambda_0} \left\{ z - \frac{P}{2} \left( \frac{1}{z_0 - z} - \frac{1}{z_0} \right) \right\}. \quad (6)$$

From (4),  $dK_{wv}/K_{wv}$  can be obtained as follows:

$$\begin{aligned} \frac{dK_{wv}}{K_{wv}} &= \left\{ \frac{2(-a \tan \theta_b + b \tan \theta_a)}{(a - 2z \tan \theta_a)(b - 2z \tan \theta_b)} \right. \\ &\quad \left. + \frac{P}{(z_0 - z)^3 - P(z_0 - z)} \right\} dz. \quad (7) \end{aligned}$$

Since the ratios  $a/b$  are equal for both the input and output terminal waveguides,

$$-a \tan \theta_b + b \tan \theta_a = 0. \quad (8)$$

Finally, by using relations (7) and (8), the formula of  $\Gamma$  is

$$\begin{aligned} \Gamma &= \frac{P}{2} \int_0^h \exp \left[ -j \frac{4\pi}{\lambda_0} \left\{ z - \frac{P}{2} \left( \frac{1}{z_0 - z} - \frac{1}{z_0} \right) \right\} \right] \\ &\quad \times \frac{dz}{(z_0 - z)^3 - P(z_0 - z)}. \quad (9) \end{aligned}$$

Eq. (9) is the general formula for the reflection coefficient of a pyramidally tapered waveguide. In general, the magnitude of  $\Gamma$  is proportional to  $P$  and independent of the height of the waveguide. For specified dimensions of the terminal waveguides, the magnitude of  $\Gamma$  decreases in an oscillatory fashion with increase in longitudinal length  $h$ .

Putting

$$z = \lambda_0 z', \quad z_0 = \lambda_0 z_0', \quad P = \lambda_0^2 P', \quad h = \lambda_0 h',$$

(9) can be normalized as follows:

$$\begin{aligned} \Gamma &= \frac{P'}{2} \int_0^{h'} \exp \left[ -j 4\pi \left\{ z' - \frac{P'}{2} \left( \frac{1}{z_0' - z'} - \frac{1}{z_0'} \right) \right\} \right] \\ &\quad \times \frac{dz'}{(z_0' - z')^3 - P'(z_0' - z')}. \quad (10) \end{aligned}$$

Since (10) depends only on  $h'$ ,  $z_0'$  and  $P'$ , calculated curves of  $\Gamma$  of some specific examples can be used as universal design charts if a set of tables of the variables is associated with them.

#### CHARACTERISTICS OF $\Gamma$ OF PYRAMIDALLY TAPERED RECTANGULAR WAVEGUIDE

Inasmuch as tapered waveguides are used in conjunction with other components in a waveguide system, it is necessary to know not only the magnitude but the phase of the reflection coefficient  $\Gamma$ . By using graphical integration, calculated values of  $\Gamma$  from (10) have been published for standard rectangular waveguides over the frequency range of 2 kmc to 14 kmc.<sup>4</sup>

First, to illustrate the general characteristics of  $\Gamma$  of these tapers, the calculated results are mentioned of typical tapers designed to connect WR-229 and WR-159 waveguides. With regard to frequency characteristics,  $\Gamma$  is calculated for three frequencies of 7.05 kmc ( $\lambda_0 = 4.25$  cm), 6.0 kmc ( $\lambda_0 = 5.00$  cm) and 5.5 kmc ( $\lambda_0 = 5.45$  cm) and the waveguide dimensions, etc., are compiled in Table I.

The tapers differing in length with parameters  $h$ ,  $h'$ ,  $z_0'$ , and  $\theta_a$  are tabulated in Tables II–IV for 7.05, 6.0, and 5.5 kmc, respectively. The calculated values of  $\Gamma$  are plotted in Figs. 2–4 and these loci correspond to the tapers described in Tables II, III and IV, respectively. The reference plane of  $\Gamma$  is at  $z=0$ , i.e., at the terminal of the larger waveguide. Figs. 2–4 depict the typical frequency characteristic of  $\Gamma$  for general cases. It is to be noted that the magnitude of  $\Gamma$  decreases with increasing taper length and the loci do not pass through the center of the chart. Moreover, the phase angle of  $\Gamma$  sweeps almost one revolution if the taper length changes by one-half guide wavelength. Fig. 5 shows the VSWR's of these tapers as a function of frequency. It should be mentioned that the VSWR decreases almost linearly with length if the taper is shorter than  $2\lambda_0$ , but not for the longer tapers. Considering the benefit of practical applications, the loci of  $\Gamma$  in Figs. 2–4 were traced as values of the admittance, even if, following the usual fashion, the conventional notations  $g-jb$  and  $g+jb$  were deleted in the graphs. Therefore, in order to use them as values of the impedance, the locations of these loci should be rotated by  $180^\circ$  about the center in the charts. (As for Figs. 2–4, the loci of  $\Gamma$  in Figs. 6–8 too, were traced as values of the admittance. Therefore, these loci also should be rotated by  $180^\circ$  about the center, in order to use them as the impedance.)

In another example, tapered waveguides, designed to connect WR-229 with WR-187 waveguides, are discussed. Table V shows the waveguide dimensions and  $\lambda_0$  in both terminal waveguides for three different frequencies in the 4-kmc band. (In this example, the tapers

<sup>4</sup> K. Matsumaru, "Considerations on tapered waveguides," *Elec. Communication Lab. Tech. J.*, vol. 7, pp. 52–62; May, 1958.



TABLE I

	Waveguide	$a$ (in)	$b$ (in)	$\lambda_g$ (cm)		
				7.05 kmc	6.0 kmc	5.5 kmc
Input terminal	WR-229	2.290	1.145	4.6	5.5	6.5
Output terminal	WR-159	1.590	0.795	5.0	6.3	7.4

TABLE II

 $f = 7.05$  KMC

$h$ (cm)	2	3	4	5	6	7
$h'$	0.47	0.70	0.94	1.18	1.41	1.64
$z_0'$	1.51	2.26	3.01	3.77	4.52	5.27
$\theta_a$	24.3°	16.8°	12.7°	10.3°	8.6°	7.4°

TABLE III

 $f = 6.0$  KMC

$h$ (cm)	2.5	4	5	6	7.5	9	10
$h'$	0.50	0.80	1.00	1.20	1.50	1.80	2.00
$z_0'$	1.60	2.57	3.21	3.85	4.80	5.75	6.40
$\theta_a$	19.9°	12.7°	10.3°	8.6°	6.9°	5.7°	5.2°

TABLE IV

 $f = 5.5$  KMC

$h$ (cm)	3	4	5	6	7	8	9	10
$h'$	0.55	0.73	0.92	1.10	1.28	1.47	1.65	1.83
$z_0'$	1.77	2.36	2.95	3.54	4.12	4.71	5.31	5.89
$\theta_a$	16.8°	12.7°	10.3°	8.6°	7.4°	6.5°	5.7°	5.2°

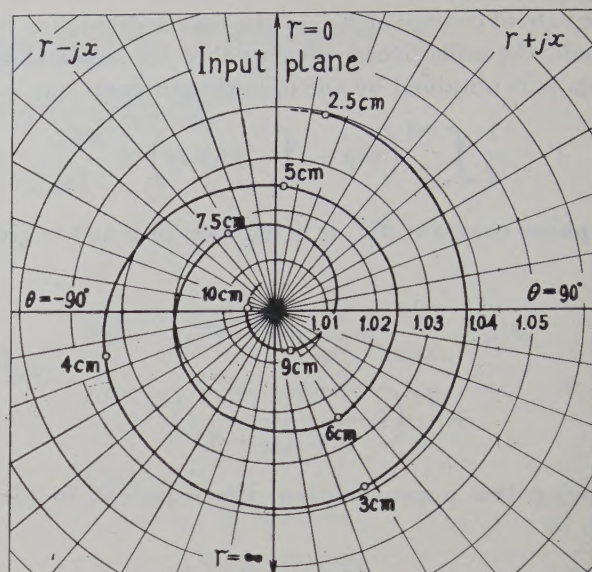


Fig. 3—The curve shows a locus of  $\Gamma$  of the same tapers in Fig. 2 but at a frequency of 6.0 kmc. Lengths of tapers are from 2.5 cm to 10 cm. See Tables I and III.

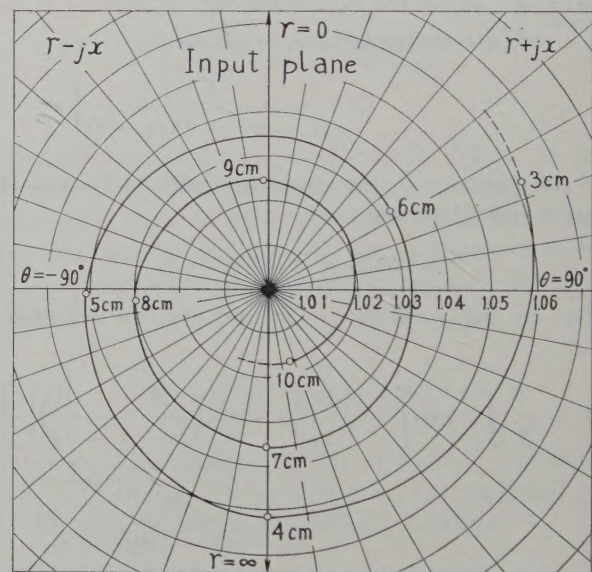


Fig. 4—The curve shows a locus of  $\Gamma$  of the same tapers in Fig. 2 but at a frequency of 5.5 kmc. Lengths of tapers are from 3 cm to 10 cm. See Tables I and IV.

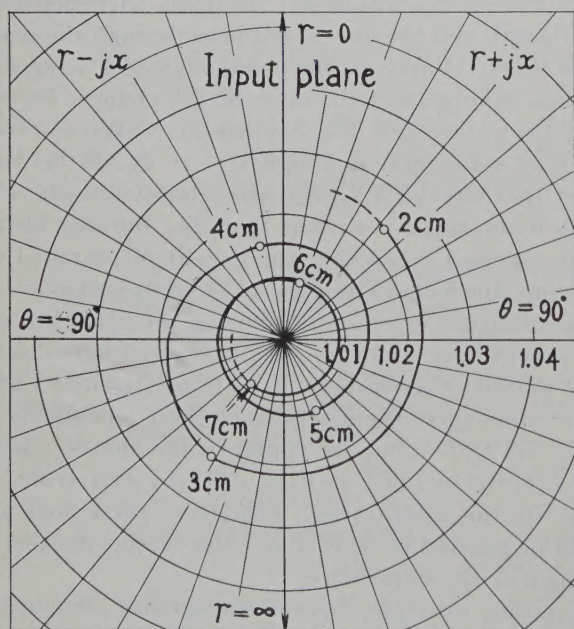


Fig. 2—The curve shows a calculated locus of  $\Gamma$  of typical tapers used to connect WR-229 and WR-159 waveguides. Lengths of tapers are from 2 cm to 7 cm, and the frequency is 7.05 kmc. See Tables I and II. In Figs. 2-4, loci were shown as the admittance even if the conventional notations  $g-jb$  and  $g+jb$  were deleted. Therefore, to use these loci as values of the impedance, they should be rotated by 180° about the centers in the diagrams.

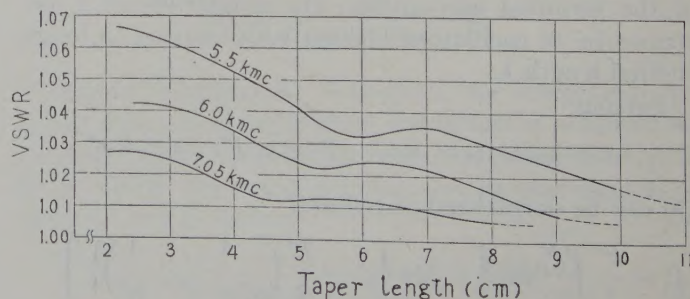


Fig. 5—The curves show the VSWR's given in Figs. 2-4 as a function of taper length for three different frequencies.



TABLE V

	Waveguide	$a$ (in)	$b$ (in)	$\lambda_g$ (cm)		
				4.6 kmc	4.2 kmc	3.9 kmc
Input terminal	WR-229	2.290	1.145	7.9	9.0	10.3
Output terminal	WR-187	1.872	0.872	8.9	10.8	13.1

TABLE VI  
 $f=4.6$  KMC

$h$ (cm)	7	9	11	13	15	17
$h'$	1.07	1.38	1.69	1.99	2.30	2.61
$z_0'$	5.85	7.52	9.21	10.88	12.54	14.20
$\theta_a$	4.3°	3.4°	2.8°	2.4°	2.0°	1.8°

TABLE VII  
 $f=4.2$  KMC

$h$ (cm)	7	9	11	13	15	17
$h'$	0.98	1.26	1.54	1.82	2.10	2.38
$z_0'$	5.35	6.86	8.40	9.94	11.45	12.99
$\theta_a$	4.3°	3.4°	2.8°	2.4°	2.0°	1.8°

TABLE VIII  
 $f=3.9$  KMC

$h$ (cm)	7	9	11	13	15	17
$h'$	0.91	1.17	1.43	1.69	1.95	2.21
$z_0'$	4.96	6.38	7.82	9.20	10.62	12.01
$\theta_a$	4.3°	3.4°	2.8°	2.4°	2.0°	1.8°

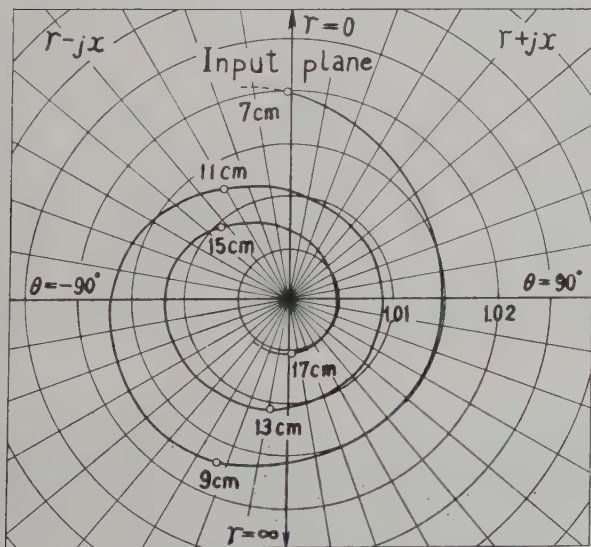


Fig. 6—The curve shows a calculated locus of  $\Gamma$  of typical tapers used to connect WR-229 and WR-187 waveguides. Lengths of tapers are from 7 cm to 17 cm, and the frequency is 4.6 kmc. See Tables V and VI. In Figs. 6–8, loci were shown as the admittance in the same way as those in Figs. 2–4. Therefore, to use these loci as values of the impedance, they also should be rotated by 180° about the centers.

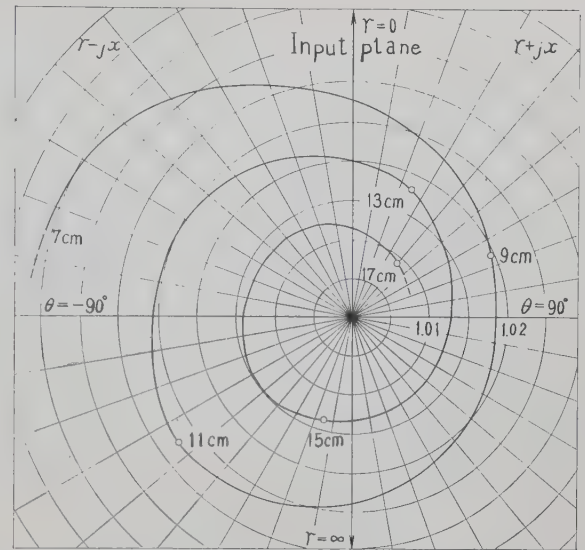


Fig. 7—The curve shows a locus of  $\Gamma$  of the same tapers in Fig. 6 but at a frequency of 4.2 kmc. See Tables V and VII.

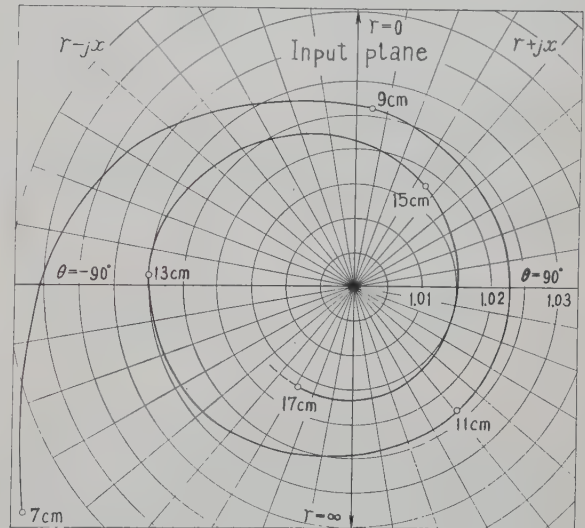


Fig. 8—The curve shows a locus of  $\Gamma$  of the same tapers in Fig. 6 but at a frequency of 3.9 kmc. See Tables V and VIII.

are not exactly pyramidal, *i.e.*,  $a_1/b_1 \neq a_2/b_2$ .) Tables VI–VIII list taper parameters  $h$ ,  $h'$ ,  $z_0'$ , and  $\theta_a$  for 4.6, 4.2, and 3.9 kmc, respectively. Figs. 6–8 show the loci of  $\Gamma$  calculated by an approximate method of graphical integration for the tapers listed in Tables VI–VIII. By using the loci of  $\Gamma$  as illustrated in the examples given in Figs. 2–8, it is possible to design any pyramidally tapered waveguide with considerable accuracy. If  $\Gamma$  is calculated from (10) for two or three discrete taper lengths, a spiral locus of  $\Gamma$  can be traced through the two or three points as illustrated in the above examples.

Finally the behavior of reflection characteristics of these tapers are compared with other tapers. For exponential tapers, Ragan shows a typical figure of VSWR's which reduces to unity at multiples of a half



wavelength and humps regularly.<sup>5</sup> However, as seen from Fig. 5, the VSWR's of these tapers do not reduce to unity for particular taper lengths. Next the reflection characteristics of linear tapers, discussed recently,<sup>6</sup> are somewhat similar to those of the subject pyramidal tapers. However, the reflection of an *E*-plane linear taper is more critically dependent on waveguide dimension (height of waveguide) rather than on frequency. For these *E*-plane linear tapers, the frequency behavior of  $\Gamma$  is quite similar to that shown in Fig. 5. From Stevenson's theoretical calculations on electromagnetic horns, (10) is valid for small flare angles.<sup>7</sup> Since the flare angles of the tapers are usually small, except for extremely short tapers, the values of  $\Gamma$  can be calculated from (10) with very little error.

### EXPERIMENTAL RESULTS

Inasmuch as the derivation of (10) is based on a number of assumptions, the calculated results should be checked experimentally. Measurements were made on the (WR-229/WR-159) tapers described in Tables I and II at a frequency of 7.05 kmc. Since the  $\Gamma$ 's of these tapers are very small, they were measured as accurately as possible. The lengths of tapers varied from 3 cm to 7 cm in intervals of 1 cm, and the data were taken at a frequency of 7.05 kmc. The reflection coefficients  $\Gamma$  were measured in the smaller WR-159 waveguide and for this case  $\Gamma$  is given by

$$\Gamma = \frac{P}{2} \int_0^h \exp j \left\{ \pi - \frac{4\pi}{\lambda_0} \left( z - \frac{P}{2} \left( \frac{1}{z_0 - h} - \frac{1}{z_0 - h + z} \right) \right) \right\} dz \times \frac{dz}{(z_0 - h + z)^3 - P(z_0 - h + z)} \quad (11)$$

Measured results are shown in Fig. 9, and these agree quite well with the data calculated from (11). The mean error in VSWR was as small as 0.004. The conically looped locus of  $\Gamma$  is quite similar to that of a linear taper.<sup>8</sup> Of course, the calculated  $\Gamma$  shown in this graph corresponds to Fig. 2 through a simple transformation. Other measurements were made at frequencies lower than 7.05 kmc, and the agreement was worse, as ex-

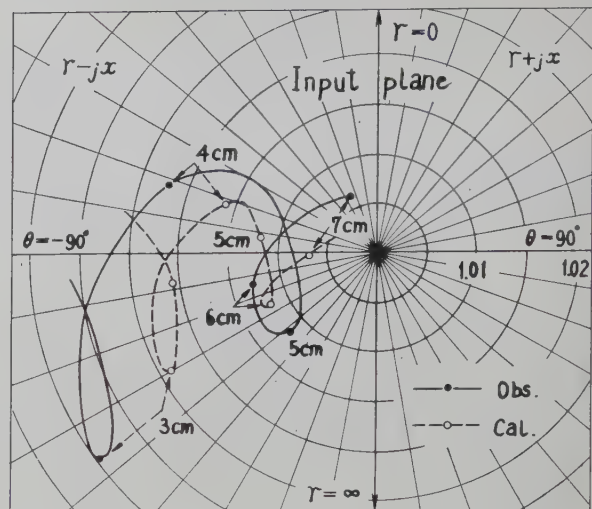


Fig. 9—Measured results of  $\Gamma$  of pyramidally tapered waveguides. The waveguides of the input and output terminals are WR-159 and WR-229. Lengths of tapers are from 3 cm to 7 cm. The solid and dashed curves show the observed and calculated values, respectively. The frequency is 7.05 kmc.

pected. In the frequency range approximately covered by Figs. 2–4, the mean error in the VSWR is less than 0.02 for VSWR smaller than 1.08. As seen from Figs. 2–8, the VSWR's of these particular tapers are smaller than 1.07 or 1.08, and therefore, in practice, the VSWR's computed from (10) or (11) should agree with observed values to within 0.02. For tapers whose VSWR's are smaller than 1.05, the mean error will be as small as 0.01.

### CONCLUSION

The reflection coefficients of pyramidally tapered waveguides can be calculated from (10). As seen from the examples, the VSWR's of typical tapers are smaller than about 1.08, and for most cases, the calculated VSWR's should agree with the experimental values to within 0.02. As shown in Figs. 2–8,  $\Gamma$  decreases almost concentrically for the tapers shorter than  $2\lambda_g$ , and the phase angle sweeps almost one cycle every half a guide wavelength of taper length. Consequently, a spiral of  $\Gamma$  can be traced in the  $K$  plane by calculating  $\Gamma$  for two or three discrete values of taper lengths. For tapers longer than  $2\lambda_g$  the VSWR does not decrease significantly with the taper length.

### ACKNOWLEDGMENT

The author is indebted to his colleagues at the Electrical Communication Laboratory for assistance in undertaking this research. Thanks are also due to K. Tomiyasu and to the PGMTT reviewers for their suggestions on the manuscript.

<sup>5</sup> G. L. Ragan, "Microwave Transmission Circuit," M.I.T. Rad. Lab. Ser., McGraw-Hill Book Co., Inc., New York, N. Y., vol. 9, p. 307; 1948. See Fig. 6.3.

<sup>6</sup> K. Matsumaru, "Reflection coefficient of *E*-plane tapered waveguides," IRE TRANS. ON MICROWAVE THEORY AND TECHNIQUES, vol. MTT-6, pp. 143–149; April, 1958.

<sup>7</sup> A. F. Stevenson, "General theory of electromagnetic horns," *J. Appl. Phys.*, vol. 22, pp. 1447–1460; December, 1951.

<sup>8</sup> K. Matsumaru, "Rebuttal to R. F. H. Yang's comments," IRE TRANS. ON MICROWAVE THEORY AND TECHNIQUES, vol. MTT-7, pp. 175–176; January, 1959.



# Cascade Directional Filter\*

OMAR WING†

**Summary**—A directional filter is a completely matched four-port which exhibits a directional and a filter-like frequency characteristic. This paper explores the properties of  $N$ -directional filters connected in cascade through sections of transmission lines. Analysis shows that if a directional filter admits the equivalent circuit representation offered here, its transfer functions are functions of only one parameter, a susceptance function. When the directional filters are cascaded in a certain way, the over-all transfer functions have the same form as before except that the susceptance function is now the sum of the susceptance functions of the component filters. The last property is an important one. Given a transfer function expressed in terms of a susceptance function, the network designer can expand the susceptance in partial fraction and realize the transfer function using directional filters in cascade, each being characterized by a much simpler susceptance function.

## INTRODUCTION

A directional filter is a completely matched four-port which exhibits a directional and a filter-like frequency characteristic. It may take any of several different physical forms.<sup>1-4</sup> In all cases, it has the following well-known properties:

- 1) It is reflectionless, *i.e.*, all four-ports are matched when they are terminated in their own characteristic impedances.
- 2) It is directional, *i.e.*, signal entering into port 1 emerges at ports 2 and 3, none at 4, etc.
- 3) The transfer function between ports 1 and 2 and that between 1 and 3 are complements of each other, *i.e.*, if one has a band-pass characteristic, the other has a band-elimination characteristic.

This paper explores the properties of  $N$  directional filters connected in cascade through sections of transmission line. Analysis shows that if a directional filter admits the equivalent circuit representation offered here, its transfer functions are functions of one parameter, a susceptance function. When the directional filters are cascaded in a certain way, the over-all transfer functions have the same form as before except that the

susceptance function is now the sum of the susceptance functions of the component directional filters. The last property is an important one, for it offers the network designer flexibility and convenience in realizing a transfer function. Given a transfer function in a form suitable for realization in a directional filter, he can synthesize the network using several directional filters in cascade, each being characterized by a much simpler susceptance function.

## TRANSFER FUNCTIONS OF A DIRECTIONAL FILTER

Let a directional filter admit an equivalent representation shown in Fig. 1. It consists of four two-port

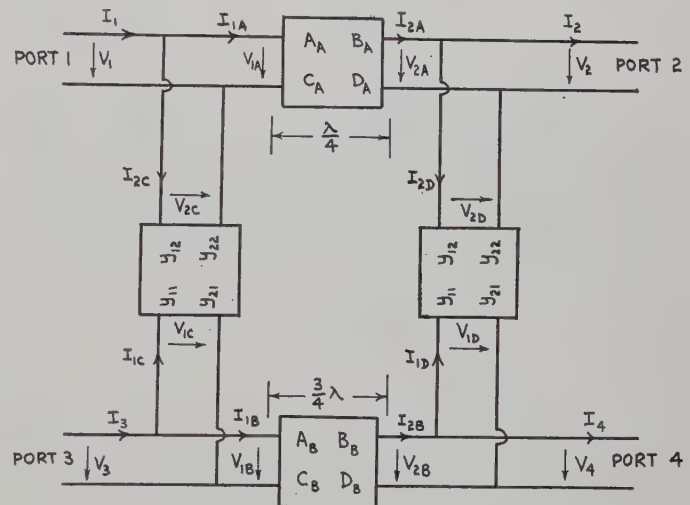


Fig. 1—Schematic diagram of a directional filter.

networks inter-connected to form a network having two input terminals and two output terminals. For a reason which will be apparent later, the two series two-ports are characterized by their  $ABCD$  matrix and the two shunt two-ports are characterized by their short-circuit admittance matrix. Since we are interested in connecting  $N$  of these networks in cascade, the obvious characterization of the filter is the generalized  $ABCD$  matrix:

$$\begin{bmatrix} V_1 \\ V_3 \\ I_1 \\ I_3 \end{bmatrix} = \begin{bmatrix} A_{11} & A_{12} & B_{11} & B_{12} \\ A_{21} & A_{22} & B_{21} & B_{22} \\ C_{11} & C_{12} & D_{11} & D_{12} \\ C_{21} & C_{22} & D_{21} & D_{22} \end{bmatrix} \begin{bmatrix} V_2 \\ V_4 \\ I_2 \\ I_4 \end{bmatrix} \quad (1)$$

In practice, the two shunt two-ports are identical and the two series two-ports are sections of transmission lines  $\lambda/4$  and  $3\lambda/4$  long. As shown in Appendix I, under these conditions the generalized  $ABCD$  matrix takes the following form:

\* Manuscript received by the PGMTT, June 2, 1958; revised manuscript received, August 25, 1958. This paper was presented orally at the joint URSI-IRE conference held in Washington, D. C., on April 24, 1958. Some of the results reported here were obtained while the author was employed at the Bell Telephone Labs., Inc., New York 14, N. Y., in the summer of 1957.

† Dept. of Elec. Eng., Columbia University, New York, N. Y.

<sup>1</sup> S. B. Cohn and F. S. Coale, "Directional channel separation filters," *PROC. IRE*, vol. 44, p. 1018-1024; August, 1956.

<sup>2</sup> R. W. Klopfenstein and J. Epstein, "The polarguide—a constant resistance waveguide filter," *PROC. IRE*, vol. 44, pp. 210-218; February, 1956.

<sup>3</sup> F. S. Coale, "A traveling-wave directional filter," *IRE TRANS. ON MICROWAVE THEORY AND TECHNIQUES*, vol. MTT-4, pp. 256-260; October, 1956.

<sup>4</sup> C. E. Nelson, "Circularly polarized microwave cavity filters," *IRE TRANS. ON MICROWAVE THEORY AND TECHNIQUES*, vol. MTT-5, pp. 136-147; April, 1957.



$$M = \begin{bmatrix} jZ_A y_{22} & iZ_A y_{12} & -jZ_A & 0 \\ -jZ_B y_{12} & -jZ_B y_{11} & 0 & iZ_B \\ -j\frac{1}{Z_A} - jZ_A y_{22}^2 + jZ_B y_{12}^2 & jZ_B y_{11} y_{12} - jZ_A y_{12} y_{22} & jZ_A y_{22} - jZ_B y_{12} \\ -jZ_A y_{22} y_{12} + jZ_B y_{12} y_{11} & \frac{1}{Z_B} - jZ_A y_{21}^2 + jZ_B y_{11}^2 & jZ_A y_{12} - jZ_B y_{11} \end{bmatrix} \quad (2)$$

where

$Z_A$  = characteristic impedance of transmission line 1.  
 $Z_B$  = characteristic impedance of transmission line 2.  
 $y_{11}$ ,  $y_{12}$ ,  $y_{22}$  = short-circuit admittance parameters of the two-port.

In operation, the ports are terminated in their own characteristic impedances, so that the terminal voltages and current satisfy a set of constraints given by

$$\begin{aligned} V_1 &= E - I_1 Z_A \\ V_2 &= Z_A I_2 \\ V_3 &= -Z_B I_3 \\ V_4 &= Z_B I_4. \end{aligned} \quad (3)$$

We shall now derive the four transfer voltage ratios and from these deduce the necessary and sufficient conditions that the parameters of  $y_{11}$ ,  $y_{12}$ , and  $y_{22}$  must satisfy in order to realize the directional and reflectionless properties mentioned earlier. As shown in Appendix II, we have

$$\frac{V_4}{E} = \frac{jZ_B y_{12}(Z_B y_{11} - Z_A y_{22})}{\Delta} \quad (4)$$

where

$$\Delta = (2 + Z_A y_{22} + Z_B y_{11} + Z_A Z_B y_{11} y_{22} - Z_A Z_B y_{12}^2)^2. \quad (5)$$

It is clear from (4) that the directional property is realized if

$$Z_B y_{11} = Z_A y_{22}. \quad (6)$$

Using (6) we find

$$\frac{V_1}{E} = \frac{2 + 4Z_A y_{22} + 2Z_A^2 y_{22}^2 + Z_A^2 y_{22}^2 (Z_A y_{22} - Z_A y_{12}^2 / y_{11})}{\Delta}.$$

The reflectionless property is realized if

$$y_{11} y_{22} = y_{12}^2 \quad (7)$$

for then  $V_1/E = \frac{1}{2}$ , and port 1 is matched. In fact, by a well-known theorem<sup>5</sup> on the properties of a directional coupler, all four ports are matched.

Eq. (7) restricts the structure of the two-terminal network to be one whose usual open circuit impedance

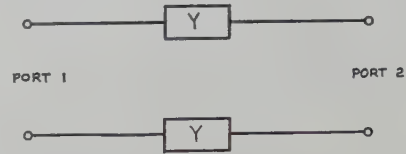


Fig. 2—The simplest realization of the shunt two-port.

parameters do not exist. The simplest realization of the network is one which has only series admittance as shown in Fig. 2.

Using (6) and (7), we find the other two transfer voltage ratios to be

$$\frac{V_2}{E} = -\frac{j}{2} \frac{1}{1 + Z_A y_{22}} = -\frac{j}{2} \frac{1}{1 + Z_B y_{11}}, \quad (8)$$

$$\begin{aligned} \frac{V_3}{E} &= -\frac{1}{2} \sqrt{\frac{Z_B}{Z_A}} \frac{Z_A y_{22}}{1 + Z_A y_{22}} \\ &= -\frac{1}{2} \sqrt{\frac{Z_B}{Z_A}} \frac{Z_B y_{11}}{1 + Z_B y_{11}}. \end{aligned} \quad (9)$$

It is seen that the two voltages are 90° out of phase—a well-known property of directional couplers. Moreover, let  $P_2$  be the power delivered to the load  $Z_A$  at port 2 and  $P_3$  be that to  $Z_B$  at port 3. Then using (8) and (9), we have

$$P_2 + P_3 = \frac{E^2}{4Z_A} = \text{constant}.$$

The two transfer characteristics are therefore complements of each other. In particular, if  $y_{22}$  is a simple resonant circuit,  $V_2/E$  exhibits a band elimination characteristic while  $V_3/E$  one of the bandpass.

The above analysis shows that a directional filter is completely characterized by one parameter, the susceptance function  $y_{22}$  (or alternately,  $y_{11}$ ), as asserted earlier. Except for the factor  $-j$ , in all aspects,  $V_2/E$  as given by (8) is much like the transfer function of a constant-resistance bridge-T network.<sup>6</sup>

#### CASCADE DIRECTIONAL FILTER

If the two-port network parameters satisfy (6) and (7), the  $ABCD$  matrix,  $M$ , is simplified to the following:

<sup>5</sup> The theorem states that if a symmetrical four-port possesses the directional property and is matched at one of its ports, all four ports are matched.

<sup>6</sup> H. W. Bode, "Network Analysis and Feedback Amplifier Design," D. Van Nostrand Co., New York, N. Y., p. 272; 1945.



$$M = j \begin{bmatrix} Z_B y_{11} & Z_A y_{11} \sqrt{\frac{Z_B}{Z_A}} & -Z_A & 0 \\ -Z_B y_{11} \sqrt{\frac{Z_B}{Z_A}} & -Z_B y_{11} & 0 & Z_B \\ -\frac{1}{Z_A} & 0 & Z_B y_{11} & -Z_B y_{11} \sqrt{\frac{Z_B}{Z_A}} \\ 0 & \frac{1}{Z_B} & Z_A y_{11} \sqrt{\frac{Z_B}{Z_A}} & -Z_B y_{11} \end{bmatrix}. \quad (10)$$

If we are to connect a transmission line of length  $\frac{1}{4}\lambda$  to port 1 and one  $\frac{3}{4}\lambda$  to port 4 (Fig. 3), the over-all  $ABCD$  matrix becomes

$$P = \begin{bmatrix} 1 & 0 & -Z_A Z_B y_{11} & Z_A Z_B y_{11} \sqrt{\frac{Z_B}{Z_A}} \\ 0 & 1 & Z_A Z_B y_{11} \sqrt{\frac{Z_B}{Z_A}} & -Z_B^2 y_{11} \\ -\frac{Z_B}{Z_A} y_{11} & -y_{11} \sqrt{\frac{Z_B}{Z_A}} & 1 & 0 \\ -y_{11} \sqrt{\frac{Z_B}{Z_A}} & -y_{11} & 0 & 1 \end{bmatrix}. \quad (11)$$

which is of the form

$$\begin{bmatrix} I & Dy_{11} \\ Ey_{11} & I \end{bmatrix}$$

where

$$I = \begin{bmatrix} 1 & 0 \\ 0 & 1 \end{bmatrix}$$

$$D = \begin{bmatrix} -Z_A Z_B & Z_A Z_B \sqrt{\frac{Z_B}{Z_A}} \\ Z_A Z_B \sqrt{\frac{Z_B}{Z_A}} & -Z_B^2 \end{bmatrix}$$

$$E = - \begin{bmatrix} \frac{Z_B}{Z_A} & \sqrt{\frac{Z_B}{Z_A}} \\ \sqrt{\frac{Z_B}{Z_A}} & 1 \end{bmatrix}.$$

Note that  $DE=0$ , and  $ED=0$ .

Let us next cascade  $N-1$  such structures, the first characterized by  $P_1$ , the second  $P_2$ , etc. The over-all matrix becomes

$$P_{N-1} P_{N-2} \cdots P_2 P_1 = \begin{bmatrix} I & Dy' \\ Ey' & I \end{bmatrix}$$

where

$$y' = y_{11}^{(1)} + y_{11}^{(2)} + \cdots + y_{11}^{(N-1)}.$$

Finally, to  $(N-1)$  such structures we must add, at the end, one more directional filter to complete an  $N$ -section cascade directional filter. The over-all network is shown in Fig. 4 and the over-all generalized  $ABCD$  matrix is given by

$$M P_{N-1} P_{N-2} \cdots P_1 = M \begin{bmatrix} I & Dy' \\ Ey' & I \end{bmatrix} = j \begin{bmatrix} Z_B Y & Z_A Y \sqrt{\frac{Z_B}{Z_A}} & -Z_A & 0 \\ -Z_B Y \sqrt{\frac{Z_B}{Z_A}} & -Z_B Y & 0 & Z_B \\ -\frac{1}{Z_A} & 0 & Z_B Y & -Z_B Y \sqrt{\frac{Z_B}{Z_A}} \\ 0 & \frac{1}{Z_B} & Z_A Y \sqrt{\frac{Z_B}{Z_A}} & -Z_B Y \end{bmatrix}. \quad (12)$$



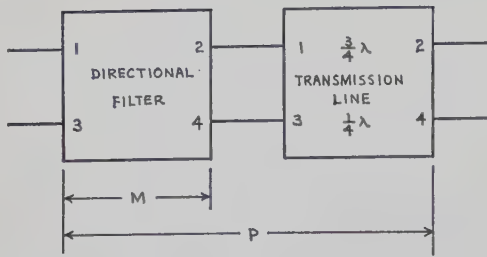
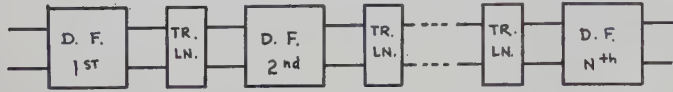


Fig. 3—One unit of a cascade directional filter.

Fig. 4—An  $N$ -section cascade directional filter.

where

$$Y = y_{11}^{(1)} + y_{11}^{(2)} + \cdots + y_{11}^{(N)}.$$

Comparing (12) with the  $ABCD$  matrix for one directional filter, we see that both are the same except  $y_{11}$  in (10) is replaced by  $Y$ . Therefore the cascade directional filter is equivalent to one directional filter whose susceptance function  $y_{11}$  (or  $y_{22}$ ) is the sum of the susceptance functions of the component directional filters. The voltage ratios for a cascade directional filter are

$$\frac{V_4}{E} = 0$$

$$\frac{V_1}{E} = \frac{1}{2}$$

$$\frac{V_2}{E} = -\frac{j}{2} \frac{1}{1 + Z_B[y_{11}^{(1)} + \cdots + y_{11}^{(N)}]} \quad (13)$$

$$\frac{V_3}{E} = -\frac{1}{2} \sqrt{\frac{Z_B}{Z_A}} \frac{Z_B[y_{11}^{(1)} + \cdots + y_{11}^{(N)}]}{1 + Z_B[y_{11}^{(1)} + \cdots + y_{11}^{(N)}]} \quad (14)$$

Eqs. (13) and (14) suggest that in synthesis, the desired susceptance  $Y$  should be expanded in the Foster's partial fraction form, each fraction being realized by one directional filter whose  $y_{11}$  is a simple resonant circuit.

In the special case in which all  $y_{11}$ 's are identical resonant circuits, the loaded  $Q$  of an  $N$ -section cascade directional filter is  $1/N$  times the loaded  $Q$  of one directional filter.

#### REMARKS

This paper has considered only one particular way of cascading the directional filters, namely, they are separated by two sections of transmission line  $\frac{1}{4}\lambda$  and  $\frac{3}{4}\lambda$  long as shown in Fig. 3. With different lengths, the over-all four-port may have other interesting properties.

The analysis given here is applicable only to directional filters which admit the equivalent circuit representation shown in Fig. 1. As evident from the figure, the unavoidable junction effect in a practical realization has been completely ignored. Moreover, the length of the sections of transmission line may be frequency dependent, as in the case of a hollow guide. In that case, the results contained here are valid only in the "immediate" neighborhood of the average resonant frequency of the various  $y$ 's. A complete analysis is very complicated even for first-order approximation. We shall leave this problem to an enterprising graduate student.

#### APPENDIX I

##### DERIVATION OF (2)

With reference to Fig. 1, the two series two-ports, which are sections of transmission line  $\frac{1}{4}\lambda$  and  $\frac{3}{4}\lambda$  long, are characterized by their respective  $ABCD$  matrix as follows:

$$\begin{aligned} \begin{bmatrix} V_{2A} \\ I_{2A} \end{bmatrix} &= \begin{bmatrix} A_A & B_A \\ C_A & D_A \end{bmatrix} \begin{bmatrix} V_{1A} \\ I_{1A} \end{bmatrix} \\ &= \begin{bmatrix} 0 & -jZ_A \\ -j\frac{1}{Z_A} & 0 \end{bmatrix} \begin{bmatrix} V_{1A} \\ I_{1A} \end{bmatrix} \end{aligned} \quad (15)$$

$$\begin{aligned} \begin{bmatrix} V_{2B} \\ I_{2B} \end{bmatrix} &= \begin{bmatrix} A_B & B_B \\ C_B & D_B \end{bmatrix} \begin{bmatrix} V_{1B} \\ I_{1B} \end{bmatrix} \\ &= \begin{bmatrix} 0 & jZ_B \\ j\frac{1}{Z_B} & 0 \end{bmatrix} \begin{bmatrix} V_{1B} \\ I_{1B} \end{bmatrix}. \end{aligned} \quad (16)$$

As stated in the text, let the two identical shunt two-ports be characterized by the short-circuit admittance parameters:

$$\begin{bmatrix} I_{1C} \\ I_{2C} \end{bmatrix} = \begin{bmatrix} y_{11} & y_{12} \\ y_{21} & y_{22} \end{bmatrix} \begin{bmatrix} V_{1C} \\ V_{2C} \end{bmatrix} \quad (17)$$

$$\begin{bmatrix} I_{1D} \\ I_{2D} \end{bmatrix} = \begin{bmatrix} y_{11} & y_{12} \\ y_{21} & y_{22} \end{bmatrix} \begin{bmatrix} V_{1D} \\ V_{2D} \end{bmatrix}. \quad (18)$$

The terminal conditions are

$$V_{1A} = V_{2C} = V_1$$

$$V_{2A} = V_{2D} = V_2$$

$$V_{1B} = V_{1C} = V_3$$

$$V_{2B} = V_{1D} = V_4$$

$$I_{1A} = I_1 - I_{2C}$$

$$I_2 = I_{2A} - I_{2D}$$

$$I_{1B} = I_3 - I_{1C}$$

$$I_4 = I_{2B} - I_{1D}. \quad (19)$$



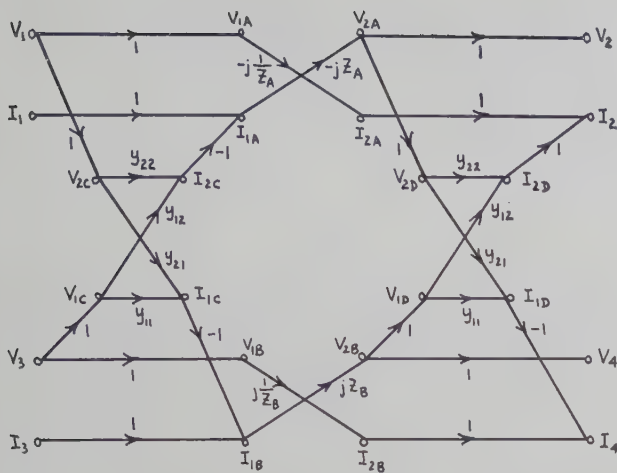


Fig. 5—The signal flow graph of a directional filter (see Fig. 1).

Algebraic manipulation of (15)–(19) to eliminate all variables except  $V_1$ ,  $V_2$ ,  $V_3$ ,  $V_4$ ,  $I_1$ ,  $I_2$ ,  $I_3$  and  $I_4$  leads to (2) in the text. Alternately, one can employ the technique of signal flow graph.<sup>7,8</sup> Fig. 5 shows the signal flow graph which corresponds to (15)–(19). Eq. (2) is obtained by finding the “gains” in the following manner:

$$A_{11} = \text{gain from } V_1 \text{ to } V_2 = jZ_A y_{22}$$

$$A_{12} = \text{gain from } V_3 \text{ to } V_2 = jZ_A y_{12}$$

$$B_{11} = \text{gain from } I_1 \text{ to } V_2 = -jZ_A$$

$$B_{12} = \text{gain from } I_2 \text{ to } V_2 = 0.$$

## APPENDIX II

### DERIVATION OF (4)–(9)

The constraints given by (3), which are the terminating conditions on each port, are

$$V_1 = E - I_1 Z_A$$

$$V_2 = Z_A I_2$$

$$V_3 = -Z_B I_3$$

$$V_4 = Z_B I_4.$$

Using these equations and those expressed by (2), one

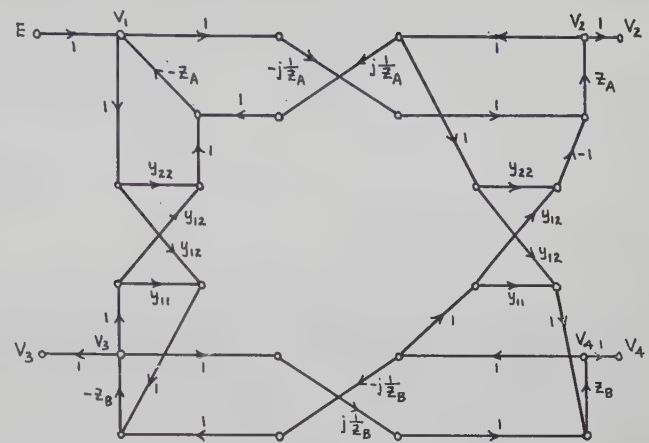


Fig. 6—The signal flow graph of a terminated directional filter.

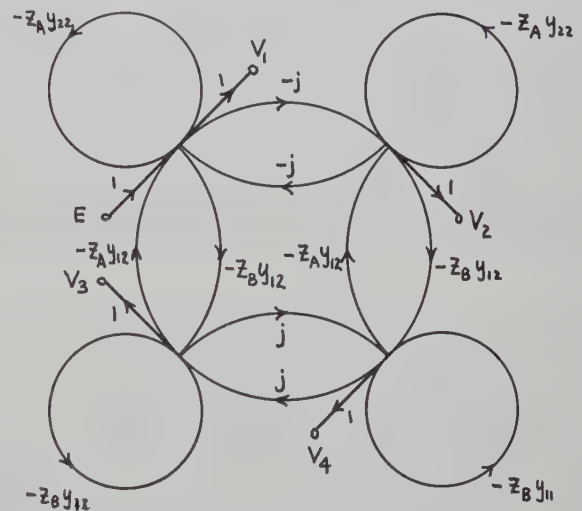


Fig. 7—The simplified version of Fig. 6.

can eliminate all current variables and obtain a set of four equations in four unknowns,  $V_1$ ,  $V_2$ ,  $V_3$ ,  $V_4$ . Solving for each in terms of  $E$ , we have (4)–(9). The algebra is straightforward though extremely involved. The author is convinced that the signal flow graph technique is superior.

With reference to Fig. 5, we first invert<sup>7</sup> the paths from  $V_2$  to  $I_1$  and from  $V_4$  to  $I_3$ . Adding the constraints of (3) to the “inverted” flow graph, we have Fig. 6.

Fig. 6 can be simplified, and the final form is shown in Fig. 7, from which the various “gains” as expressed by (4)–(9) are obtained by inspection.

<sup>7</sup> S. Mason, “Properties of signal flow graph,” PROC. IRE, vol. 41, pp. 1144–1156; September, 1953.

<sup>8</sup> S. Mason, “Further properties of signal flow graph,” PROC. IRE, vol. 44, pp. 920–926; July, 1956.



# Propagation in a Dielectric-Loaded Parallel Plane Waveguide\*

MARVIN COHN†

**Summary**—A theoretical analysis of wave propagation in a parallel plane waveguide partially filled with a dielectric is performed. This transmission line is a symmetrical three-region structure consisting of two infinite parallel conducting planes with a dielectric slab of rectangular cross section between and contacting each of the planes. It has been found that TEM and TM modes cannot propagate on this structure. This investigation is concerned with TE modes, although hybrid modes can also propagate on this line. The lowest order TE mode, which is the dominant mode, has no cutoff and hence is inherently suited to extremely wide bandwidth operation. Equations have been presented for the field components, guide wavelength, cutoff criteria, power handling capabilities, wall losses, and dielectric losses as a function of the operating wavelength, waveguide dimensions, and material constants. In the case of the dominant mode, design curves covering a large range of wavelengths, dimensions, and dielectric constants are presented. For a loosely bound wave, the losses are comparable or less than those of conventional rectangular waveguide and the power handling capacity is an order of magnitude greater.

## INTRODUCTION

THE structure to be analyzed consists of two infinite parallel conducting planes with a dielectric slab of rectangular cross section between, and contacting each of the planes (see Fig. 1). It will be shown that this line is capable of extremely broad-band and high-power operation and that its losses are comparable to that of conventional rectangular waveguide. It has the disadvantages of being a partially open structure and being larger than conventional guide. In the millimeter wavelength region the last property may, however, be an advantage.

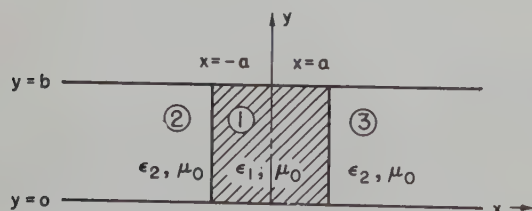


Fig. 1—Cross section of the parallel plane waveguide partially filled with a dielectric. The positive  $z$ -direction is out of the paper.

The propagation of TE modes on this line has been theoretically investigated. Expressions are presented for the field intensities, guide wavelength, cutoff conditions, power handling capabilities, wall losses, and dielectric losses as a function of the operating wavelength, waveguide dimensions, and material constants. In the case of the lowest order TE mode, which is the dominant mode

of this line, many of these quantities have been computed and plotted to serve as design curves.

It can be shown that both TEM and TM waves cannot be propagated on this line. The propagation of hybrid modes on this type of line has been analyzed by Tischer,<sup>1,2</sup> and in an independent investigation, Moore and Beam<sup>3</sup> have studied both TE and hybrid modes. The report of the latter authors, however, has not been referenced by the principal indexes in the field. The latter paper contains errors in the equations concerning dielectric and metallic losses and in the curve of metallic attenuation. One of the curves showing the cutoff condition for the hybrid modes is also in error.<sup>4</sup>

In a recent paper, Vartanian, Ayres, and Helgesson<sup>5</sup> have shown that improved bandwidth and power handling capabilities can be obtained with a related structure consisting of a dielectric slab centered in a rectangular waveguide.

Interest has been aroused in both this structure and a coaxial line partially filled with a dielectric, which is similar to a parallel plane line wrapped in a circle, because they have properties suitable for use in a non-reciprocal ferrite device.<sup>6-8</sup>

## FIELD COMPONENTS OF THE TE MODES

Since the derivation of the field components is available in the paper by Moore and Beam,<sup>3</sup> it will not be repeated here. A report<sup>9</sup> has been published which gives a detailed derivation of the TE mode field components and includes an extensive discussion of the next higher order TE mode.

<sup>1</sup> F. J. Tischer, "Microwellenleitung mit geringen Verlusten," (Waveguides with small losses), *Arch. elekt. Übertragung*, vol. 7, pp. 592-596; December, 1953.

<sup>2</sup> F. J. Tischer, "The H-guide, a waveguide for microwaves," 1956 IRE CONVENTION RECORD, pt. 5, pp. 44-47.

<sup>3</sup> R. A. Moore and R. E. Beam, "A duo-dielectric parallel plane waveguide," *Proc. NEC*, vol. 12, pp. 689-705; April, 1957.

<sup>4</sup> During recent communications with R. A. Moore, he has verified the existence of the cited errors.

<sup>5</sup> P. H. Vartanian, W. P. Ayres, and A. L. Helgesson, "Propagation in dielectric slab-loaded rectangular waveguide," *IRE TRANS. ON MICROWAVE THEORY AND TECHNIQUES*, Vol. MTT-6, pp. 215-222; April, 1958.

<sup>6</sup> B. J. Duncan, L. Swern, and K. Tomiyasu, "Microwave magnetic field in dielectric-loaded coaxial line," *PROC. IRE*, vol. 46, pp. 500-502; February, 1958. This qualitative analysis, however, yields an erroneous picture of the field configuration in dielectric-loaded parallel plane line.

<sup>7</sup> M. Cohn, "Parallel plane waveguide partially filled with a dielectric," *Proc. IRE*, vol. 46, pp. 1952-1953; December, 1958.

<sup>8</sup> K. J. Button, "Theory of non-reciprocal ferrite phase shifters in dielectric-loaded coaxial line," *J. Appl. Phys.*, vol. 29, pp. 998-1000; June, 1958.

<sup>9</sup> M. Cohn, "Parallel Plane Waveguide Partially Filled with a Dielectric," The Johns Hopkins Univ., Radiation Lab., Baltimore, Md., Tech. Rep. No. AF-56; November, 1958.

\* Manuscript received by the PGM-TT, June 23, 1958; revised manuscript received, December 29, 1958.

† Radiation Lab. The Johns Hopkins University, Baltimore, Md.



A cross section of the transmission line to be analyzed and the coordinate system used are shown in Fig. 1. The symmetry of the transmission line causes all solutions to fall into two groups, even and odd modes. These modes are defined by

$$E_{ye}(x) = E_{ye}(-x) \quad \text{and} \quad E_{yo}(x) = -E_{yo}(-x), \quad (1)$$

where the subscripts *e* and *o* refer to the even and odd modes, respectively. The expressions for the field components of the even and odd order TE modes in each of the three regions are listed below. The factor  $e^{j(\omega t - \beta z)}$ , which is common to each of these expressions, has been eliminated in the interest of brevity.

#### Region 1, even modes

$$H_{x1e} = A_e \frac{\beta}{k_{1e}} \cos k_{1e}x \quad (2a)$$

$$H_{z1e} = jA_e \sin k_{1e}x \quad (2b)$$

$$E_{y1e} = -A_e \frac{\omega\mu_0}{k_{1e}} \cos k_{1e}x \quad (2c)$$

#### Region 2, even modes

$$H_{x2e} = A_e \frac{\beta}{k_{2e}} (\sin k_{1e}a) e^{k_{2e}(a+x)} \quad (3a)$$

$$H_{z2e} = -jA_e (\sin k_{1e}a) e^{k_{2e}(a+x)} \quad (3b)$$

$$E_{y2e} = -A_e \frac{\omega\mu_0}{k_{2e}} (\sin k_{1e}a) e^{k_{2e}(a+x)} \quad (3c)$$

#### Region 3, even modes

$$H_{x3e} = A_e \frac{\beta}{k_{2e}} (\sin k_{1e}a) e^{k_{2e}(a-x)} \quad (4a)$$

$$H_{z3e} = jA_e (\sin k_{1e}a) e^{k_{2e}(a-x)} \quad (4b)$$

$$E_{y3e} = -A_e \frac{\omega\mu_0}{k_{2e}} (\sin k_{1e}a) e^{k_{2e}(a-x)} \quad (4c)$$

#### Region 1, odd modes

$$H_{x1o} = jA_o \frac{\beta}{k_{1o}} \sin k_{1o}x \quad (5a)$$

$$H_{z1o} = A_o \cos k_{1o}x \quad (5b)$$

$$E_{y1o} = -jA_o \frac{\omega\mu_0}{k_{1o}} \sin k_{1o}x \quad (5c)$$

#### Region 2, odd modes

$$H_{x2o} = jA_o \frac{\beta}{k_{2o}} (\cos k_{1o}a) e^{k_{2o}(a+x)} \quad (6a)$$

$$H_{z2o} = A_o (\cos k_{1o}a) e^{k_{2o}(a+x)} \quad (6b)$$

$$E_{y2o} = -jA_o \frac{\omega\mu_0}{k_{2o}} (\cos k_{1o}a) e^{k_{2o}(a+x)} \quad (6c)$$

#### Region 3, odd modes

$$H_{x3o} = -jA_o \frac{\beta}{k_{2o}} (\cos k_{1o}a) e^{k_{2o}(a-x)} \quad (7a)$$

$$H_{z3o} = A_o (\cos k_{1o}a) e^{k_{2o}(a-x)} \quad (7b)$$

$$E_{y3o} = jA_o \frac{\omega\mu_0}{k_{2o}} (\cos k_{1o}a) e^{k_{2o}(a-x)} \quad (7c)$$

$A_e$  and  $A_o$  are arbitrary constants.

The inner and outer transverse distribution constants ( $k_1$  and  $k_2$ ) are related to the propagation constant ( $\beta$ ), frequency ( $\omega$ ), and properties of the medium ( $\mu$  and  $\epsilon$ ) by the following equations:

$$\beta^2 = -k_1^2 + \omega^2\mu_0\epsilon_1 \quad (8)$$

$$\beta^2 = k_2^2 + \omega^2\mu_0\epsilon_2 \quad (9)$$

In order to match boundary conditions at the air-dielectric interfaces ( $x = \pm a$ ), the following conditional equations must be satisfied.

$$k_{2e} = k_{1e} \tan k_{1e}a \quad (10)$$

where ( $k_{1e}a$ ) must be between 0 and  $\pi/2$ ,  $\pi$  and  $3\pi/2$ , etc.

$$k_{2o} = -k_{1o} \cot k_{1o}a \quad (11)$$

where ( $k_{1o}a$ ) must be between  $\pi/2$  and  $\pi$ ,  $3\pi/2$  and  $2\pi$ , etc.

#### SOLUTION OF THE CONDITIONAL EQUATION AND MODE DESIGNATION

Since the propagation constant must be the same in all regions, the following equations must be satisfied:

$$k_{1e}^2 - \omega^2\mu_0\epsilon_1 = -k_{2e}^2 - \omega^2\mu_0\epsilon_2 \quad (12)$$

$$k_{1o}^2 - \omega^2\mu_0\epsilon_1 = -k_{2o}^2 - \omega^2\mu_0\epsilon_2 \quad (13)$$

By substituting (10) into (12) (eliminating  $k_{2e}$ ), and substituting (11) into (13) (eliminating  $k_{2o}$ ), the following equations result.

$$\pi^2 \left( \frac{2a}{\lambda_0} \right)^2 (K_1 - K_2) = \left[ \frac{k_{1e}a}{\cos k_{1e}a} \right]^2, \quad \text{even modes} \quad (14)$$

$$\pi^2 \left( \frac{2a}{\lambda_0} \right)^2 (K_1 - K_2) = \left[ \frac{k_{1o}a}{\sin k_{1o}a} \right]^2, \quad \text{odd modes} \quad (15)$$

where  $K_1 = \epsilon_1/\epsilon_o$ ,  $K_2 = \epsilon_2/\epsilon_o$ ,  $\lambda_o$  = free-space wavelength. Since (14) and (15) are transcendental, graphical techniques have been used to obtain their roots. If the quantities

$$y = \left[ \frac{k_{1e}a}{\cos k_{1e}a} \right]^2 \quad \text{and} \quad y = \left[ \frac{k_{1o}a}{\sin k_{1o}a} \right]^2$$

are plotted as functions of ( $k_{1e}a$ ) and ( $k_{1o}a$ ) over their respective restricted intervals, the curves of Fig. 2 will result. Both sets of curves can be plotted on the same graph since their intervals of applicability are contiguous and interlaced, but do not overlap. Each curve



corresponds to a different TE mode. Values of  $(2a/\lambda_o)$  and  $(K_1 - K_2)$  can be selected and a horizontal line corresponding to the equation

$$y = \pi^2 \left( \frac{2a}{\lambda_o} \right)^2 (K_1 - K_2)$$

can be drawn across the family of curves of Fig. 2. The values of  $(k_{1e}a)$  and  $(k_{2e}a)$  at the intersections of the horizontal line and the curves are the roots of (14) and (15).

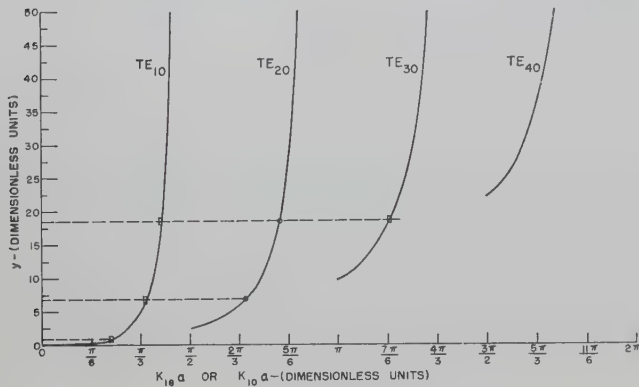


Fig. 2—Graphical technique for obtaining the roots of the conditional equation for the even and odd order TE modes.

It should be noted from Fig. 2 that the lowest order even mode ( $0 < k_{1e}a < \pi/2$ ) can exist down to zero frequency. It is the dominant mode of this structure and will be designated the  $TE_{10}$  mode. Successively higher modes will be designated  $TE_{20}$ ,  $TE_{30}$ , etc. The  $m$ th mode is designated  $TE_{mo}$ . The even modes correspond to  $m$  being an odd integer, and vice versa. The zero shows that there is no variation of the fields in the  $y$  direction. Eqs. (14) and (15) show that in order for the  $TE_{mo}$  mode to propagate, the following inequality must be satisfied.

$$\frac{2a}{\lambda_o} > \frac{m-1}{2\sqrt{\Delta K}}, \quad \Delta K = K_1 - K_2. \quad (16)$$

The procedure for obtaining the roots of (14) and (15), as shown in Fig. 2, was repeated for many values of  $(2a/\lambda_o)$  and  $\Delta K$ . The results for the dominant mode are shown in Fig. 3. The cutoff loci for various higher order TE modes are shown on this and many succeeding families of curves. Using the results of Fig. 3 and (10), values of  $(k_{2e}a)$ , the transverse distribution parameter for the outer regions, can be calculated as a function of  $(2a/\lambda_o)$  and  $\Delta K$ . The results of this calculation for the dominant mode are presented in Fig. 4.

The values of  $(k_{1e}a)$  and  $(k_{2e}a)$  are sufficient to enable one to plot the transverse field distributions. Sample plots of the field configuration, as well as graphs of the field magnitudes for the dominant mode ( $TE_{10}$ ) and the

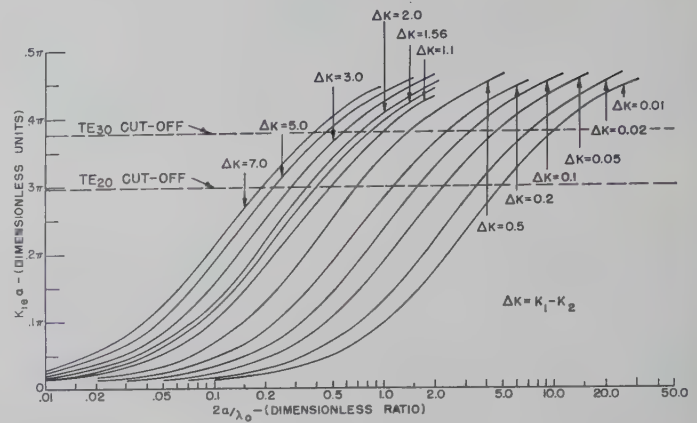


Fig. 3—Curves of the inner transverse distribution parameter  $(k_{1e}a)$  of the dominant mode as a function of the normalized slab width  $(2a/\lambda_o)$ , and the difference of the dielectric constants  $(\Delta K)$ .

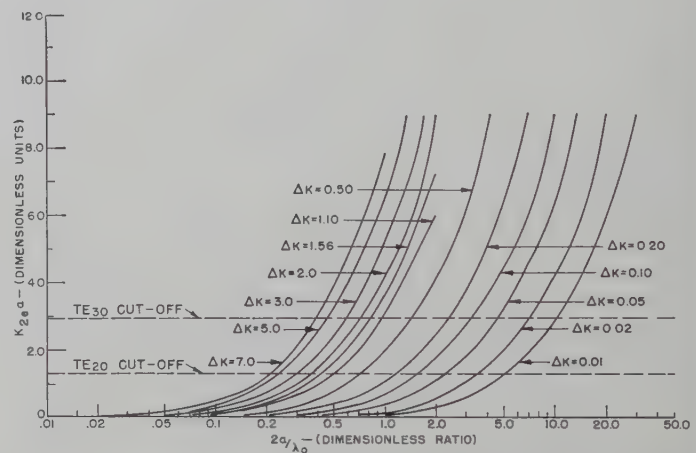


Fig. 4—Curves of the outer transverse distribution parameter  $(k_{2e}a)$  of the dominant mode as a function of the normalized slab width  $(2a/\lambda_o)$ , and the difference of the dielectric constants  $(\Delta K)$ .

lowest order odd mode ( $TE_{20}$ ), are shown in Fig. 5 and Fig. 6. The amount of sinusoidal or cosinusoidal variation in Region 1 is determined by  $(k_{1e}a)$ , and the rate of exponential decay in Regions 2 and 3 is determined by  $k_{2e}$ , which is found from  $(k_{2e}a)$ .

It should be noted from (2) through (7) and Fig. 5 and Fig. 6, that none of the field components is a function of  $y$ . Guide wavelength, cutoff wavelength, and field extent of the TE modes are, therefore, independent of the distance  $b$  between the two conducting planes. This distance can be varied to suppress the hybrid modes, which are a function of  $y$ , and yet not cause cutoff of the TE modes. The cutoff criterion for the hybrid modes has been derived by Moore and Beam.<sup>8</sup> Their formula for determining the critical distance between the conducting planes,  $b_c$ , which suppresses all hybrid modes, is re-expressed below.

$$\frac{b_c}{\lambda_o} = \frac{1}{2} \sqrt{\frac{1 + \tan^2 k_{1e}a}{1 + K_1 \tan^2 k_{1e}a}}. \quad (17)$$



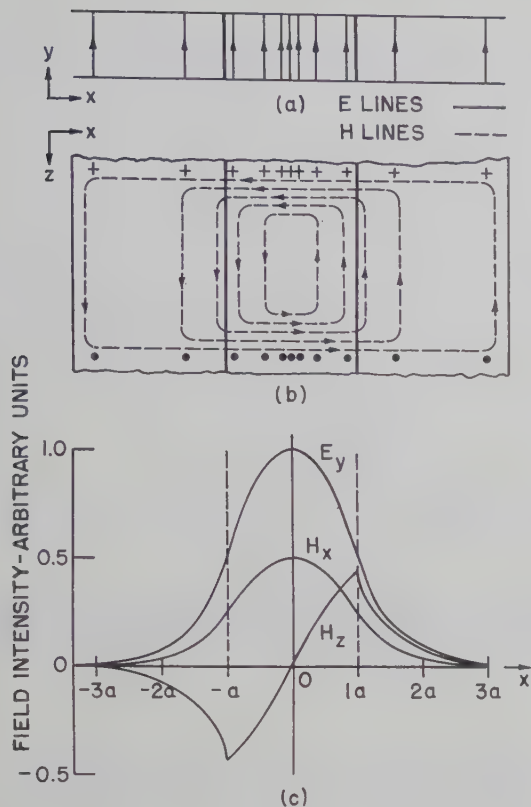


Fig. 5—(a) Cross-sectional view, and (b) top view of the field configuration of the dominant mode (TE<sub>10</sub>); (c) magnitude of the field components of this mode.

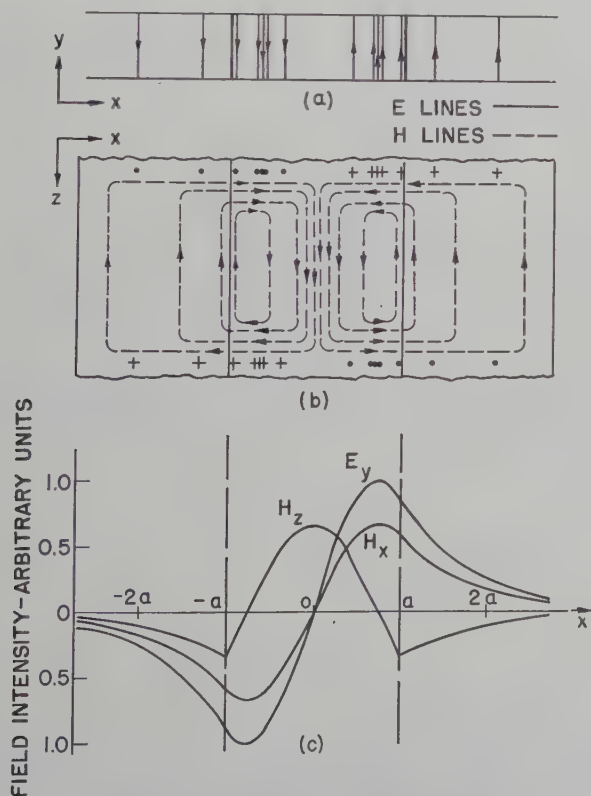


Fig. 6—(a) Cross-sectional view, and (b) top view of the field configuration of the lowest order antisymmetric mode (TE<sub>20</sub>); (c) magnitude of the field components of this mode.

This relationship is presented graphically in Fig. 7. Since TEM and TM modes cannot propagate on this line, only TE modes can exist if  $b < b_c$ . If, in addition, the following inequality is satisfied, single mode (TE<sub>10</sub>) operation is assured.

$$\frac{2a}{\lambda_0} < \frac{1}{2\sqrt{\Delta K}} \quad (18)$$

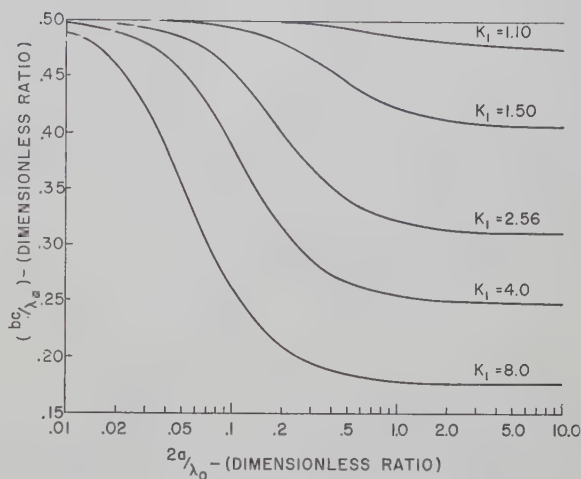


Fig. 7—Cutoff condition for the hybrid modes as a function of the normalized slab width ( $2a/\lambda_0$ ) and dielectric constant ( $K_1$ ).

If a conducting wall is placed at the  $x=0$  plane, all of the even TE modes will be suppressed, but the odd modes will be unaffected. The dominant mode of the resulting trough line (half of the original line) will be the TE<sub>20</sub> mode.

The ratio of the cutoff wavelengths of the TE<sub>20</sub> and the TE<sub>40</sub> mode is 3:1. This modified structure, therefore, also has an inherent bandwidth advantage over conventional rectangular waveguide. Although it does not have the bandwidth capability of the TE<sub>10</sub> mode on the original line, it has the advantages of being a smaller guide and being closed on three sides. The trough line geometry is appropriate for the design of ferrite devices employing transverse magnetization.

#### GUIDE WAVELENGTH

Making use of (8) and the fact that  $\lambda_g = 2\pi/\beta$ , it is easily shown that

$$\frac{\lambda_g}{\lambda_0} = \frac{\pi \left( \frac{2a}{\lambda_0} \right)}{\sqrt{\pi^2 \left( \frac{2a}{\lambda_0} \right)^2 K_1 - (k_{1e}a)^2}}, \text{ even modes.} \quad (19)$$

The corresponding expression for the odd modes is the same as (19) except that  $(k_{1o}a)$  replaces  $(k_{1e}a)$ . For the case where the outer regions are air or vacuum ( $K_2=1$ ),  $\lambda_g/\lambda_0$  has been calculated for the TE<sub>10</sub> and TE<sub>20</sub> modes.

The results of these calculations are shown in Fig. 8 and Fig. 9. For small values of  $(2a/\lambda_o)$ ,  $(\lambda_g/\lambda_o)$  approaches unity; and for large values of  $(2a/\lambda_o)$ ,  $(\lambda_g/\lambda_o)$  approaches  $1/\sqrt{K_1}$ . This result is in agreement with the transverse field distribution picture of this mode, since small values of  $(2a/\lambda_o)$  correspond to most of the energy being propagated in regions 2 and 3, and large values of  $(2a/\lambda_o)$  correspond to most of the energy confined in the dielectric slab. The cutoff loci for higher order TE modes are shown as dashed curves superimposed on the  $\lambda_g/\lambda_o$  curves.

#### POWER HANDLING CAPABILITIES

Since  $E_x = H_y = 0$ , and the product  $E_y H_x$  is an even function of  $x$ , the axial power flow is

$$P_z = -\text{Real} \int_{y=0}^{y=b} \left[ \int_{x=0}^a E_{y1} H_{x1}^* dx + \int_{x=-a}^0 E_{y3} H_{x3}^* dx \right] dy. \quad (20)$$

If the proper expressions from (2) through (7) are inserted in (20), and the indicated integration is performed, the following formulas for the power flow of the even and odd modes result:

$$P_{ze} = |A_e|^2 \pi b a \sqrt{\frac{\mu_0}{\epsilon_0}} \left( \frac{2a}{\lambda_o} \right) \frac{\sqrt{\pi^2 K_1 \left( \frac{2a}{\lambda_o} \right)^2 - (k_{1e} a)^2}}{2(k_{1e} a)^2} \cdot \left[ 1 + \frac{\cot k_{1e} a}{k_{1e} a} \right] \quad (21)$$

$$P_{zo} = |A_o|^2 \pi b a \sqrt{\frac{\mu_0}{\epsilon_0}} \left( \frac{2a}{\lambda_o} \right) \frac{\sqrt{\pi^2 K_1 \left( \frac{2a}{\lambda_o} \right)^2 - (k_{1o} a)^2}}{2(k_{1o} a)^2} \cdot \left[ 1 - \frac{\tan k_{1o} a}{k_{1o} a} \right]. \quad (22)$$

For the dominant mode, the maximum electric field is located at  $x=0$ . As a safety factor, the breakdown power level  $P_{bd}$  will be calculated assuming that the maximum electric field  $E_{bd}$ , which can exist at  $x=0$ , is the breakdown field of air (despite the fact that a dielectric material occupies this central region).  $E_{bd}$  will be taken as 15,000 volts per centimeter (a safety factor of approximately 2) to conform to standard waveguide calculations. From (2c) it is seen that at  $x=0$

$$|A_e| = \frac{k_{1e}}{\omega \mu_0} |E_{bd}|. \quad (23)$$

If (23) is substituted into (21), the following equation is obtained for the breakdown power level of the dominant mode.

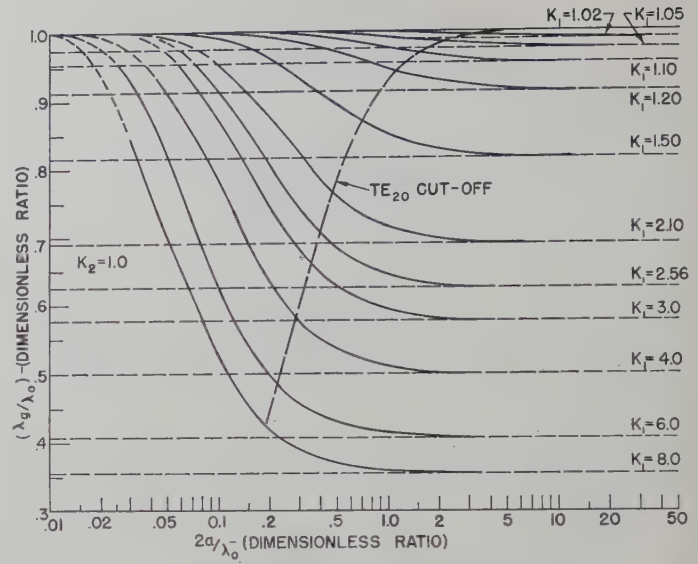


Fig. 8—Curves of the normalized waveguide wavelength  $(\lambda_g/\lambda_o)$  of the dominant mode, for the case where the outer regions are air or vacuum, as a function of the normalized slab width  $(2a/\lambda_o)$  and dielectric constant  $(K_1)$ .

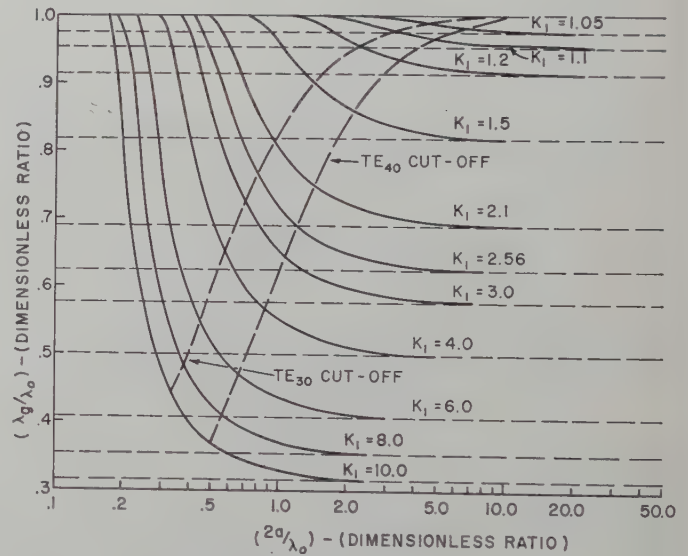


Fig. 9—Curves of the normalized waveguide wavelength  $(\lambda_g/\lambda_o)$  of the  $TE_{20}$  mode, for the case where the outer regions are air or vacuum, as a function of the normalized slab width  $(2a/\lambda_o)$  and dielectric constant  $(K_1)$ .

$$\frac{P_{bd}}{ab} = \frac{9.51 \cdot 10^8}{(2a/\lambda_o)} \left[ 1 + \frac{\cot k_{1e} a}{k_{1e} a} \right] \cdot \sqrt{\pi^2 K_1 \left( \frac{2a}{\lambda_o} \right)^2 - (k_{1e} a)^2}. \quad (24)$$

For the case where  $K_2=1$ , this function has been calculated for many values of  $(2a/\lambda_o)$  and  $K_1$ . The resulting family of curves is shown in Fig. 10. These curves show that for very small values of  $(2a/\lambda_o)$ , which corresponds to a very loosely bound wave,  $P_{bd}$  becomes very large. Any practical transmission line will have to be of finite



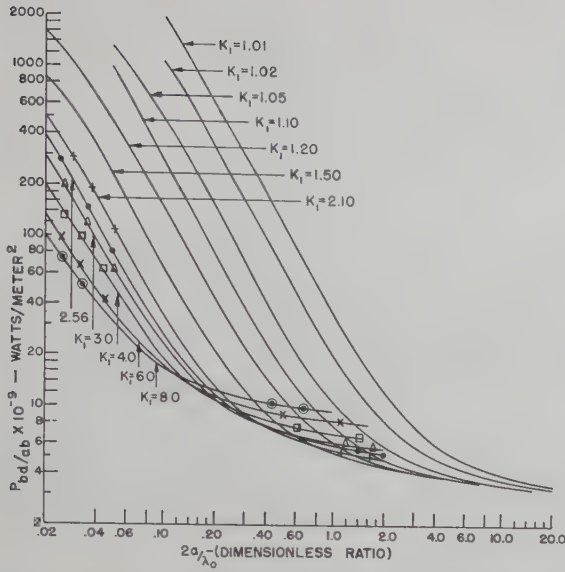


Fig. 10—Curves of the power handling capability ( $P_{bdaab}$ ) as a function of the normalized slab width ( $2a/\lambda_0$ ) and dielectric constant ( $K_1$ ). These curves are for the dominant mode and the case where the outer regions are air or vacuum.

extent in the  $x$ -direction, and hence there is a practical lower bound on  $(2a/\lambda_0)$  and an upper bound on the power handling capability. The improved power handling capabilities of this line are a result of its larger size and resultant reduced power density. The advantage is that single mode operation can be assured even with the large waveguide. The curves of Fig. 10 should provide an accurate measure of the power handling capacity if the width of the guide (in the  $x$ -direction) is sufficiently large so that nearly all of the power is propagated in the region between the two conducting planes.

#### TRANSMISSION LOSSES

Thus far, it has been assumed that the two parallel conducting planes had infinite conductivity and that the dielectric material had zero conductivity. This ideal line, of course, will have no losses. Practical transmission line conductors will have large but finite conductivity and the dielectric will have small but finite conductivity. Approximate attenuation formulas will be derived for these low loss materials. Since these losses are assumed to be small, separate equations can be derived for the wall loss and the dielectric loss.

The wall loss per unit length in the  $z$ -direction  $P_w$  is given by:

$$P_w = 2 \cdot \frac{1}{2} R_s \int_{-\infty}^{\infty} |H_t|^2 dx, \quad (25)$$

where  $R_s = \sqrt{\omega\mu_0/2\sigma_w}$  = surface resistance of the metal walls,

$$|H_t| = (|H_x|^2 + |H_z|^2)^{1/2}$$

= magnitude of the magnetic field at the walls

$\sigma_w$  = conductivity of the metal walls.

The extra factor of two in (25) accounts for the two conducting walls. The attenuation per unit length due to the wall loss is

$$\alpha_w = \frac{P_w}{2P_z}. \quad (26)$$

The proper expressions for the magnetic field should be substituted into (25), and the integration performed. If the resulting expression and either (21) or (22) are then substituted in (26), the following equations for the attenuation due to the wall loss for the even and odd TE modes result.

$$\alpha_{we} b \sqrt{\lambda_0} = \frac{.0291}{\sqrt{\sigma_w}} \cdot \frac{\left[ \pi^2 K_1 \left( \frac{2a}{\lambda_0} \right)^2 - \frac{(k_{1e}a)^2 \cot k_{1e}a}{k_{1e}a + \cot k_{1e}a} \right]}{\left( \frac{2a}{\lambda_0} \right) \sqrt{\pi^2 K_1 \left( \frac{2a}{\lambda_0} \right)^2 - (k_{1e}a)^2}} \quad (27)$$

$$\alpha_{wo} b \sqrt{\lambda_0} = \frac{.0291}{\sqrt{\sigma_w}} \cdot \frac{\left[ \pi^2 K_1 \left( \frac{2a}{\lambda_0} \right)^2 (k_{1o}a - \tan k_{1o}a) + (k_{1o}a)^2 \tan k_{1o}a \right]}{\left( \frac{2a}{\lambda_0} \right) (k_{1o}a - \tan k_{1o}a) \sqrt{\pi^2 K_1 \left( \frac{2a}{\lambda_0} \right)^2 - (k_{1o}a)^2}}. \quad (28)$$

For the case of the dominant mode, and for  $K_2=1$ , (27) has been plotted in Fig. 11 for a range of  $(2a/\lambda_0)$  and many values of  $K_1$ . The conductivity of copper ( $\sigma_w = 5.80 \times 10^7$  mhos per meter) was used in this computation. The curves of Fig. 11 can be used for other wall materials if the values of attenuation obtained from them are multiplied by the square root of the relative resistance of the substituted material.

The equation for the dielectric attenuation is derived for the case where Regions 2 and 3 are air or vacuum, and hence the dielectric loss all occurs in Region 1. The dielectric loss per unit length in the  $z$ -direction  $P_d$  is given by

$$P_d = \frac{\sigma_d}{2} \int_{y=0}^b \int_{x=-a}^+ |E_{y1}|^2 dx dy, \quad (29)$$

where  $\sigma_d = \omega\epsilon_0 K_1 \phi_d$  = conductivity of the dielectric material,

$\phi_d$  = loss tangent of the dielectric material.

The attenuation per unit length due to the dielectric loss is

$$\alpha_d = \frac{P_d}{2P_z}. \quad (30)$$

The proper expressions for the electric field, (2c) or (5c), should be inserted in (29) and the integral evaluated to

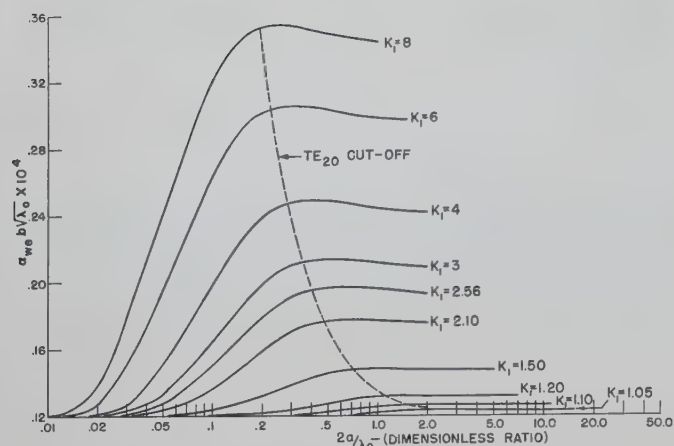


Fig. 11—Attenuation (in nepers per meter) due to the loss in the walls as a function of the normalized slab width ( $2a/\lambda_0$ ) and dielectric constant ( $K_1$ ). These curves are for the dominant mode and the case where the outer regions are air or vacuum and the wall material is copper ( $\sigma = 5.80 \times 10^7$  mhos per meter).

obtain equations for the dielectric power loss of the even and odd TE modes. The resulting expressions and either (21) or (22) are substituted into (30) to obtain the following formulas for the attenuation due to the dielectric loss.

$$\alpha_{de}\lambda_0 = \frac{\pi^2 K_1 \phi_d \left(\frac{2a}{\lambda_0}\right)}{\sqrt{\pi^2 K_1 \left(\frac{2a}{\lambda_0}\right)^2 - (k_{1e}a)^2}} \cdot \left[ \frac{k_{1e}a + \sin k_{1e}a \cos k_{1e}a}{k_{1e}a + \cot k_{1e}a} \right] \quad (31)$$

$$\alpha_{do}\lambda_0 = \frac{\pi^2 K_1 \phi_d \left(\frac{2a}{\lambda_0}\right)}{\sqrt{\pi^2 K_1 \left(\frac{2a}{\lambda_0}\right)^2 - (k_{1o}a)^2}} \cdot \left[ \frac{k_{1o}a - \sin k_{1o}a \cos k_{1o}a}{k_{1o}a - \tan k_{1o}a} \right] \quad (32)$$

Fig. 12 is a plot of  $\alpha_{de}\lambda_0$  as a function of ( $2a/\lambda_0$ ) and many values of  $K_1$  for the dominant mode. These calculated results were plotted for a value of dielectric loss tangent  $\phi_d = 0.001$ . These curves can be used for other values of  $\phi_d$  if the values of  $\alpha_d$  obtained are divided by 0.001 and multiplied by the loss tangent of the dielectric used.

#### DISCUSSION

The parallel plane waveguide partially filled with a dielectric can support a class of TE modes, whose field

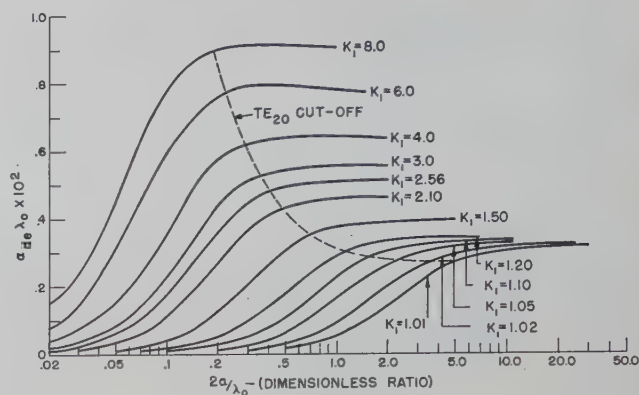


Fig. 12—Attenuation (in nepers per meter) due to the dielectric loss as a function of the normalized slab width ( $2a/\lambda_0$ ) and dielectric constant ( $K_1$ ). These curves are for the dominant mode and the case where the outer regions are air or vacuum. The loss tangent ( $\phi_d$ ) equals 0.001.

structure is similar to the  $TE_{m0}$  modes of rectangular waveguide. These TE modes display either even or odd symmetry about the geometrical plane of symmetry ( $x=0$ ). It is not possible to support TEM or TM waves on this structure. It has been previously shown that hybrid modes can also propagate on this line.<sup>1-3</sup> A sufficiently small, yet convenient, value for the distance between the conducting planes can be found which will suppress the hybrid modes and not affect the TE modes.

The dominant mode of this line ( $TE_{10}$ ) has no cutoff frequency, and hence it is inherently capable of very wide bandwidth operation. For a loosely bound wave, the losses are comparable to those of conventional rectangular waveguide, and the power handling capacity is an order of magnitude greater. In order to obtain the advantages of a loosely bound wave on this line, the structure must be substantially larger than rectangular waveguide. This line may, therefore, offer its greatest utility at millimeter wavelengths, where its size is still convenient. The availability of low loss, low dielectric constant materials allows the use of a reasonably wide dielectric center strip. The dielectric strip will, therefore, be mechanically self-supporting, while retaining the advantages of a loosely bound wave structure even at millimeter wavelengths. In the case of the dielectric loaded trough guide propagating the  $TE_{20}$  mode, thin layers of higher dielectric constant materials can be supported alongside the vertical conducting wall.

#### ACKNOWLEDGMENT

The author would like to thank Dr. M. E. Brodwin and J. C. Wiltse for their helpful discussions and criticisms. Acknowledgment is due Miss M. D. Velten and Mrs. B. H. Medcalf for the numerical calculations and curve plotting.



# Electromagnetic Backscattering Measurements by a Time-Separation Method\*

CHARLES C. H. TANG†

**Summary**—The object of this research is to investigate the feasibility of adapting the conventional pulsed radar technique for close-range back-scattering measurements for obstacles of arbitrary shape and small scattering cross sections. The time-separation or microwave-pulse method described in this paper differs essentially from all previously used laboratory methods in that the scattered field does not mix with the incident field at the detector and is separated from it in time. The essential experimental arrangement of this method is similar to that of the CW magic-T method except that a source generating very short pulses is used instead of CW. Preliminary experimental data for thin circular metallic disks show that the pulse method is a feasible one, since the measured results are in close agreement with the theoretical values. Accurate back-scattering measurements for obstacles of arbitrary shape and small scattering cross sections should be obtainable by this method provided a short microwave pulse of high power level is available.

## INTRODUCTION

IN a recent report King and Wu<sup>1</sup> made a summary of the available methods in the measurement of back-scattering cross sections of obstacles of various configurations. The frequency-separation or doppler-shift method<sup>2,3</sup> yields accurate measurements for obstacles with small scattering cross sections, but its usefulness is limited only to obstacles with rotational symmetry. The space-separation method used by Schmitt<sup>4</sup> may prove to be a promising method of precision when necessary refinements are made. The free-space time-separation method to be described in this paper is suitable for accurate back-scattering measurements for three-dimensional obstacles of arbitrary shape and small scattering cross sections. The essential experimental arrangement of the time-separation method is similar to that of the CW magic-T method<sup>3</sup> except that in the present experiment a source generating very short pulses is used instead of continuous waves. When a very short microwave pulse (of the order of forty  $\mu\text{sec}$ ) is used as a source, the scattered field from the obstacle in question

is separated from the incident field in time and accurate measurements can be made for arbitrarily shaped obstacles of relatively small scattering cross sections. It becomes evident that in the CW magic-T arrangement it is desirable to use a power level that is sufficient to lift the level of the back-scattered signal above both the noise level of the receiving system and the level of the leakage signal due to imperfect decoupling between the E-arm and H-arm of the magic-T or hybrid junction. However, if the scattered field is mixed with the leakage field due to imperfect decoupling and the reflection field due to discontinuities of the horn in any given proportion, this proportion can not be altered by simply increasing the source power level. Under such circumstances an increase in input power level does not extend the range of accurate measurements. The microwave-pulse method does not have this limitation and the range of the lower limit of accurate measurement may be extended linearly by raising the power level of the source, as the scattered field in this case is separated from the leakage field and reflection field in time.

The series of obstacles used in testing the feasibility of the time-separation method are thin circular metallic disks. These disks have the largest back-scattering cross sections among all obstacles which have geometrical cross-sectional areas equal to those of the corresponding disks. It was necessary to use these disks as test samples because a short microwave-pulse of high-power level was not available in addition to the fact that exact theoretical results could be calculated<sup>5</sup> for comparison. In some respects spheres would have been more convenient as test samples because of their complete symmetry property if a source of high-power level had been available.

## DESCRIPTION OF THE APPARATUS

Fig. 1 shows a schematic diagram of the microwave pulse system. Measurements were made at 3675 mc because the waveguide equipment for this frequency happened to be immediately available. However, it is generally preferable to use S-band waveguide since a source of high-power pulses of about 40- $\mu\text{sec}$  width in this band can be obtained more easily. The whole equipment was installed on the roof of the Laboratory so that the obstacles could be placed in surroundings practically free from electromagnetic reflections.

\* Manuscript received by the PGMTT, June 25, 1958; revised manuscript received, September 8, 1958. This research was performed under Air Force Contract No. AF (604) 786 between the AF Cambridge Res. Cntr. and the President and Fellows of Harvard College.

† Elec. Eng. Dept., University of California, Berkeley, Calif. Formerly of the Gordon McKay Lab., Harvard University, Cambridge, Mass.

<sup>1</sup> R. King and T. T. Wu, "The Reflection of Electromagnetic Waves from Surfaces of Complex Shape," Cruft Lab. Sci. Rep. No. 12, Harvard University; 1957.

<sup>2</sup> H. Scharfman and D. D. King, "Antenna scattering measurements by modulation of the scatterer," Proc. IRE, vol. 42, pp. 854-860; 1954.

<sup>3</sup> C. C. H. Tang, "Back-scattering from dielectric-coated infinite cylindrical obstacles," *J. Appl. Phys.*, vol. 28, pp. 628-633; 1957.

<sup>4</sup> H. J. Schmitt, "Back-Scattering Measurements with a Space-Separation Method," Cruft Lab. Sci. Rep. No. 14, Harvard Univ.; 1957.

<sup>5</sup> W. Andrejewski, "Die Beugung elektromagnetischer Wellen an der leitenden Kreisscheibe und an der kreisförmigen Öffnung in leitenden ebenen Schirm," Ph.D. Dissertation, Westfälische Technische Hochschule, Aachen, Germany; 1952.

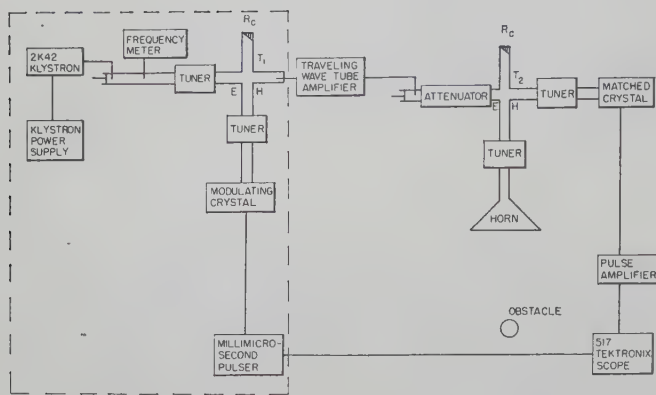


Fig. 1—Block diagram of microwave pulse system for back-scattering measurements.

The equipment in the dotted line block of Fig. 1 is used to generate a microwave-pulse with a width of about 40  $\mu\text{sec}$ . The CW magic-T method requires an extremely high decoupling between the E-arm and H-arm in order to yield reliable results. The CW magic-T method suffers the limitation that it can be used only when the magnitude of the back-scattered signal in question is considerably larger than that of the leakage signal or horn reflection signal. Since it is difficult to eliminate the small leakage, this condition imposes a lower limit on the magnitude of the back-scattered signal. The time-separation method circumvents the difficulty due to imperfect decoupling. This is accomplished by using a very short pulse so that the leakage pulse will be separated from the back-scattered pulse in time scale as viewed on a high-speed scope (such as Tektronix 517 which has a rise time of 7  $\mu\text{sec}$ ).

Although it is not necessary to eliminate the leakage signal in this system, it is still highly desirable to make it as small as possible. Accordingly, the hybrid junction  $T_2$ , specially machined to a high degree of symmetry, is used instead of a magic-T, which is very difficult to make with a corresponding degree of symmetry. The symmetry in the hybrid T is obtained at the expense of narrower bandwidth.

Since the distance between the source point and the obstacle is limited by the available space in the laboratory, the width of the generated pulse must be restricted accordingly in order to prevent the overlapping of the leakage pulse and reflection pulse with the back-scattered pulse on the viewing scope. With an available separation of from 10 to 20 meters between the source and the obstacle, the maximum pulse width is in the range of 50 to 100  $\mu\text{sec}$ . Although it is desirable to use as short a pulse as possible from the standpoint of reducing the necessary distance between the source and the obstacle, it is undesirable from the point of view of frequency spread. A very broad frequency spread not only gives inaccurate scattering measurements but also difficulties of broad-band matching.

The method finally used in producing the short microwave-pulse is shown in the arrangement in the dotted

block of the schematic diagram of Fig. 1. A millimicro-second dc pulser is used to modulate the crystal in one of the side arms of the hybrid junction  $T_1$  and a microwave pulse is generated in the fourth arm of the hybrid junction. Before the dc pulse is applied to the crystal, the tuner in front of the crystal must be so adjusted that it appears as a matched load and there is no output from the fourth arm of the junction  $T_1$ . When the dc pulse is applied to the crystal, the condition of matching is destroyed and a short microwave-pulse is produced in the fourth arm of the junction  $T_1$ . This is amplified by a traveling-wave tube and then used as the pulse source for back-scattering measurements. The pulsed output power from the horn with the present arrangement is of the order of 0.1 watt.

The rectangular dc modulating pulse used has a width of 20  $\mu\text{sec}$ . Owing to the finite response and decay times of the crystal (each of the order of a few millimicroseconds) and the rise time of 7  $\mu\text{sec}$  of the scope, the microwave pulse as observed at the input to the horn has a base width of about 40  $\mu\text{sec}$  and a top width (10 per cent down from the top) of 20  $\mu\text{sec}$ . A pulse of 40- $\mu\text{sec}$  width has a frequency spread of about 50 mc. Although the conventional slide-screw tuners are frequency-sensitive, it is found that these tuners are still fairly effective in matching such pulses. In order to preserve the original pulse shape it is necessary to avoid the use of long waveguide sections in order to prevent excessive dispersion.

Fig. 2 shows the polyfoam obstacle-stand with a disk as obstacle in place. The reflection from the polyfoam is negligible at this frequency. The turntable at the bottom can be rotated and tilted for proper orientation of the obstacle. Eleven disks were made of 3-mils copper sheet and each was glued to a polyfoam block for flatness and ease in handling. These blocks can be slid into the slot at the top of the polyfoam stand shown in Fig. 2.

#### MEASUREMENT AND COMPARISON

Initial measurements were made at 3675 mc with a pulsed peak output of about 0.1 watt. The total power received by the horn from the back-scattered field is expressed by the equation<sup>6</sup>

$$P_r = \frac{P_i \sigma \lambda^2 G^2}{(4\pi)^3 R^4} \quad \text{or} \quad \sigma = \left( \frac{P_r}{P_i} \right) \frac{(4\pi)^3 R^4}{\lambda^2 G^2}$$

where

- $P_i$  is the total power radiated from the horn,
- $\sigma$  is the back-scattering cross section of the obstacle,
- $\lambda$  is the wavelength,
- $G$  is the gain of the horn,
- $R$  is the distance between the horn and the obstacle.

<sup>6</sup> S. Silver, "Microwave Antenna Theory and Design," M.I.T. Rad. Lab. Ser., vol. 12, McGraw-Hill Book Co., Inc., New York, N. Y., vol. 12, p. 5; 1949.





Fig. 2—Polyfoam stand with obstacle on it.

For the present arrangement of  $G=350$  and  $R=8$  meters, an obstacle with  $\sigma=\lambda^2$  will give a back-scattered power of the order of  $10^{-9}$  watt, which is above the noise power level of crystals. However with the limited transmitter power and available detecting system, the minimum detectable signal appears when  $\sigma$  is about  $15\lambda^2$ . The received back-scattered signal is first detected by a video crystal detector and its output is fed into the pulse amplifiers having 60 db of amplification. The output of the amplifier is fed into the 517 Tektronix scope and the height of the pulse on the scope gives a measure of the back-scattering cross section of the obstacle in question. Fig. 3 shows the "broader base" pulse and the back-scattered pulses (right-side ones) for three disks. The broader base pulse is a superposition of two pulses: the leakage pulse due to imperfect decoupling and the reflection pulse due to discontinuities at the ends of the horn. The magnitude of the broader base pulse does not affect that of the back-scattered pulse on the right as long as the former is not large enough to saturate the pulse amplifiers.

During measurements the scattered pulse amplitude for each disk is read from the scope scale which is calibrated against the crystal output in the detecting arm of the hybrid junction  $T_2$ . The calibration is made to include both the scope and the pulse amplifiers by using

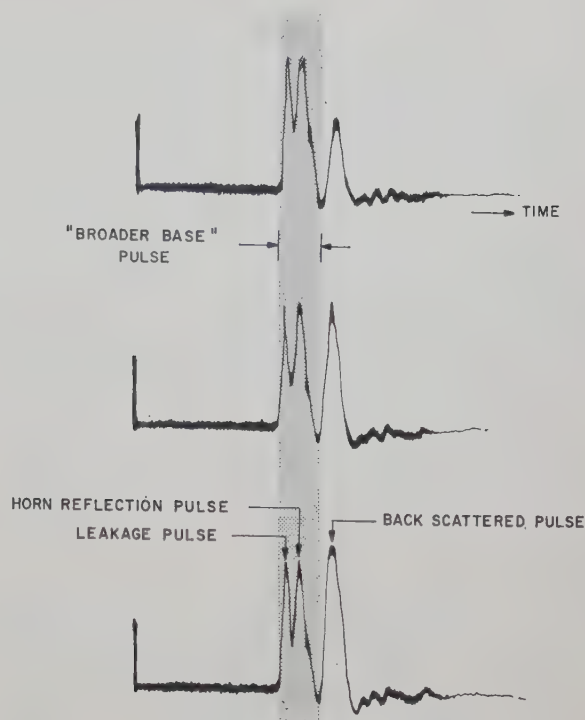


Fig. 3—Oscilloscope traces of broader base pulse and back-scattered pulse (right).

a calibrated pulse attenuator and a millimicrosecond dc pulse generator. The calibrated pulse attenuator has a precision of 5 per cent. Including the errors in scale reading and source amplitude variation, the over-all precision is of the order of 10 per cent. This can be improved by using a precision pulse attenuator, an enlarged scope scale, and a monitored source amplitude. The experimental results are plotted in Fig. 4, normalized to the theoretical value at  $ka=10$ . These results are in close agreement with the theory. The back-scattering coefficient of the circular disk is closely proportional to the square of its radius at large  $ka$ . The results at small  $ka$  cannot be obtained with the present available power level. From the data obtained it is seen that the minimum detectable scattering cross section for the present receiving sensitivity and source power level is of about  $15\lambda^2$ . Should a high-power traveling-wave tube amplifier such as the VA-121B (40 watts) be available, scattering cross sections of about  $\lambda^2$  could be measured by the present system. The smallest back-scattering cross section thus far accurately measured by any method is of the order of  $10^{-1}\lambda^2$  according to the published data.<sup>3</sup>

The nose-on back-scattering cross section<sup>7</sup> of a perfectly conducting prolate spheroid with a major-axis-to-minor-axis ratio of  $a/b=10$  has its first differential minimum at  $ka=2.3$ . Its back-scattering cross section at this  $ka$  is about  $10^{-5}\lambda^2$ . To measure  $10^{-5}\lambda^2$  cross sec-

<sup>7</sup> K. M. Siegel, F. V. Schultz, B. H. Gere, and F. B. Sleator, "The theoretical and numerical determination of the radar cross section of a prolate spheroid," IRE TRANS. ON ANTENNAS AND PROPAGATION, vol. AP-4, pp. 266-275; July, 1956.

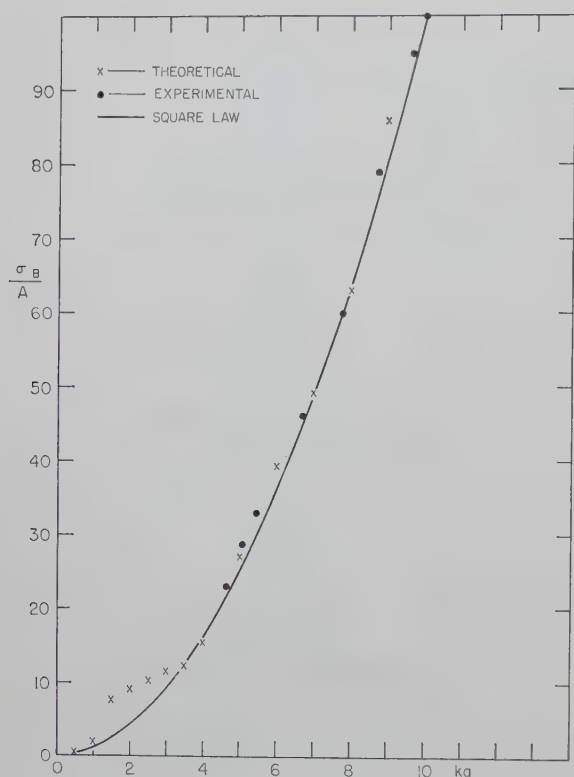


Fig. 4—Back-scattering coefficients of thin circular disks.

tion by the present system of 60 db amplification from the pulse amplifier it is necessary to have an input pulse power of the order of 10 kw. If the receiving pulse amplification can be increased from 60 db to 80 db or 90 db by using a superheterodyne receiving system, the input pulse power level can be reduced to the order of 100 watts or 10 watts. This requires specially designed IF strips with bandwidths at least of the order of 20 mc, since the pulse to be detected has a bandwidth of the order of 50 mc. The use of a specially selected crystal detector and an increase in gain of the horn would also permit an increase in the sensitivity of the system.

If the necessary input power level is so high that the leakage pulse and reflection pulse begin to saturate the amplifiers or burn out the crystal, it is necessary to reduce these pulse levels. The leakage pulse level can only be reduced by increasing the decoupling of the hybrid junction by improving symmetry. To eliminate or reduce the reflections from the discontinuities of the horn, it may be advisable to replace the  $R_c$  termination of the hybrid junction  $T_2$  by an identical horn and tuner in order to cancel the reflections by complete symmetry.

In order to reduce possible errors arising from the scale reading of the scope and a nonsquare-law response of the crystal, a precision microwave attenuator can be inserted between the tuner and the matched crystal in the detecting arm of the hybrid junction  $T_2$ . In this way all the signals to be detected can be normalized to one convenient scope scale reading by adjusting the precision attenuator, so that the relative attenuator decibel reading is directly proportional to the back-

scattered field of the scattering obstacle in question. The precision of the system as a whole then is limited by that of the precision attenuator.

The theoretical values of the back-scattering coefficient of thin circular disks are calculated with the help of the tabulation by Andrejewski<sup>5</sup> and are plotted in Fig. 4. It is seen that the coefficient is closely proportional to the square of  $ka = \gamma$  when  $\gamma$  is larger than 3. In other words, the back-scattering cross section is roughly proportional to the fourth power of the radius of the disk for  $\gamma$  larger than 3.

The evaluation<sup>5</sup> of the back-scattered field shows that its imaginary part begins to dominate when  $\gamma$  is larger than 3. For an infinitely thin circular disk it is evident that the scattering pattern is symmetrical with respect to the plane of the disk and consequently the scattering in the forward direction is equal to that in the backward direction. According to a theorem by Levine and Schwinger,<sup>8</sup> it is stated that the plane-wave total scattering cross section of an obstacle is simply proportional to the magnitude of the imaginary part of the forward scattered field, i.e.,

$$\sigma_t = \frac{4\pi}{k^2} \text{Im } F$$

where  $F$  is the scattered amplitude in the forward direction. From the calculated theoretical values<sup>9</sup> of the total scattering coefficient (usually called "scattering coefficient") it is found that the total scattering cross section is closely proportional to the square of the radius of the disk for  $\gamma$  greater than 3. It can be concluded, therefore, that for thin circular disks the back-scattering cross sections are approximately proportional to the square of the total scattering cross sections. This apparently paradoxical statement is a consequence of the definition of the back-scattering cross section. The back-scattering cross sections of thin circular disks with  $\gamma$  smaller than 1 are found to be proportional to the sixth power of disk radius as shown by various approximations. The transitional region from a sixth-power law to fourth-power law lies between  $\gamma=1$  and  $\gamma=3$ . The back-scattering cross sections of circular disks at small  $\gamma=ka$  from 0.6 to 3 have been measured by Schmitt<sup>4</sup> using an interferometer technique. They are in close agreement with the theoretical results.

It is pertinent at this point to make a comparison among the cylindrical obstacles, spherical obstacles, and infinitely thin symmetrical obstacles for both total scattering cross sections and back-scattering cross sections in the high-frequency limit. It is to be expected that the total scattering cross sections of cylindrical obstacles,<sup>10</sup>

<sup>8</sup> H. Levine and J. Schwinger, "On the theory of diffraction by an aperture in an infinite plane screen," pt. 1, *Phys. Rev.*, vol. 74, pp. 958-969; 1948.

<sup>9</sup> C. Huang and R. Kodis, "The Measurement of Aperture Transmission Coefficients," Cruft Lab. Tech. Rep. 165, Harvard Univ.; 1953.

<sup>10</sup> T. T. Wu, "High frequency scattering," *Phys. Rev.*, vol. 104, pp. 1201-1212; 1956.



spherical obstacles<sup>10</sup> and infinitely thin symmetrical obstacles<sup>9</sup> all approach twice the value obtained by geometrical optics. It is found, however, that the back-scattering cross sections of circular cylinders<sup>3</sup> are  $\pi/2$  times the geometrical area, those of spheres<sup>11</sup> unity times the geometrical area, and those of thin circular disks square of the geometrical area.

### CONCLUSION

It is concluded from this preliminary investigation that the time-separation or microwave-pulse method of

<sup>11</sup> A. Aden, "Electromagnetic Scattering from Metal and Water Spheres," Ph.D. Dissertation, Harvard Univ.; 1950.

back-scattering measurements can yield accurate results for three-dimensional obstacles of very small scattering cross section and arbitrary shape provided that a judicious choice and design of each component part of the system is made. Thus it supplements the frequency separation method used by Tang<sup>3</sup> for two-dimensional obstacles.

### ACKNOWLEDGMENT

The author is indebted to Prof. R. W. P. King for his encouragement during the course of the investigation. He also wishes to express his appreciation to Dr. H. Schmitt for his help on numerous occasions.

## On Network Representations of Certain Obstacles in Waveguide Regions\*

H. M. ALTSCHULER† AND L. O. GOLDSTONE†

**Summary**—Network representations for a class of obstacles in waveguide regions when the diffraction problem is of a vector type can be obtained by the use of *E*- and *H*-type modes. The special properties of these modes are discussed and highlighted by an example involving the network representation of a periodic strip grating in free space for oblique incidence. Transformations relating the different networks based on various modal representations in rectangular coordinate systems are also discussed.

### I. INTRODUCTION

THE problems of the diffraction of electromagnetic waves by obstacles in waveguide or free space are, in general, vector problems. However, in the case of "two-dimensional" obstacles such as the perfectly conducting half plane, infinite periodic gratings, or the infinite circular cylinder in free space, the vector diffraction problem may be decomposed into two independent scalar problems. The same is true in the case of certain structurally similar obstacles in rectangular and parallel plate waveguide. Such decompositions have been employed, for example, by Heins<sup>1</sup> in treating the diffraction of a dipole by a perfectly conducting half plane, and by Levy and Keller<sup>2</sup> in their discussion of diffraction

by finitely conducting cylinders at oblique incidence.

In this paper it is shown that modal techniques leading directly to network representations may be employed systematically in the solution of such problems. When the attempt is made to base this approach on the familiar *E* and *H* modes propagating perpendicular to the symmetry axis, the desired separation into scalar problems is not possible. On the other hand, the separation into the simpler scalar problems can be effected by appealing to an expansion of the fields in terms of an appropriate alternative set of orthonormal modes. These modes also make it possible to obtain the network representations of problems involving arbitrary angles of incidence directly from the results of the corresponding, strictly two dimensional (incident vector perpendicular to obstacle axis) problems. The matrix relations derived here, which relate the networks based on these modes to networks based on standard *E* and *H* modes, further increase the area of applicability of the network solutions.

The modes employed here, which form a complete orthonormal set of vector modes, are designated as the *E*- and *H*-type modes. They differ from the familiar *H* and *E* modes in that they are characterized by the vanishing of a *transverse*, rather than a longitudinal, field component. To effect the separation into two scalar problems, the modes are chosen such that one sub-set (*E*-type) has no component of the magnetic field parallel to the axial direction of the "two-dimensional" obstacle, while the second sub-set (*H*-type) has no com-

\* Manuscript received by the PGM-TT, July 7, 1958; revised manuscript received, November 4, 1958. The research reported was conducted under Contract AF-19(604)2031, sponsored by the A.F. Cambridge Res. Center, Air Res. and Dev. Command.

† Microwave Res. Inst., Polytech. Inst. of Brooklyn, Brooklyn, N. Y.

<sup>1</sup> A. E. Heins, "The excitation of a perfectly conducting half-plane by a dipole field," IRE TRANS. ON ANTENNAS AND PROPAGATION, vol. AP-4, pp. 294-296; July, 1956.

<sup>2</sup> B. R. Levy and J. S. Keller, "Diffraction by a Smooth Object," Inst. Math. Sci., New York Univ., N. Y., Res. Rep. EM-109; December, 1957.

ponent of electric field in this direction. In the strictly two-dimensional case, the  $E$ - and  $H$ -type modes are identical with the  $H$  and  $E$  modes, respectively.

While the emphasis in this paper is primarily directed towards the application of  $E$ - and  $H$ -type modes to a technique whereby the network representations for a class of obstacles under general incidence conditions can be obtained, it is necessary to consider the modes themselves in some detail. Modes classified on the basis of vanishing transverse field components have been discussed and employed previously by a number of authors.<sup>3-9</sup>

In Section II the eigenvalue problem for  $E$ - and  $H$ -type modes in both rectangular and circular cylindrical coordinates is discussed. The connection between the strictly two-dimensional diffraction problem and the general case involving arbitrary angle of incidence is obtained in Section III. Section IV contains an illustration in which the  $E$ - and  $H$ -type modes are employed to obtain a network representation of a periodic, perfectly conducting strip grating for arbitrary angle of incidence and arbitrary polarization of the incident wave. The linear transformation connecting the various modal representations in rectangular and parallel plate waveguides is treated in Section V. Finally, the  $E$ - and  $H$ -type mode functions in rectangular coordinates appropriate to free space and to periodic structures in free space are presented in an Appendix.

## II. MODAL REPRESENTATIONS

The total electromagnetic fields in an open or closed waveguide region which possesses an axial direction,<sup>10</sup> here arbitrarily designated as the  $y$  direction, can always be represented in terms of two uncoupled scalar functions, each of which satisfies the wave equation<sup>11</sup> when the region is bounded, if at all, by perfect electric or magnetic walls. These scalar functions are essentially the  $y$  components of the electric and magnetic fields,  $E_y$

and  $H_y$ . It is, therefore, suggestive to classify modes on a similar basis (*i.e.*, a sub-set for which  $E_y=0$ , and one for which  $H_y=0$ ) so that uncoupling of the two modal sub-sets will always result. It must be noted, however, that the above classifications are not sufficient to completely define the mode sets but that a "transmission line direction," *i.e.*, the direction in which the modes are taken to propagate, must also be chosen. It must be noted that the transmission line direction does not necessarily coincide with the axial direction defined above. If the transmission line direction is chosen to coincide with  $y$ , then the familiar  $E$  and  $H$  modes result.<sup>12</sup> If one of the other coordinates is chosen as the transmission line direction, then the resulting modes are  $E$ -type ( $H_y=0$ ) and  $H$ -type ( $E_y=0$ ) modes. These modes constitute a complete set of vector modes possessing orthogonality properties on surfaces transverse to the transmission line direction.

In the following section, the eigenvalue problems for  $E$ - and  $H$ -type modes are formulated for waveguide cross sections for which rectangular or polar coordinates are appropriate. The general solutions of these eigenvalue problems are then obtained. Certain explicit mode functions in free space are listed in the Appendix. Mode functions appropriate to parallel plate waveguide, to the conducting wedge, and to periodic structures in free space rotated with respect to the  $x, y$  coordinates are available elsewhere.<sup>13</sup>

### 1. The Eigenvalue Problem in Rectangular Coordinates

Waveguide regions where rectangular coordinates are appropriate are highly degenerate in that three axial directions exist. Here the  $z$  direction is arbitrarily chosen as the transmission line direction. The time dependence is taken as  $\exp j\omega t$ .

The vectors transverse (to  $z$ ) field equations for any uniform waveguide, in the absence of sources, are:<sup>12</sup>

$$\begin{aligned}\frac{\partial}{\partial z} \mathbf{E}_t &= -j\omega\mu \left(1_t + \frac{\nabla_t \nabla_t}{k^2}\right) \cdot \mathbf{H}_t \times \mathbf{z}_0, \\ \frac{\partial}{\partial z} \mathbf{H}_t &= -j\omega\epsilon \left(1_t + \frac{\nabla_t \nabla_t}{k^2}\right) \cdot \mathbf{z}_0 \times \mathbf{E}_t\end{aligned}\quad (1)$$

where, for rectangular coordinates,

$$\begin{aligned}1_t &\text{ is the transverse unit dyadic } \mathbf{x}_0\mathbf{x}_0 + \mathbf{y}_0\mathbf{y}_0, \\ \nabla_t &\text{ is the transverse gradient operator } \mathbf{x}_0\partial/\partial x \\ &\quad + \mathbf{y}_0\partial/\partial y,\end{aligned}$$

$$\mathbf{x}_0, \mathbf{y}_0 \text{ and } \mathbf{z}_0 \text{ are unit vectors,}$$

and  $k$  is the free space wave number  $2\pi/\lambda$ .

The desired modal representation of the transverse fields is

<sup>12</sup> N. Marcuvitz, *op. cit.*, Sec. 1.2.

<sup>13</sup> H. M. Altschuler and L. O. Goldstone, "A Class of Alternative Modal Representations for Uniform Waveguide Regions," *Microwave Res. Inst., Polytech. Inst. of Brooklyn*; Rep. No. R-557-57 February, 1957.

<sup>3</sup> N. Marcuvitz, "Waveguide Handbook," Rad. Lab. Ser., vol. 10, McGraw-Hill Book Co., Inc., New York, N. Y., pp. 89-96; 1951.

<sup>4</sup> J. Van Bladel, "Field expandability in normal modes for a multi-layered rectangular or circular waveguide," *J. Franklin Inst.*, vol. 253, pp. 313-321, April, 1952.

<sup>5</sup> C. M. Angulo, "Discontinuities in rectangular waveguide partially filled with dielectric," *IRE TRANS. ON MICROWAVE THEORY AND TECHNIQUES*, vol. MTT-5, pp. 68-74; January, 1957.

<sup>6</sup> A. D. Bresler and N. Marcuvitz, "Operator Methods in Electromagnetic Field Theory, chap. 2, Guided Modes in Uniform Cylindrical Waveguide Regions," *Microwave Res. Inst., Polytech. Inst. of Brooklyn*, N. Y., Rep. No. R-565-57; March, 1957.

<sup>7</sup> R. E. Collin and R. M. Vaillancourt, "Application of Raleigh-Ritz method to dielectric steps in waveguides," *IRE TRANS. ON MICROWAVE THEORY AND TECHNIQUES*, vol. MTT-5, pp. 177-184; July, 1957.

<sup>8</sup> L. O. Goldstone and A. A. Oliner, "Leaky Wave Antennas, I: Rectangular Waveguides, II: Circular Waveguides," *Microwave Res. Inst., Polytech. Inst. of Brooklyn*, N. Y., Reps. No. R-606-57 and R-629-57; August, 1957, and January, 1958.

<sup>9</sup> W. L. Weeks, "Phase Velocities in Rectangular Waveguide Partially Filled with Dielectric," *Antenna Lab., Univ. of Illinois, Urbana, Ill.*, Tech. Rep. No. 28; December, 1957.

<sup>10</sup> Axial direction is defined as a direction such that all cross sections transverse to it are identical in size and shape.

<sup>11</sup> J. A. Stratton, "Electromagnetic Theory," McGraw-Hill Book Co., Inc., New York, N. Y., pp. 350-351; 1941.



$$\begin{aligned} E_i(x, y, z) &= \sum_i V_i(z) \mathbf{e}_i(x, y), \\ H_i(x, y, z) &= \sum_i I_i(z) \mathbf{h}_i(x, y). \end{aligned} \quad (2)$$

Upon substitution of (2) into (1), the transmission line equations and the vector eigenvalue problem for the transverse mode functions [(3) and (4) below] follow readily with the products,  $\kappa_i Z_i$  and  $\kappa_i Y_i$ , playing the role of separation constants.  $V_i(z)$  and  $I_i(z)$  are hence identified as the modal voltages and currents:

$$\frac{dV_i}{dz} = -j\kappa_i Z_i I_i, \quad \frac{dI_i}{dz} = -j\kappa_i Y_i V_i, \quad (3)$$

where  $\kappa_i$  is the modal wave number for propagation along  $z$ , and  $Z_i = 1/Y_i$  is the modal characteristic impedance. The actual value of  $Z_i$  must be chosen appropriately in connection with each particular case. The vector eigenvalue problem for the transverse mode functions is

$$\begin{aligned} \kappa_i Z_i \mathbf{e}_i &= \omega \mu \left( 1_t + \frac{\nabla_t \nabla_t}{k^2} \right) \cdot \mathbf{h}_i \times \mathbf{z}_0, \\ \kappa_i Y_i \mathbf{h}_i &= \omega \epsilon \left( 1_t + \frac{\nabla_t \nabla_t}{k^2} \right) \cdot \mathbf{z}_0 \times \mathbf{e}_i. \end{aligned} \quad (4)$$

Eq. (4) may be combined to yield the second order problems for  $\mathbf{e}_i$  and  $\mathbf{h}_i$ ,

$$(\nabla_t^2 + k_{ti}^2) \mathbf{e}_i = 0, \quad (\nabla_t^2 + k_{ti}^2) \mathbf{h}_i = 0, \quad (5)$$

where

$$k_{ti}^2 = k^2 - \kappa_i^2 = k_{xi}^2 + k_{yi}^2.$$

In rectangular coordinates, the preceding equations do not uniquely specify a modal set since the eigenvalue problem posed by (4) is degenerate, in the sense that corresponding to each pair of transverse wave numbers  $k_{xi}$ ,  $k_{yi}$  there are two independent mode functions. These two mode functions may be chosen to be orthogonal to each other in a variety of ways. Each such choice will result in a particular mode set. Two of these sets are of interest here. One is obtained if the familiar condition  $\mathbf{e}_i = \mathbf{h}_i \times \mathbf{z}_0$  is imposed. It is comprised of two sub-sets of modes, both associated with the same eigenvalues, namely, the usual  $E$  and  $H$  modes. These are characterized by vanishing field components in the transmission line direction; in detail, the  $E$  modes by  $H_z = 0$ , and the  $H$  modes by  $E_z = 0$ . If, on the other hand, the condition  $e_{yi} = 0$  is imposed, a sub-set of  $H$ -type modes results with transverse wave numbers  $k_{xi}$  and  $k_{yi}$ . The associated modal sub-set ( $E$ -type modes) which corresponds to the same transverse wave numbers results upon the imposition of the condition  $h_{yi} = 0$ . These two modal sub-sets again constitute a complete orthogonal set; the transmission line direction is along  $z$ , but the modes are now characterized by vanishing field components along  $y$ .

Solutions for the components of the  $E$ - and  $H$ -type mode functions can be obtained from (5); in particular, it is convenient to fix upon the  $y$  components:

$$\left( \frac{\partial^2}{\partial x^2} + \frac{\partial^2}{\partial y^2} + k_{ti}^2 \right) e_{yi}' = 0, \quad k_{ti}^2 = k^2 - \kappa_i^2 \quad (6a)$$

for the  $E$ -type modes, where  $h_{yi}' = 0$ , and

$$\left( \frac{\partial^2}{\partial x^2} + \frac{\partial^2}{\partial y^2} + k_{ti}^{\prime\prime 2} \right) h_{yi}'' = 0, \quad k_{ti}^{\prime\prime 2} = k^2 - \kappa_i^{\prime\prime 2} \quad (6b)$$

for the  $H$ -type modes, where  $e_{yi}'' = 0$ . In order to insure the proper relationship between the components of these transverse vector mode functions, one rewrites the components of (4) in the following forms:

For the  $E$ -type modes ( $h_{yi}' = 0$ ),

$$h_{xi}' = -Z_i' \left( \frac{\kappa_i' \omega \epsilon}{k^2 - k_{yi}^2} \right) e_{yi}', \quad e_{xi}' = \frac{1}{k^2 - k_{yi}^2} \frac{\partial^2 e_{yi}'}{\partial x \partial y}. \quad (7)$$

$Z_i'$  may be defined as

$$Z_i' = \frac{k^2 - k_{yi}^2}{\kappa_i' \omega \epsilon}, \quad (8)$$

so that

$$h_{xi}' = -e_{yi}'. \quad (9)$$

For the  $H$ -type modes ( $e_{yi}'' = 0$ ),

$$e_{xi}'' = Y_i'' \left( \frac{\kappa_i'' \omega \mu}{k^2 - k_{yi}^2} \right) h_{yi}'', \quad h_{xi}'' = \frac{1}{k^2 - k_{yi}^2} \frac{\partial^2 h_{yi}''}{\partial x \partial y}. \quad (10)$$

$Y_i''$  may be defined as

$$Y_i'' = \frac{k^2 - k_{yi}^2}{\kappa_i'' \omega \mu}, \quad (11)$$

so that

$$e_{xi}'' = h_{yi}''. \quad (12)$$

It can be seen from (7) and (10) that these mode functions do not exist when  $k^2 = k_{yi}^2$ . In such cases an alternative modal description must be employed.

As can be demonstrated, the  $E$ -type and  $H$ -type mode functions possess the following orthogonality properties:

$$\int_{y_1}^{y_2} \int_{x_1}^{x_2} \mathbf{h}_i^\alpha \times \mathbf{z}_0 \cdot \mathbf{e}_j^{\beta*} dx dy = 0, \quad \alpha \neq \beta \text{ and/or } i \neq j, \quad (13)$$

where  $x_1$ ,  $x_2$ ,  $y_1$ , and  $y_2$  are the appropriate limits of integration, and where both  $\alpha$  and  $\beta$  can stand for the prime or the double prime indices; the asterisk stands for complex conjugate. The definition of  $Z_i'$  in (8) and  $Y_i''$  in (11) assures that the mode functions are normalized so that

$$\int_{y_1}^{y_2} \int_{x_1}^{x_2} \mathbf{h}_i^\alpha \times \mathbf{z}_0 \cdot \mathbf{e}_j^{\beta*} dx dy = \delta_{ij} \delta_{\alpha\beta} \quad (14)$$

for bounded<sup>14</sup> regions. It is stressed again that for these modes  $\mathbf{e}_i^\alpha \neq \mathbf{h}_i^\alpha \times \mathbf{z}_0$ , in contrast to the usual  $E$  and  $H$  mode case where  $\mathbf{e}_i^\alpha = \mathbf{h}_i^\alpha \times \mathbf{z}_0$ . In view of this, there is an additional arbitrariness here which has been exploited by defining characteristic impedances as in (8) and (11). The following two scalar orthogonality conditions may be written as a consequence of (14), (9), and (12):

$$\int_{y_1}^{y_2} \int_{x_1}^{x_2} e_{yij}' e_{yij}'^* dx dy = \delta_{ij},$$

$$\int_{y_1}^{y_2} \int_{x_1}^{x_2} h_{yij}'' h_{yij}''^* dx dy = \delta_{ij}. \quad (15)$$

It is, therefore, apparent that the above choices of characteristic impedance [see (8) and (11)] correspond to a normalization demand on the scalar components of the mode functions  $e_{yij}'$  and  $h_{yij}''$  as well.

For the case  $h_y = 0$ , i.e., when there is no field variation in the  $y$  direction, (7)–(12) take on much simpler form. The equations in this form are recognized to be appropriate to the familiar  $H$  and  $E$  modes; the scalar field components involved satisfy the relation  $\mathbf{e}_i^\alpha = \mathbf{h}_i^\alpha \times \mathbf{z}_0$ . Eq. (13) now reduces to the usual normalization statement for  $H$  and  $E$  modes:

$$\int_{x_1}^{x_2} \mathbf{e}_i^\alpha \cdot \mathbf{e}_j^{\beta*} dx = \delta_{ij} \delta_{\alpha\beta}. \quad (16)$$

It is seen, then, that when the fields have no variation in the  $y$  direction, the  $E$ - and  $H$ -type mode functions are identically the familiar  $H$  and  $E$  mode functions (in  $z$ ), respectively.

The explicit form of the  $E$ - and  $H$ -type mode functions, of course, depends on the boundary conditions. The actual mode functions for some special cases are presented in the Appendix.

## 2. The Eigenvalue Problem for Radial Transmission Line Modes

The circular cylinder coordinate system appropriate to the following discussion is shown in Fig. 1. The time dependence is again taken as  $\exp j\omega t$ ; the radial direction is the transmission line direction. The description employed here is called a radial transmission line description<sup>15</sup> which, it will be shown, is based on a set of  $E$ - and  $H$ -type modes possessing vector orthogonality properties.

The transverse (to  $r$ ) field equations in this case are those given in the "Waveguide Handbook."<sup>15</sup> The desired modal representation of the transverse fields is

$$E_y = \sum_i V_i(r) e_{yi}(y, \Phi), \quad H_y = \sum_i I_i(r) h_{yi}(y, \Phi),$$

$$rE_\Phi = \sum_i V_i(r) e_{\Phi i}(y, \Phi), \quad rH_\Phi = \sum_i I_i(r) h_{\Phi i}(y, \Phi), \quad (17)$$

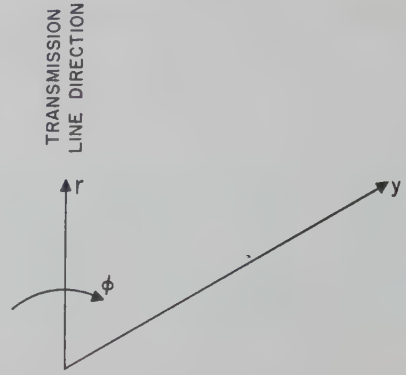


Fig. 1—Circular cylindrical coordinates.

where, upon substituting (17) into the field equations and applying a separation of variables argument, the modal voltages and currents can be shown to satisfy the radial transmission line equations:

$$\frac{dV_i}{dr} = -j\kappa_i(r) Z_i(r) I_i, \quad \frac{dI_i}{dr} = -j\kappa_i(r) Y_i(r) V_i. \quad (18)$$

From the field equations, the following two scalar eigenvalue problems are obtained:

$$\left( \frac{\partial^2}{\partial y^2} + \frac{\partial^2}{\partial \Phi^2} + k^2 - k_{yi}'^2 + p_i'^2 \right) e_{yi}' = 0$$

for  $E$ -type modes:  $h_{yi}' = 0$ , (19)

$$\left( \frac{\partial^2}{\partial y^2} + \frac{\partial^2}{\partial \Phi^2} + k^2 - k_{yi}''^2 + p_i''^2 \right) h_{yi}'' = 0$$

for  $H$ -type modes:  $e_{yi}'' = 0$ . (20)

Here  $k_{yi}'$ ,  $p_i'$ ,  $k_{yi}''$ , and  $p_i''$  are separation constants. The remaining components of the mode functions are obtained from the field equations and (17) and (18):

$$h_{\Phi i}' = \frac{-\omega \epsilon r}{(k^2 + k_{yi}'^2)} \kappa_i'(r) Y_i'(r) e_{yi}' \quad (21a)$$

$$e_{\Phi i}' = \frac{1}{(k^2 - k_{yi}'^2)} \frac{\partial^2 e_{yi}'}{\partial \Phi \partial y} \quad (21b)$$

for  $E$ -type modes;

$$e_{\Phi i}'' = \frac{\omega \mu r}{(k^2 - k_{yi}''^2)} \kappa_i''(r) Z_i''(r) h_{yi}'' \quad (22a)$$

$$h_{\Phi i}'' = \frac{1}{(k^2 - k_{yi}''^2)} \frac{\partial^2 h_{yi}''}{\partial \Phi \partial y} \quad (22b)$$

for  $H$ -type modes.

In exact analogy with the preceding rectangular case, the following choices are now made:

$$Z_i'(r) = \frac{(k^2 - k_{yi}'^2)}{r\omega\epsilon\kappa_i'(r)}; \quad Y_i''(r) = \frac{(k^2 - k_{yi}''^2)}{r\omega\mu\kappa_i''(r)}. \quad (23)$$

Eqs. (21a) and (22a) then reduce to

$$h_{\Phi i}' = -e_{yi}'; \quad e_{\Phi i}'' = h_{yi}''. \quad (24)$$

As before the choices embodied in (23) are equivalent to the following normalization demand:

<sup>14</sup> This and all subsequent orthogonality or normalization statements hold for unbounded regions if  $\delta_{ij}$  is replaced by  $\delta(i-j)$ .

<sup>15</sup> N. Marcuvitz, *op. cit.*, sec. 1.7.



$$\int_{y_1}^{y_2} \int_{\Phi_1}^{\Phi_2} e_{y_i}' e_{y_j}'^* d\Phi dy = \delta_{ij};$$

$$\int_{y_1}^{y_2} \int_{\Phi_1}^{\Phi_2} h_{y_i}'' h_{y_j}''^* d\Phi dy = \delta_{ij}. \quad (25)$$

In terms of the scalar functions, with  $\mathbf{r}_0$ ,  $\Phi_0$ , and  $\mathbf{y}_0$  taken as unit vectors, one defines the vector mode functions as

$$\mathbf{e}_i = \Phi_0 e_{\Phi i} + \mathbf{y}_0 e_{y i} \quad \text{and} \quad \mathbf{h}_i = \Phi_0 h_{\Phi i} + \mathbf{y}_0 h_{y i}. \quad (26)$$

Now (23) is equivalent to the following normalization demand on the vector mode functions:

$$\int_{y_1}^{y_2} \int_{\Phi_1}^{\Phi_2} \mathbf{h}_j^\alpha \times \mathbf{r}_0 \cdot \mathbf{e}_i^{\beta*} d\Phi dy = \delta_{ij} \delta_{\alpha\beta}. \quad (27)$$

Eq. (23) expresses  $Z_i'$  and  $Y_i''$  in terms of  $\kappa_i'$  and  $\kappa_i''$ , which, it can be shown, are given by

$$[\kappa_i(\mathbf{r})]^2 = (k^2 - k_{y i}^2) - \frac{\dot{p}_i^2}{r^2}. \quad (28)$$

These modes exist only when  $k^2 \neq k_{y i}^2$ . The explicit form of the mode functions in specific cases, of course, depends on boundary conditions.

### III. APPLICATION TO TWO-DIMENSIONAL SCATTERING PROBLEMS—ARBITRARY ANGLES OF INCIDENCE

As has already been pointed out, the total fields in homogeneous waveguide regions uniform in the  $y$  direction can be expressed in terms of the scalar field components,  $E_y$  and  $H_y$ . These components satisfy the scalar wave equation

$$[\nabla_t^2 + (k^2 - k_y^2)]_{H_y}^{E_y} = 0, \quad (29)$$

where the operator  $\nabla_t^2$  is taken as  $\nabla^2 - (\partial^2/\partial y^2)$  and the operator  $\partial^2/\partial y^2$  as  $-k_y^2$ . It is apparent that the *functional form* of the solutions of (30) is independent of the value of  $k_y$  and that solutions for  $k_y \neq 0$  are readily inferred from those for  $k_y = 0$ . If the solutions for  $k_y = 0$  are  $E_y = E_y(k)$  and  $H_y = H_y(k)$ , then those for  $k_y \neq 0$  are obtained by replacing  $k$  by  $\sqrt{k^2 - k_y^2}$  wherever it occurs. This property can be usefully applied, when the field solution of a two-dimensional problem ( $k_y = 0$ ) is known, to obtain a solution for the corresponding problem with  $k_y \neq 0$ .

It will now be shown that the ( $E$ - and  $H$ -type) network parameters appropriate to certain two dimensional problems can be similarly modified to yield the network parameters for the case  $k_y \neq 0$ . This procedure is applicable when the  $E$ - and  $H$ -type modes are uncoupled both for  $k_y = 0$  and  $k_y \neq 0$ .

Since the  $y$  components of the  $E$ -type mode functions,  $e_{y i}'$ , are independent of both  $k$  and  $k_y$ , the dependence of  $E_y$  on  $\sqrt{k^2 - k_y^2}$  is associated only with the mode voltages, *i.e.*,

$$E_y(\sqrt{k^2 - k_y^2}) = \sum_i V_i'(\sqrt{k^2 - k_y^2}) e_{y i}'. \quad (30)$$

The elements of the normalized scattering matrix for a discontinuity which is uniform in  $y$ , but otherwise arbitrary, are defined as:

$$\frac{V'_{\text{ref } i}}{V'_{\text{inc } j}} = S_{ij}, \quad (i, j = 1, 2, 3 \cdots N), \quad (31)$$

where

$$V_i'(\sqrt{k^2 - k_y^2}) = V'_{\text{inc } i}(\sqrt{k^2 - k_y^2}) + V'_{\text{ref } i}(\sqrt{k^2 - k_y^2}). \quad (32)$$

From (31) and (32) it may be concluded that

$$S_{ij} = S_{ij}(\sqrt{k^2 - k_y^2}).$$

In view of the dependence of the scattering coefficients on  $\sqrt{k^2 - k_y^2}$ , it is seen that the scattering matrix for the case  $k_y \neq 0$  can be obtained from that for the case  $k_y = 0$  by replacing  $k$  by  $\sqrt{k^2 - k_y^2}$ .

When the corresponding impedance matrix  $Z$  is normalized, it can be expressed in terms of the scattering matrix. The normalization of the impedance matrix can be accomplished in a variety of ways. The relationship between the scattering matrix and the normalized impedance matrix  $Z'$  is

$$Z' = \sqrt{\overrightarrow{Y}_0}(1 + S)(1 - \overrightarrow{Z}_0 \overleftarrow{Y}_0 S)^{-1} \sqrt{\overleftarrow{Z}_0} \quad (33)$$

where the impedance matrix has been normalized in the following manner:

$$Z' = \sqrt{\overrightarrow{Y}_0} Z \sqrt{\overleftarrow{Y}_0}; \quad \overleftarrow{Z}_0 = (\overleftarrow{Y}_0)^{-1}. \quad (34)$$

Each element of the diagonal matrices  $\overrightarrow{Y}_0$  and  $\overleftarrow{Y}_0$  is the admittance seen by a mode traveling on an infinite transmission line.<sup>16</sup> The arrows indicate the two directions of travel. Upon examination of (33) one finds that  $Z'$ , like  $S$ , depends only on  $\sqrt{k^2 - k_y^2}$ . This follows from the fact that the dependence on  $k$  (other than that on  $\sqrt{k^2 - k_y^2}$ ) of the admittance matrices  $\overrightarrow{Y}_0$  and  $\overleftarrow{Y}_0$  is the same, and that this dependence can be factored out as a constant multiplier  $F(k)$ :

$$\overleftarrow{Y}_0 = F(k) \overleftarrow{y}_0(\sqrt{k^2 - k_y^2}).$$

Therefore, for the normalized impedance matrix  $Z'$ , as for the scattering matrix  $S$ , the results for  $k_y \neq 0$  can be obtained from those for  $k_y = 0$  by replacing  $k$  by  $\sqrt{k^2 - k_y^2}$ . Although  $Z'$  is normalized in a symmetric manner here ( $Z_{ij}' = Z_{ji}'$ ), the conclusion has been shown to hold for any type of normalization. A similar procedure results in the same conclusions for the scattering and normalized impedance matrices associated with  $H$ -type modes.

It is important to recall at this point that the earlier conclusion that  $E$ - and  $H$ -type modes with  $k_y = 0$  are respectively identical to the conventional  $H$  and  $E$  modes.

<sup>16</sup> For radial and other nonuniform transmission lines  $\overrightarrow{Y}_0$  and  $\overleftarrow{Y}_0$  are not the characteristic admittances of the transmission lines. An infinite radial line extends from  $r = 0$  to  $r = \infty$ . In the case of uniform transmission lines,  $\overrightarrow{Y}_0 = \overleftarrow{Y}_0 = \text{characteristic admittance}$ .

One can consequently take advantage of the known equivalent circuits associated with two dimensional ( $k_y=0$ )  $E$  or  $H$  mode problems in order to find the networks associated with  $E$ - and  $H$ -type modes when  $k_y \neq 0$ . A specific illustration is embodied in the following section.

#### IV. ILLUSTRATION OF APPLICATION OF $E$ - AND $H$ -TYPE MODES: DIFFRACTION BY AN INFINITE STRIP GRATING

The properties of the  $E$ - and  $H$ -type modes make them particularly convenient for application to a certain class of diffraction problems associated with uniform homogeneous open and closed waveguide regions which may be of unconventional cross section. In more detail, their virtue lies in the fact that these problems involve uncoupled  $E$ - and  $H$ -type modal sets which can immediately be solved as scalar problems. The solutions of such diffraction problems can be phrased in either field or network terms. They may be exploited to obtain the improper modes of open structures (for given  $k_y$ ), or the propagation wave numbers  $k_{yi}$  for leaky and closed waveguides, via a transverse resonance procedure.

Let a plane wave

$$\mathbf{E} = A e^{-j\mathbf{k} \cdot \mathbf{r}}, \quad A = x_0 a_x + y_0 a_y + z_0 a_z$$

be incident at an arbitrary angle upon the doubly infinite strip grating shown in Fig. 2 which is uniform in the  $y$  direction. When  $z$  is taken as the transmission line direction, the transverse electric field with suppressed  $y$  dependence is expressed by the superposition of the two lowest ( $m=0$ )  $E$ -type and  $H$ -type mode functions (see Appendix) appropriate to such a periodic structure:

$$A_i e^{-j(k_{x0}x + \kappa_0 z)} = V_0' \text{inc}(z) e_0'(x) + V_0'' \text{inc}(z) e_0''(x),$$

where it can be shown that, in terms of the incident wave amplitudes,

$$V_0' \text{inc}(z) = \sqrt{a} a_y e^{-j\kappa_0 z},$$

$$V_0'' \text{inc}(z) = \sqrt{a} \left( a_x + a_y \frac{k_{x0} k_y}{k^2 - k_y^2} \right) e^{-j\kappa_0 z}.$$

One can therefore regard the problem as two uncoupled scalar problems. For  $k_y=0$ , these are identically the scalar  $H$  mode and  $E$  mode problems for which network solutions are known<sup>17</sup> for the  $E$ -type mode (*i.e.*, the scalar field  $e_y$ ) and the  $H$ -type mode (*i.e.*, the scalar field  $h_y$ ) incident, the equivalent circuits are shown in Figs. 3(a) and 3(b), respectively. The representations are at the plane  $T$  (taken as  $z=0$ ) in which the strips are located. These solutions are subject to the restriction  $a(1 - k_{x0}/k)/\lambda < 1$ , so that only the lowest  $E$ -type mode and  $H$ -type mode propagate. The propagation wave number of the associated transmission lines is  $\kappa_0$ ; impedances have been normalized to the respective char-

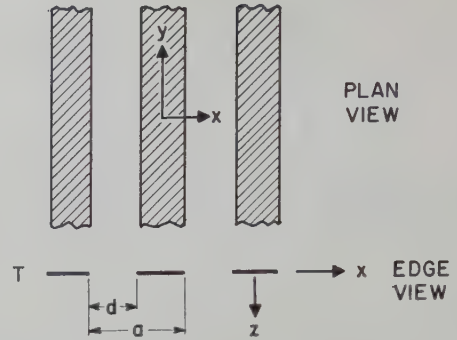


Fig. 2—Doubly infinite strip grating and associated coordinates.

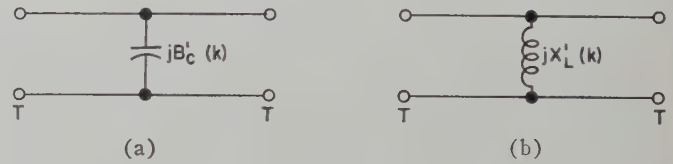


Fig. 3—Equivalent circuits appropriate to the two uncoupled scalar problems when there is no variation in  $y$ .

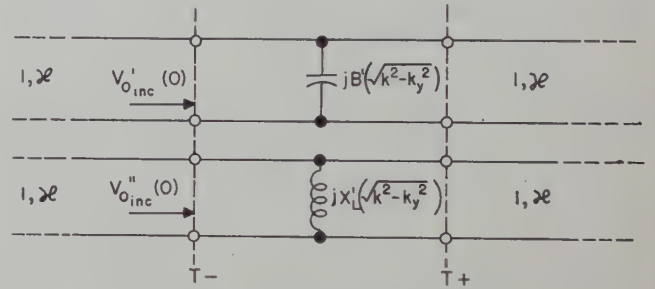


Fig. 4—Equivalent circuit appropriate to the strip grating when there is variation in  $y$ .

acteristic impedances. Explicit expressions for the parameters  $B_c'(k)$  and  $X_L'(k)$  are available<sup>17</sup> in the form

$$B_c'(k) = B_c(a, d, \lambda, \cos \theta) / Y_0'; \quad Y_0' = \kappa_0 / \omega \mu,$$

$$X_L'(k) = X_L(a, d, \lambda, \cos \theta) / Y_0''; \quad Y_0'' = \omega \epsilon / \kappa_0,$$

where  $\cos \theta = \kappa_0 / k$ , and, of course,  $\lambda = 2\pi / k$ . The corresponding parameters with  $k_y \neq 0$  are  $B_c'(\sqrt{k^2 - k_y^2})$  and  $X_L'(\sqrt{k^2 - k_y^2})$ . The network solutions with the original plane wave incident then is given by the uncoupled network of Fig. 4, together with the specified incident voltages  $V_0' \text{inc}(z)$  and  $V_0'' \text{inc}(z)$  at  $z=0$ . The voltage reflection coefficients (with the  $\sqrt{k^2 - k_y^2}$  dependence understood) at  $T_-$  are

$$\Gamma' = -jB_c' / (jB_c' + 2), \quad \Gamma'' = jX_L' / (jX_L' + 2),$$

from which the voltages at any point  $z$  are

$$V_0^\alpha(z) = V_0^\alpha \text{inc}(0) (e^{-j\kappa_0 z} + \Gamma^\alpha e^{j\kappa_0 z}), \quad z < 0,$$

$$V_0^\alpha(z) = V_0^\alpha \text{inc}(0) (1 + \Gamma^\alpha) e^{-j\kappa_0 z}, \quad z > 0,$$

with  $\alpha$  standing for prime or double prime. The far field can therefore be written at once as

$$E_i(x, y, z) = [V_0'(z) e_0'(x) + V_0''(z) e_0''(x)] e^{-jk_y y}.$$

<sup>17</sup> Marcuvitz, *op. cit.*, secs. 5.18 and 5.19.



## V. RELATIONSHIP BETWEEN MODAL REPRESENTATIONS IN RECTANGULAR COORDINATES

### 1. General

In rectangular waveguide regions, which possess more than one axial direction, the eigenvalue problem for the modes is highly degenerate. In such cases a variety of modal representations is possible for the same transmission line direction ( $z$ ). These sets are not in general independent. In particular, any mode function (corresponding to wave numbers  $k_{yi}$  and  $k_{xi}$ ) of one set can be expressed as a linear combination of two mode functions (corresponding to the same wave numbers) of any one of the other possible sets. In matrix notation<sup>18</sup>

$$\hat{\mathbf{e}}_i = A_i \mathbf{e}_i, \quad \hat{\mathbf{h}}_i = B_i \mathbf{h}_i, \quad (35)$$

where one defines the vectors

$$\begin{aligned} \hat{\mathbf{e}}_i &\rightarrow \begin{pmatrix} \hat{\mathbf{e}}_i' \\ \hat{\mathbf{e}}_i'' \end{pmatrix}, & \hat{\mathbf{h}}_i &\rightarrow \begin{pmatrix} \hat{\mathbf{h}}_i' \\ \hat{\mathbf{h}}_i'' \end{pmatrix}, \\ \mathbf{e}_i &\rightarrow \begin{pmatrix} \mathbf{e}_i' \\ \mathbf{e}_i'' \end{pmatrix}, & \mathbf{h}_i &\rightarrow \begin{pmatrix} \mathbf{h}_i' \\ \mathbf{h}_i'' \end{pmatrix}, \end{aligned} \quad (36)$$

and the transformation matrices

$$A_i \rightarrow \begin{pmatrix} a_{11}^i & a_{12}^i \\ a_{21}^i & a_{22}^i \end{pmatrix}, \quad B_i \rightarrow \begin{pmatrix} b_{11}^i & b_{12}^i \\ b_{21}^i & b_{22}^i \end{pmatrix}. \quad (37)$$

The orthogonality and normalization of such sets of modes, it is recalled, is given in (13) and (14). By exploiting the orthogonality properties of the two sets of modes in conjunction with (35), the coefficients  $a_{11}^i$ ,  $a_{12}^i \dots b_{22}^i$  are determined at once. For example,

$$b_{11}^i = \int_{y_1}^{y_2} \int_{x_1}^{x_2} \hat{\mathbf{h}}_i' \cdot \mathbf{z}_0 \times \mathbf{e}_i'^* dx dy.$$

The relationship between the  $a$  and the  $b$  coefficients follows upon substitution of the appropriate term from (35), as in

$$b_{11}^i = \int_{y_1}^{y_2} \int_{x_1}^{x_2} \hat{\mathbf{h}}_i' \cdot \mathbf{z}_0 \times (\alpha_{11} \hat{\mathbf{e}}_i' + \alpha_{12} \hat{\mathbf{e}}_i'')^* dx dy = \alpha_{11}^*,$$

where

$$A^{-1} \rightarrow \begin{pmatrix} \alpha_{11} & \alpha_{12} \\ \alpha_{21} & \alpha_{22} \end{pmatrix}.$$

It follows readily that  $A_i$  and  $B_i$  satisfy the condition

$$A_i^* \tilde{B}_i = 1. \quad (38)$$

Upon defining the modal voltage and current vectors

$$\begin{aligned} V_i &\rightarrow \begin{pmatrix} V_i' \\ V_i'' \end{pmatrix}, & \hat{V}_i &\rightarrow \begin{pmatrix} \hat{V}_i' \\ \hat{V}_i'' \end{pmatrix}, \\ I_i &\rightarrow \begin{pmatrix} I_i' \\ I_i'' \end{pmatrix}, & \hat{I}_i &\rightarrow \begin{pmatrix} \hat{I}_i' \\ \hat{I}_i'' \end{pmatrix}, \end{aligned}$$

<sup>18</sup> The caret notation serves to distinguish one of the modal sets from the other; prime denotes the  $E$ -type sub-set, double prime the  $H$ -type sub-set.

one can write

$$\tilde{V}_i \hat{\mathbf{e}}_i = \tilde{V}_i \mathbf{e}_i, \quad \tilde{I}_i \hat{\mathbf{h}}_i = \tilde{I}_i \mathbf{h}_i, \quad (39)$$

since the same transverse fields must be represented by either set of modes. The tilde sign indicates transposed vectors or matrices. From (39), (13), and (14), the following relations are then obtained:

$$V_i = \tilde{A}_i \hat{V}_i; \quad I_i = \tilde{B}_i \hat{I}_i. \quad (40)$$

When there is a discontinuity structure in the waveguide region, in which a number of modes are propagating, the voltages and currents at appropriate terminal planes for each mode set are related by appropriate impedance matrices  $Z$  and  $\hat{Z}$ :

$$V = ZI, \quad \hat{V} = \hat{Z}\hat{I}, \quad (41)$$

where  $V$ ,  $\hat{V}$ ,  $I$  and  $\hat{I}$  are the column matrices

$$V \rightarrow (V_i), \quad \hat{V} \rightarrow (\hat{V}_i), \quad I \rightarrow (I_i), \quad \hat{I} \rightarrow (\hat{I}_i).$$

Here the subscript  $i$  not only distinguishes the mode voltage and current associated with  $k_{xi}$  and  $k_{yi}$  but also serves as an index to distinguish two such quantities associated with the same  $k_{xi}$  and  $k_{yi}$ , when these occur at the input and output terminal planes of the structure. From (40) these voltage and current matrices can be related for the two mode sets as follows:

$$V = \tilde{A} \hat{V}, \quad I = \tilde{B} \hat{I}, \quad (42)$$

where  $A$  and  $B$  are diagonal matrices whose elements are the two by two matrices  $A_i$  and  $B_i$ :

$$A \rightarrow (A_i), \quad B \rightarrow (B_i),$$

and where

$$A^* \tilde{B} = 1. \quad (43)$$

From (41), (42), and (43) the relationship between the impedance matrices for the two sets of modes then is

$$\hat{Z} = B^* Z \tilde{B} \quad \text{or} \quad Z = \tilde{A} \hat{Z} A^*. \quad (44)$$

Eq. (44) can be represented schematically as shown in Fig. 5, where the transformation which each pair ( $i$ ) of the mode voltages and currents is subjected to is explicitly exhibited.

The ability to obtain the network description of a discontinuity for one set of modes from that for the other set is useful for certain cases involving more than one discontinuity. For example, if there are two discontinuities in a waveguide region which are far enough apart so that there is no higher mode interaction, the network parameters for each discontinuity may be obtained by using the most convenient set of modes for each. The separate networks may then be combined in a over-all representation in terms of one of the mode sets, via the transformation relations of (44). Such a case is that shown in Fig. 6, where a parallel plate guide contains a slit iris at the plane  $T_1$  and a change in dielectric constant at the plane  $T_2$ . Since the  $E$  and  $H$  modes would

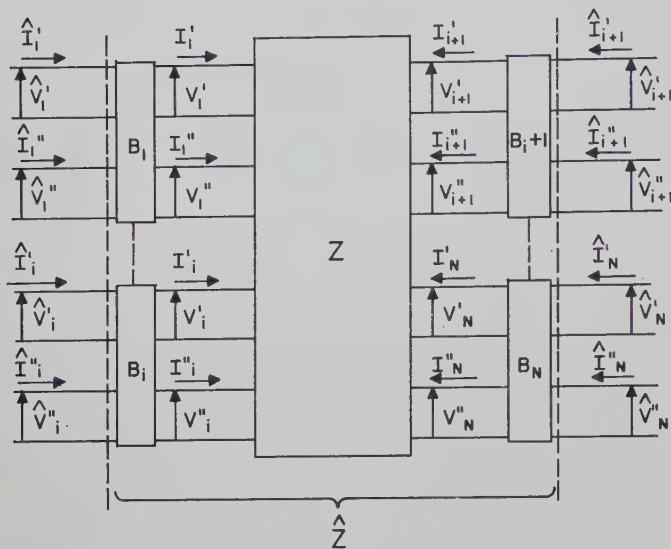


Fig. 5—Schematic representation of the transformation  $\hat{Z} = B^* Z \tilde{B}$ .

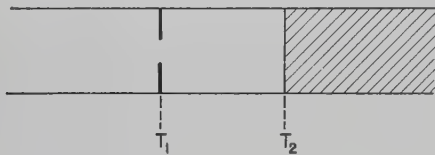


Fig. 6—Parallel plate waveguide containing a slit iris and a change in dielectric constant.

be coupled by the iris but not by the dielectric interface, and vice versa, for the  $E$ -type and  $H$ -type modes, it is convenient to treat the discontinuity problem at plane  $T_1$  in terms of the  $E$ -type and  $H$ -type modes, and that at  $T_2$  in terms of  $E$  and  $H$  modes. Eq. (44) would be employed in combining these results.

## VI. SUMMARY

In waveguide regions possessing at least one axial direction the fields can be expanded in terms of  $E$ - and  $H$ -type modes. In contrast to the usual  $H$  and  $E$  modes, they are respectively characterized by vanishing magnetic and electric field components in an axial direction (taken as the  $y$  direction) transverse to the direction of propagation. They form a complete orthonormal set. The  $E$ - and  $H$ -type modes, having no periodicity in  $y$  (when  $k_y = 0$ ), are, respectively, identical to the corresponding  $H$  and  $E$  modes.

The  $E$ - and  $H$ -type modes are usefully applied in certain scattering problems in which the obstacles possess uniformity in  $y$ , and the modal direction of propagation (or transmission line direction) lies in the plane transverse to  $y$ . Under such circumstances the scattering problem is a scalar one in that  $E$ - and  $H$ -type modes do not couple; under the same set of conditions the familiar  $E$  and  $H$  modes are coupled, the problem appears to have a vector character, and the usual difficulties associated with vector problems occur.

Assuming that either the field or the network solution of a problem involving incidence normal to the  $y$  direction ( $k_y = 0$ ) is known, the solution is readily extended to

the case with arbitrary angles of incidence ( $k_y \neq 0$ ) by replacing  $k$  by  $\sqrt{k^2 - k_y^2}$  in the scalar fields  $E_y$  and  $H_y$  of the  $E$ - and  $H$ -type modes or in the scattering, impedance or admittance parameters of the associated network. This permits the extension to arbitrary angles of incidence of the many known  $E$  and  $H$  mode solutions of such problems as the half plane, the capacitive slit in parallel plate waveguide, and gratings of various cross sections.

Rectangular waveguide regions (including free space, of course) possess more than one axial direction. In consequence, a variety of modal representations is possible for the same transmission line direction. The relationship between two such representations is given by a transformation matrix which, in turn, can be described in simple network terms. One can consequently combine the networks representing tandem discontinuities even if the emergent transmission lines of each network are defined with respect to different modal representations. This is done by interposing the appropriate transformation matrix or network.

## APPENDIX: $E$ - AND $H$ -TYPE MODES FOR FREE SPACE (RECTANGULAR COORDINATES)

A variety of  $E$ - and  $H$ -type modal representations is possible for free space. In particular, a representation in terms of either the rectangular or the radial modes can be employed. The modes given below are based on rectangular coordinates.

$$\begin{aligned}
 &E\text{-type Modes } h_{yi}' = 0 & H\text{-type Modes } e_{yi}'' = 0 \\
 &e_{yi}' = -h_{xi}' = \frac{e^{-j(k_{xi}'x + k_{yi}'y)}}{2\pi}, & h_{yi}'' = e_{xi}'' = \frac{e^{-j(k_{xi}''x + k_{yi}''y)}}{2\pi}, \\
 &e_{xi}' = \frac{-k_{yi}'k_{xi}'}{k^2 - k_{yi}'^2} e_{yi}', & h_{xi}'' = \frac{k_{yi}''k_{xi}''}{k^2 - k_{yi}''^2} h_{yi}'', \\
 &Z_i' = \frac{k^2 - k_{yi}'^2}{k_{xi}'\omega\epsilon}, & Z_i'' = \frac{k_{xi}''\omega\mu}{k^2 - k_{yi}''^2}, \\
 &k_i'^2 = k^2 - k_{yi}'^2 - k_{xi}'^2, & k_i''^2 = k^2 - k_{yi}''^2 - k_{xi}''^2, \\
 &-\infty < k_{xi}' < \infty, & -\infty < k_{xi}'' < \infty, \\
 &-\infty < k_{yi}' < \infty; & -\infty < k_{yi}'' < \infty.
 \end{aligned}$$

These modes, when slightly modified, are also appropriate to the consideration of discontinuity structures in free space which possess periodicities along both  $x$  and  $y$ . The modified modes are then orthogonal in the cell  $-a/2 < x < a/2$  and  $-b/2 < y < b/2$ . The modification consists of replacing the normalization factor  $2\pi$  by  $\sqrt{ab}$  and recognizing that the wave numbers  $k_{xi}'$ ,  $k_{xi}''$ ,  $k_{yi}'$  and  $k_{yi}''$  take on the discrete values

$$\begin{aligned}
 k_{xi}' &= k_{xi}'' = \frac{2m\pi}{a} + k_{x0}, & m &= 0, \pm 1, \pm 2, \dots, \\
 k_{yi}' &= k_{yi}'' = \frac{2n\pi}{b} + k_{y0}, & n &= 0, \pm 1, \pm 2, \dots,
 \end{aligned}$$

where  $k_{x0}$  and  $k_{y0}$  are the  $x$  and  $y$  components of the



propagation wave number of the exciting field,  $a$  and  $b$  are the periods of the structure in  $x$  and  $y$ .

In the case of a structure in free space which is periodic (with period  $a$ ) in  $x$  and arbitrary in  $y$ , the free space modes are modified by replacing the normalization factor  $2\pi$  by  $\sqrt{2\pi a}$  and recognizing that the wave numbers  $k_{xi}'$  and  $k_{xi}''$  take on the discrete values

$$k_{xi}' = k_{xi}'' = \frac{2m\pi}{a} + k_{x0}, \quad m = 0, \pm 1, \pm 2, \dots,$$

while the wave numbers  $k_{yi}'$  and  $k_{yi}''$  are given by

$$k_{yi}' = k_{yi}'' = \eta + k_{y0}, \quad -\infty < \eta < \infty.$$

These modes are orthogonal in the strip  $-a/2 < x < a/2$  and  $-\infty < y < \infty$ . In the special case of a structure periodic in  $x$  but uniform in  $y$ , such as an infinite strip grating, the normalization factor is taken as  $\sqrt{a}$ , and  $\eta = 0$ . The exponential  $y$  dependence is suppressed.

#### ACKNOWLEDGMENT

The authors wish to express their appreciation to Dr. N. Marcuvitz and A. D. Bresler for helpful discussions and suggestions in connection with this work.

## Reflectors for a Microwave Fabry-Perot Interferometer\*

W. CULSHAW†

**Summary**—The advantages of microwave interferometers for wavelength and other measurements at millimeter wavelengths are indicated, and a microwave Fabry-Perot interferometer discussed in detail. Analogous to the cavity resonator, this requires reflectors of high reflectivity, small absorption, and adequate size. Stacked dielectric plates, and stacked planar or rod gratings are shown to be suitable forms of reflectors, and equations for the reflectivity, optimum spacing, and bandwidth of such structures are derived. A series of stacked metal plates with regularly spaced holes represents a good design of reflector for very small wavelengths. Fringes and wavelength measurements at 8-mm wavelength are given for one design of interferometer, these being accurate to 1 in  $10^4$  without any diffraction correction. For larger apertures and reflectors in terms of the wavelength, errors due to diffraction will decrease.

### I. INTRODUCTION

IN conjunction with the efforts directed toward the generation and use of shorter wavelengths in the millimeter region, it is necessary to develop new techniques of transmission and measurement. The facility with which methods based on optical techniques can be used for this purpose improves as the wavelength decreases, in contrast to the conventional waveguide methods, where the dimensions of cavity resonators and other components are in general comparable with the wavelength, with a consequent increase in attenuation and fabrication difficulties. Wavelength measurements can be made with interferometers based on optical principles, and at wavelengths around a few millimeters, such methods would be preferable to the use of a cavity resonator.

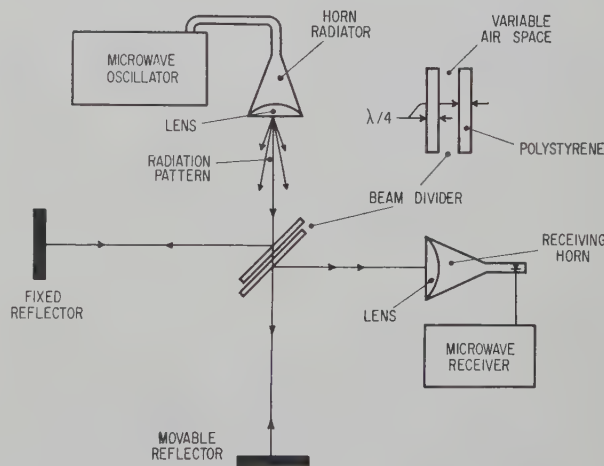


Fig. 1—Microwave form of Michelson interferometer.

A free-space form of Michelson interferometer is shown in Fig. 1; here the beam from the radiating horn is divided by the beam divider into two beams which travel different paths. The two beams then are recombined in the receiving horn, and interference is observed between the two sinusoidal wave trains as one of the reflectors is moved. This interferometer has been operated at  $\lambda = 1.25$  cm,<sup>1</sup> the wavelength measurements with a particular form being accurate to a few parts in  $10^4$  without any correction for diffraction. The free-space beam divider and reference arm can be replaced by a hybrid tee at these wavelengths, and then only a single radiator and reflector are required for the open arm.

<sup>1</sup> W. Culshaw, "The Michelson interferometer at millimeter wavelengths," *Proc. Phys. Soc. B*, vol. 63, pp. 939-954; November, 1950.

\* Manuscript received by the PGM-TT, July 10, 1958; revised manuscript received, November 10, 1958.

† National Bureau of Standards, Boulder Laboratories, Boulder, Colo.

Such an interferometer was used by Froome for the accurate determination of the velocity of electromagnetic waves by microwave interferometry.<sup>2</sup> By applying a diffraction correction for the open arm of the interferometer, he obtained a result in agreement with recent determinations by other methods, including the cavity resonator.<sup>3</sup>

Microwave interferometers can also be used with advantage at wavelengths around 1 cm and below for the measurement of dielectric constants, and at very short wavelengths would again be preferable. Both the Michelson and Fabry-Perot types of interferometer have been used for this purpose,<sup>1,4</sup> and more recently Blair<sup>5</sup> has described a microwave interferometer designed specifically for the measurement of dielectric constants of materials in sheet form at wavelengths around 3 cm.

The fringes in the Michelson interferometer are due to the interference of two wave trains, and for maximum sensitivity the beams must be accurately balanced to give a sharp null. In the Fabry-Perot interferometer shown in Fig. 2 the fringes are made very sharp by multiple reflections between two highly reflecting surfaces, and in the microwave region it represents the free-space analog of the cavity resonator. The narrow bright rings in the optical form of this interferometer show the increased resolution possible.<sup>6</sup> The principle of the microwave form is exactly analogous, though the technique of reflector design is different because any metallic film would seriously attenuate the microwave radiation. Also, we deal essentially with a single plane-wave train in the microwave form so that the circular fringe system is not obtained, except that the distance  $d$  between the reflectors can be adjusted to pass various portions of the continuous plane-wave spectrum radiated by the aperture.

To obtain high sensitivity in this interferometer the reflectivity of the reflectors must approximate that of metals such as silver, and undue attenuation in the reflector system must be avoided. The reflectors and apertures used must also be large compared with the wavelength, so that errors in the wavelength measurement due to diffraction are reduced, and their consideration facilitated as required in work of high precision. We shall be mainly concerned with ways of meeting these requirements on the reflectors, bearing in mind that any reflector technique developed should be applicable to wavelengths extending down to 1 millimeter and below, when adequate sources are available.

<sup>2</sup> K. D. Froome, "Determination of the velocity of short electromagnetic waves by interferometry," *Proc. Roy. Soc. A*, vol. 213, pp. 123-141; 1952.

<sup>3</sup> L. Essen, "The velocity of propagation of electromagnetic waves derived from the resonant frequencies of a cylindrical cavity resonator," *Proc. Roy. Soc. A*, vol. 204, pp. 260-277; December, 1950.

<sup>4</sup> W. Culshaw, "The Fabry-Perot interferometer at millimeter wavelengths," *Proc. Phys. Soc. B*, vol. 66, pp. 597-608; July, 1953.

<sup>5</sup> G. R. Blair, "An ultra-precise microwave interferometer," 1958 IRE NATIONAL CONVENTION RECORD, pt. 1, pp. 48-56.

<sup>6</sup> F. A. Jenkins and H. E. White, "Fundamentals of Optics," McGraw-Hill Book Co., Inc., New York, N. Y., pp. 269-274; 1950.

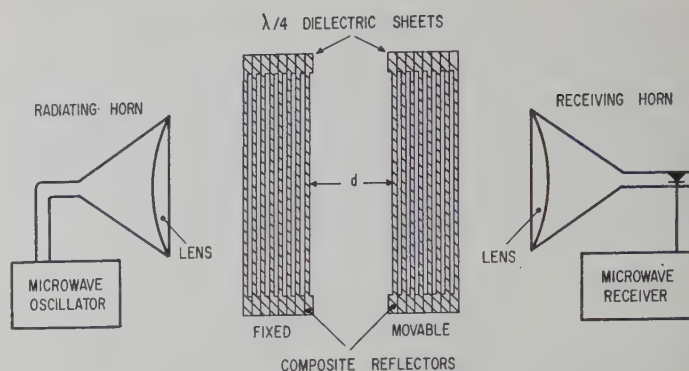


Fig. 2—Microwave Fabry-Perot interferometer.

The theory of the Fabry-Perot interferometer as applied to the microwave region will be dealt with first, together with the theory necessary for the consideration of composite reflecting systems. These will consist of lattice structures such as stacked dielectric plates, stacked metal rod gratings, and stacked metal plates with holes in them.

## II. THE FABRY-PEROT INTERFEROMETER

An arrangement of this is shown in Fig. 2, electromagnetic horn radiators with lenses being used to produce efficient radiating and receiving apertures. Radiated energy passes between the reflectors, represented by the dielectric sheet reflectors shown, and at certain spacings of the reflectors, separated by  $\lambda/2$  intervals, the multiply reflected waves reinforce each other to give a sharp transmitted fringe. The sharpness of the fringe as  $d$  varies depends on the reflectivity obtained, and on the angular width of the radiated and received spectra, since  $d$  can be optimized for each plane wave in the spectrum. This interferometer is basically quite simple, it does not require any form of beam divider, and the problem of preserving a balance with displacement between two interfering beams, as in the Michelson type, does not arise. It is, however, necessary to use highly reflecting devices for the reflectors, as the setting accuracy and the diffraction correction will depend on this.

The theory of operation of the interferometer may be developed using transmission line theory. Referring to Fig. 3, the general transmission line matrix of the symmetrical four terminal network may be written

$$\begin{bmatrix} V_{n+1} \\ I_{n+1} \end{bmatrix} = \begin{bmatrix} A & B \\ C & A \end{bmatrix} \begin{bmatrix} V_n \\ I_n \end{bmatrix}. \quad (1)$$

For matched conditions at the output, and all impedances normalized with respect to the characteristic impedance of the line, the input impedance  $Z_{in}$  may be determined. The voltage amplitude reflection coefficient is then,

$$r_v = \frac{B - C}{2A + B + C}, \quad (2)$$



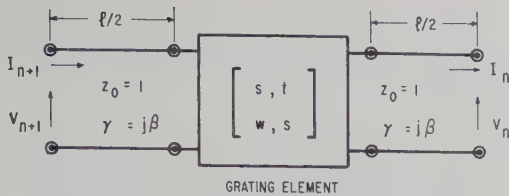


Fig. 3—Line symmetrically loaded by transmission matrix of grating element.

and the ratio of the voltage or current at the output terminals to the incident voltage or current is given by

$$t = \frac{2}{2A + B + C} \quad (3)$$

Assuming a single plane wave propagating along its axis, the equation governing the transmission and reflection in the complete interferometer may be written in matrix form as

$$\begin{bmatrix} V_{n+1} \\ I_{n+1} \end{bmatrix} = \begin{bmatrix} a & b \\ c & a \end{bmatrix} \begin{bmatrix} \cosh \gamma d & \sinh \gamma d \\ \sinh \gamma d & \cosh \gamma d \end{bmatrix} \begin{bmatrix} a & b \\ c & a \end{bmatrix} \begin{bmatrix} V_n \\ I_n \end{bmatrix}, \quad (4)$$

where the elements  $a$ ,  $b$ , and  $c$ , refer to the symmetrical reflectors,  $\gamma = \alpha + j\beta$  is the propagation constant for the medium between the reflectors, and  $d$  is the distance between them. With matched conditions at the output terminals, the condition for no reflection from the interferometer is

$$\tanh \gamma d = -\frac{2a}{b+c} \quad (5)$$

At this separation the whole system is matched, and assuming no loss in the reflectors or in the medium between them, the modulus of the transmission coefficient is unity.

Using (4), and substituting the matrix elements corresponding to  $A$ ,  $B$ , and  $C$  in (2) and (3), the reflection and transmission coefficients of the interferometer,  $r_I$  and  $t_I$ , may be determined. For no loss in the reflectors, and with  $\gamma = j\beta$  these may be written

$$|r_I|^2 = \frac{4R \sin^2 \phi}{1 - 2R \cos 2\phi + R^2} \quad (6)$$

$$|t_I|^2 = \frac{(1 - R)^2}{1 - 2R \cos 2\phi + R^2} \quad (7)$$

where

$$\phi = (\beta d + \psi), \quad R = |r|^2,$$

and

$$|r| \exp(-j\psi) = j(b - c)/[2a + j(b + c)].$$

Hence  $|t_I|^2$  and  $|r_I|^2$  have maximum values when

$$\phi = n\pi, \quad \text{and} \quad \phi = (2n + 1)\pi/2 \quad (8)$$

respectively, where  $n$  is the order of interference.

Eqs. (6) and (7) show that the sharpness of the fringes depends on the value of reflection coefficient,  $R$ , obtained, and some fringe shapes for various reflectivities are shown in Fig. 4. For precise work high reflectivity must be used since the discrimination with  $d$ , or setting accuracy achieved, will depend on this. A measure of the fringe sharpness may be obtained by deducing the  $Q$  factor of the reflectors from (7), since the value of  $\phi$  at which the transmitted power is half the maximum is given by

$$\cos 2\phi_1 = [2R - (1 - R)^2]/2R. \quad (9)$$

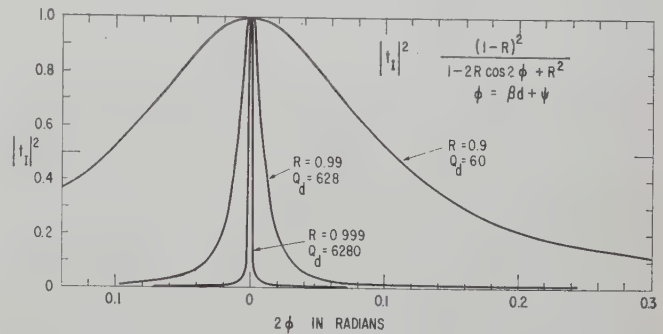


Fig. 4—Variation of fringe sharpness with reflectivity.

The change in  $\beta d$  required to obtain the angle  $\phi_1$ , can be effected by changing the wavelength, or the spacing of the reflectors, and the respective  $Q$  values deduced are

$$Q_\lambda = \frac{\lambda}{2\Delta\lambda} = \frac{1}{2\phi_1} (n\pi - \psi)$$

and

$$Q_d = \frac{\lambda}{2\Delta d} = \frac{\pi}{\phi_1}. \quad (10)$$

Actually instead of the single plane wave assumed so far, the aperture will radiate an angular spectrum of plane waves determined by its size, and its field distribution. The portion of this angular spectrum which is effective between the reflectors at any particular spacing  $d$  may be deduced from (8) and (10), since a wave traveling at an angle  $\theta$  to the axis corresponds to a change in path length given by

$$\Delta d = d(1 - \cos \theta), \quad (11)$$

and can also be regarded as a change in effective wavelength to  $\lambda/\cos \theta$ . As an approximation considering only those waves propagated between the positions of half-maximum intensity the result is

$$\cos \theta = 1 - 1/2Q_\lambda, \quad (12)$$

which shows that the higher the reflectivity, the smaller the number of plane waves which are transmitted through the interferometer at optimum, and other spacings of the reflectors.

For reflectors very large compared with the wavelength, the angular width of the plane-wave spectra generated will correspond to the radiation pattern of the horns, and depending on the reflectivity as indicated by (12), a number of these will be passed by the reflector system at any particular distance  $d$ , the reflector system thus acting as a plane-wave filter. The summation of the plane waves which pass through the complete interferometer will lead to an optimum setting slightly different from that given by (8), which assumes a single plane wave along the axis, and in the measurement of length with the interferometer the diffraction correction is the difference between the errors due to the two summations of plane waves effective in the interferometer at the initial and final reflector separations used. The correction can be made small if the reflectivity and order of interference used are such that  $\theta$  becomes a very small angle. In general, for the high values of reflectivity discussed later, and apertures and reflectors some 15 wavelengths in extent, it is found experimentally that the error due to diffraction in a wavelength measurement on the interferometer is around a part in  $10^4$ . For apertures and reflectors larger in terms of wavelengths the error would decrease. Some quantitative discussion on the diffraction correction could be made using (7) to find the transmission coefficient through the interferometer for different distances  $d$  and reflectivities. The radiated and received angular spectra of the apertures, their distances from the reflectors, and the reflector size would also have to be considered.

### III. THEORY OF REFLECTOR DESIGN

One type of reflector which has been used<sup>4</sup> is shown in Fig. 2, and consists of a number of quarter-wave plates of dielectric with quarter-wave air spacings between them. If  $\epsilon$  is the dielectric constant and zero dielectric loss is assumed, the amplitude reflection coefficient from  $n$  such sheets and spacings is equal to that of a single quarter-wave sheet having a dielectric constant of  $\epsilon^n$ . In view of the high reflectivities involved, however, the effect of a finite dielectric loss must be considered, and it is found<sup>4</sup> that if  $A_1$  refers to the amplitude reflection coefficient from a single quarter-wave sheet, and  $A_n$  that from  $n$  such sheets with quarter-wavelength spacings between them, then

$$A_{n+1} = \frac{A_1 + A_n(R_0^2 + \psi)/(1 + R_0^2\psi)}{1 + A_1A_n}, \quad (13)$$

where  $A_1 = R_0(1 + \psi)/(1 + R_0^2\psi)$ ,  $\psi = \exp(-\pi \tan \delta/2)$ ,  $\tan \delta$  is the loss tangent of the dielectric, and  $R_0$  is the

$$\begin{bmatrix} V_{n+1} \\ I_{n+1} \end{bmatrix} = \begin{bmatrix} s \cos \theta + j/2 \sin \theta(t + w), \\ \cos \theta(w + t)/2 + js \sin \theta + (w - t)/2, \end{bmatrix}$$

amplitude reflection coefficient at the air-dielectric boundary. The effect of dielectric loss is to limit the reflectivity obtainable by stacking such sheets. For poly-

styrene  $\epsilon = 2.56$  and  $\tan \delta = 0.001$  approximately, and the values of  $A_n$  shown in Table I are obtained, the limiting value being 0.9982.

TABLE I  
VALUES OF THE AMPLITUDE REFLECTION COEFFICIENT  
OBTAINED FROM  $n$  QUARTER-WAVE PLATES OF  
POLYSTYRENE WITH  $\lambda/4$  AIR  
SPACE BETWEEN THEM.

$n$	1	2	3	4	5	6	7	8
$A_n$	0.4378	0.7340	0.8861	0.9528	0.9806	0.9913	0.9961	0.9977

Fig. 5 shows the fringes obtained, at given spacings of the reflectors, as  $d$  is varied for an interferometer with reflectors consisting of eight such plates of polystyrene.<sup>4</sup> These had a diameter of about 11 inches, the radiating and receiving apertures being 6 inches square, and the wavelength around 8.33 mm. The sharpness of the fringes illustrates the potentialities of this interferometer for accurate measurements at very short wavelengths. For a dielectric with smaller loss and higher dielectric constant, such as fused quartz, higher values of reflectivity can be obtained. Such reflectors would be very costly due to the required size, except at very short wavelengths, but here the reflector plates become very thin. Odd multiples of quarter wavelength may be used, but the ultimate reflectivity obtained and the bandwidth of the reflectors will decrease.

This leads to the consideration of other types of reflectors, such as a stacked system of gratings, consisting of plane layers of inductive, or capacitive, irises or rods placed symmetrically behind each other, similar to the structures used in delay dielectrics.<sup>7</sup> Fig. 3 shows the basic element which can be used for all the structures considered, the particular grating being represented by a discontinuity transmission matrix symmetrically located on a length of parallel plate transmission line. The transmission line matrix representing the discontinuity may be derived from the equivalent networks of the various gratings, and the reflectivity from a finite number of such elements must be determined. Only TEM mode interaction between the gratings is considered, and all other modes on the structure must be evanescent. Since only even order modes are excited on such a symmetrical structure, a spacing between grating elements less than  $\lambda$  is sufficient for this, but in practice a spacing less than  $\lambda/2$  is preferable.

The matrix representing the basic element shown in Fig. 3 may be written for a lossless transmission line as,

$$\begin{bmatrix} \cos \theta(w + t)/2 + js \sin \theta - (w - t)/2 \\ s \cos \theta + j/2 \sin \theta(t + w) \end{bmatrix} \begin{bmatrix} V_n \\ I_n \end{bmatrix} \quad (14)$$

<sup>7</sup> J. Brown, "Microwave Lenses," Methuen and Co. Ltd., London, Eng., pp. 53-68; 1953.



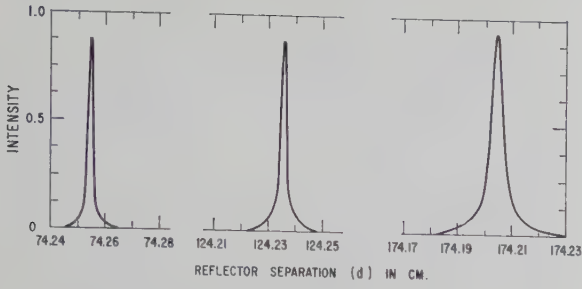


Fig. 5—Fringe shapes measured on microwave Fabry-Perot interferometer.

where  $\theta = 2\pi l/\lambda$ . Also referring to (2) and (3), and Fig. 6, we obtain for the general four terminal network,

$$\begin{bmatrix} b_{n+1} \\ a_{n+1} \end{bmatrix} = \begin{bmatrix} \frac{B-C}{2}, & \frac{2A-(B+C)}{2} \\ \frac{2A+B+C}{2}, & -\frac{B-C}{2} \end{bmatrix} \begin{bmatrix} b_n \\ a_n \end{bmatrix}, \quad (15)$$

and since  $r_{n+1} = b_{n+1}/a_{n+1}$ , and  $r_n = a_n/b_n$ , the recurrence relation between the reflection coefficients for elements in cascade is,

$$r_{n+1} = \frac{[2A - (B+C)]r_n + B - C}{2A + B + C - (B-C)r_n}, \quad (16)$$

and by inserting elements corresponding to  $A$ ,  $B$ , and  $C$ , from (14), the reflectivity from a number of basic elements may be determined. The transmission coefficient  $t_n = b_n/a_{n+1}$  may also be deduced from (15).

The spacing  $l$  between gratings for optimum reflection may be deduced from the equivalent matrix of the basic element by deducing its effective propagation constant  $\Gamma$ , and characteristic impedance  $Z$ . Using (1), these are given by<sup>8</sup>

$$\cosh \Gamma l = A, \quad \text{and} \quad Z^2 = B/C \quad (17)$$

and may be determined from (14) for any particular structure. Putting  $\phi = \Gamma l$ , the over-all matrix for  $n$  such structures in cascade may then be written as

$$\begin{bmatrix} V_n \\ I_n \end{bmatrix} = \begin{bmatrix} \cosh n\phi, & Z \sinh n\phi \\ \frac{1}{Z} \sinh n\phi, & \cosh n\phi \end{bmatrix} \begin{bmatrix} V_0 \\ I_0 \end{bmatrix} \quad (18)$$

Consider such a periodic structure, then by (14)

$$\cosh \phi = A = s \cos \theta + j/2 \sin \theta(t+w), \quad (19)$$

and putting  $\phi = (\alpha + j\beta)l$ , since  $\cosh \phi$  must be real, the stop bands of the structure are given by  $\sin \beta = 0$ , and the pass bands by  $\sinh \alpha = 0$ . Thus for the pass bands:

$$\cos \beta = A \quad \text{where} \quad |A| < 1, \quad (20)$$

and in the stop bands:

$$\cosh \alpha = |A| \quad \text{where} \quad |A| > 1. \quad (21)$$

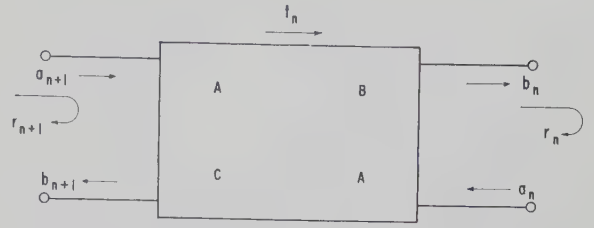


Fig. 6—Reflection and transmission coefficients of four-terminal network.

Thus from (2) and (18), if the spacing  $l$  between gratings is such that  $\theta$  lies within a pass band of the structure, the reflection coefficient  $r_n$  becomes

$$r_n = \frac{j(Z^2 - 1) \sin n\beta}{2Z \cos n\beta + j(Z^2 + 1) \sin n\beta} \quad (22)$$

while for spacings corresponding to a stop band,

$$r_n = \frac{(Z^2 - 1) \sinh n\alpha}{2Z \cosh n\alpha + (Z^2 + 1) \sinh n\alpha}. \quad (23)$$

For spacings such that  $\theta$  lies within the pass band, the reflection coefficient  $r_n$  will oscillate with increase in  $n$ , and become zero when  $\sin n\beta = 0$ . As an example, a thin grating may be represented by an admittance  $Y = jB$  on the line and (14) and (20) give

$$\cos \beta = \cos \theta - B/2 \sin \theta \quad (24)$$

and  $r_3 = 0$  when  $\tan^2 \theta(1 - B^2) + 4B \tan \theta - 3 = 0$ , with similar results for other values of  $n$ .

When  $l$  is such that  $\theta$  lies in the stop band of the structure, the reflectivity will increase monotonically with  $n$ , and it is found from (17), (22), and (23) that the spacing for maximum reflectivity, corresponds to the value of  $\theta$  which gives the maximum value of  $\cosh \alpha = |A|$  within the stop band. Eq. (24) is plotted in Fig. 7 for various values of  $B$ ; for inductive admittances the pass band extends from values of  $\theta < \pi$  to  $\theta = \pi$ , the interval diminishing with increasing values of  $B$ . Similar remarks apply to capacitive admittances, the pass band now extending from  $\theta = \pi$  to  $\theta > \pi$ . Thus  $l = \lambda/2$  is not a good spacing for gratings of this type since it corresponds to the edge of the pass band and will be frequency sensitive. The spacing for optimum reflection corresponds to the maxima of these curves, which shows that, except for small values of  $B$ , a spacing of  $l = \lambda/4$  will be satisfactory for thin gratings. For  $B = -2$  the pass band extends from  $\theta = \pi/2$  to  $\theta = \pi$ , and Fig. 8 shows the variation in reflectivity, and the zeros which occur within the pass band for different values of  $n$  and spacing  $l$ . Similar considerations apply to thick gratings, and will be used to optimize the design of reflectors of this type.

#### IV. APPLICATION TO GRATING REFLECTORS

##### A) Thin Planar Gratings

Fig. 9 shows a good structure for the reflectors, which consists of a series of circular holes regularly spaced in a

<sup>8</sup> L. Brillouin, "Wave Propagation in Periodic Structures," Dover Publications Inc., New York, N. Y., pp. 193-226; 1953.

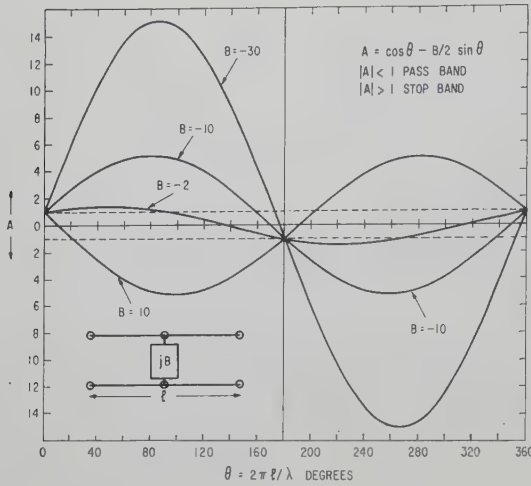
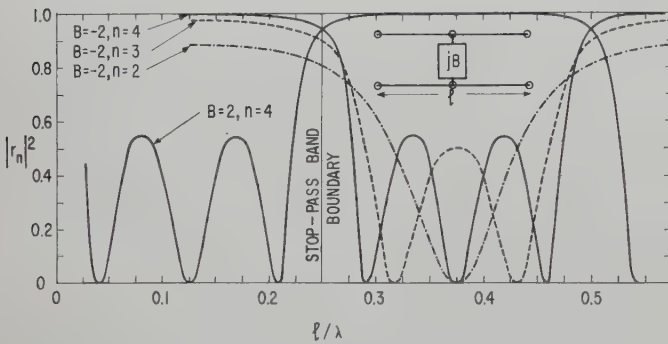


Fig. 7—Pass and stop bands for periodic structure shown.

Fig. 8—Reflectivity  $|r_n|^2$  versus spacing  $l$  for thin gratings, showing oscillations of reflectivity in pass band of structure.

thin metal sheet. Such a system of gratings is equivalent to a number of inductive susceptances across the parallel plate transmission line, and values of the normalized susceptances are given by (25),<sup>9</sup> when the transverse spacings  $a$  and  $b$  are  $< \lambda$ , and where  $R/a$  and  $R/b < 1$ ,  $R$  being the hole radius.

$$B = \frac{3ab\lambda}{8\pi R^3} - \frac{72}{\pi\lambda R^2} \left[ \sum_{m=0}^{\infty} \sum_{n=0}^{\infty} (\epsilon_m n^2/b^2 + \epsilon_n m^2/a^2) J_1^2(X) \right] \quad (25)$$

where  $X = [\pi R(m^2/a^2 + n^2/b^2)]^{1/2} / (m^2/a^2 + n^2/b^2)^{5/2}$ , the primes denote summation over even integers only,  $J_1$  is the Bessel function of order unity, and  $\epsilon_{m,n} = 1$  if  $m, n = 0$ , and  $= 2$  if  $m, n \neq 0$ . For  $a/R > 5$  the term  $3ab\lambda/8\pi R^3$ , which agrees with the usual value of susceptance for such a small hole,<sup>10</sup> is adequate.

Values of the reflectivity  $|r_n|^2$  for such a structure, calculated from (16) or (23), are shown in Table II for

<sup>9</sup> J. Munushian, "Electromagnetic Propagation Characteristics of Space Arrays of Apertures-in-Metal Discontinuities and Complementary Structures," University of California, Berkeley, Electronics Res. Lab. Rep., Ser. No. 60, Issue 126; September, 1954.

<sup>10</sup> C. G. Montgomery, R. H. Dicke, and E. M. Purcell, "Principles of Microwave Circuits," M.I.T. Rad. Lab. Ser., McGraw-Hill Book Co., Inc., New York, N. Y., pp. 176-179; 1948.

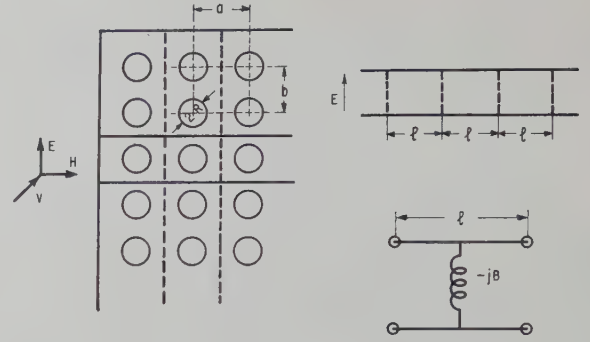


Fig. 9—Thin perforated metal plate gratings and equivalent transmission line circuit. Electric wall ———, magnetic wall - - - - -.

TABLE II  
VALUES OF REFLECTIVITY,  $|r_n|^2$ , OBTAINED FROM A  
NUMBER OF THIN INDUCTIVE GRATINGS  
AT  $l = \lambda/4$  SPACING.

$n$	$B = -2$	$B = -5$	$B = -10$	$B = -30$
1	0.5000	0.86207	0.96154	0.99558
2	0.8000	0.99364	0.99960	0.99999

a spacing  $l$  of  $\lambda/4$ , the reflectivity increasing when further gratings are added. At a wavelength of 6.28 mm, with spacing  $a = b = 0.125$  inch, and a hole diameter of  $1/16$  inch, the normalized susceptance would be around  $-15$ , and the attenuation constant for the first higher mode on the structure would be 86 db per wavelength, representing a suitable design for this wavelength.

Similarly the reflectivities possible by stacking inductive or capacitive strip gratings may be calculated using the appropriate formula for the equivalent reactances.<sup>11</sup>

### B) Thick Gratings

A capacitive rod type of grating structure is shown in Fig. 10, with the equivalent circuit, the electric vector being perpendicular to the metal rods. Values of the appropriate reactances are given by<sup>12</sup>

$$X_a = -\frac{1}{2} \frac{a}{\pi\beta r^2} \left[ 1 + \frac{7\beta^2 r^2}{8} + \frac{1}{2} \beta^2 r^2 \ln \left( \frac{2\pi r}{a} \right) - \frac{\pi^2 r^2}{3a^2} \right]$$

$$X_b = -\frac{1}{2} \frac{\pi\beta^2 r^2}{a} \left[ 1 + \frac{1}{2} \beta^2 r^2 \ln (2\pi r/a) - \frac{3\beta^2 r^2}{8} \right], \quad (26)$$

where  $\beta = 2\pi/\lambda$ ,  $a$  is the rod spacing in the grating, and  $r$  is the rod radius. Using these values the discontinuity matrix is determined, and substitution of its elements into (17), gives the effective propagation constant, and characteristic impedance of the basic element. The reflectivity follows from (16) or (23), once the spacing for

<sup>11</sup> N. Marcuvitz, "Waveguide Handbook," M.I.T. Rad. Lab. Ser., McGraw-Hill Book Co., New York, N. Y., pp. 280-285; 1951.

<sup>12</sup> L. Lewin, "Advanced Theory of Waveguides," Iliffe and Sons Ltd., London, Eng., pp. 37-44; 1951.



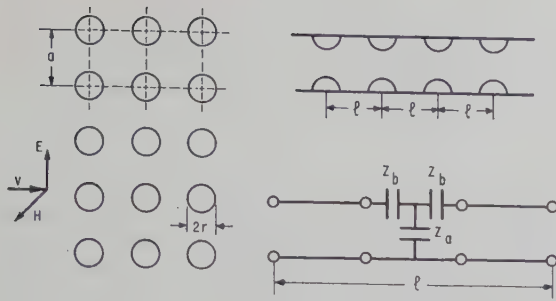


Fig. 10—Stacked capacitive rod gratings and equivalent circuits.

optimum is determined; this is done by finding the value of  $l$  which gives the maximum value of  $\cosh \alpha$ , as indicated in Section III.

Consider a wavelength of 6.28 mm and rods of diameter 0.063 inch, which are readily available, then  $r/\lambda = 0.1275$ , and for  $a/\lambda = 0.417$ , (26) gives  $X_a = -0.95$  and  $X_b = -0.372$ , and hence  $s = 1.3916$ ,  $t = -0.890j$ , and  $w = 1.053j$ . The effective propagation constant of the basic element is then

$$\cosh \phi = A = 1.3916 \cos \theta - 0.0815 \sin \theta. \quad (27)$$

Fig. 11 shows the variation of  $A$  with  $\theta$ , the optimum value of  $l$  being close to  $\lambda/2$  for this grating. Values of reflectivity  $|r_n|^2$  are shown in Table III for this spacing. A spacing  $l$  of  $3\lambda/4$  was also considered, but as indicated by Fig. 11, such a spacing is within the pass band of the infinite structure, and is not suitable. The values  $|r_1|^2 = 0.48542$  and  $|r_2|^2 = 0.0244$  obtained, showed this conclusion to be correct.

At a wavelength of 6 mm the bulk reflectivity  $|r|^2$  of silver is around 0.99958, and thus the reflectivity obtained by stacking 5 or 6 such capacitive gratings should be comparable. Losses in the grating elements have been neglected, and will limit the ultimate reflectivity from the structure. For good conductors losses should be small and the values of reflectivity obtained should approach those calculated above. The spacing  $a/\lambda = 0.417$  gives an attenuation constant of 100 db per wavelength for the lowest even order  $TM_{0n}$  mode, and such a structure should adequately satisfy our requirements.

Similarly inductive rod grating structures can be considered using the appropriate equivalent circuits to find the discontinuity matrix.<sup>13</sup> For a spacing of  $a/\lambda = 0.417$ , and rod diameter given by  $d/a = 0.2$ ,  $s = 0.3195$ ,  $t = -0.216j$ , and  $w = -4.149j$ , and the effective propagation constant of the basic element is

$$\cosh \phi = A = 0.3195 \cos \theta + 2.1829 \sin \theta. \quad (28)$$

The curve of this in Fig. 11 shows that  $l = \lambda/4$  or  $3\lambda/4$  is the optimum spacing for this type, and the values of reflectivity obtained are given in Table IV.

The effect of a finite sheet thickness on the perforated hole grating system can be seen by discussing the similar problem of stacked waveguide hole or iris gratings

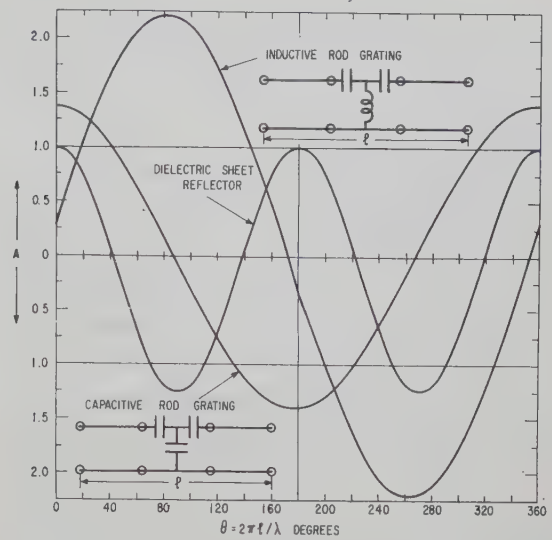


Fig. 11—Pass and stop bands for thick gratings.

TABLE III  
CALCULATED REFLECTIVITY  $|r_n|^2$  FROM A NUMBER  $n$  OF  
STACKED CAPACITIVE ROD GRATINGS AT  $\lambda/2$  SPACINGS.  
ROD DIAMETER 0.063 INCH, SPACING  $a = 0.103$   
INCH,  $\lambda = 6.28$  MM.

$n$	1	2	3	4	5	6
$ r_n ^2$	0.48542	0.87963	0.97699	0.99583	0.99925	0.99986

TABLE IV  
REFLECTIVITY  $|r_n|^2$  OF STACKED INDUCTIVE ROD  
GRATINGS AT  $3\lambda/4$  SPACING. ROD DIAMETER  $= 0.2\lambda$ ,  
SPACING  $a = 0.417\lambda$ .

$n$	1	2	3	4
$ r_n ^2$	0.794 <sup>88</sup>	0.98660	0.99876	0.99992

shown in Fig. 12. Values of the susceptances  $B_a$  and  $B_b$  of the equivalent circuit, and other parameters are available,<sup>14</sup> and as before it is found that the optimum spacing for this is  $l = \lambda_g/4$  or  $3\lambda_g/4$ , the pass bands being very narrow in the region of  $\theta = \pi$  for the parameters  $\lambda/a = 1.40$ ,  $a/b = 2$ ,  $d/a = 0.3$ , and  $t/d = 0.27$ , corresponding to an iris thickness of 0.020 inch at  $\lambda = 6.28$  mm. Values of reflectivity obtained are higher than those for thin irises of the same hole diameter, which agrees with the usual values of coupling factors for thick irises.<sup>15</sup> The behavior of the thick perforated metal plate gratings will be similar, and the reflectivity from a few of these at  $\lambda/4$  or  $3\lambda/4$  spacings will be quite high.

An indication of the bandwidth of the various structures is given by the effective propagation constant curves shown in Fig. 7 and Fig. 11; Fig. 13 shows the reflectivity of capacitive and inductive rod gratings as a function of  $l$ , and shows that provided a sufficient number of gratings is used the reflectivity obtained will be

<sup>14</sup> Marcuvitz, *op. cit.*, pp. 408–412.

<sup>15</sup> Montgomery *et al.*, *op. cit.*, p. 201.

<sup>13</sup> Marcuvitz, *op. cit.*, pp. 285–289.

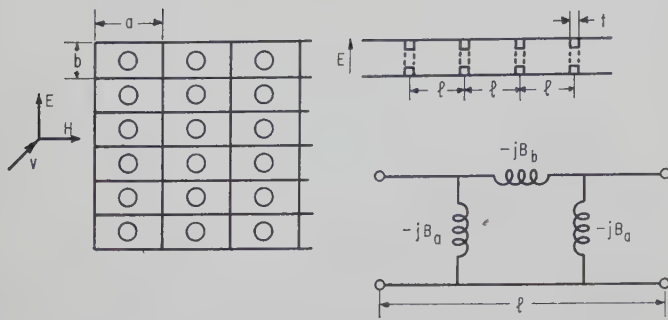
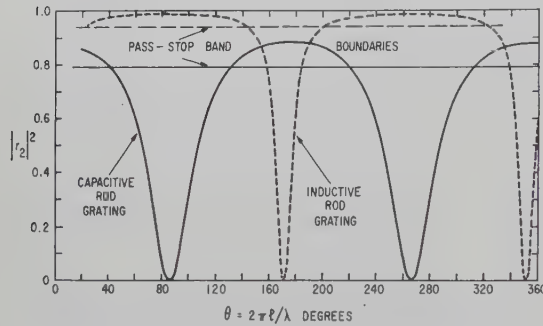


Fig. 12—Waveguide iris gratings and equivalent circuits.

Fig. 13—Reflectivity versus  $(\theta)$  for capacitive and inductive rod gratings. No. of gratings  $(n)=2$ .

quite high throughout the range of  $\theta$  corresponding to a stop band. In an accurate treatment the variation of the discontinuity reactances with wavelength must be considered, and (16) and (23) used to determine the reflectivity for different wavelengths. For comparison the effective propagation constant of a symmetrical element of the dielectric sheet-air space reflector system was calculated, taking the path lengths  $l$  in the dielectric and air equal. If  $\epsilon$  is the dielectric constant, and  $\theta_d = 2\pi l\epsilon^{1/2}/\lambda$ , then for no dielectric loss,

$$\cosh \phi = (2\epsilon^{1/2})^{-1}[(\epsilon + 2\epsilon^{1/2} + 1) \cos^2 \theta_d - (\epsilon - 1)]. \quad (29)$$

Fig. 11 shows such a curve for  $\epsilon=4$ , indicating that  $\lambda/4$  is best as regards the air space and thickness of dielectric.

## V. CONCLUSIONS

The transmission line treatment of the reflector problem, which is also applicable to the complete interferometer, indicates that the desired performance can be achieved in a number of ways. Reflectors consisting of quarter-wavelength dielectric sheets spaced quarter-wavelength apart are a good solution at longer wavelengths where the sheets are of reasonable thickness, although if a good dielectric such as fused quartz is used they are rather costly, and the size required leads to difficulties in fabrication. The new types of reflector structure considered such as stacked capacitive and in-

ductive rod gratings are suitable structures for the interferometer. They are not too difficult to make, and can be made large without serious difficulty, this being especially so for the perforated metal plate gratings, which seems a good structure in all respects. Errors in the values of the equivalent reactances used for the discontinuities would only affect the reflectivity obtained from a given number of gratings and not the general method.

Resistive losses in the grating structures have been neglected, but although these will limit the ultimate reflectivity obtained by stacking gratings, it is expected that it will still be quite high. Optimum spacing of the gratings must be decided by deducing the effective propagation constant of the discontinuity involved, and the results on the gratings considered show that, depending on the type, either a half-wavelength or an odd quarter-wavelength spacing will be satisfactory. This also gives an indication of the bandwidth of the particular reflector system, the results indicating that this will be adequate. A more accurate treatment of this can be made, if necessary, using the appropriate equations and considering the variation of the reactances with wavelength.

Only dominant mode interaction between the discontinuities has been considered, and the dimensions of the structures must be such that higher-order modes are highly attenuated over the distance between gratings. While the amplitude of each mode will depend on the geometry of the discontinuity, it is felt that their effects will be small in the structures considered. The effect of any residual higher mode coupling would be to change the equivalent reactances,<sup>16</sup> not the general method of reflector design. Also the rod and strip grating structures considered depend on the polarization, but the perforated hole grating can be designed to work for any arbitrary polarized wave.

The ultimate reflectivity obtained will not be unduly sensitive to the dimensions of the rods, or hole diameter and plate thickness, provided a sufficient number of gratings is used. It is important, however, to maintain the required spacing and alignment of the rods or holes in the stacked gratings, and also to ensure that the gratings are parallel. As regards the complete interferometer, the sharpness of the fringes will be quite sensitive to the parallelism of the two reflectors.

## ACKNOWLEDGMENT

The author would like to acknowledge the assistance derived from discussions with colleagues, Dr. D. M. Kerns and Dr. J. M. Richardson, on the various aspects of the work presented here.

<sup>16</sup> S. B. Cohn, "Analysis of the metal strip delay structure for microwave lenses," *J. Appl. Phys.*, vol. 20, pp. 257-262; March, 1949.



# Precise Control of Ferrite Phase Shifters\*

D. D. KING†, C. M. BARRACK‡, AND C. M. JOHNSON†

**Summary**—Hysteresis and thermal drifts can prevent accurate calibration of ferrite phase shifters. To provide a precise setting of phase in response to a control signal a servo system has been developed. This system utilizes a control frequency to determine uniquely the phase shift in a ferrite element. The desired phase shift is then a function only of control frequency and line length. Performance data are given for various operating conditions of the control system.

## INTRODUCTION

ELECTRICAL control of the phase shift in transmission line and waveguide elements has many applications, notably in antenna arrays. Ferrite phase shifters giving phase changes of 360 degrees or more with very low loss have been developed, particularly at the higher microwave frequencies.<sup>1</sup> Perhaps the principal drawback of these devices is their poor calibration accuracy. Hysteresis can cause changes of 30 degrees or more in the phase shift prevailing at a given applied magnetic field. In some cases, thermal drifts may also alter the phase shift obtained. The circuits described in this paper permit a precise electrical control of phase shift that is independent of any hysteresis or thermal drifts in the ferrite. A somewhat similar scheme has been described for phase measurement.<sup>2</sup>

## FREQUENCY CONTROLLED PHASE SHIFTER

The frequency controlled phase shifter consists of an electrically variable phase shifting element, a comparison loop, and a feedback control system. In the simplest version of this device, the insertion phase shift is controlled precisely by the frequency of a control signal sent through the same line as the signal whose phase is to be varied. A schematic diagram of the device is shown in Fig. 1.

The phase changing element shown with a control coil may be any electrically variable phase shifter in any type of transmission line or guide. Both reciprocal and nonreciprocal devices can be controlled in the same manner. The control current or voltage is furnished through a servo amplifier coupled to a phase detector in the comparison loop. The position of the phase detector is indicated by a dotted reference plane in Fig. 1.

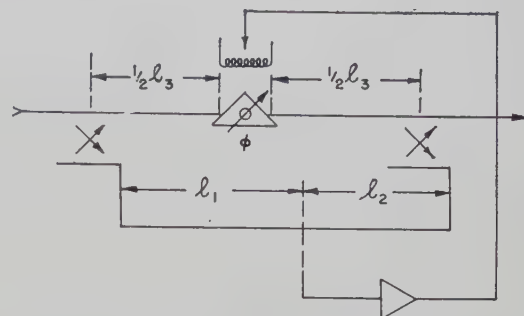


Fig. 1—Frequency controlled phase shifter.

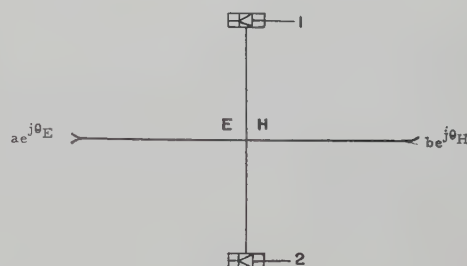


Fig. 2—Hybrid sensing element.

A pair of probes or a balanced loop are possible phase detectors, but a hybrid junction seems best suited for the needs of this circuit.

A hybrid sensing element placed at the reference plane in Fig. 1 receives signals from both directional couplers. These waves enter the shunt and series arms, as shown in Fig. 2. Balanced crystals are mounted in the side arms, so the entire unit is identical with a standard balanced mixer assembly.

In terms of the two input waves, the voltage amplitudes at the two crystals are

$$A_1 = (1/\sqrt{2})ae^{j\theta_E} + (1/\sqrt{2})be^{j\theta_H} \\ = \left[1 + \frac{b}{a}e^{j(\theta_H - \theta_E)}\right] \left[\frac{a}{\sqrt{2}}e^{j\theta_E}\right] \quad (1a)$$

$$A_2 = -(1/\sqrt{2})ae^{j\theta_E} + (1/\sqrt{2})be^{j\theta_H} \\ = \left[1 - \frac{b}{a}e^{j(\theta_H - \theta_E)}\right] \left[\frac{a}{\sqrt{2}}e^{j\theta_E}\right] \quad (1b)$$

The signal difference of the two crystals is

$$|A_1| - |A_2| \\ = \frac{a}{\sqrt{2}} \left\{ \left|1 + \frac{b}{a}e^{j\Delta\theta}\right| - \left|1 - \frac{b}{a}e^{j\Delta\theta}\right| \right\} \quad (2)$$

where  $\Delta\theta = \theta_H - \theta_E$ .

\* Original manuscript received by the PGMTT, July 16, 1958; revised manuscript received, September 25, 1959.

This work was sponsored by ARDC's Rome Air Dev. Center under Contract AF 30(602)-1776.

† Electronic Communications, Inc., Timonium, Md.

‡ Miller Research Laboratories, Baltimore, Md., formerly Electronic Communications, Inc., Timonium, Md.

<sup>1</sup> F. Reggia and E. G. Spencer, "A new technique in ferrite phase shifting for beam scanning of microwave antennas," *PROC. IRE*, vol. 45, pp. 1510-1517; November, 1957.

<sup>2</sup> H. A. Dropkin, "Direct reading microwave phase meter," *IRE CONVENTION RECORD*, pt. 1, pp. 57-63; March, 1958.

When  $\Delta\theta = \pi/2$ , the difference output is zero, corresponding to a bridge balance. For smaller values of  $\Delta\theta$ , the difference is positive; for larger values it is negative. Adequate sense information is, therefore, provided for maintaining a balance condition at  $\Delta\theta = \pi/2$ . With a servo amplifier it is then possible to position the standing wave pattern by controlling the phase  $\theta_H$  of the output wave. The position of the standing wave pattern is also a function of relative line lengths and of the frequency. The relationship between these quantities is now examined quantitatively.

From Fig. 1, the condition for balance (zero difference output) at the hybrid junction can be written down in terms of individual phase delays. It is

$$\phi + \frac{2\pi}{\lambda} (l_3 + l_2) = \frac{2\pi}{\lambda} l_1 \pm (2n + 1) \frac{\pi}{2}. \quad (3)$$

Eq. (3) is multiple valued with interval  $\pi$ . However, the slope of the error signal versus angular deviation curve given by (2) alternates in sign from one balance point to another. Once negative feedback has been established for a particular control amplifier, the system is then stable only at alternate balance points having the proper slope. Therefore, the effective balance equation is periodic with an interval  $2\pi$ .

$$\phi = \frac{2\pi}{\lambda} (l_3 + l_2) = \frac{2\pi}{\lambda} l_1 \pm (4n + 1) \frac{\pi}{2}. \quad (4)$$

A path difference  $l$  may be defined:

$$l = l_1 - (l_2 + l_3). \quad (5)$$

The normalized phase shift introduced by the phase shifter being controlled then becomes

$$\frac{\phi}{2\pi} = \frac{l}{\lambda} \pm \frac{4n + 1}{4}. \quad (6)$$

The phase excursion is assumed to run from  $\phi_1 = 0$  to  $\phi_2 = m\pi$  radians. The balance (6) then becomes

$$\frac{l}{\lambda_1} = \frac{4n_1 + 1}{4} \quad (\phi_1 = 0) \quad (7)$$

$$\frac{l}{\lambda_2} = \frac{4n_2 + 2m + 1}{4} \quad (\phi_2 = m\pi). \quad (8)$$

The difference in wave numbers between the two expressions is

$$\frac{1}{\lambda_1} - \frac{1}{\lambda_2} = \frac{1}{l} \left( n_1 - n_2 - \frac{m}{2} \right). \quad (9)$$

For  $m \leq 2$ , corresponding to the gamut of useful excursions,  $0 < \phi < 2\pi$ , the difference in wave numbers can be kept to one or less. This eliminates the possibility of ambiguities from  $n_1 \neq n_2$ , i.e., from harmonic operation.

The minimum path difference  $l$  for a 360 degree phase shift occurs for  $n = 0$ . Then (7) and (8) yield,

$$l = \frac{\lambda_1}{4} = \frac{5\lambda_2}{4}; \quad \frac{\lambda_1}{\lambda_2} = 5.$$

To achieve a small ratio of wavelengths, higher values of  $n$  may be chosen. For example, for  $n = 5$ ,

$$l = \frac{21}{4} \lambda_1 = \frac{25}{4} \lambda_2; \quad \frac{\lambda_1}{\lambda_2} = \frac{25}{21}.$$

By suitable choice of the path difference  $l$ , all control frequencies  $f_c$  necessary to produce phase shifts in the interval  $0 < \phi < 2\pi$  can be located in a narrow interval  $f_1 \leq f_c \leq f_2$ . This interval is chosen to lie close to the signal frequency  $f$ . The phase shift at the signal frequency then differs by a negligible amount from its precisely determined value at the control frequency. A discussion of servo operation and limits of error is deferred to a later section.

A typical system for precise electronic phase control is shown in Fig. 3.

Only milliwatts are required to operate the servo; hence, the control signal need not be large. In waveguide systems, a beyond-cut-off section in the directional coupler suffices to eliminate coupling to a lower signal frequency.

#### HETERODYNE CONTROLLED PHASE SHIFTER

The circuit of Fig. 3 may be modified in a simple but significant way by inserting two mixers in place of the filters. The revised system appears in Fig. 4.

Since the mixing operation is linear, phases are preserved. With equiphase injection of the control or local oscillator signal, the relative phases of the signals in the lower part of the control loop remain the same, but are referred to the sum or difference frequency  $f' = f \pm f_c$ . For sum frequency operation (5) need only be scaled to the different wavelengths in the upper and lower portions of the control loop.

$$\frac{l}{\lambda'} = \frac{l_1}{\lambda'} - \left( \frac{l_2}{\lambda'} + \frac{l_3}{\lambda} \right)$$

or

$$l = l_1 - l_2 - l_3 \left( \frac{\lambda'}{\lambda} \right). \quad (10)$$

The average wavelength in the loop is now shorter; hence, a more compact structure is possible. Operation at the difference frequency with low-frequency discriminators is also feasible.

The actual signal phase shift is controlled in the heterodyne system, rather than the phase shift at a nearby frequency. This eliminates the need for filters, and provides absolute accuracy. However, the modulation characteristic of the signal must permit the servo to operate. In general, very short duty cycles and rapid frequency modulations are not suitable for this purpose.



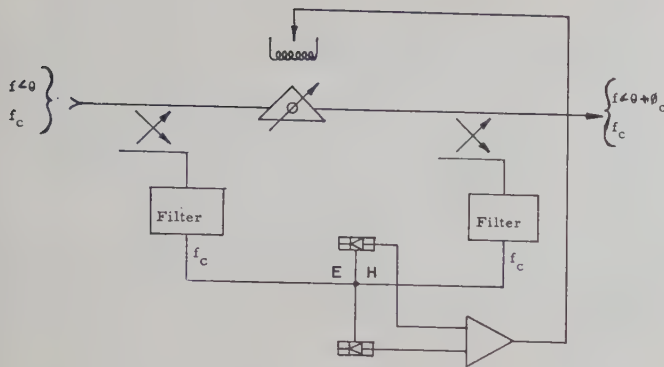


Fig. 3—Phase control system.

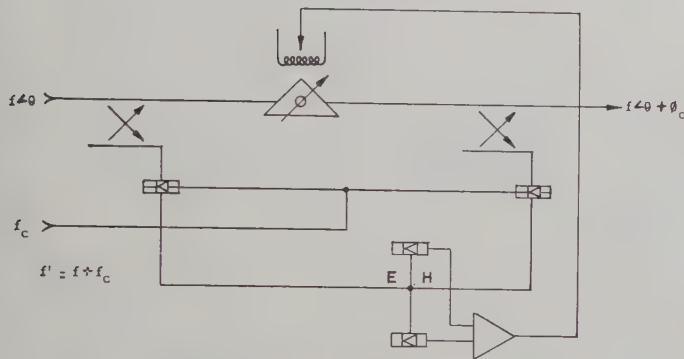


Fig. 4—Heterodyne phase control system.

The previously described system using separate control frequencies is, of course, free from such limitations.

#### PROPORTIONAL CONTROL SERVO

The servo system applies a control voltage to the active element controlling the current through the ferrite phase shifter coil. This control voltage is generated in response to an error signal developed at the hybrid junction. The functional relationship between error signal magnitude and phase error can be derived directly in terms of the quantities in Fig. 2.

Eq. (2) is the starting point for the calculation, and is written explicitly below.

$$|A_1| - |A_2| = \frac{a}{\sqrt{2}} \left\{ \left( \frac{b}{a} \cos \Delta\theta + 1 \right)^2 + \left( \frac{b}{a} \sin \Delta\theta \right)^2 \right\}^{1/2} - \frac{a}{\sqrt{2}} \left\{ \left( \frac{b}{a} \cos \Delta\theta - 1 \right)^2 + \left( \frac{b}{a} \sin \Delta\theta \right)^2 \right\}^{1/2} \quad (11)$$

The difference vanishes for  $\Delta\theta = (2n+1)\pi/2$ , as noted in connection with (3) previously. To represent this explicitly, we write

$$\Delta\theta = (2n+1)\frac{\pi}{2} + \epsilon \quad (12)$$

where  $\epsilon$  is the phase deviation from the balance condition. Inserting (12) into (11) and assuming an identical

detection efficiency  $\beta$  for each crystal yields the following exact relation between difference output  $\Delta e$  and the phase error  $\epsilon$ .

$$\frac{\Delta e}{a} = \frac{\beta}{\sqrt{2}} \left\{ \left( \frac{b}{a} \right)^2 + 1 - \frac{2b}{a} (-1)^n \sin \epsilon \right\}^{1/2} - \frac{\beta}{\sqrt{2}} \left\{ \left( \frac{b}{a} \right)^2 + 1 + \frac{2b}{a} (-1)^n \sin \epsilon \right\}^{1/2} \quad (13)$$

For operation near the balance point, only small errors apply, and (13) can be expanded,

$$\frac{\Delta e}{a} = -\beta \epsilon \left\{ \frac{\sqrt{2}(-1)^n}{(1 + (a/b)^2)^{1/2}} \right\} \quad (14)$$

The ratio of input amplitudes evidently has only a second order effect on the sensitivity. By keeping  $b > a$ , the maximum phase sensitivity is achieved. Per unit amplitude in the  $E$  arm (14) can then be written as

$$\Delta e \sim -\beta \epsilon \sqrt{2} (-1)^n \quad (15)$$

The factor  $(-1)^n$  shows that the control loop feedback is either positive or negative, depending on the interval of  $\pi$  occupied by the phase shift. Choosing the sign of feedback therefore determines whether  $n$  is even or odd for stable balance. This effectively makes the system periodic in  $2\pi$ , as indicated previously.

For unit rectification efficiency, (15) yields a sensitivity

$$\Delta e \approx 25 \text{ millivolts/degree phase error.} \quad (16)$$

#### EXPERIMENTAL RESULTS

To demonstrate the operation of the frequency control system under both open and closed loop conditions, a phase comparison bridge was assembled for  $C$ -band operation. The measurement system utilizes two reflex klystrons, one, furnishing the control frequency for the phase shifter and the other, simulating the signal frequency whose phase is to be controlled. In this test system beyond-cut-off waveguide for the signal frequency is not used for the control loop. Instead, the control frequency is propagated in the opposite direction from the signal frequency, and directional couplers are oriented to accept only the control frequency into the loop. This arrangement assumes a reciprocal phase shifter.

A simple dc control amplifier with a voltage gain of about 62 db is used in the servo loop. The phase shifter in the control loop uses Trans-Tech type TT-414 ferrite. This material was used because of its availability and is probably not optimum for  $C$ -band use. The ferrite element is a strip .2"  $\times$  .4"  $\times$  6.0" mounted vertically in the center of a section of standard 1"  $\times$  .5" waveguide filled with teflon. A longitudinal external magnetic field produces the phase shift in the ferrite. Two series of tests were made on the complete phase shifter control loop. In the first measurements the ferrite phase shifter solenoid was disconnected. The control frequency was then

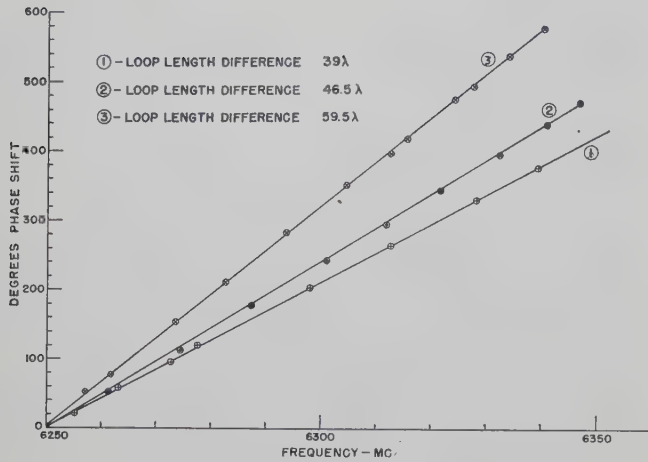


Fig. 5—Loop characteristics, manual control.

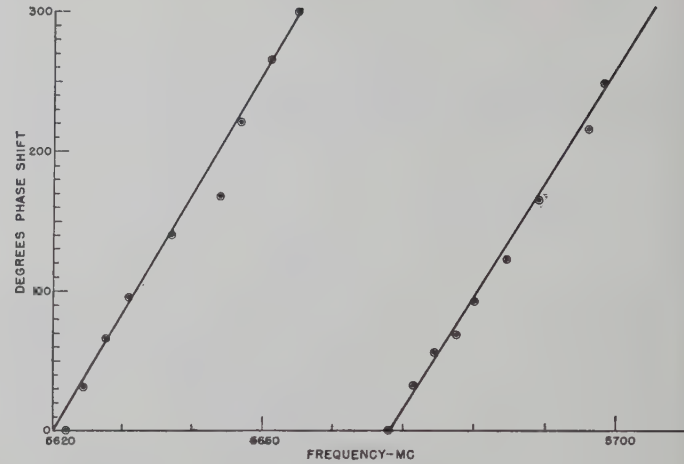


Fig. 6—Loop characteristics, servo control.

changed and the loop was balanced manually by varying a precision phase shifter in one of the loop arms. This measurement was repeated for several different lengths of one branch of the control loop. In the second group of tests the servo system was active. The control frequency was varied and the resulting change in phase of the operating signal was measured. This measurement was also repeated for several different loop lengths as well as for several different regions of operating frequency. If the difference in length of the two arms of the control loop is known, the change in control frequency can be computed from (9).

If  $\lambda_1$  and  $\lambda_2$  in (9) are the free space wavelengths, (9) can be written as

$$\frac{2l}{c} \Delta f = m, \quad (17)$$

where  $\Delta f$  is the change in control frequency,  $l$  is the loop length difference,  $c$  is the velocity of light, and  $m$  is the phase shift in units of  $\pi$  radians.

If  $\lambda_1$  and  $\lambda_2$  are not free space wavelengths, as is actually the case since the microwave energy is propagated in waveguide, then (17) can be written approximately as

$$\frac{2l}{c} \Delta f \left\{ \frac{\Delta_{av} f_c - \left( \frac{\lambda_g}{\lambda} \right)_{av}}{\left( \frac{\lambda_g}{\lambda} \right)_{av}^2} \right\} = m, \quad (18)$$

where  $(\lambda_g/\lambda)_{av}$  is the average value of the ratio of guide wavelength to free space wavelength in the vicinity of  $f_c$ , the initial value of the control frequency, and  $\Delta_{av}$  is the change in  $(\lambda_g/\lambda)_{av}$  per megacycle change in the control frequency.

Fig. 5 shows the results obtained in the first series of measurements when the servo loop was balanced manually. Theoretical curves were computed for three different loop lengths using (18). The experimentally determined values are in excellent agreement with the com-

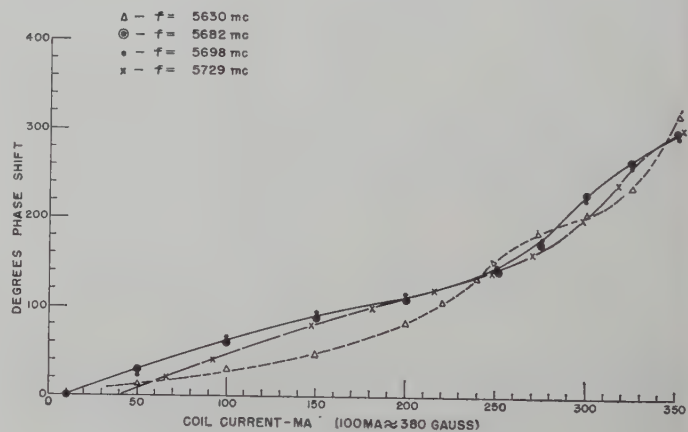


Fig. 7—Ferrite phase shifter characteristics.

puted values, the largest difference being only on the order of 2 degrees.

Fig. 6 shows the results obtained in the second series of measurements when the servo loop was used as a phase shifter. Eq. (18) was again used to compute the expected phase shift for several values of  $f_c$  and for several different loop lengths. In this instance, the measured values of phase shift are not in as close agreement with the predicted values as was the case in the measurements shown in Fig. 5.

The discrepancy between the measured and computed values of phase shift for the data in Fig. 6 is due primarily to the change in the phase shift characteristics of the ferrite phase shifter. Fig. 7 illustrates this. It is apparent that the shape of the phase shift curve changes appreciably with frequency; hence the changes in phase at signal and control frequencies can no longer be expected to track. Even with the very different characteristics shown in Fig. 7, the deviation of the measured phase shift from the computed values is only about 3 per cent of the maximum value of phase shift attained for the higher range in Fig. 6. This could certainly be reduced if the range of control frequencies required for a desired phase shift was reduced by making the loop length difference greater. This would tend to minimize



changes in the shapes of the phase shifter characteristics. A more suitable ferrite or geometry should also reduce this error.

The effect of servo error signal in these measurements is negligible: the gain of the system is sufficient to insure errors of only 2 or 3 degrees.

### CONCLUSION

A control loop has been placed around a ferrite phase shifter to permit precise phase settings. The frequency

of a control signal determines these phase settings. The range of control frequencies required can be varied to suit the dispersive characteristics of the ferrite and the stability of the control signal sources. When the duty cycle of the signal whose phase is being shifted is large enough, a heterodyne method can be applied. In this case, the dispersive effects are eliminated as a possible source of error. Preliminary experimental data confirms the expected performance characteristics of the phase control system.

# Tables for Cascaded Homogeneous Quarter-Wave Transformers\*

LEO YOUNG†

**Summary**—Quarter-wave transformers are frequently required in microwave and UHF systems. An exact design procedure is known but involves lengthy calculations. Faced with the design of many such transformers, the calculations were programmed on an IBM 704 digital computer. The speed of computation is such that several hundred designs for 2, 3, and 4 section transformers were systematically computed in a few minutes. The results are reproduced here in tables, which should permit the calculation of most cases of practical interest by interpolation.

### INTRODUCTION

MICROWAVE and UHF systems frequently require transformer sections to connect transmission lines of different characteristic impedances with minimum reflection. The multisection quarter-wave transformer serves this purpose well, but it is only comparatively recently that exact design procedures have been published. These are limited to homogeneous transformers, such as coaxial line or *E*-plane waveguide transformers.

### COMPUTATION OF IMPEDANCE RATIOS

Design formulas resulting in an equal ripple or Tchebycheff-type response were given by Cohn,<sup>1</sup> Collin,<sup>2</sup>

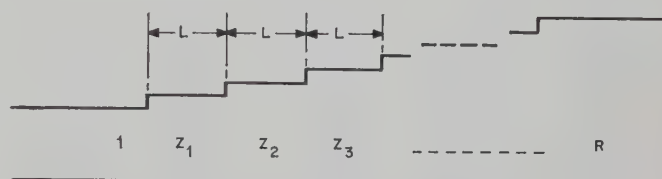


Fig. 1—Quarter-wave stepped transformer.

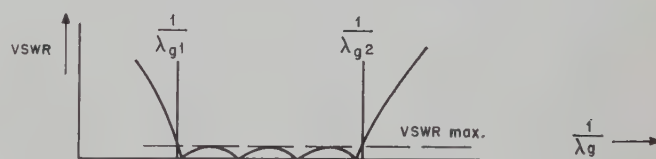


Fig. 2—Typical response curve.

and Riblet,<sup>3</sup> and were experimentally verified. As the computations are somewhat tedious, they were programmed on an IBM Type 704 electronic digital computer for transformers with 2, 3, and 4 sections. For the computation of the characteristic impedance ratios  $Z_1, Z_2, Z_3, \dots$  (Fig. 1), the computer program follows the exact method of Collin and Riblet. The length  $L$  of each section (Fig. 1) is nominally a quarter guide wavelength and is defined by

$$L = \frac{\lambda_{g1} \lambda_{g2}}{2(\lambda_{g1} + \lambda_{g2})} \quad (1)$$

where  $\lambda_{g1}$  is the longest and  $\lambda_{g2}$  is the shortest guide wavelength in the pass band (Fig. 2).

\* Manuscript received by the PGMTT, August 19, 1958; revised manuscript received, October 22, 1958. This work was part of a project sponsored by the Rome Air Development Center, Rome, N. Y.

† Westinghouse Electric Corp., and The Johns Hopkins University, Baltimore, Md.

<sup>1</sup> S. B. Cohn, "Optimum design of stepped transmission-line transformers," IRE TRANS. ON MICROWAVE THEORY AND TECHNIQUES, vol. MTT-3, pp. 16–21; April, 1955.

<sup>2</sup> R. E. Collin, "Theory and design of wide-band multisection quarter-wave transformers," PROC. IRE, vol. 43, pp. 179–185, February, 1955.

<sup>3</sup> H. J. Riblet, "General synthesis of quarter-wave impedance transformers," IRE TRANS. ON MICROWAVE THEORY AND TECHNIQUES, vol. MTT-5, pp. 36–43; January, 1957.

TABLE I  
MAXIMUM VSWR FOR 2-SECTION QUARTER-WAVE TRANSFORMERS

Impedance Ratio, $R$	Bandwidth, $W$								
	0.10	0.20	0.30	0.40	0.50	0.60	0.80	1.00	1.20
1.25	1.00	1.00	1.01	1.01	1.02	1.03	1.05	1.08	1.11
1.50	1.00	1.01	1.01	1.02	1.03	1.05	1.09	1.15	1.22
1.75	1.00	1.01	1.02	1.03	1.05	1.07	1.13	1.21	1.32
2.00	1.00	1.01	1.02	1.04	1.06	1.08	1.16	1.27	1.41
2.50	1.00	1.01	1.03	1.05	1.08	1.12	1.22	1.37	1.58
3.00	1.00	1.01	1.03	1.06	1.10	1.14	1.27	1.47	1.74
4.00	1.00	1.02	1.04	1.08	1.13	1.19	1.37	1.64	2.04
5.00	1.01	1.02	1.05	1.09	1.15	1.23	1.45	1.80	2.33
6.00	1.01	1.03	1.06	1.11	1.17	1.26	1.53	1.95	2.60
8.00	1.01	1.03	1.07	1.13	1.22	1.33	1.67	2.23	3.13
10.00	1.01	1.04	1.08	1.15	1.25	1.38	1.80	2.50	3.64
12.50	1.01	1.04	1.10	1.18	1.29	1.45	1.95	2.82	4.27
15.00	1.01	1.05	1.11	1.20	1.33	1.51	2.09	3.13	4.89
17.50	1.01	1.05	1.12	1.22	1.36	1.57	2.23	3.44	5.50
20.00	1.01	1.05	1.13	1.24	1.40	1.62	2.36	3.74	6.11
25.00	1.01	1.06	1.14	1.27	1.46	1.72	2.62	4.33	7.32
30.00	1.02	1.07	1.16	1.30	1.51	1.82	2.87	4.91	8.52
40.00	1.02	1.08	1.19	1.36	1.62	2.00	3.36	6.06	10.91
50.00	1.02	1.09	1.21	1.41	1.72	2.17	3.83	7.20	13.29
60.00	1.02	1.10	1.24	1.46	1.81	2.34	4.30	8.33	15.66
80.00	1.03	1.12	1.28	1.55	1.98	2.65	5.21	10.57	20.41
100.00	1.03	1.13	1.32	1.63	2.15	2.96	6.11	12.81	25.15

TABLE II  
MAXIMUM VSWR FOR 3-SECTION QUARTER-WAVE TRANSFORMERS

Impedance Ratio, $R$	Bandwidth, $W$								
	0.10	0.20	0.30	0.40	0.50	0.60	0.80	1.00	1.20
1.25	1.00	1.00	1.00	1.00	1.00	1.01	1.02	1.03	1.06
1.50	1.00	1.00	1.00	1.00	1.01	1.01	1.03	1.06	1.11
1.75	1.00	1.00	1.00	1.00	1.01	1.02	1.04	1.08	1.16
2.00	1.00	1.00	1.00	1.01	1.01	1.02	1.05	1.11	1.20
2.50	1.00	1.00	1.00	1.01	1.02	1.03	1.07	1.14	1.28
3.00	1.00	1.00	1.00	1.01	1.02	1.03	1.08	1.18	1.35
4.00	1.00	1.00	1.00	1.01	1.02	1.04	1.11	1.24	1.47
5.00	1.00	1.00	1.01	1.01	1.03	1.05	1.13	1.29	1.59
6.00	1.00	1.00	1.01	1.02	1.03	1.06	1.15	1.33	1.69
8.00	1.00	1.00	1.01	1.02	1.04	1.07	1.18	1.42	1.88
10.00	1.00	1.00	1.01	1.02	1.05	1.08	1.21	1.49	2.06
12.50	1.00	1.00	1.01	1.03	1.05	1.09	1.25	1.58	2.28
15.00	1.00	1.00	1.01	1.03	1.06	1.11	1.28	1.66	2.48
17.50	1.00	1.00	1.01	1.03	1.06	1.12	1.31	1.73	2.68
20.00	1.00	1.00	1.01	1.03	1.07	1.12	1.34	1.81	2.87
25.00	1.00	1.00	1.02	1.04	1.08	1.14	1.39	1.95	3.25
30.00	1.00	1.01	1.02	1.04	1.09	1.16	1.43	2.08	3.62
40.00	1.00	1.01	1.02	1.05	1.10	1.19	1.52	2.33	4.34
50.00	1.00	1.01	1.02	1.06	1.12	1.21	1.60	2.57	5.05
60.00	1.00	1.01	1.03	1.06	1.13	1.23	1.68	2.80	5.75
80.00	1.00	1.01	1.03	1.07	1.15	1.28	1.82	3.25	7.13
100.00	1.00	1.01	1.03	1.08	1.17	1.31	1.95	3.69	8.51

The bandwidth  $W$  is defined by

$$W = 2 \left( \frac{\lambda_{g1} - \lambda_{g2}}{\lambda_{g1} + \lambda_{g2}} \right). \quad (2)$$

Given the output-to-input impedance ratio  $R$  (taken greater than unity) and the bandwidth  $W$ , the computer calculates the relative characteristic impedances  $Z_1, Z_2, \dots$  of the intermediate sections for all three transformers ( $n=2, 3$ , and 4 sections).

#### TABLES

Tables I to III give the maximum VSWR in the pass band of the transformers for impedance transformations up to  $R=100$  and bandwidths up to  $W=1.20$  (or 120 per cent).

Tables IV to XIII give the values of the intermediate impedances  $Z_1$  and  $Z_2$ . Only the lower impedances are given in the tables since the impedance ratios are symmetrical about the center. Thus the remaining impedances are obtained as follows:

For  $n=2$ ,

$$Z_2 = R/Z_1.$$

For  $n=3$ ,

$$Z_2 = \sqrt{R},$$

$$Z_3 = R/Z_1.$$

For  $n=4$ ,

$$Z_3 = R/Z_2,$$

$$Z_4 = R/Z_1.$$



TABLE III  
 MAXIMUM VSWR FOR 4-SECTION QUARTER-WAVE TRANSFORMERS

Impedance Ratio, $R$	Bandwidth, $W$								
	0.10	0.20	0.30	0.40	0.50	0.60	0.80	1.00	1.20
1.25	1.00	1.00	1.00	1.00	1.00	1.00	1.00	1.01	1.03
1.50	1.00	1.00	1.00	1.00	1.00	1.00	1.01	1.02	1.06
1.75	1.00	1.00	1.00	1.00	1.00	1.00	1.01	1.03	1.08
2.00	1.00	1.00	1.00	1.00	1.00	1.00	1.02	1.04	1.10
2.50	1.00	1.00	1.00	1.00	1.00	1.01	1.02	1.06	1.14
3.00	1.00	1.00	1.00	1.00	1.00	1.01	1.03	1.07	1.17
4.00	1.00	1.00	1.00	1.00	1.00	1.01	1.03	1.09	1.22
5.00	1.00	1.00	1.00	1.00	1.01	1.01	1.04	1.11	1.27
6.00	1.00	1.00	1.00	1.00	1.01	1.01	1.05	1.13	1.31
8.00	1.00	1.00	1.00	1.00	1.01	1.02	1.06	1.16	1.39
10.00	1.00	1.00	1.00	1.00	1.01	1.02	1.07	1.18	1.46
12.50	1.00	1.00	1.00	1.00	1.01	1.02	1.08	1.21	1.54
15.00	1.00	1.00	1.00	1.00	1.01	1.02	1.08	1.24	1.62
17.50	1.00	1.00	1.00	1.00	1.01	1.03	1.09	1.26	1.69
20.00	1.00	1.00	1.00	1.01	1.01	1.03	1.10	1.28	1.76
25.00	1.00	1.00	1.00	1.01	1.02	1.03	1.11	1.33	1.88
30.00	1.00	1.00	1.00	1.01	1.02	1.04	1.13	1.36	2.01
40.00	1.00	1.00	1.00	1.01	1.02	1.04	1.15	1.43	2.24
50.00	1.00	1.00	1.00	1.01	1.02	1.05	1.17	1.50	2.46
60.00	1.00	1.00	1.00	1.01	1.02	1.05	1.18	1.56	2.67
80.00	1.00	1.00	1.00	1.01	1.03	1.06	1.22	1.67	3.08
100.00	1.00	1.00	1.00	1.01	1.03	1.07	1.25	1.78	3.48

 TABLE IV  
 MAXIMALLY FLAT QUARTER-WAVE TRANSFORMERS

$R$	$n=2$	$n=3$	$n=4$		$R$	$n=2$	$n=3$	$n=4$	
	$Z_1$	$Z_1$	$Z_1$	$Z_2$		$Z_1$	$Z_1$	$Z_1$	$Z_2$
1.00	1.00000	1.00000	1.00000	1.00000	12.50	1.88030	1.38110	1.17961	2.21803
1.25	1.05737	1.02829	1.01405	1.07223	15.00	1.96799	1.41512	1.19506	2.35186
1.50	1.10668	1.05202	1.02570	1.13512	17.50	2.04531	1.44475	1.20847	2.47169
1.75	1.15016	1.07255	1.03568	1.19120	20.00	2.11474	1.47108	1.22035	2.58072
2.00	1.18921	1.09068	1.04444	1.24206	25.00	2.23607	1.51650	1.24078	2.77447
2.50	1.25743	1.12177	1.05933	1.33204	30.00	2.34035	1.55498	1.25803	2.94423
3.00	1.31607	1.14793	1.07176	1.41051	40.00	2.51487	1.61832	1.28632	3.23492
4.00	1.41421	1.19071	1.09190	1.54417	50.00	2.65915	1.66978	1.30920	3.48136
5.00	1.49535	1.22524	1.10801	1.65686	60.00	2.78316	1.71340	1.32853	3.69752
6.00	1.56508	1.25439	1.12153	1.75529	80.00	2.99070	1.78522	1.36025	4.06810
8.00	1.68179	1.30219	1.14356	1.92323	100.00	3.16228	1.84359	1.38591	4.38263
10.00	1.77828	1.34089	1.16129	2.06509					

 TABLE V  
 QUARTER-WAVE TRANSFORMERS OF BANDWIDTH 0.10

$R$	$n=2$	$n=3$	$n=4$		$R$	$n=2$	$n=3$	$n=4$	
	$Z_1$	$Z_1$	$Z_1$	$Z_2$		$Z_1$	$Z_1$	$Z_1$	$Z_2$
1.00	1.00000	1.00000	1.00000	1.00000	12.50	1.88503	1.38341	1.18058	2.21984
1.25	1.05755	1.02843	1.01412	1.07230	15.00	1.97349	1.41772	1.19612	2.35396
1.50	1.10703	1.05227	1.02582	1.13526	17.50	2.05155	1.44761	1.20962	2.47405
1.75	1.15067	1.07290	1.03585	1.19140	20.00	2.12169	1.47417	1.22158	2.58333
2.00	1.18986	1.09113	1.04465	1.24231	25.00	2.24437	1.52002	1.24216	2.77755
2.50	1.25835	1.12238	1.05962	1.33240	30.00	2.34993	1.55888	1.25954	2.94775
3.00	1.31725	1.14868	1.07211	1.41097	40.00	2.52686	1.62290	1.28804	3.23925
4.00	1.41585	1.19171	1.09235	1.54482	50.00	2.67341	1.67495	1.31111	3.48642
5.00	1.49741	1.22645	1.10855	1.65767	60.00	2.79957	1.71911	1.33060	3.70327
6.00	1.56755	1.25578	1.12215	1.75625	80.00	3.01116	1.79188	1.36259	4.07510
8.00	1.68501	1.30391	1.14430	1.92448	100.00	3.18653	1.85108	1.38849	4.39079
10.00	1.78219	1.34289	1.16214	2.06660					

## CORRECTION FOR STEP CAPACITANCES

Cohn<sup>1</sup> gave a method whereby the length of each section is usually reduced below a quarter wavelength for a first-order compensation of the shunt capacitances at the step discontinuities. This correction is in practice often negligible for coaxial line transformers, but worth making in many waveguide transformers. The wave-

guide case therefore was programmed for the computer using the formulas given by Marcuvitz<sup>4</sup> and Cohn.<sup>1</sup>

This program is available, but has not been used so far to compile tables, which would have to be somewhat

<sup>4</sup> N. Marcuvitz, "Waveguide Handbook," M.I.T. Rad. Lab. Series, vol. 10, pp. 307-310, McGraw-Hill Book Co., Inc., New York, N. Y.; 1951.

TABLE VI  
QUARTER-WAVE TRANSFORMERS OF BANDWIDTH 0.20

R	n=2	n=3	n=4		R	n=2	n=3	n=4	
	Z <sub>1</sub>	Z <sub>1</sub>	Z <sub>1</sub>	Z <sub>2</sub>		Z <sub>1</sub>	Z <sub>1</sub>	Z <sub>1</sub>	Z <sub>2</sub>
1.00	1.00000	1.00000	1.00000	1.00000	12.50	1.89934	1.39048	1.18351	2.22533
1.25	1.05810	1.02883	1.01431	1.07251	15.00	1.99014	1.42564	1.19936	2.36030
1.50	1.10808	1.05303	1.02619	1.13566	17.50	2.07045	1.45630	1.21313	2.48120
1.75	1.15218	1.07396	1.03636	1.19199	20.00	2.14275	1.48359	1.22534	2.59124
2.00	1.19181	1.09247	1.04530	1.24307	25.00	2.26955	1.53075	1.24635	2.78689
2.50	1.26113	1.12422	1.06049	1.33349	30.00	2.37903	1.57080	1.26411	2.95843
3.00	1.32079	1.15096	1.07317	1.41236	40.00	2.56334	1.63691	1.29328	3.25238
4.00	1.42080	1.19474	1.09373	1.54676	50.00	2.71681	1.69080	1.31691	3.50180
5.00	1.50366	1.23013	1.11019	1.66012	60.00	2.84956	1.73661	1.33690	3.72073
6.00	1.57501	1.26003	1.12402	1.75917	80.00	3.07359	1.81232	1.36974	4.09640
8.00	1.69473	1.30916	1.14656	1.92827	100.00	3.26067	1.87411	1.39637	4.41559
10.00	1.79402	1.34900	1.16472	2.07118					

TABLE VII  
QUARTER-WAVE TRANSFORMERS OF BANDWIDTH 0.30

R	n=2	n=3	n=4		R	n=2	n=3	n=4	
	Z <sub>1</sub>	Z <sub>1</sub>	Z <sub>1</sub>	Z <sub>2</sub>		Z <sub>1</sub>	Z <sub>1</sub>	Z <sub>1</sub>	Z <sub>2</sub>
1.00	1.00000	1.00000	1.00000	1.00000	12.50	1.92361	1.40261	1.18851	2.23468
1.25	1.05903	1.02952	1.01465	1.07286	15.00	2.01842	1.43925	1.20489	2.37110
1.50	1.10985	1.05431	1.02681	1.13635	17.50	2.10256	1.47128	1.21912	2.49336
1.75	1.15474	1.07577	1.03724	1.19298	20.00	2.17857	1.49982	1.23176	2.60471
2.00	1.19511	1.09476	1.04639	1.24436	25.00	2.31245	1.54927	1.25353	2.80281
2.50	1.26581	1.12736	1.06196	1.33533	30.00	2.42867	1.59139	1.27196	2.97663
3.00	1.32676	1.15486	1.07497	1.41472	40.00	2.62570	1.66118	1.30227	3.27478
4.00	1.42915	1.19992	1.09607	1.55006	50.00	2.79116	1.71830	1.32687	3.52805
5.00	1.51420	1.23642	1.11299	1.66428	60.00	2.93535	1.76704	1.34772	3.75057
6.00	1.58761	1.26731	1.12721	1.76413	80.00	3.18102	1.84798	1.38205	4.13285
8.00	1.71119	1.31815	1.15041	1.93470	100.00	3.38855	1.91438	1.40994	4.45808
10.00	1.81407	1.35949	1.16913	2.07896					

TABLE VIII  
QUARTER-WAVE TRANSFORMERS OF BANDWIDTH 0.40

R	n=2	n=3	n=4		R	n=2	n=3	n=4	
	Z <sub>1</sub>	Z <sub>1</sub>	Z <sub>1</sub>	Z <sub>2</sub>		Z <sub>1</sub>	Z <sub>1</sub>	Z <sub>1</sub>	Z <sub>2</sub>
1.00	1.00000	1.00000	1.00000	1.00000	12.50	1.95846	1.42039	1.19579	2.24816
1.25	1.06034	1.03051	1.01514	1.07337	15.00	2.05909	1.45924	1.21292	2.38669
1.50	1.11236	1.05616	1.02771	1.13733	17.50	2.14880	1.49328	1.22785	2.51095
1.75	1.15837	1.07839	1.03849	1.19441	20.00	2.23019	1.52371	1.24111	2.62419
2.00	1.19979	1.09808	1.04796	1.24621	25.00	2.37439	1.57661	1.26400	2.82586
2.50	1.27247	1.13192	1.06409	1.33797	30.00	2.50046	1.62184	1.28341	3.00301
3.00	1.33526	1.16050	1.07757	1.41810	40.00	2.71614	1.69719	1.31541	3.30730
4.00	1.44105	1.20746	1.09947	1.55479	50.00	2.89921	1.75924	1.34146	3.56620
5.00	1.52925	1.24557	1.11704	1.67026	60.00	3.06024	1.81246	1.36359	3.79399
6.00	1.60563	1.27790	1.13183	1.77127	80.00	3.33788	1.90144	1.40014	4.18597
8.00	1.73475	1.33128	1.15600	1.94397	100.00	3.57565	1.97500	1.42993	4.52011
10.00	1.84281	1.37482	1.17553	2.09018					

TABLE IX  
QUARTER-WAVE TRANSFORMERS OF BANDWIDTH 0.50

R	n=2	n=3	n=4		R	n=2	n=3	n=4	
	Z <sub>1</sub>	Z <sub>1</sub>	Z <sub>1</sub>	Z <sub>2</sub>		Z <sub>1</sub>	Z <sub>1</sub>	Z <sub>1</sub>	Z <sub>2</sub>
1.00	1.00000	1.00000	1.00000	1.00000	12.50	2.00472	1.44469	1.20561	2.26621
1.25	1.06205	1.03184	1.01579	1.07405	15.00	2.11313	1.48661	1.22379	2.40759
1.50	1.11564	1.05865	1.02891	1.13863	17.50	2.21034	1.52349	1.23966	2.53454
1.75	1.16311	1.08192	1.04017	1.19631	20.00	2.29897	1.55656	1.25378	2.65036
2.00	1.20593	1.10254	1.05007	1.24867	25.00	2.45707	1.61431	1.27820	2.85686
2.50	1.28121	1.13805	1.06694	1.34149	30.00	2.59642	1.66397	1.29897	3.03853
3.00	1.34643	1.16811	1.08106	1.42260	40.00	2.83728	1.74725	1.33332	3.35119
4.00	1.45672	1.21763	1.10402	1.56111	50.00	3.04417	1.81638	1.36140	3.61779
5.00	1.54908	1.25796	1.12249	1.67823	60.00	3.22797	1.87610	1.38531	3.85278
6.00	1.62941	1.29227	1.13804	1.78079	80.00	3.54879	1.97678	1.42497	4.25810
8.00	1.76591	1.34913	1.16353	1.95635	100.00	3.82733	2.06088	1.45744	4.60454
10.00	1.88089	1.39572	1.18416	2.10520					



TABLE X  
QUARTER-WAVE TRANSFORMERS OF BANDWIDTH 0.60

R	n=2	n=3	n=4		R	n=2	n=3	n=4	
	Z <sub>1</sub>	Z <sub>1</sub>	Z <sub>1</sub>	Z <sub>2</sub>		Z <sub>1</sub>	Z <sub>1</sub>	Z <sub>1</sub>	Z <sub>2</sub>
1.00	1.00000	1.00000	1.00000	1.00000	12.50	2.06334	1.47674	1.21838	2.28945
1.25	1.06418	1.03356	1.01663	1.07491	15.00	2.18171	1.52282	1.23794	2.43453
1.50	1.11973	1.06186	1.03045	1.14029	17.50	2.28850	1.56355	1.25505	2.56499
1.75	1.16904	1.08646	1.04233	1.19872	20.00	2.38640	1.60023	1.27032	2.68415
2.00	1.21360	1.10830	1.05278	1.25180	25.00	2.56229	1.66464	1.29679	2.89698
2.50	1.29215	1.14600	1.07061	1.34597	30.00	2.71863	1.72040	1.31937	3.08459
3.00	1.36042	1.17799	1.08555	1.42834	40.00	2.99167	1.81471	1.35688	3.40825
4.00	1.47640	1.23087	1.10990	1.56917	50.00	3.72888	1.89378	1.38768	3.68503
5.00	1.57405	1.27412	1.12952	1.68843	60.00	3.44157	1.96266	1.41402	3.92957
6.00	1.65937	1.31105	1.14608	1.79299	80.00	3.81681	2.08004	1.45792	4.35264
8.00	1.80527	1.37253	1.17327	1.97225	100.00	4.14625	2.17928	1.49407	4.71550
10.00	1.92906	1.42320	1.19535	2.12449					

TABLE XI  
QUARTER-WAVE TRANSFORMERS OF BANDWIDTH 0.80

R	n=2	n=3	n=4		R	n=2	n=3	n=4	
	Z <sub>1</sub>	Z <sub>1</sub>	Z <sub>1</sub>	Z <sub>2</sub>		Z <sub>1</sub>	Z <sub>1</sub>	Z <sub>1</sub>	Z <sub>2</sub>
1.00	1.00000	1.00000	1.00000	1.00000	12.50	2.22139	1.57157	1.25503	2.35502
1.25	1.06979	1.03839	1.01896	1.07727	15.00	2.36672	1.63055	1.27870	2.51076
1.50	1.13051	1.07092	1.03477	1.14487	17.50	2.49938	1.68331	1.29952	2.65136
1.75	1.18469	1.09933	1.04839	1.20539	20.00	2.62224	1.73135	1.31821	2.78024
2.00	1.23388	1.12466	1.06039	1.26046	25.00	2.84580	1.81693	1.35085	3.01151
2.50	1.32117	1.16862	1.08093	1.35838	30.00	3.04734	1.89229	1.37895	3.21651
3.00	1.39764	1.20621	1.09820	1.44427	40.00	3.40499	2.02249	1.42613	3.57268
4.00	1.52892	1.26891	1.12650	1.59161	50.00	3.72073	2.13434	1.46537	3.87971
5.00	1.64084	1.32078	1.14944	1.71688	60.00	4.00711	2.23376	1.49930	4.15287
6.00	1.73970	1.36551	1.16889	1.82708	80.00	4.51833	2.40750	1.55659	4.62954
8.00	1.91107	1.44091	1.20106	2.01680	100.00	4.97177	2.55856	1.60451	5.04246
10.00	2.05879	1.50397	1.22738	2.17873					

TABLE XII  
QUARTER-WAVE TRANSFORMERS OF BANDWIDTH 1.00

R	n=2	n=3	n=4		R	n=2	n=3	n=4	
	Z <sub>1</sub>	Z <sub>1</sub>	Z <sub>1</sub>	Z <sub>2</sub>		Z <sub>1</sub>	Z <sub>1</sub>	Z <sub>1</sub>	Z <sub>2</sub>
1.00	1.00000	1.00000	1.00000	1.00000	12.50	2.43686	1.72651	1.31212	2.45476
1.25	1.07725	1.04567	1.02244	1.08072	15.00	2.61818	1.80797	1.34251	2.62727
1.50	1.14495	1.08465	1.04121	1.15155	17.50	2.78500	1.88193	1.36949	2.78393
1.75	1.20572	1.11892	1.05743	1.21515	20.00	2.94048	1.95013	1.39387	2.92830
2.00	1.26122	1.14966	1.07177	1.27316	25.00	3.22539	2.07364	1.43691	3.18917
2.50	1.36043	1.20344	1.09642	1.37665	30.00	3.48399	2.18447	1.47439	3.42234
3.00	1.44816	1.24988	1.11727	1.46778	40.00	3.94578	2.38028	1.53827	3.83169
4.00	1.60049	1.32837	1.15166	1.62490	50.00	4.35536	2.55256	1.59228	4.18880
5.00	1.73205	1.39428	1.17976	1.75926	60.00	4.72769	2.70860	1.63965	4.50975
6.00	1.84951	1.45187	1.20377	1.87804	80.00	5.39296	2.98700	1.72101	5.07692
8.00	2.05579	1.55057	1.24383	2.08385	100.00	5.98279	3.23420	1.79038	5.57534
10.00	2.23607	1.63471	1.27697	2.26079					

TABLE XIII  
QUARTER-WAVE TRANSFORMERS OF BANDWIDTH 1.20

R	n=2	n=3	n=4		R	n=2	n=3	n=4	
	Z <sub>1</sub>	Z <sub>1</sub>	Z <sub>1</sub>	Z <sub>2</sub>		Z <sub>1</sub>	Z <sub>1</sub>	Z <sub>1</sub>	Z <sub>2</sub>
1.00	1.00000	1.00000	1.00000	1.00000	12.50	2.70282	1.97543	1.39926	2.60341
1.25	1.08650	1.05636	1.02743	1.08558	15.00	2.92611	2.09480	1.44053	2.80190
1.50	1.16292	1.10495	1.05049	1.16102	17.50	3.13212	2.20457	1.47753	2.98360
1.75	1.23199	1.14805	1.07051	1.22899	20.00	3.32447	2.30687	1.51129	3.15225
2.00	1.29545	1.18702	1.08829	1.29123	25.00	3.67741	2.49446	1.57156	3.45984
2.50	1.40979	1.25594	1.11902	1.40276	30.00	3.99798	2.66499	1.62476	3.73777
3.00	1.51179	1.31621	1.14519	1.50152	40.00	4.57017	2.97034	1.71689	4.23225
4.00	1.69074	1.41972	1.18876	1.67300	50.00	5.07697	3.24219	1.79614	4.67007
5.00	1.84701	1.50824	1.22475	1.82083	60.00	5.53691	3.49018	1.86661	5.06832
6.00	1.98768	1.58676	1.25579	1.95244	80.00	6.35680	3.93524	1.98958	5.78224
8.00	2.23693	1.72383	1.30817	2.18248	100.00	7.08181	4.33178	2.09615	6.41923
10.00	2.45663	1.84304	1.35208	2.38228					

more extensive than the impedance ratio tables, owing to the greater number of independent parameters. Also, graphs are available,<sup>4</sup> in this case to reduce the time of a calculation by hand.

#### ACKNOWLEDGMENT

The advice and assistance of W. M. Etchison and the skillful programming of A. C. Robertson are gratefully acknowledged.

# The Synthesis of Symmetrical Waveguide Circulators\*

B. A. AULD†

**Summary**—A method for synthesizing symmetrical waveguide circulators by adjusting the eigenvalues of the scattering matrix is described. This procedure is particularly useful for the design of very compact circulators in the form of waveguide junctions containing ferrite obstacles. Permissible structural symmetries for a circulator are listed, and a standard form for the scattering matrix of a symmetrical circulator is defined. The synthesis procedure is then described in detail, stating the conditions to be imposed on the scattering matrix eigenvalues, and an expression is obtained for the changes in the eigenvalues due to the placing of anisotropic material within the junction.

By applying the theory to Allen's 4-port turnstile circulator, it is shown that the use of a matched turnstile junction and a reflectionless Faraday rotator is not essential. The theory is also applied to the design of novel 3- and 4-port circulators, and two 6-port circulators, one of which may be used as a 5-position waveguide switch, are described. Some experimental results are presented for a compact 3-port circulator in the form of an  $H$ -plane  $Y$  junction, in 1 inch by  $\frac{1}{2}$  inch waveguide, containing a ferrite post obstacle. This circulator, which operates with a bias field of approximately 25 oersted, has a useful bandwidth of 3 per cent. Greater bandwidths would be expected in a Stripline or a fin-line version of this device.

## INTRODUCTION

THE usual approach to the synthesis problem for microwave circuits is to use lumped-element network representations of the waveguide components. A lumped-element network having the desired characteristics is first obtained by conventional synthesis procedures, and a microwave structure exhibiting the same characteristics is then synthesized by interconnecting basic waveguide components, represented by lumped element networks and sections of transmission line. This method has been extended by Carlin<sup>1</sup> to the synthesis at a single frequency of non-reciprocal networks. At microwave frequencies the physical structure of the circuit is not defined by the network diagram as at lower frequencies, and for this reason there is often no particular advantage in working from an explicit network representation of the desired circuit.

A more direct approach is to consider the microwave circuit as a waveguide junction characterized by a scattering matrix  $S$ , without reference to a specific network representation. The scattering matrix coefficients are then fixed in accordance with the desired circuit characteristics by suitably adjusting the geometry of the boundary-value problem. It has been shown by

Dicke<sup>2</sup> that this is a useful approach when the microwave circuit has structural symmetry, in which case it is convenient to regard the eigenvectors and eigenvalues of  $S$ , rather than the scattering coefficients themselves, as adjustable parameters of the circuit. Given a specific scattering matrix  $S_d$  to be realized by a symmetrical junction at a single frequency, the synthesis procedure is as follows:

- Determine which structural symmetries are consistent with the form of the matrix  $S_d$ .
- Find the eigenvectors and eigenvalues of  $S_d$ .
- Select a junction having one of the symmetries found in a) and, by making symmetrical perturbations of the junction geometry, adjust the scattering matrix eigenvectors and eigenvalues so as to coincide with b).

As in the case of the equivalent network approach, the procedure outlined above does not lead to a specific microwave circuit. However, once one of the permissible symmetries in a) has been chosen, the *nature* of the adjustments required in c) is strongly suggested by symmetry. The *range* of adjustment required must be determined experimentally. This procedure is particularly useful in the design of very compact structures which perform rather complicated circuit functions, such as the magic- $T$  hybrid and the waveguide Wheatstone bridge.<sup>3</sup> However, it is also applicable to the design of symmetrical circuits which comprise interconnections of distinct waveguide components. The procedure provides for the realization of the desired circuit characteristics at a single frequency only. Nevertheless, as is usual with microwave circuits designed at a single frequency, the circuit will function with somewhat degraded performance over a band of frequencies in the vicinity of the design frequency. The bandwidth depends on the minimum performance specifications and also on details of the circuit structure not under direct control of the synthesis procedure. For example, a Stripline or a fin-line structure would be expected to have greater bandwidth than a rectangular waveguide structure with the same symmetry. A disadvantage of the symmetry method of synthesis is that circuit losses are not easily taken into account. Consequently, it is mainly applicable to circuits in which the losses are small and incidental.

\* Original manuscript received by the PGMTT, September 3, 1958. Revised manuscript received, December 23, 1958. The research reported in this paper was supported by the National Research Council of Canada.

† Dept. of Electrical Engineering, Univ. of British Columbia, Vancouver, B. C., Can.; now at the Microwave Laboratory, Stanford University, Stanford, Calif.

<sup>1</sup> H. J. Carlin, "Principles of Gyrator Networks," *Proc. Symp. on Modern Advances in Microwave Techniques*, Brooklyn Inst. Polytech., pp. 175-204; November, 1954.

<sup>2</sup> C. Montgomery, R. H. Dicke, and E. M. Purcell, "Principles of Microwave Circuits," McGraw-Hill Book Co., Inc., New York, N. Y., ch. 12; 1948.

<sup>3</sup> M. Chodorow, E. L. Ginzton, and J. F. Kane, "A microwave impedance bridge," *PROC. IRE*, vol. 37, pp. 634-639; June, 1949.



Although symmetrical circulators of several types have been described in the literature by Allen,<sup>4</sup> Fowler,<sup>5</sup> Vartanian,<sup>6</sup> and Kock,<sup>7</sup> symmetry methods have not been widely applied to non-reciprocal networks. However, Treuhaft<sup>8</sup> has described some of the general symmetry properties of circulators, and Fowler's circulator was designed by adjusting the eigenvalues of  $S$ , although full use was not made of the advantages of the method. The purpose of this paper is to apply the synthesis procedure outlined above to symmetrical waveguide circulators in general. In this connection the term "waveguide" is understood to include TEM structures such as coaxial line and Stripline.

## THEORY OF SYMMETRICAL CIRCULATORS

### Permissible Symmetries

It has been shown by Dicke<sup>2</sup> that the scattering matrix  $S$  of any symmetrical junction must satisfy a set of commutation relations,

$$F_{q_i} S = S F_{q_i}, \quad (1)$$

which determine the restrictions imposed on  $S$  by the junction symmetry. In (1) the  $F_{q_i}$ 's are a set of independent generators for a group of "symmetry operators"  $F$  for the junction. The "symmetry operators"  $F$  are matrices which indicate how the terminal fields transform under the operations of the symmetry group of the junction, *i.e.*, rotations and reflections that carry the junction into itself. For a detailed discussion of the properties of the  $F$ -matrices the above-mentioned reference and others<sup>9,10</sup> may be consulted. In the present application it is sufficient to note that the group of  $F$ -matrices constitute a "representation" of the symmetry group of the junction. That is, if  $F_1$  is the matrix corresponding to a symmetry operation  $T_1$ , and  $F_2$  corresponds to  $T_2$ , then the matrix product  $F_1 F_2$  corresponds to the symmetry operation  $T_1 T_2$  (operation  $T_2$  followed by operation  $T_1$ ). For an  $n$ -port circulator, defined as a device whose scattering matrix  $S_{en}$  performs a cyclic substitution on the  $n$  incident wave amplitudes, the group of  $F$ -matrices can include only 1) matrices contained in any one of the subgroups of the cyclic group

generated by  $S_{en}$ ; and 2) the products of these matrices with  $-I$ .<sup>8</sup> Since a cyclic group possesses only cyclic subgroups,<sup>8</sup> the only possible  $F$ -groups for a circulator are those generated by the following sets of generators:

$$a) F_1 = (S_{en})^p \text{ (} p \text{ a factor of } n \text{), and } F_2 = -I$$

$$F_1^{n/p} = F_2^2 = I, \quad F_1 F_2 = F_2 F_1,$$

$$b) F_1 = (S_{en})^p \text{ (} p \text{ a factor of } n \text{)}$$

$$F_1^{n/p} = I,$$

$$c) F_2 = -I$$

$$F_2^2 = I,$$

where case c) is trivial, since every  $n \times n$  matrix commutes with  $-I$ . It is found by consulting tabulations of all the possible symmetry groups for a physical structure (3-dimensional point groups),<sup>10,11</sup> that only those symmetry groups listed in Table I, where the usual

TABLE I  
PERMISSIBLE SYMMETRIES FOR AN  $n$ -PORT CIRCULATOR

(p is a factor of n)	
(a)	$C_{(n/p)h}$
(b)	$C_{n/p}, S_{n/p} (n/p \text{ even}), C_{(n/2p)h} (n/2p \text{ odd}), C_s (p=n/2)$

Schoenflies notation is used, can be represented by the groups of  $F$ -matrices a) and b). Accordingly, these are the only permissible non-trivial symmetries for an  $n$ -port circulator (Fig. 1). It should be noted that the boundaries of the junction may possess more than the permitted number of symmetries, these extra symmetries being removed by the anisotropic material placed within the junction in order to induce non-reciprocity. In Figs. 1(a), (b), (c), and (d) for example, the vertical planes of symmetry for the junction boundaries might be removed by a circular ferrite post placed along the axis of symmetry of the junction, with a bias field parallel to the symmetry axis. It is demonstrated in the theory of finite groups<sup>12</sup> that when a cyclic substitution on  $n$  symbols is raised to a power  $p=n/q$  the result is a noncyclic substitution consisting of  $p$  cycles, each operating on a distinct set of  $q$  symbols. Consequently, when  $p \neq 1$  the "symmetry operator"  $F_1$  permutes the junction ports *within* sets of  $q=n/p$  ports but does not interchange sets of ports, as in Figs. 1(d), (e), and (f).

Treuhaft's definition of a circulator does not specify uniquely the form of the scattering matrix, and for a given  $n$ -port circulator different systems of port numbering will lead to  $(n-1)!$  distinct scattering matrices. In the case of a structurally symmetrical circulator the number of possibilities may be reduced, however, by specifying a standard numbering system. For an  $n$ -port

<sup>4</sup> P. J. Allen, "The turnstile circulator," IRE TRANS. ON MICROWAVE THEORY AND TECHNIQUES, vol. MTT-4, pp. 223-228; October, 1956.

<sup>5</sup> H. Fowler, paper presented at Symposium on Microwave Properties and Applications of Ferrites, Harvard Univ., Cambridge, Mass.; April, 1956.

<sup>6</sup> P. H. Vartanian, "Theory and Applications of Ferrites at Microwave Frequencies," Sylvania Electronic Defense Lab. Rep. E 15, pp. 119-126; April, 1956.

<sup>7</sup> W. E. Kock, "Signal Routing Apparatus," U. S. Patent No. 2,794,172; May 28, 1957.

<sup>8</sup> M. A. Treuhaft, "Network properties of circulators based on the scattering concept," IRE TRANS. ON CIRCUIT THEORY, vol. CT-3, pp. 127-135; June, 1956. See also PROC. IRE, vol. 44, pp. 1394-1402; October, 1956.

<sup>9</sup> D. M. Kerns, "Analysis of symmetrical waveguide junctions," J. of Research Nat. Bur. of Standards, vol. 46, pp. 267-282; April, 1951.

<sup>10</sup> B. A. Auld, "Applications of Group Theory in the Study of Symmetrical Waveguide Junctions," MLR-157, Stanford University, Stanford, Calif.; March, 1952.

<sup>11</sup> F. D. Murnaghan, "The Theory of Group Representations," The Johns Hopkins Press, Baltimore, Md.; 1938.

<sup>12</sup> H. Hilton, "An Introduction to the Theory of Groups of Finite Order," Clarendon Press, Oxford, Eng., p. 8; 1908.

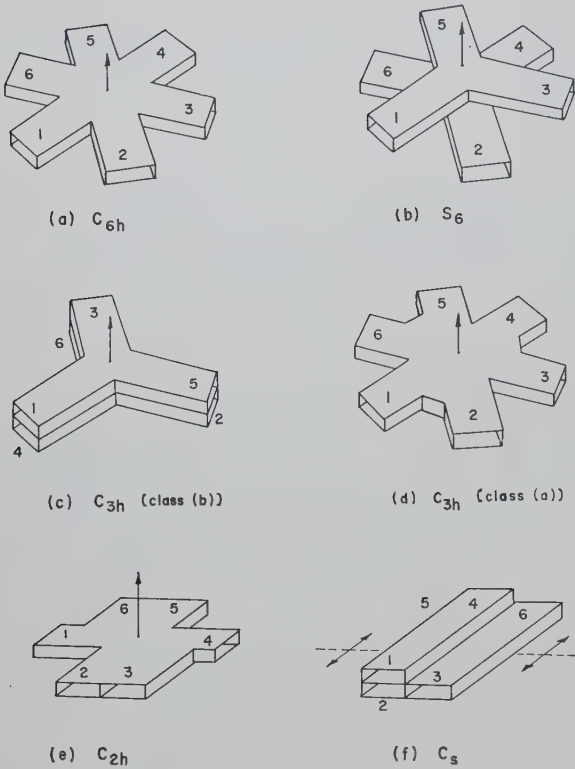


Fig. 1—Examples of some permissible symmetries for a 6-port circulator.

junction having any of the symmetries listed in Table I it is always possible to number the port, so that the generators of the  $F$ -group are  $F_1 = K_n^p$  and  $F_2 = -I$ , where  $K_n$  is the matrix representing the cyclic substitution  $(1, 2, 3, \dots, n)$ , and  $K_n^p$  represents, therefore, the substitution<sup>12</sup>

$$(1, 1+p, 1+2p, \dots, 1+[q-1]p) \dots \\ \dots (r, r+p, r+2p, \dots, r+[q-1]p) \dots \\ \dots (p, 2p, 3p, \dots, n).$$

This is, in fact, a natural system of port numbering for such junctions (Fig. 1). If the ports are numbered according to this system, the form of the scattering matrix  $S$  of the junction is determined by the commutation relation<sup>13</sup>

$$SK_n^p = K_n^p S, \quad (2)$$

and the scattering matrices  $S_{scn}$  of all symmetrical circulators are then restricted to those cyclic substitution matrices which satisfy (2). This may be taken as the standard form for the scattering matrix of a symmetrical circulator. When  $p=1$ , which will be shown to be the most useful case in practice,  $S_{scn}$  commutes with the cyclic substitution matrix  $K_n$ , and the standard form may be given explicitly. That is,

$$S_{scn} = K_n^f (f = 1, \text{ or is prime to } n), \quad (3)$$

<sup>13</sup> The second commutation relation,  $S(-I) = (-I)S$ , is redundant, since it is satisfied by any matrix  $S$ .

since the only substitutions on  $n$  letters commutative with  $K_n$  are  $K_n^f$ , and  $K_n^f$  is cyclic only if  $f=1$  or is prime to  $n$ .<sup>8,12</sup>

### The Synthesis Procedure

The procedure used for the synthesis of symmetrical circulators follows Dicke's work on symmetrical *reciprocal* junctions. In essence, the method requires finding the eigenvectors and eigenvalues of the desired scattering matrix, and then making symmetrical perturbations of the junction geometry until the eigenvectors and eigenvalues of the junction scattering matrix coincide with those of the desired scattering matrix. Each junction eigenvector  $\mathbf{v}$  and its associated eigenvalue  $s$  specify a set of incident wave amplitudes  $\mathbf{v}$  and reflected wave amplitudes  $s\mathbf{v}$  at the terminal planes of the junction, and therefore describe uniquely a solution (eigen-solution) to the junction boundary-value problem. For a lossless junction  $|s|=1$ ,<sup>2</sup> and each eigensolution is characterized by pure standing waves in the arms of the junction, the amplitudes of the fields in the arms being specified by the elements of the eigenvector, and the reflection coefficient at the terminal planes by the associated eigenvalue. In determining the *nature* of the perturbations required for adjusting the eigensolutions, it is necessary to make use of the symmetry properties of the eigensolutions. For this reason the synthesis procedure is of greatest practical use when the eigenvectors are completely determined by the symmetry of the junction, and the discussion will be limited to this case.

Let  $S$  be the scattering matrix of any lossless  $n$ -port junction having one of the permissible symmetries listed in Table I. If the ports are numbered appropriately,  $S$  satisfies the particular commutation relation (2), from which the symmetry restrictions on the eigenvectors and eigenvalues of  $S$  may be derived by means of the theory of group representations.<sup>9,10</sup> It is found that the eigenvectors are completely determined by symmetry only for symmetry groups  $C_{nh}$ ,  $C_n$ ,  $S_n$  ( $n$  even), or  $C_{(n/2)h}$  ( $n/2$  odd), that is, when  $p=1$  in Table I. In this case, the general form of the scattering matrix eigenvectors is given by the set of column matrices  $\mathbf{u}_a$ :

$$(u_a)_i = \frac{e^{-j2\pi a(i-1)/n}}{\sqrt{n}} \quad (4)$$

$$a = 0, \pm 1, \pm 2, \dots, \left(\frac{n}{2}\right)$$

$$i = 1, 2, 3, \dots, n,$$

and the associated eigenvalues  $s_a$  are, in general, non-degenerate. Since  $p=1$ , the standard form for the scattering matrix of a circulator with one of the above symmetries is  $K_n^f$ , and the first step in the synthesis procedure is to find the eigenvectors and eigenvalues of this matrix.

For the matrix  $K_n$  the characteristic equation is

$$|K_n - \lambda I| = |\lambda^n - 1| = 0$$



from which the eigenvalues are

$$\lambda_a = e^{-j2\pi a/n} \quad (5)$$

$$a = 0, \pm 1, \pm 2, \dots, \left(\frac{n}{2}\right).$$

The eigenvectors  $\mathbf{v}_a$  are found by substituting (5) into

$$K_n \mathbf{v}_a = \lambda_a \mathbf{v}_a$$

from which it follows directly that

$$(v_a)_i = e^{-j2\pi a/n} (v_a)_{i-1}.$$

Taking  $(v_a)_1 = 1/\sqrt{n}$ , a set of normalized eigenvectors,

$$(v_a)_i = \frac{e^{-j2\pi a(i-1)/n}}{\sqrt{n}} \quad (6)$$

is obtained. These are also eigenvectors for the matrix  $K_n^f$ , with associated eigenvalues

$$\lambda_a^f = e^{-j2\pi a f/n}. \quad (7)$$

Since the junction eigenvectors (4) already coincide with the required circulator eigenvectors (6), the final step in the synthesis procedure is to adjust the junction eigenvalues  $s_a$  in accordance with (7). It should be noted that the  $s_a$ 's may all be rotated through an arbitrary angle  $\theta$  by moving all the terminal reference planes through the electrical angle  $\theta/2$ . Consequently, only the relative phase angles of the eigenvalues are of importance, and the circulator conditions may be written

$$s_0 = e^{-j2\pi a f/n} \quad \left(a = \pm 1, \pm 2, \dots, \left(\frac{n}{2}\right)\right), \quad (8)$$

where  $f=1$  or is prime to  $n$ . When the eigenvalues have been adjusted so as to satisfy (8), the scattering matrix of the junction takes the desired form

$$S_{scn} = e^{j\theta} K_n^f$$

where the exponential factor allows for an arbitrary shift of the terminal reference planes.

#### *Perturbation Theorem for the Scattering Matrix Eigenvalues*

It has been shown that to realize a circulator in the form of a symmetrical junction it is necessary to perturb the junction geometry so as to fulfill condition (8). The perturbations take the form of deformations of the walls and the placing of isotropic and anisotropic materials within the junction, due regard being paid to the preservation of symmetry in order that the eigenvectors (4) are not disturbed. Changes in the eigenvalues due to a particular perturbation are functions of both the nature of the perturbation and its position within the junction, and may be expressed as integrals of the eigensolution fields over the volume of the perturbation.

Assuming that the parameters within a volume  $V_1$  inside the junction are changed from  $\mu, \epsilon$  (scalars) to  $\mu', \epsilon'$  (either scalars or tensors), let  $\mathbf{E}^{(-a)}, \mathbf{H}^{(-a)}$  represent

the electromagnetic field of the  $-a$ th eigensolution for the unperturbed junction, and let  $\mathbf{E}^{(a)'} \mathbf{H}^{(a)'}$  represent the electromagnetic field of the  $a$ th eigensolution for the perturbed junction. Then

$$\nabla \cdot (\mathbf{E}^{(-a)} \times \mathbf{H}^{(a)'} - \mathbf{E}^{(a)'} \times \mathbf{H}^{(-a)}) = j\omega (\mathbf{H}^{(-a)} \cdot \overset{\leftrightarrow}{\delta\mu} \mathbf{H}^{(a)'} - \mathbf{E}^{(-a)} \cdot \overset{\leftrightarrow}{\delta\epsilon} \mathbf{E}^{(a)'}) \quad (9)$$

where  $\overset{\leftrightarrow}{\delta\mu} = \mu' - \mu$  and  $\overset{\leftrightarrow}{\delta\epsilon} = \epsilon' - \epsilon$ . Eq. (9) is integrated over the volume bounded by the junction and the left-hand side is converted in the usual manner into a sum of surface integrals over the terminal planes. Since the fields are eigensolutions, this sum may be expressed in matrix notation as

$$\sum_i \int_{S_i} (\mathbf{E}_i^{(-a)} \times \mathbf{H}_i^{(a)'} - \mathbf{E}_i^{(a)'} \times \mathbf{H}_i^{(-a)}) \cdot \mathbf{n}_i dS_i = 2(s_a' - s_{-a}) \tilde{\mathbf{u}}_{-a} \mathbf{u}_a$$

where the symbol  $\tilde{\mathbf{u}}_{-a}$  means the transpose of the column matrix  $\mathbf{u}_{-a}$ . From (4)

$$\tilde{\mathbf{u}}_{-a} \mathbf{u}_a = 1.$$

Hence,

$$s_a' - s_{-a} = j \frac{\omega}{2} \int_{V_1} (\mathbf{H}^{(-a)} \cdot \overset{\leftrightarrow}{\delta\mu} \mathbf{H}^{(a)'} - \mathbf{E}^{(-a)} \cdot \overset{\leftrightarrow}{\delta\epsilon} \mathbf{E}^{(a)'}) dV. \quad (10)$$

For the  $a$ th and  $-a$ th eigensolutions of the unperturbed junction,

$$\begin{aligned} S \mathbf{u}_a &= s_a \mathbf{u}_a \\ S \mathbf{u}_{-a} &= s_{-a} \mathbf{u}_{-a}. \end{aligned}$$

Multiplying the transpose of the second equation by  $\mathbf{u}_a$  on the right and the first equation by  $\tilde{\mathbf{u}}_{-a}$  on the left, and subtracting,

$$\tilde{\mathbf{u}}_{-a} (\tilde{S} - S) \mathbf{u}_a = (s_{-a} - s_a)$$

Since the unperturbed junction is assumed to contain only isotropic material,  $\tilde{S} = S$  and it follows that  $s_a = s_{-a}$  (reciprocity degeneracy).<sup>9</sup> Substituting this result into (10),

$$\delta s_a = s_a' - s_a = j \frac{\omega}{2} \int_{V_1} (\mathbf{H}^{(-a)} \cdot \overset{\leftrightarrow}{\delta\mu} \mathbf{H}^{(a)'} - \mathbf{E}^{(-a)} \cdot \overset{\leftrightarrow}{\delta\epsilon} \mathbf{E}^{(a)'}) dV \quad (11)$$

which gives the change of the  $a$ th eigenvalue due to the perturbation.

#### APPLICATIONS

##### *Turnstile Circulators*

A familiar example of a circulator with symmetry group  $C_4$  is Allen's 4-port circulator, based on the well-known 4-arm turnstile junction [Fig. 2(a)]. In this circulator a *matched* turnstile junction is used, and the circular arm is terminated by a Faraday rotator in front of an adjustable short-circuit plunger. Allen treated the device as an interconnection of two distinct

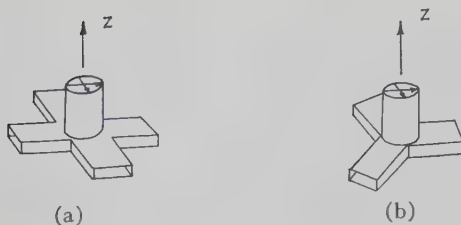


Fig. 2—(a) Four-arm turnstile junction.  
(b) Three-arm turnstile junction.

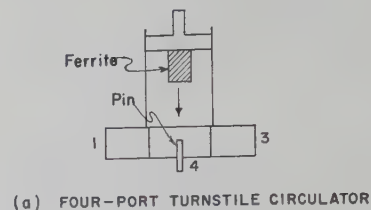
components and, assuming that the Faraday rotator was reflectionless and did not extend into the fringing fields of the turnstile, demonstrated that circulator action can be achieved by suitably adjusting the plane of polarization and the phase of the reflected wave in the circular arm. An alternative approach would be to apply the symmetry theory outlined above, the scattering matrix eigenvalues being adjusted in accordance with (8) by means of the Faraday rotator and the sliding short-circuit. This approach, which might appear to be unnecessarily complicated, leads to several conclusions not readily apparent from Allen's analysis.

When applying symmetry theory to a composite junction, it is often convenient to express the composite eigensolutions as linear combinations of eigensolutions for the component parts of the junction, thereby arriving at expressions for the eigenvalues of the composite junction in terms of the eigenvalues of its component parts. In the case of the turnstile circulator, no initial assumption is made regarding the matching of the turnstile junction. The composite eigensolutions are constructed by taking linear combinations of the turnstile eigensolutions, subject to restrictions imposed by the load attached to the circular arm. Relations between the composite eigenvalues  $s_a$  and the turnstile eigenvalues  $s_{bt}$  are obtained, and certain circulator conditions on the  $s_{bt}$ 's are derived by applying the circulator conditions (8) to the  $s_a$ 's.

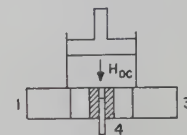
Several general conclusions may be drawn from such an analysis.<sup>14</sup> In the first place, the ferrite element does not have to be matched. If the circular pipe propagates only the lowest mode and the fringing fields of the termination and the turnstile do not interact, the termination does not even have to be of the same symmetry as the turnstile. The ferrite element may, in fact, have any  $n$ -fold rotational symmetry ( $n \neq 2$ ). Furthermore, matching of the turnstile is not essential. It is necessary only to insert a thin metal pin along the axis of symmetry, and this adjustment is not sufficient to match the turnstile.<sup>15</sup> By deliberately mismatching the turnstile, thereby converting the terminated circular pipe into a resonant cavity, a reduction in the volume of ferrite required may be obtained at the expense of bandwidth. Similar results are obtained in the case of Fowler's circulator, based on the 3-arm turnstile junction [Fig. 2(b)].

<sup>14</sup> B. A. Auld, "The Synthesis of Symmetrical Waveguide Circulators," Electrical Engineering Report, Univ. of British Columbia, Vancouver, Canada; Aug., 1958.

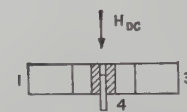
<sup>15</sup> Montgomery, Dicke, and Purcell, *op. cit.*, pp. 459-466.



(a) FOUR-PORT TURNSTILE CIRCULATOR



(b) MODIFIED TURNSTILE CIRCULATOR



(c) FOUR-PORT STAR CIRCULATOR

Fig. 3—Modifications of the 4-port turnstile junction.

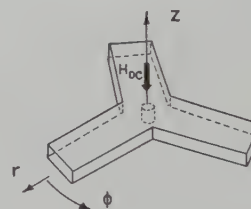


Fig. 4—Three-port star circulator.

The above discussion has been based on the explicit assumption that the fringing fields of the ferrite element and the turnstile do not interact. This restriction is not essential, and circulator action can still be realized even when the ferrite element is placed entirely within the junction region [Fig. 3(b)]. The advantage of this is that the short-circuit plunger can now be placed closer to the junction, shortening the electrical length of the side arm and reducing the frequency sensitivity of the circulator.<sup>16</sup> Since the short circuit plunger is placed outside the fringing fields, the composite junction theory may again be used. However, in this case the results are more complicated, owing to the nonreciprocity of the turnstile junction itself; and the adjustment procedure is consequently more difficult.

#### Star Junction Circulators

Further reduction of frequency sensitivity is achieved if the plunger and the ferrite element are both placed within the fringing fields, resulting in a star junction structure [Fig. 3(c)]. This structure cannot be treated as a

<sup>16</sup> The writer has recently learned that another method for increasing the bandwidth of a turnstile circulator has been used very successfully in the 3-port case by T. Schaug-Pettersen ("Novel Design of a 3-Port Circulator," Internal Rep., Norwegian Defence Res. Est., Bergen, Norway; January, 1958). In this method the phase-frequency response curves for all the scattering matrix eigenvalues are adjusted so as to approximately coincide over a band of frequencies, thus permitting the circulator conditions (8) to be approximately satisfied over this entire frequency band.



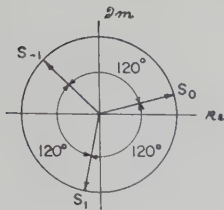


Fig. 5—Scattering matrix eigenvalues for a 3-port circulator.

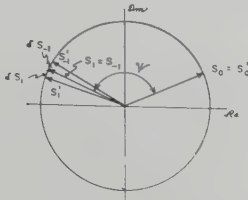


Fig. 6—Splitting of the reciprocity degeneracy due to the application of a small bias field.

composite junction, and the circulator conditions (8) are established by altering the geometry of the junction region. As an example of this type of circulator, a 3-port circulator in the form of a symmetrical  $H$ -plane  $Y$ -junction with a ferrite post across the guide on the axis of symmetry (Fig. 4), will be considered.

The circulator conditions for a 3-port junction are, from (8),

$$s_1 = \epsilon^{\mp j2\pi/3} s_0$$

$$s_{-1} = \epsilon^{\pm j2\pi/3} s_0,$$

the upper signs corresponding to circulation in the direction 1→2→3 (Fig. 5), and the lower signs to circulation in the reverse direction. To satisfy these conditions, it is necessary to set only two of the junction parameters, the phases of  $s_1$  and  $s_{-1}$  relative to  $s_0$ , and only two physical adjustments are required. These may be taken to be the diameter of the ferrite post and the strength of the bias field.

Let it be assumed that with no bias field applied, the eigenvalues are  $s_0$  and  $s_1 = s_{-1}$  (Fig. 6). Assuming no losses, these will lie on the unit circle in the complex plane with a relative angular spacing  $\psi$ , which is a function of the post diameter. The eigenvalues are, in effect, reflection coefficients and must have phase angles which increase with frequency. Consequently,  $s_0$  and  $s_1 = s_{-1}$  rotate around the unit circle in a counter-clockwise direction with increasing frequency, and, since the phase angles of  $s_0$  and  $s_1 = s_{-1}$  will not generally have the same frequency dependence, the angular spacing  $\psi$  will vary with frequency as well as with post diameter.

In general, the effect of applying bias field [ $\delta\epsilon=0$  in (11)] is to alter the phases of all the eigenvalues. Because of this, the circulator conditions cannot be set up by a straightforward balancing procedure as in the case of the turnstile circulator. However, if only small perturbations are considered and second-order effects neglected, the results are sufficiently simple to serve as the basis for a fairly systematic adjustment procedure. When second-order terms are neglected, (11) becomes

$$\delta s_a = j \frac{\omega}{2} \int_{V_1} \mathbf{H}^{(-a)} \cdot \overleftrightarrow{\delta\mu} \mathbf{H}^{(a)} dV \quad (a = 0, +1, -1). \quad (12)$$

If the internal bias field is assumed to be uniform, the biased ferrite medium is characterized by the Polder permeability tensor, and

$$\delta\mu = \begin{bmatrix} \mu - \mu_u & j\kappa & 0 \\ -j\kappa & \mu - \mu_u & 0 \\ 0 & 0 & \mu_z - \mu_u \end{bmatrix} \quad (13)$$

where  $\mu_u$  is the scalar permeability of the unbiased ferrite. The terminal conditions for the eigensolution fields  $\mathbf{E}^{(a)}$ ,  $\mathbf{H}^{(a)}$  are defined by the scattering matrix eigenvectors, in this case

$$\mathbf{u}_0 = \frac{1}{\sqrt{3}} \begin{bmatrix} 1 \\ 1 \\ 1 \end{bmatrix} \quad \mathbf{u}_1 = \frac{1}{\sqrt{3}} \begin{bmatrix} 1 \\ \epsilon^{-j2\pi/3} \\ \epsilon^{j2\pi/3} \end{bmatrix}$$

$$\mathbf{u}_{-1} = \frac{1}{\sqrt{3}} \begin{bmatrix} 1 \\ \epsilon^{j2\pi/3} \\ \epsilon^{-j2\pi/3} \end{bmatrix}. \quad (14)$$

Accordingly, the electric fields of the eigensolutions must satisfy relations

$$E_z^{(a)}(r, \phi) = \epsilon^{j2\pi am/3} E_z^{(a)}(r, \phi + \frac{2\pi m}{3})$$

$$(a = 0, +1, -1), \quad (m \text{ any integer})$$

where only the  $z$  component appears because the structure is uniform in the  $z$  direction. The eigensolution electric fields within the ferrite post must therefore take the form

$$E_z^{(a)} = \sum_{p=-\infty}^{\infty} A_p^{(a)} J_{|a+3p|}(\bar{k}r) \epsilon^{-j(a+3p)\phi}$$

where  $k = \omega\sqrt{\mu_u\epsilon}$  and the magnetic fields are of the form

$$\mathbf{H}^{(a)} = - \frac{\nabla \times \mathbf{k} E_z^{(a)}}{j\omega\mu_u}$$

$$= \frac{-\epsilon^{-ja\phi}}{j\omega\mu_u} \sum_{p=-\infty}^{\infty} A_p^{(a)} \mathbf{f}_p^{(a)}(\bar{k}r) \epsilon^{-j3p\phi}. \quad (15)$$

Substituting (13) and (15) into (12),

$$\delta s_a = -j \frac{b}{2\omega\mu_u^2} \sum_{p=-\infty}^{\infty} A_{-p}^{(-a)} A_p^{(a)} \cdot \left\{ (\mu - \mu_u) \int_0^R \mathbf{f}_{-p}^{(-a)} \cdot \mathbf{f}_p^{(a)} r dr \right. \\ \left. + j\kappa \int_0^R \mathbf{k} \cdot \mathbf{f}_{-p}^{(-a)} \times \mathbf{f}_p^{(a)} r dr \right\} \quad (a \neq 0)$$

$$\delta s_0 = -j \frac{b}{2\omega\mu_u^2} \sum_{p=-\infty}^{\infty} A_{-p}^{(0)} A_p^{(0)} (\mu - \mu_u) \cdot \int_0^R \mathbf{f}_{-p}^{(0)} \cdot \mathbf{f}_p^{(0)} r dr \quad (16)$$

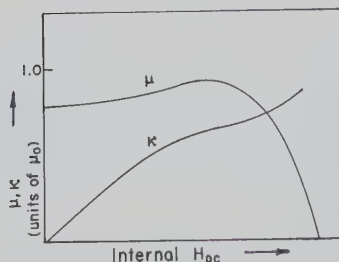


Fig. 7—Typical variation of ferrite permeability components as a function of internal bias field.

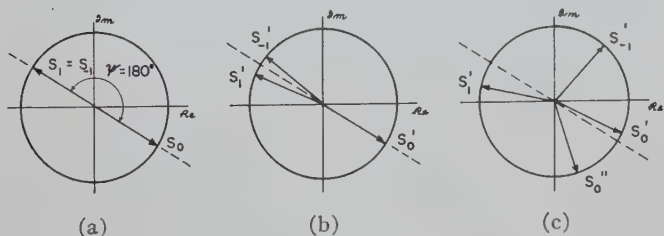


Fig. 8—Stages in the adjustment of a 3-port star circulator.

where  $R$  is the radius of the ferrite-post and  $b$  is the height of the waveguide.

For a typical ferrite, the components  $\mu$ ,  $\kappa$  of the Polder tensor vary with applied field as shown in Fig. 7. It is seen from this that for small bias fields  $\mu - \mu_u = 0$ , and the changes in the eigenvalues are  $\delta s_0 = 0$  and  $\delta s_1 = -\delta s_{-1}$  (Fig. 6). In attempting to establish the conditions for circulation, it is desirable, before applying the bias field, to adjust the post diameter so that  $\psi = 180^\circ$  [Fig. 8(a)]. (This condition is satisfied by determining experimentally the post diameter  $d_{opt}$  required for optimum matching of the unbiased junction; from the Appendix,  $|S_{11}|_{opt} = \frac{1}{3}$ .) Then, when a small bias field is applied, the reciprocity degeneracy is split symmetrically [Fig. 8(b)], the amount of splitting increasing with the strength of the bias field. However, as the separation of  $s_1'$  and  $s_{-1}'$  is increased by increasing the bias field, terms in  $(\mu - \mu_u)$  can no longer be neglected in (16), and asymmetrical splitting, as well as a change in  $s_0$ , occurs. Higher order perturbation terms in (11) will contribute further to this effect. Consequently when the required  $120^\circ$  splitting of  $s_1'$ ,  $s_{-1}'$  has been reached,  $s_0'$  will not lie in the position required for circulation [Fig. 8(c)]. To obtain circulator action, the angle  $\psi$  must be adjusted, by varying either the frequency or the post diameter, so as to compensate for this effect. If a post diameter  $d_{opt}$  is used, circulation may be established by varying the frequency and the bias field until the junction is matched. Alternatively, the circulator may be adjusted at a fixed frequency by selecting various post diameters in the neighborhood of  $d_{opt}$  and varying the bias field until a combination is found for which the junction is matched. The adjustment procedure is simplified greatly if a third adjustment, a thin metal pin along the axis of symmetry, is added. Since the pin affects only the 0th eigensolution it

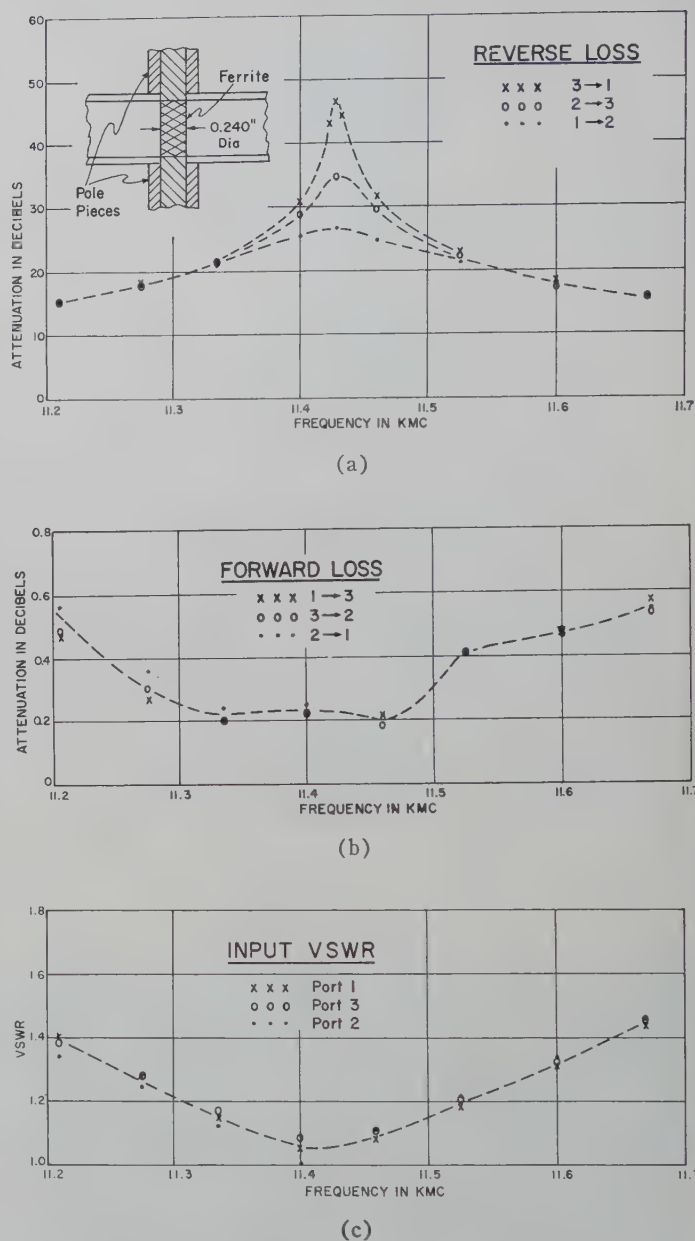


Fig. 9—Typical performance curves for a 3-port star circulator in 1 inch by  $\frac{1}{2}$  inch waveguide.  $H_{dc} \approx 25$  oersted in the empty gap.

may be used to shift  $s_0'$  in Fig. 8(c) to its correct position  $s_0''$ , without changing  $s_1'$  and  $s_{-1}'$ ; and circulation is obtained by alternately adjusting the pin and the bias field for minimum reflection until a match is obtained.

In practice, ferrite circulator performance is degraded to some extent by incidental losses in the ferrite, which have not been taken into account in the above theory. Consequently, the synthesis procedure will be useful in practice only if the eigenvalues can be adjusted over a sufficiently large range without biasing the ferrite into the region of high losses. For the 8.2 to 12.4 kmc band the usefulness of the procedure has been demonstrated by the construction of 3-port star junction circulators in 1 by  $\frac{1}{2}$  inch waveguide. In these circulators the ferrite element, a cylindrical post across the waveguide (Fig. 4), was placed directly between the magnet pole pieces



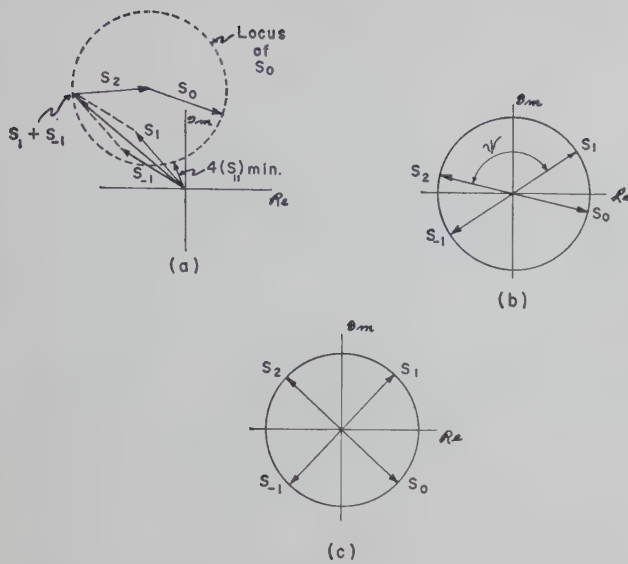


Fig. 10—Stages in the adjustment of a 4-port star circulator.

so as to form a closed magnetic circuit. With Ferramic R-1 posts the bias field strengths required were found to be less than 100 oersted in the empty gap. Typical performance curves are presented in Fig. 9, showing the effect of small asymmetries in the structure. In the case of one of the circulators tested it was found that the effects of asymmetries could be partially cancelled by rotating the ferrite post to an optimum position. The peaks of the three reverse loss curves were then all greater than 40 db, with no deterioration of the forward loss or VSWR characteristics.<sup>17</sup>

The synthesis of a 4-port star circulator would proceed in similar fashion. For a 4-port junction the circulator conditions are given by (8) with  $n=4$ , Fig. 10(c). To meet these conditions, it is necessary to set three of the junction parameters, and three physical adjustments are required. As in the case of the 3-port, two of these adjustments may be the post diameter and the bias field strength. A convenient choice for the third adjustment is the length of a thin metal pin on the axis of symmetry. This perturbs only the 0th eigensolution and permits the setting of  $s_0$  independently. Since the other two adjustments change the phase angles of all four eigenvalues, the adjustment procedure is necessarily somewhat involved. With a given post diameter, bias field is applied, splitting the degeneracy  $s_1 = s_{-1}$ ; and  $4|S_{11}| = |s_0 + s_1 + s_{-1} + s_2|$  (see Appendix) is minimized by adjusting the pin [Fig. 10a]. The splitting of  $s_1$  and  $s_{-1}$  is increased in steps by increasing the bias field, the pin being adjusted for minimum  $|S_{11}|$  at each step, until both  $(S_{11})_{\min}$  and  $S_{13}$  vanish for the same pin setting. This can occur only when the splitting of  $s_1$  and  $s_{-1}$  is  $180^\circ$ , so that  $S_{11} = S_{13} = (s_0 + s_2)/4$  (see Appendix), the null condition then being  $s_2 = -s_0$  [Fig. 10(b)]. Unless the initial choice of post diameter has been very fortu-

nate, the angle  $\psi$  will not be  $90^\circ$ , and the procedure must then be repeated for various post diameters until

$$S_{12} = \frac{s_0 + js_1}{2} = 0, \text{ or } S_{21} = \frac{s_0 - js_1}{2} = 0.$$

At this point,  $s_1 = \pm js_0$  and circulation is established [Fig. 10(c)]. This result can be achieved only if the metal pin provides a sufficiently large range of adjustment of  $s_0$ . If this is not the case, other methods for adjusting  $s_0$  must be considered.

The synthesis procedure may, in principle, be applied to circulators having any number of ports. In practice, however, the difficulties increase rapidly with the number of ports. Taking 5- and 6-port star circulators as examples, it is seen from the circulator conditions (8) that in both cases it is necessary to split two sets of reciprocity degenerate eigenvalues. This requires the use of two biased ferrite elements, and results in greatly increased complexity of the adjustment procedure. Fortunately, it may be shown that 6- and 8-port symmetrical circulators can easily be obtained without having recourse to the theory.

#### Symmetrical Ring Circulators

An alternative physical arrangement for an  $n$ -port circulator with symmetry group  $C_n$  is the symmetrical ring structure. Vartanian<sup>6</sup> has proposed a 3-port circulator of this type, using three gyrators, and a similar device is described by Kock.<sup>7</sup> Design formulas for the analogous 4-port symmetrical ring circulator, using four gyrators, are easily derived by regarding the circuit as a composite junction and applying symmetry theory, as in the case of the turnstile circulator. However, a more useful type of symmetrical ring circulator is obtained by simply interconnecting six 3-port star or turnstile circulators [Fig. 11(a)]. If the bias fields for the six circulators all have the same polarity, this structure functions as a 6-port circulator, with symmetry group  $C_6$ . A useful property of this circuit is that it degenerates into two disconnected circulators when symmetry is destroyed by reversing some of the bias fields. Accordingly, it may be used as a five position waveguide switch [Fig. 11(b)], the output being selected by applying an appropriate set of bias fields to the six circulators. Similarly, an 8-port symmetrical ring circulator with symmetry group  $C_4$  is obtained by connecting four 4-port star or turnstile circulators in a square array.

#### DISCUSSION

The synthesis procedure described in this paper is particularly useful for the design of symmetrical circulators in the form of waveguide junctions containing ferrite obstacles.<sup>18</sup> A typical example of a circulator of

<sup>17</sup> Experimental results for circulators of this type are also reported by H. N. Chait and T. R. Curry in a paper, "A new Y-type circulator," to be published in *J. Appl. Phys.*; March, 1959.

<sup>18</sup> An unsymmetrical circulator of this type, based on an  $H$ -plane Tee structure, has been described by W. E. Swanson and G. J. Wheeler in a paper, "Tee Circulator," 1958 IRE WESCON CONVENTION RECORD, vol. 2, pt. 1, pp. 151-156. This device has no symmetries, except for the trivial reflection symmetry in the  $H$ -plane, and a matching device is required in the side arm of the tee.

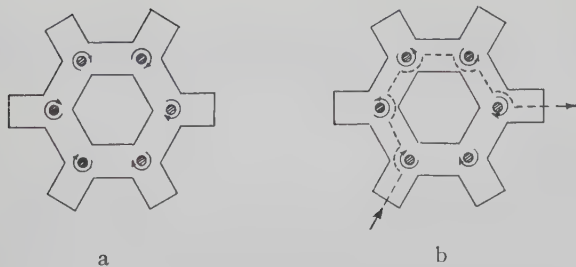


Fig. 11—(a) Six-port ring circulator. (b) Five-position waveguide switch.

this type is the 3-port star circulator shown in Fig. 5. Such circulators are compact and structurally simple, and have the important practical advantage of requiring only a small volume of ferrite material.

The specific applications which have been discussed in this paper have all used  $C_{nh}$  (class (a)) or  $C_n$  symmetry. Other circulators of novel design may be devised by using some of the alternative symmetries listed on Table I. For example, a circulator having  $S_4$  symmetry may in principle be realized by coupling two crossed guides with a ferrite-loaded aperture, the bias field being applied along the axis of symmetry (Fig. 12). The coupling arrangement might conveniently take the form of a ferrite post passing through the coupling hole and extending across the full height of both waveguides. Another example, with  $C_{3h}$  (class (b)) symmetry, is shown in Fig. 13. A wave with amplitude  $a$  incident at port 1 passes through the 3 db coupler and divides into incident waves with amplitudes  $0.707a$  and  $j0.707a$  in arms 1 and 4, respectively. These waves pass through the star circulators into arms 5 and 2 and combine in the 3 db coupler to give a transmitted wave of amplitude  $a$  at port 2. Similarly, a wave incident at port 2 emerges at port 3, etc. The scattering matrix, therefore, performs a cyclic substitution on the incident wave amplitudes, and the junction functions as a circulator. This device is more compact than the 6-port ring circulator [Fig. 12(a)]. It also has the advantage of requiring only two ferrite posts, which may both be biased by the same magnet.

Applications of the synthesis procedure are not necessarily restricted to junctions of rectangular waveguide. For example, a 3-port star circulator might be realized in the form of an  $H$ -plane  $Y$  junction of fin-line waveguide. Such a structure would be expected to have a larger bandwidth than the corresponding rectangular waveguide structure. Furthermore, the volume of ferrite material required would be reduced, owing to the localization of the microwave fields. The adjustment procedure would be identical with that outlined above for the rectangular waveguide version. In similar fashion, 3-port circulators might be realized in the form of either Stripline or coaxial line  $Y$  junctions.

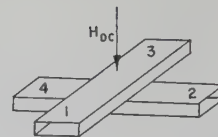


Fig. 12—Circulator with  $S_4$  symmetry, using crossed guides coupled with a ferrite-loaded aperture.

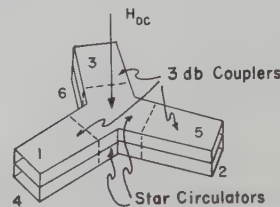


Fig. 13—Six-port circulator with  $C_{3h}$  (class (b)) symmetry, using two 3-port star circulators and three 3 db couplers.

## APPENDIX

Let  $S$  be the scattering matrix of a lossless 3-port junction with  $C_3$  or  $C_{3h}$  symmetry.  $S$  is diagonalized by a unitary matrix  $U$  having for its columns the normalized eigenvectors (14). Then,

$$S = U \begin{bmatrix} s_0 & 0 & 0 \\ 0 & s_1 & 0 \\ 0 & 0 & s_{-1} \end{bmatrix} U^{-1}$$

where  $s_0, s_1, s_{-1}$  are the eigenvalues of  $S$ . When the right-hand side of this equation is multiplied out, the scattering coefficients are obtained as functions of the eigenvalues.

$$\begin{aligned} S_{11} = S_{22} = S_{33} &= \frac{s_0 + s_1 + s_{-1}}{3} \\ S_{12} = S_{23} = S_{31} &= \frac{s_0 + e^{j2\pi/3}s_1 + e^{-j2\pi/3}s_{-1}}{3} \\ S_{13} = S_{32} = S_{21} &= \frac{s_0 + e^{-j2\pi/3}s_1 + e^{j2\pi/3}s_{-1}}{3} \end{aligned}$$

Similarly, the scattering coefficients of a lossless 4-port junction with  $C_4, C_{4h}$ , or  $S_4$  symmetry are given as functions of the eigenvalues  $s_0, s_1, s_{-1}, s_2$  by the equations,

$$\begin{aligned} S_{11} = S_{22} = S_{33} = S_{44} &= \frac{s_0 + s_1 + s_{-1} + s_2}{4} \\ S_{12} = S_{23} = S_{34} = S_{41} &= \frac{s_0 + js_1 - js_{-1} - s_2}{4} \\ S_{13} = S_{31} = S_{24} = S_{42} &= \frac{s_0 - s_1 - s_{-1} + s_2}{4} \\ S_{14} = S_{43} = S_{32} = S_{21} &= \frac{s_0 - js_1 + js_{-1} - s_2}{4} \end{aligned}$$



# Delay Distortion in Crystal Mixers\*

T. KAWAHASHI† AND T. UCHIDA†

**Summary**—Delay distortion is one of the most important characteristics in the frequency-modulated supermultichannel microwave repeater. With regard to receiving crystal mixers, the cause, shape, vanishing condition, etc., of delay distortion are analyzed, and the experiments show good agreement with the results of this analysis.

To eliminate this delay distortion, the electrical length between the crystal and the image suppression filter must be determined so that the image frequency impedance may not be infinite in a desired frequency band, or the intermediate frequency load impedance must be fixed at a certain definite value.

## I. INTRODUCTION

A group-delay-time characteristic with small irregular indentations is frequently observed in a crystal mixer which is used conventionally in a microwave repeater. Extremely important problems in the frequency-modulated supermultichannel microwave systems are the reduction and the stabilization of the delay distortion.

Such indentations of delay distortion in mixers are generally very sharp, unlike those encountered in ordinary passive circuits, and vary at each adjustment of the matching circuit. For these reasons, this distortion is practically impossible to equalize, and becomes a serious cause of deterioration for the quality of relay systems.

A number of studies [1]–[9] have been made so far on the equivalent circuit, conversion loss, and noise figure, etc., of crystal mixers. Detailed studies [3]–[7] relating to the effects of the image frequency component on the above characteristics are also available. On delay distortion in mixers, however, there is no literature within the knowledge of the authors. With respect to broadband receiving mixers, the authors first investigated general performance; second, analyzed the cause, shape, and magnitude of delay distortion; and third, made clear the condition under which the distortion would vanish, and proved this experimentally. The following is the result of these analyses and experiments.

## II. EQUIVALENT CIRCUIT OF MIXER

There are a number of studies [1]–[3], [5]–[7] on the equivalent circuit of a mixer. Since the same symbols are not always used in these works they are defined as follows in this report:

$f_L = \omega_L/2\pi$  Local Oscillator Frequency,

$f_s = \omega_s/2\pi$  Input Signal Frequency,

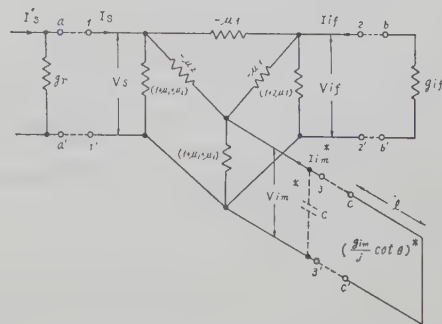


Fig. 1—Equivalent circuit of mixer (normalized by  $g_0$ ) when  $f_s > f_L$ .

$f_{if} = \omega_{if}/2\pi$  IF Signal Frequency,

$f_{im} = \omega_{im}/2\pi$  Image Frequency; (1)

$V_s, I_s$ : Vector indication of  $f_s$  voltage and current,

$V_{if}, I_{if}$ : Vector indication of  $f_{if}$  voltage and current,

$V_{im}, I_{im}$ : Vector indication of  $f_{im}$  voltage and current; (2)

$\mu_1 = g_1/g_0$  Conversion constant,

$\mu_2 = g_2/g_0$  Conversion constant; (3)

where  $g_0, g_1$ , and  $g_2$  are given by the following equation [1], [3], [5], [6] when the crystal characteristic is expressed as  $i=f(v)$ :

$$\frac{di}{dv} = f'(v) = g_0 + \sum_{m=1}^{\infty} 2g_m \cos m\omega_L t. \quad (4)$$

The relationship of voltages and currents of the signal frequency, intermediate frequency, and in age frequency is given by (5) when  $f_s > f_L$ , while the equivalent circuit is denoted by the 3-terminal-pair network made up of terminal pairs 1-1', 2-2', and 3-3', as in Fig. 1.

$$\begin{bmatrix} I_s \\ I_{if} \\ I_{im}^* \end{bmatrix} = g_0 \begin{bmatrix} 1 & \mu_1 & \mu_2 \\ \mu_1 & 1 & \mu_1 \\ \mu_2 & \mu_1 & 1 \end{bmatrix} \begin{bmatrix} V_s \\ V_{if} \\ V_{im}^* \end{bmatrix}, \quad (5)$$

where\* denotes a conjugate value.

Although (5) and Fig. 1 are usually expressed in terms of  $g_0, g_1$ , and  $g_2$ , since  $g_0, \mu_1$ , and  $\mu_2$  are of the utmost importance [9], they are normalized by and expressed in  $g_0$ . Now, let a crystal detector characteristic be

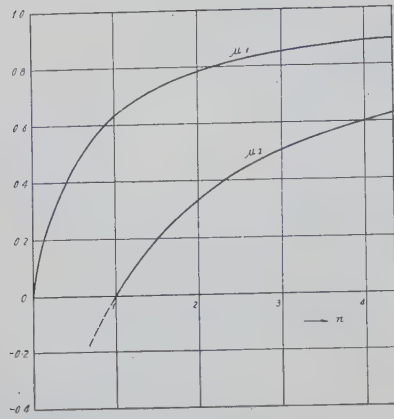
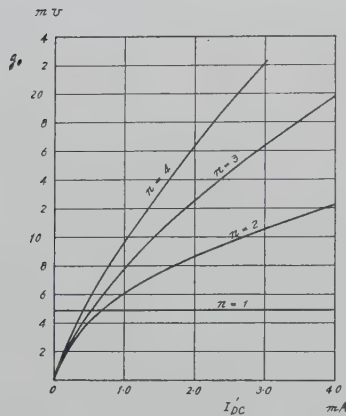
$i = KV^n$  when  $V > 0$ ,

$i = 0$  when  $V < 0$ , (6)

and dc bias voltage = 0. Then, conversion constants  $\mu_1$ , and  $\mu_2$  are determinable by  $n$  alone as in Fig. 2, [5], [9].

\* Manuscript received by the PGMTT, September 10, 1958; revised manuscript received December 15, 1958.

† Radio Industrial Division, Nippon Electric Co., Ltd., Kawasaki City, Japan.

Fig. 2—Variation of  $\mu_1$  and  $\mu_2$  with  $n$ .Fig. 3—Variation of  $g_0$  with dc rectified current (1 mw 2 ma crystal).

In a type 1N23B, which we used, the dc rectified current  $I_{dc}$  was assumed to be about 2 ma for a local oscillator power of 1 milliwatt, and so  $g_0$  is given by Fig. 3.

In the case where  $f_s < f_L$ , the intermediate frequency component has to take its conjugate value. But since the result is the same with regard to delay distortion in either case, analysis in this report has been made in the case where  $f_s > f_L$ .

### III. GENERAL PERFORMANCE OF MIXER

#### 1. When Barrier Capacitance of Crystal is Ignored

The receiving mixer consists of the image suppression filter, impedance matching circuit, crystal detector, and intermediate frequency preamplifier. These elements determine synthetically the over-all characteristics of the mixer. Therefore, the admittances connected, respectively, to terminal pairs 1-1', 2-2', and 3-3' of the equivalent circuit in Fig. 1 may be assumed as follows: 1) Intermediate frequency terminal pair 2-2' is connected to an input circuit of the intermediate frequency preamplifier, and this admittance is regarded as an almost constant conductance  $G_{if}$  within the desired band. 2) Since input signal terminal pair 1-1' is well matched to reduce echo distortion of the feeder line, this side can be con-

sidered to be connected to constant current source  $I_s'$  and constant source conductance  $G_r$ ,  $G_r$  being almost equal to the input admittance of the crystal mixer. 3) On the contrary, image terminal pair 3-3' can be considered to be connected to a shorted line, since the image frequency component generated at the crystal mixer is perfectly reflected by the image suppression filter. If  $l$  be the electrical equivalent length of the shorted line for image frequency,  $G_{im}$  be the equivalent characteristic admittance,  $\beta$  be the propagation constant, then the arrangement at this side becomes equivalent to the case where image terminal pair 3-3' is connected to a susceptance,  $-jG_{im} \cot \beta l$ .

By normalizing all these quantities to  $g_0$ , we have

$$g_r = G_r/g_0 \quad \text{normalized source conductance,}$$

$$g_{if} = G_{if}/g_0 \quad \text{normalized intermediate frequency conductance,}$$

$$g_{im} = G_{im}/g_0 \quad \text{normalized equivalent characteristic admittance,}$$

$$Y_{im} = -jg_{im} \cot \beta l \quad \text{normalized image frequency admittance;} \quad (7)$$

and letting

$$\theta = \beta l \quad \text{electrical angle for image frequency,}$$

we obtain a 3-terminal-pair network made up of terminal pairs  $a-a'$ ,  $b-b'$ , and  $c-c'$  in Fig. 1. From (5) we have also

$$\begin{bmatrix} I_s' \\ 0 \\ 0 \end{bmatrix} = \begin{bmatrix} 1 + g_r & \mu_1 & \mu_2 \\ \mu_1 & 1 + g_{if} & \mu_1 \\ \mu_2 & \mu_1 & 1 + Y_{im}^* \end{bmatrix} \begin{bmatrix} V_s \\ V_{if} \\ V_{im}^* \end{bmatrix}. \quad (8)$$

Calculating the transfer admittance  $G_T$  from (8),

$$G_T = \frac{I_s'}{V_{if}} = G_{T0} \frac{1 + jK_1 \cot \theta}{1 + jK_2 \cot \theta}, \quad (9)$$

where

$$G_{T0} = -g_0 \frac{\Delta_0}{\mu_1(1 - \mu_2)},$$

$$K_1 = g_{im} \Delta_{33} / \Delta_0,$$

$$K_2 = g_{im} / 1 - \mu_2,$$

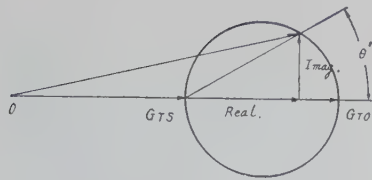
$$\Delta_0 = \begin{vmatrix} 1 + g_r & \mu_1 & \mu_2 \\ \mu_1 & 1 + g_{if} & \mu_1 \\ \mu_2 & \mu_1 & 1 \end{vmatrix},$$

and

$$\Delta_{33} = \begin{vmatrix} 1 + g & \mu_1 \\ \mu_1 & 1 + g_{if} \end{vmatrix}. \quad (10)$$

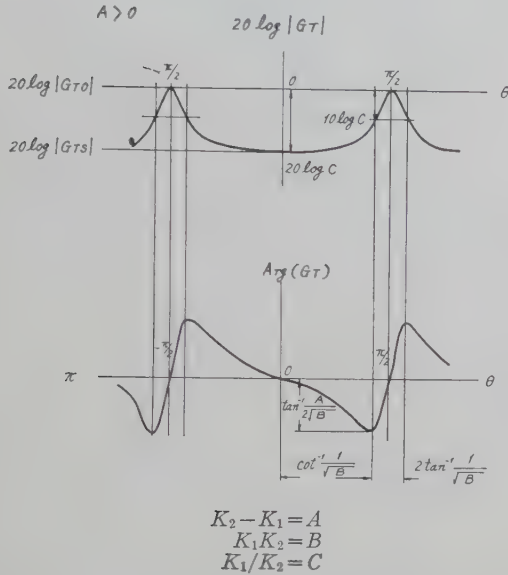
$G_{T0}$  is the transfer admittance in the case where the image frequency impedance is infinite, that is,  $\cot \theta = 0$ ,





$$A = K_2 - K_1 > 0$$

Fig. 4—Vector of transfer admittance.

Fig. 5—Variation of transfer admittance  $G_T$ , when barrier capacitance is ignored.

and the transfer admittance  $G_{TS}$ , when the image frequency impedance is short, *i.e.*,  $\cot \theta = \infty$ , is given by

$$G_{TS} = G_{TO} \frac{K_1}{K_2} = -g_0 \frac{(1 + g_r)(1 + g_{if}) - \mu_1^2}{\mu_1}. \quad (11)$$

With (11), (9) is expressed as follows,

$$\begin{aligned} G_T &= G_{TS} + (G_{TO} - G_{TS}) \left\{ \frac{1}{1 + K_2^2 \cot^2 \theta} - j \frac{K_2 \cot \theta}{1 + K_2^2 \cot^2 \theta} \right\} \\ &= G_{TS} + (G_{TO} - G_{TS})(\text{Re.} - j \text{Imag.}) \end{aligned} \quad (12)$$

The second term of (12) is interesting in comparison to ordinary resonance circuits, and the transfer admittance of a mixer can be obtained schematically from  $G_{TS}$ ,  $G_{TO}$ , and  $\text{Imag.}/\text{Re.} = \tan \theta' = K_2 \cot \theta$ , as shown in Fig. 4.

Moreover, the amplitude and the phase characteristics of transfer admittance are easily derived from (9):

$$20 \log |G_T| = 20 \log |G_{TO}| + 10 \log \frac{1 + K_1^2 \cot^2 \theta}{1 + K_2^2 \cot^2 \theta}, \quad (13)$$

$$\Theta = \text{Arg } G_T = -\tan^{-1} \left\{ \frac{(K_2 - K_1) \cot \theta}{1 + K_1 K_2 \cot^2 \theta} \right\} + \pi, \quad (14)$$

which are shown in Fig. 5; and the sharpness of shape depends on  $K_1 \cdot K_2$  alone. (The inversions of these curves

are the transfer frequency response of a mixer.) The input admittance of a mixer is given by (15), similar to (9):

$$G_{in} = g_{in0} \frac{1 + jK_1' \cot \theta}{1 + jK_2' \cot \theta}, \quad (15)$$

where

$$g_{in0} = g_0(1 - \mu_2) \left\{ 1 + \mu_2 - \frac{\mu_1^2(1 - \mu_2)}{1 + g_{if} - \mu_1^2} \right\}, \quad (16)$$

$$K_1' = g_{im} \frac{1}{G_{in0}/g_0}, \quad (17)$$

and

$$K_2' = \frac{1 + g_{if}}{1 + g_{if} - \mu_1^2}. \quad (18)$$

Fig. 6 shows the normalized input admittance in the case where image frequency impedance is short or open.

Assuming that the source admittance  $g_r$  is nearly equal to the input admittance  $g_{in} = G_{in}/g_0$  for the purpose of reducing echo distortion, that is, of impedance matching, the output admittance of a mixer is described as follows:

$$G_{out} = g_{out0} \frac{1 + jK_1'' \cot \theta}{1 + jK_2'' \cot \theta}, \quad (19)$$

where

$$g_{out0} = g_0 \frac{(1 - \mu_2)(1 + \mu_2 - 2\mu_1^2) + (1 - \mu_1^2)g_r}{1 - \mu_2^2 + g_r}, \quad (20)$$

$$K_1'' = \frac{g_{im}(1 - \mu_1^2 + g_r)}{(1 - \mu_2)(1 + \mu_2 - 2\mu_1^2) + (1 - \mu_1^2)g_r}, \quad (21)$$

and

$$K_2'' = \frac{g_{im}(1 + g_r)}{1 - \mu_2^2 + g_r}. \quad (22)$$

The normalized output admittance is shown in Fig. 7.

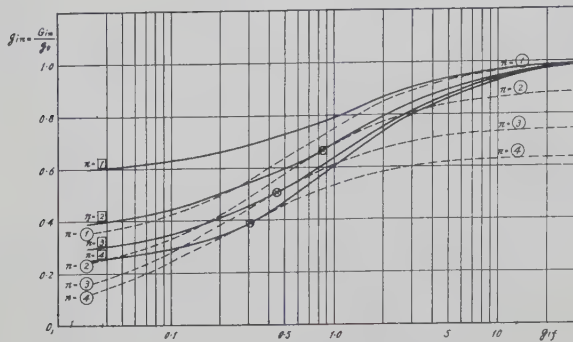
Under the same condition as the output admittance, *i.e.*,  $g_r = g_{in}$ , the conversion loss of a mixer is obtained as follows:

$$\begin{aligned} L &= \left( 1/2 \cdot \frac{I'^2 s^2}{2g_r \cdot g_0} \right) / (V_{if}^2 \cdot g_{if} \cdot g_0) \\ &= \frac{1}{4} \cdot \frac{(G_T/g_0)^2}{g_r \cdot g_{if}}, \end{aligned} \quad (23)$$

the value of which is indicated in Fig. 8, in the case where the image frequency impedance is open or short.

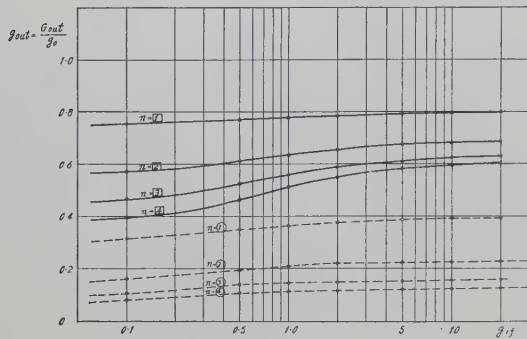
## 2. When Barrier Capacitance of Crystal is Considered

Let  $C$  be the barrier capacitance. Then,  $C$  is connected in parallel to terminal pairs 1-1', 2-2', and 3-3' of Fig. 1. At terminal pairs 1-1' and 2-2', however, capacitance  $C$  is tuned out by the impedance matching circuit and intermediate frequency tuning circuit, respectively, and



$n = \square$  when image frequency impedance is short.  
 $n = \circ$  when image frequency impedance is open.

Fig. 6—Variation of input admittance with IF admittance.



$n = \square$  when image frequency impedance is short.  
 $n = \circ$  when image frequency impedance is open.

Fig. 7—Variation of output admittance with IF admittance.

it may be considered that capacitance  $C$  is connected only to terminal pair 3-3'. Since the bandwidth under consideration is 20 mc and  $f_{im}$  is about 4000 mc, susceptance  $\omega_{im}C$  may be considered also to be constant within the band. Therefore, by substituting  $(\cot \theta - a)$  for  $\cot \theta$  in the above equations, the various impedances of a mixer, in the case where barrier capacitance is considered, can be easily calculated. Where

$$a = \omega_{im}C/G_{im}, \quad (24)$$

for example, the transfer admittance becomes unsymmetric, as shown in Fig. 9, and unlike the one encountered in Fig. 5.

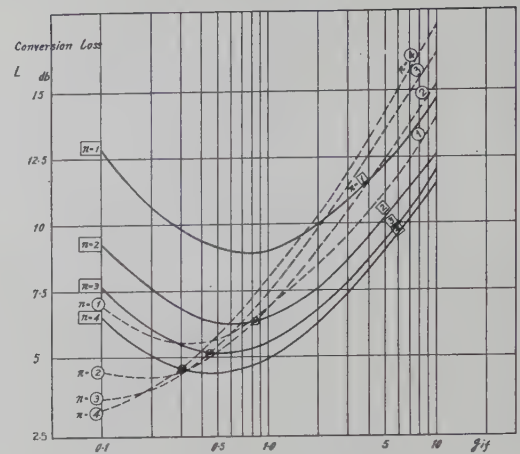
#### IV. THE CONDITION THAT MAKES IMAGE FREQUENCY VOLTAGE ZERO

When the intermediate frequency conductance is a special value of  $g_{ifo}$ , no image frequency component is generated. In (8), the condition that makes  $V_{im}^* = 0$  is the following:

$$\Delta_{13} = \begin{vmatrix} \mu_1 & 1 + g_{ifo} \\ \mu_2 & \mu_1 \end{vmatrix} = 0; \quad (25)$$

that is,

$$g_{ifo} = \frac{\mu_1^2}{\mu_2} - 1. \quad (26)$$



$n = \square$  when image frequency impedance is short.  
 $n = \circ$  when image frequency impedance is open.

Fig. 8—Variation of conversion loss with IF admittance.

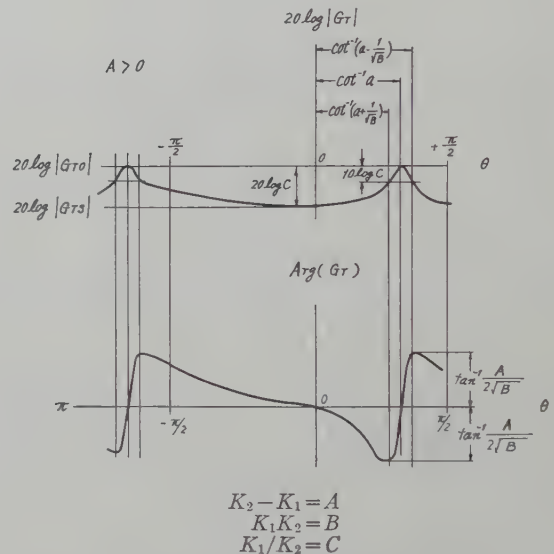


Fig. 9—Variation of transfer admittance  $G_T$  when barrier capacitance is considered.

Eq. (26) is the condition where amplitude and delay distortion always vanish independently of the image frequency impedance, meaning, physically, that no appreciable image frequency component is generated under this condition.

This is due to the following reason: an image frequency component generated at terminal pair 3-3', which is derived from signal component coming through arm  $\mu_2$  from terminal pair 1-1' on the one hand, and a similar component generated at terminal pair 3-3' through terminal pair 2-2' from terminal pair 1-1' on the other hand, neutralize each other, resulting in no image frequency component present at terminal pair 3-3'. Of the above two image frequency components, the one through arm  $\mu_2$  is the difference of the input signal and a second harmonic of the local oscillator frequency, while the other through 2-2' is the difference of the local oscillator frequency and the intermediate frequency component derived from the input signal.



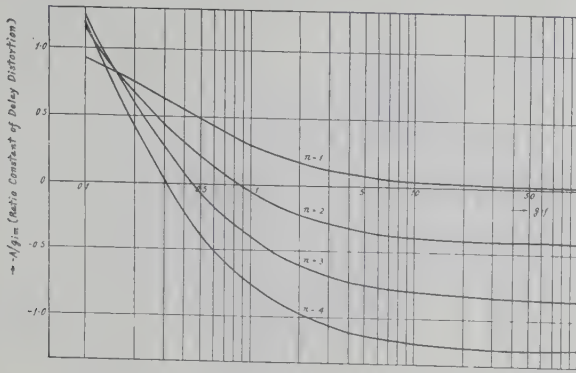


Fig. 10—Variation of  $A$  with IF admittance (delay time, when  $\theta=90^\circ$ ).

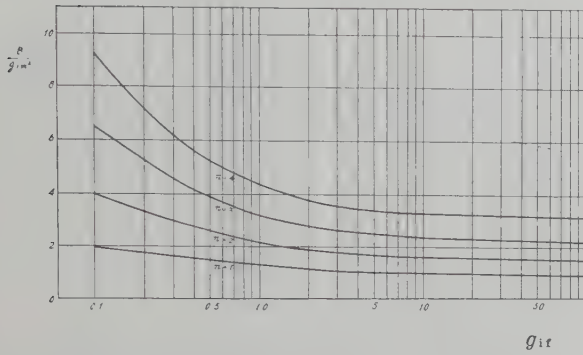


Fig. 11—Variation of  $B$  with IF admittance.

The condition in (26) is very interesting theoretically:  $g_{ifo}$  is determinable by  $\mu_1$  and  $\mu_2$ , that is to say, detector characteristic  $n$  alone.

From  $\mu_1$  and  $\mu_2$  in Fig. 2,  $g_{ifo}$  is seen in Table I.

TABLE I

$n$	1	2	3	4
$g_{ifo}$	$\infty$	0.85	0.43	0.31

Hence, the characteristics of a mixer, *i.e.*, input admittance  $G_{in}$ , transfer admittance  $G_T$ , and conversion loss  $L$ , can be said to be independent of image frequency impedance in the case of  $g_{if}=g_{ifo}$ , and this  $g_{ifo}$  is the cross point in Figs. 6 and 8, that is, the zero point in Figs. 10, 12, and 14.

## V. DELAY DISTORTION OF MIXER

### 1. When Barrier Capacitance of Crystal is Ignored

The phase delay  $\Theta$  of  $V_{if}$  relative to  $I$ 's is given from (14) as follows:

$$\Theta = -\tan^{-1} \left\{ A \cot \theta / (1 + B \cot^2 \theta) \right\} + \pi, \quad (27)$$

where

$$A = K_2 - K_1 = \frac{g_{im}}{1 - \mu_2 (1 + g_{if} - \mu_1^2) \{ (1 - \mu_2) + g_r \} + (1 - \mu_2) \{ (1 + g_{if}) \mu_2 - \mu_1^2 \}},$$

$$B = K_1 - K_2 = \frac{g_{im}^2}{1 - \mu_2 (1 + g_{if} - \mu_1^2) \{ (1 - \mu_2) + g_r \} + (1 - \mu_2) \{ (1 + g_{if}) \mu_2 - \mu_1^2 \}}. \quad (28)$$

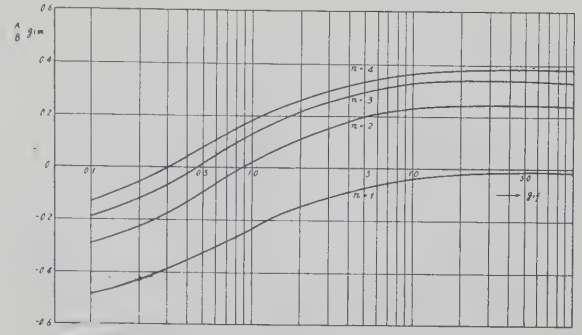


Fig. 12—Variation of  $A/B$  with IF admittance (delay time, when  $\theta=0$ ).

Differentiating (27) with respect to  $\omega_s$ , we obtain the group-delay-time  $T$ . But since there is a relation that  $\omega_{im} = \omega_s - 2\omega_{if} = 2\omega_L - \omega_s$ , we have

$$\begin{aligned} T &= \frac{d\Theta}{d\omega_s} \\ &= - \frac{d\Theta}{d\omega_{im}} \\ &= -A \frac{(1 - B \cot^2 \theta)(1 + \cot^2 \theta)}{(1 + B \cot^2 \theta)^2 + A^2 \cot^2 \theta} T_0, \end{aligned} \quad (29)$$

where

$$\begin{aligned} T_0 &= \frac{d\theta}{d\omega_{im}} \\ &= l \frac{d\beta}{d\omega_{im}}. \end{aligned} \quad (30)$$

$T_0$  is the time required by the image frequency component to propagate over line  $l$  at its own group velocity. It is clear from (29) that delay time characteristic in this case is symmetric with respect to  $\theta=0$ , and is given by

$$\begin{aligned} T_1 &= [A/B] \cdot T_0, \\ T_2 &= -A \cdot T_0, \end{aligned} \quad (31)$$

where

$$T_1 = \text{delay time when } \theta = 0 \quad (i.e. \text{ short})$$

$$T_2 = \text{delay time when } \theta = 90^\circ \quad (i.e. \text{ open}).$$

Also, we have

$$\theta_1 = \pm \tan^{-1} \sqrt{B} \quad (32)$$

where  $\theta_1$  is an electric angle when delay time is zero, *i.e.*,  $T=0$ . Then,  $A/g_{im}$ ,  $B/g_{im}^2$ , and  $[A/B]g_{im}$  can be expressed respectively as in Figs. 10–12. From these graphs, we can easily calculate  $T_1$  and  $T_2$ , if  $g_{im}$  is given.

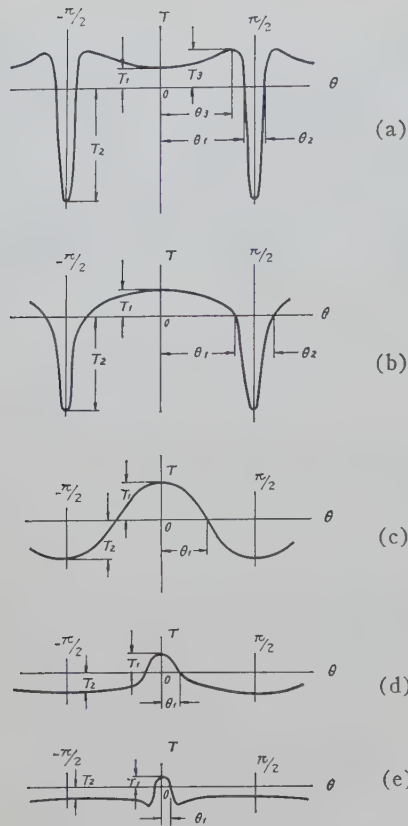


Fig. 13—Shape of delay distortion in mixers (when barrier capacitance is ignored).

In the case of  $g_{if} = g_{ifo}$ , i.e.,  $A = 0$ , delay time is always zero, delay distortion is entirely absent, and  $A$  changes its sign with this  $g_{ifo}$  as the critical value.

From what has been described, delay time characteristic is now fairly apparent. Further detailed study by  $dT/d\theta$  (see Appendix II) shows that, when  $A > 0$ , this delay distortion assumes various shapes as shown in Fig. 13. Fig. 13(a) is the case when  $B > [3 + \sqrt{9 + 4A^2}]/2$ . A sharp hump of delay distortion occurs when  $\theta = 90^\circ$ , that is, when image impedance is infinite. As  $B$  grows smaller and smaller in comparison with  $A$ , the delay time characteristic assumes the shapes shown in (b) and (c), and approaches the sinusoidal shape, like an ordinary echo distortion. Further decrease in  $B$  relative to  $A$  makes the shape like that in (d). When  $B < (1 - A^2)/3$ , a hump presents such a shape as in (e) at  $\theta = 0$ , that is, when the image impedance is zero. In practice, however, delay distortion in mixers hardly takes the shape as in (e). Also, in the case of echo distortion on the feeder line, the conditions that lead to the formation of shapes as in (a) and (e) do not exist.

When  $A < 0$ , the curves in Fig. 13 are only upside-down, and the conditions for (a), (b), (c), (d), and (e) are entirely the same as when  $A > 0$ . Thus the shape of delay distortion in mixers assumes in general the shape shown in Fig. 14, except the case when  $n = 1$ . At the value of  $g_{ifo}$  which satisfies (26), delay distortion vanishes entirely, and changes its polarity with this value

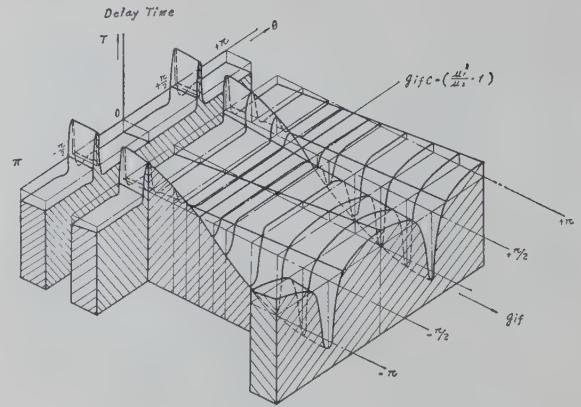


Fig. 14—Variation of delay distortion due to IF admittance.

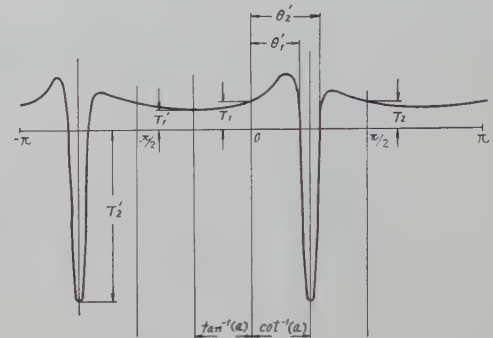


Fig. 15—Shape of delay distortion in mixers (when barrier capacitance is considered).

as the critical condition. The manner of this variation can be anticipated easily from curves in Figs. 10 and 12.

## 2. When Barrier Capacitance of Crystal is Considered

In this case, taking account of the fact described in Section III-2, delay time  $T$  is given from (8) and (29).

$$T = -A \frac{[1 - B(\cot \theta - a)^2] \cdot (1 + \cot^2 \theta)}{[1 + B(\cot \theta - a)^2]^2 + A^2(\cot \theta - a)^2} \cdot T_0, \quad (33)$$

where  $a$  is expressed in (24).

The shape and magnitude of delay distortion can be estimated by comparing (33) with (29), as shown in Fig. 15. Namely, when  $\theta = 0$ ,

$$T_1 = [A/B]T_0;$$

when

$$\theta = \cot^{-1} a,$$

$$T_2' = -A(1 + a^2)T_0;$$

when

$$\theta = -\tan^{-1} a,$$

$$T_1' = -A \frac{\{1 - B(a^{-1} + a)^2\} \cdot (1 + a^{-2})}{\{1 + B(a^{-1} + a)^2\}^2 + A^2(a^{-1} + a)^2} \cdot T_0,$$

when

$$\theta = 90^\circ$$

$$T_2 = -A \frac{(1 - a^2 B)}{(1 + a^2 B)^2 + a^2 A^2} \cdot T_0. \quad (34)$$



Hence, the condition that makes  $T=0$  when  $\theta$  is in the range of  $-90^\circ$  to  $+90^\circ$ , is

$$\theta_1' = \cot^{-1}(a + B^{-1/2});$$

when

$$a < B^{-1/2},$$

$$\theta_2' = \cot^{-1}(a - B^{-1/2});$$

when

$$a > B^{-1/2},$$

similarly,

$$\theta_3' = \cot^{-1}(a - B^{-1/2}). \quad (35)$$

Since, in general, it suffices to consider  $T_2'$  as delay distortion, we may say that the magnitude of delay distortion in this case is  $(1+a^2)$  times larger, hence, a great deal sharper, compared with that when the barrier capacitance is ignored.

## VI. EXAMPLE OF NUMERICAL VALUE CALCULATION

Numerical values were calculated, expressing the crystal characteristic as in (6); namely,  $i = Kv^n$  for the positive direction, and  $i=0$  for the negative direction, assuming the dc bias voltage is zero. Since one of the most easily measurable physical quantities in the microwave band is dc rectified current  $I_{dc}$  against the local oscillator power, and in a type 1N23B, which we used,  $I_{dc} \approx 2$  ma at 1 milliwatt, we regarded as  $I_{dc} = 2$  ma for the local oscillator power of 1 milliwatt. Under this condition, we can find the value for  $g_0$  in Fig. 3, and then values for  $\mu_1$  and  $\mu_2$  from Fig. 2. The equivalent circuit of Fig. 1 was determined in this way. We took  $f_s = 3810$  mc and  $f_L = 3880$  mc, and, for the purpose of exaggerating the result, made  $l = 6$  m; i.e.,  $T_0 = 26.4$   $\mu$ sec.

In the calculations and graphs to follow, the abscissa indicates the deviation from the center value of intermediate frequency  $f_{if}$ . In practice, because  $l$  in the mixer is in the range from 0.6 m to 0.3 m, the actual magnitude of delay distortion would be about 1/10 to 1/20 the calculated example, and the pitch of delay distortion would be from 10–20 times the actual value.

Fig. 16 is the result of calculation showing variation of delay time characteristic with  $n$ , when the crystal, of which dc rectified current is 2 ma for the local oscillator power of 1 milliwatt, is used at  $I_{dc}' = 1$  ma, and  $G_{if} = 1/85 \Omega$  and  $G_{im} = 1/75 \Omega$ .

Fig. 17 shows variation of delay distortion with equivalent characteristic admittance  $G_{im}$  for the image frequency, when  $I_{dc}' = 1$  ma,  $G_{if} = 1/85 \Omega$ , and  $n = 2$ .

Fig. 18 is the result of calculation showing variation of delay distortion with variation of barrier capacitance  $C$  when  $G_{if} = 1/85 \Omega$ ,  $G_{im} = 1/75 \Omega$ , and  $n = 2$ .

It is evident from the above graphs that delay distortion generally increases with increase in  $G_{im}$  and  $C$ .

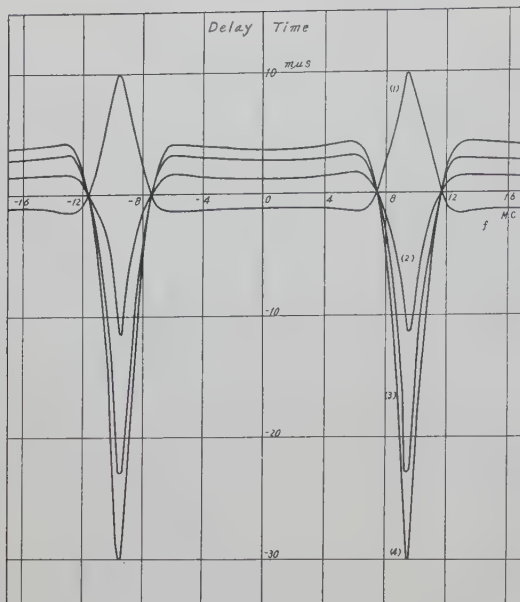
## VII. EXPERIMENTAL RESULT

Experiments were made with the circuit shown in Fig. 19, which uses an  $L$ -type branching circuit [12]. The intermediate frequency preamplifier of this experiment was an inverted type amplifier employing a type 6J4 tube and having an input impedance of about 85 ohms, while the crystal detector was the type 1N23B crystal diode. The delay time characteristic of the measuring system was about 12  $\mu$ sec within the 20 mc band; but since it had a single peaked and smooth characteristic, and was not considered to disturb the measurement of a sharply humped delay distortion in the mixer, the system delay time characteristic was not equalized. Accordingly, the base curve of the measured result is almost the delay time characteristic of the measuring system.

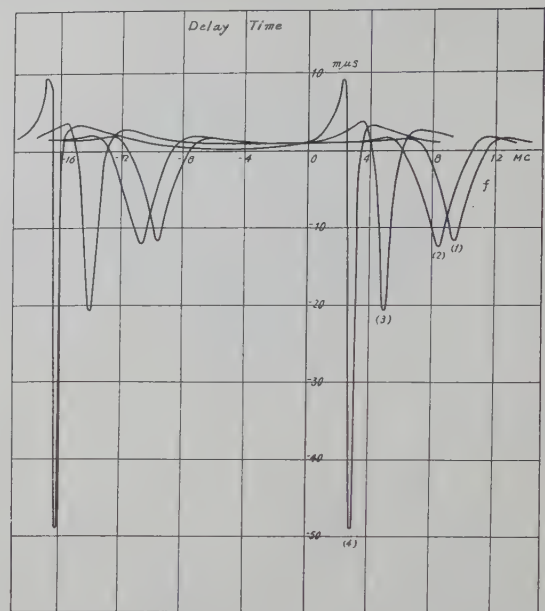
Fig. 20 shows two delay distortion curves when  $1/G_{if} \approx 85$  ohms,  $f_s = 3810$  mc, and  $f_L = 3880$  mc. Curve 1 corresponds to the case when length  $l$  between the image suppression filter and the crystal detector was about 6 meters; while curve 2 is the case when  $l \approx 3.8$  meters. Note that the magnitude of the humped distortion is proportional to  $l$  and the pitch is inversely proportional to  $l$ .

Fig. 21 shows variation of delay distortion as the intermediate frequency impedance  $Z_{if}$  was varied from 22 ohms to 2 kilo-ohms when  $l \approx 5.3$  m,  $I_{dc}' \approx 1$  ma,  $f_s = 3930$  mc,  $f_L = 4000$  mc; and Fig. 22 indicates variation of amplitude frequency response in the same case.  $Z_{if}$  is the load of the crystal detector and corresponds to  $1/G_{if}$ . When the magnitudes of the above humped distortions were arranged as functions of  $Z_{if}$ , Fig. 23 was obtained. (In the graph, either of amplitude and delay distortion is zero when  $Z_{if} \approx 200$  ohms, and changes its sign with this load as the critical value.) The tendency of this variation agrees with that of Figs. 10 and 14. The theoretical value  $Z_{if}$  calculated from both  $g_{ifo} = 0.85$  in Table I and  $g_0 = 6.1$  millimho of the crystal detector in Fig. 3 is about 194 ohms ( $n$  is always regarded as 2), and shows good agreement with the experimental value  $Z_{if} \approx 200$  ohms.

Fig. 24(a) to Fig. 24(c) shows change in delay distortion due to crystal current  $I_{dc}'$  as  $Z_{if}$  is taken 85 ohms, 205 ohms, and 785 ohms, respectively, when  $f_s = 3,930$  mc,  $f_L = 4000$  mc, and  $l \approx 5.3$  m. Since  $g_0$  increases as  $I_{dc}'$  increases, and  $g_0$  decreases as  $I_{dc}'$  decreases, the condition is opposite in (a) and (c) whether  $g_{if}$  approaches or leaves the critical values  $g_{ifo}$  which satisfies (26). This fact is clearly shown in these graphs. In practice, since  $l$  is shorter, and delay distortion is about 1/10 to 1/20 of the above results, it can be said from Fig. 24(b) that delay distortion hardly occurs in the actually operated range of 0.75 ma–1.5 ma, when  $Z_{if} \approx 200$  ohms. Since this distortionless condition, i.e.  $g_{ifo}$ , is independent of equivalent characteristic admittance  $G_{im}$  for image frequency component and barrier capacitance  $C$ , the value of  $g_{ifo}$  is almost constant. Con-

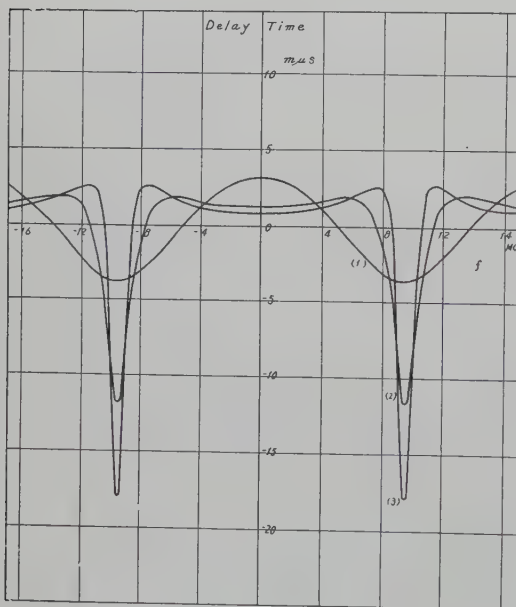


$I_{d0}' = 1$  ma (1-mw 2-ma crystal). (1)  $n = 1$   
 $G_{if} = 1/85 \Omega$  (2)  $n = 2$   
 $G_{im} = 1/75 \Omega$  (3)  $n = 3$   
 $l = 6$  m (4)  $n = 4$

Fig. 16—Variation of delay distortion with  $n$ .

$I_{d0}' = 1$  ma ( $n = 2$ , 1-mw 2-ma crystal). (1)  $C = 0$  pF  
 $G_{if} = 1/85 \Omega$  (2)  $C = 0.1$  pF  
 $G_{im} = 1/75 \Omega$  (3)  $C = 0.5$  pF  
 $l = 6$  m (4)  $C = 1.0$  pF

Fig. 18—Delay distortion when barrier capacitance is considered.

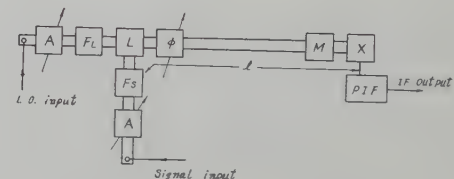


$I_{d0}' = 1$  ma ( $n = 2$ , 1-mw 2-ma crystal). (1)  $G_{im} = 4.8$  millimho=  
 $G_{in}$  m  
 $G_{if} = 1/85 \Omega$  (2)  $G_{im} = 13.3$  millimho  
 $l = 6$  m (3)  $G_{im} = 20.0$  millimho

Fig. 17—Variation of delay distortion with equivalent characteristic admittance  $G_{im}$  for image frequency.

sequently, in practice, hardly any difference of  $g_{if0}$  value was observed when several crystal detectors were replaced during the measurements.

It will be noticed that the delay distortion curves in Figs. 20, 21, and 24 are somewhat different from one another in magnitude and shape.



$A$  = Variable attenuator  
 $F_s$  = Image suppression filter  
 $\phi$  = Phase shifter  
 $X$  = Crystal detector  
 $L$  = L-type branching circuit  
 $F_L$  = Local oscillator filter  
 $M$  = Impedance matching circuit  
 $PIF$  = Intermediate frequency preamplifier

Fig. 19—Measuring system.

These differences are attributed to the variation of each element in the matching circuit, which is adjusted to retain a good matching condition for the input signal. In other words, this implies the variation of the equivalent characteristic admittance  $G_{im}$  for image frequency components due to the adjustment of the matching circuit.

$G_{im}$  also varies with the frequency response of the matching circuit as well as its relative distance from the image suppression filter.

Graph (b) of Fig. 25 shows the variation of noise figure with  $Z_{if}$  under the circuit arrangement shown in (a), and indicates that noise figure is best when  $Z_{if} = 200$  ohms. The use of an inverted type amplifier with 6J4 tube for the intermediate frequency preamplifier therefore makes the distortionless condition and optimum noise figure condition approximately coincide with each other. The above experimental results agree in tendencies with the preceding analyses and the examples of numerical value calculations.



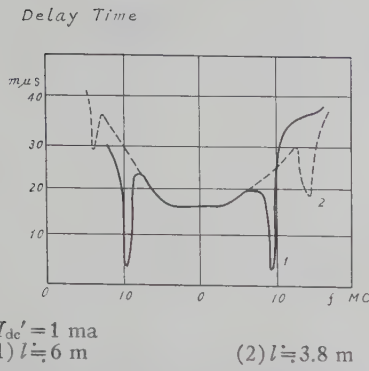


Fig. 20—Experimental result of delay distortion vs equivalent length  $l$  for image frequency component.

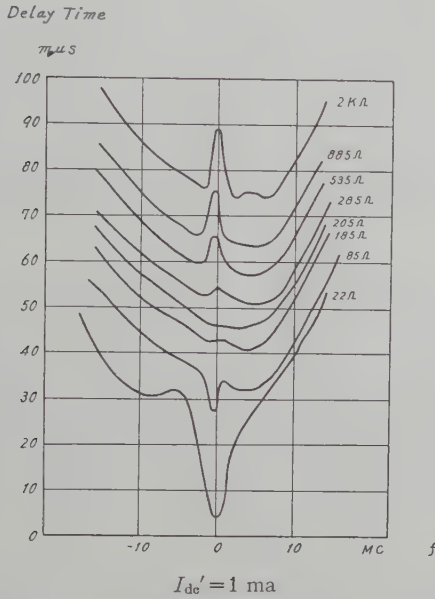


Fig. 21—Variation of delay distortion with IF impedance.

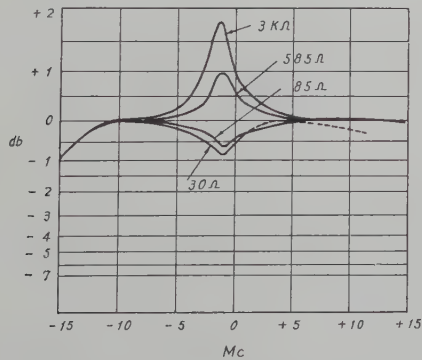


Fig. 22—Variation of amplitude frequency response with IF impedance.

### VIII. CONCLUSION

From the above analysis, calculations, and experiments, delay distortion in mixers has been illustrated. The results may be summarized as follows:

#### Characteristics of Delay Distortion

- 1) The magnitude of delay distortion in mixers is, like echo distortion in a feeder, directly proportional

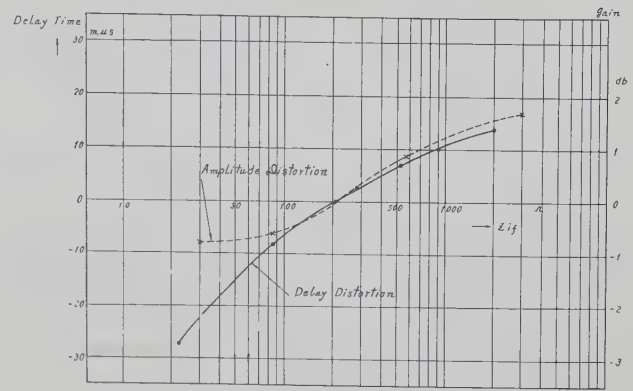


Fig. 23—Variations of amplitude and delay distortion with IF impedance.

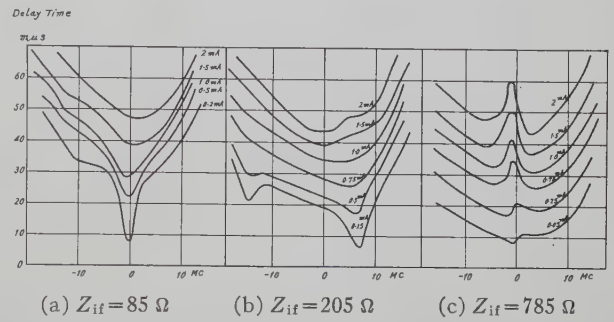


Fig. 24—Variation of delay distortion with crystal current.

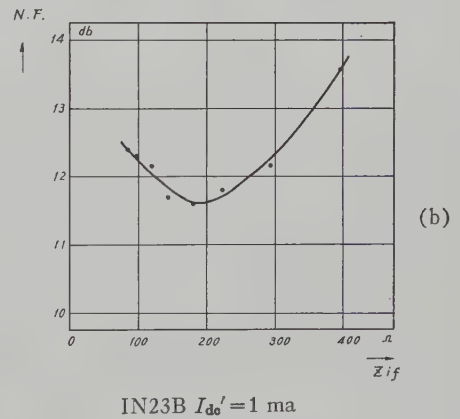
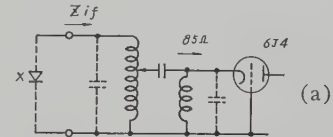


Fig. 25—Variation of noise figure with IF impedance.

to the length of the transmission line for the image frequency component. The pitch is inversely proportional to the length.

- 2) In many cases, delay distortion in mixers is different from echo distortion, in that it is sharply humped.
- 3) This delay distortion takes the maximum value at the frequency where image frequency impedance becomes infinite.
- 4) This delay distortion increases abruptly with increase in the barrier capacitance of the mixer.

### Conditions That Reduce Delay Distortion [14]

- 1) One of the conditions is to avoid the image frequency impedance reaching infinity within the desired band.
- 2) Another is to select the load conductance of the mixer, *i.e.*, intermediate frequency conductance  $g_{if}$ , as  $g_{if} = (\mu_1^2/\mu_2) - 1$ .
- 3) Still another is to terminate the image frequency impedance in an appropriate resistance load; namely, to provide a branching circuit which absorbs the image frequency component.

Of these three conditions, 2) cannot be expected to coincide always with the condition that makes noise figure a minimum, while 3) calls for a complicated waveguide circuit. Condition 1), therefore, is most desirable from the practical viewpoint. It may be said, therefore, without such special consideration paid to the mixer design, that a sharply humped distortion may appear with a pitch of 200–400 mc with the magnitude of a few millimicroseconds in an ordinary mixer. Such distortion will be observed with a probability of about 1/10–1/20 in the 20-mc band of a repeater.

Spreading resistance of crystal detector has been omitted from consideration, since it involves very complicated problems. This, of course, mitigates delay distortion, and so in practice seems to put the delay distortion about intermediate between the two conditions; that is, the condition when the barrier capacitance is ignored and the condition when it is considered. Qualitatively, the above conclusions are applicable equally to mixers other than the receiving crystal mixers.

### APPENDIX I

The normalized input admittance of a mixer, when the image frequency impedance is short or open, is given by

$$g_{in s} = \frac{1 + g_{if} - \mu_1^2}{1 + g_{if}}, \quad (36)$$

and

$$g_{in o} = (1 - \mu_2) \frac{(1 + \mu_2)(1 + g_{if}) - 2\mu_1^2}{1 + g_{if} - \mu_1^2}. \quad (37)$$

When both input signal and image frequency terminals are connected and matched to identical impedances, the input admittance is

$$g_{in m} = \sqrt{g_{in s} \cdot g_{in o}} \quad (38)$$

The numerical calculation was made by substituting  $g_{in m}$  for  $g_r$  in (28). Substitution of either  $g_{in s}$  or  $g_{in o}$  instead of  $g_{in m}$ , does not vary the values in Figs. 10–12 by more than 5 per cent in the given  $g_{if}$  range.

### APPENDIX II

#### Shape of Delay Time Characteristic

When (29) is differentiated,

$$\frac{dT}{d\theta} = - \frac{2AT_0 \cot \theta (1 + \cot^2 \theta)}{\{(1 + B \cot^2 \theta)^2 + A^2 \cot^2 \theta\}^2} \cdot [B\{A^2 + B(3 - B)\} \cot^4 \theta + 2B(1 + B) \cot^2 \theta + (3B + A^2 - 1)]. \quad (39)$$

The conditions that make (39) zero except when  $\theta = 0$  and  $\theta = 90^\circ$ , exist in the following cases:

$$B > [3 + \sqrt{9 + 4A^2}]/2, \quad (40)$$

$$B < [1 - A^2]/3. \quad (41)$$

Under the condition that satisfies (40), and when it is assumed that  $B \gg 3$  and  $A^2 \ll 1$ ,  $\theta_3$ , and  $T_3$  in Fig. 13(a) become

$$\theta_3 = \pm \cot^{-1} \left[ \frac{1 - 3B}{B(3 - B)} \right]^{1/2} \doteq \pm \cot^{-1} \sqrt{\frac{3}{B}} \quad (42)$$

$$T_3 \doteq \frac{A}{8} T_0. \quad (43)$$

and  $\theta_2$  in Fig. 13; *i.e.*, the width of hump may be expressed by

$$\theta_2 = 2 \cot^{-1} \sqrt{B}. \quad (44)$$

### ACKNOWLEDGMENT

The authors are greatly indebted to Dr. K. Kobayashi and Dr. M. Morita for their leadership and advice, and are equally grateful to the members of the Microwave Group of Nippon Electric Company for their kind assistance and encouragement.

### BIBLIOGRAPHY

- [1] E. Peterson and L. W. Hussey, "Equivalent modulator circuits," *Bell Sys. Tech. J.*, vol. 18, pp. 32–48; January, 1939.
- [2] L. C. Peterson and F. B. Llewellyn, "The performance and measurement of mixers in terms of linear-network theory," *PROC. IRE*, vol. 33, pp. 458–476; July, 1945.
- [3] E. W. Herold, R. R. Bush, and W. R. Ferris, "Conversion loss of diode mixers having image-frequency impedance," *PROC. IRE*, vol. 33, pp. 603–609; September, 1945.
- [4] C. F. Edwards, "Microwave converters," *PROC. IRE*, vol. 35, pp. 1181–1191; November, 1947.
- [5] P. D. Strum, "Some aspects of mixer crystal performance," *PROC. IRE*, vol. 41, pp. 875–889; July, 1953.
- [6] E. Willwacher, "Der Einfluss der Spiegelfrequenz bei Mikrowellenempfängern mit Detektormischung," *FTZ*, Jg. 7, pp. 608–615; November, 1954.
- [7] H. C. Torrey and C. A. Whitmer, "Crystal Rectifiers," vol. 15, *Rad. Lab. Ser.*, McGraw-Hill Book Co., Inc., New York, N. Y., pp. 111–178; 1948.
- [8] R. V. Pound, "Microwave Mixers," vol. 16, *Rad. Lab. Ser.*, McGraw-Hill Book Co., Inc., New York, N. Y., pp. 52–97; 1948.
- [9] T. Kawahashi, "Some considerations of the conversion loss of the crystal mixer," *J. Inst. Elec. Comm. Eng. (Japan)*, vol. 33, pp. 187–194; April, 1950.
- [10] T. Kawahashi and T. Uchida, "Delay distortion in receiving crystal mixers," *Conv. Rec. of the Inst. Elec. Comm. Eng. (Japan)*, no. 601, p. 601; 1956.
- [11] T. Kawahashi and R. Kuroda, "Some considerations of the impedance matching circuits in crystal mixers," *Conv. Rec. of the Inst. Elec. Comm. Eng. (Japan)*, no. 600, p. 600; April, 1956.
- [12] T. Kawahashi, "L-type Branching Circuit," *Congrès International Circuits et Antennes Hyperfréquences*, Paris; October, 1957 (to be published in near future).
- [13] T. Kawahashi and T. Uchida, "Amplitude Frequency Response of Mixers," *Conv. Rec. of the Inst. Elec. Comm. Eng. (Japan)*, no. 123, p. 123; Autumn, 1956.
- [14] T. Kawahashi, "Microwave Mixer without the Influence of Undesired Sideband Components," *Congrès International Circuits et Antennes Hyperfréquences*, Paris; October, 1957 (to be published in near future).



# The Efficiency of Excitation of a Surface Wave on a Dielectric Cylinder\*

J. W. DUNCAN†

**Summary**—This paper presents a theoretical and experimental study of the excitation of the lowest order TM surface wave on an infinite dielectric cylinder. The source is a circular filament of magnetic current within the dielectric rod. The integral solution for the field is evaluated as a contour integral by applying Cauchy's theorem. The far zone radiation field is obtained by means of a saddle point integration. Curves are presented which show excitation efficiency as a function of  $k_0 a$ , the normalized circumferential length of the filament. A filament 0.83 wavelength in diameter will launch the TM mode with an efficiency of 95 per cent. A narrow annular slot in a large metal sheet was used to approximate the magnetic current filament and efficiency was measured using Deschamps' method for a two-port junction. The experimental measurements verify the theoretical analysis. In addition, it was found that the slot launching efficiency was essentially independent of the ground plane dimensions.

## INTRODUCTION

A NUMBER of papers published in the last decade have treated the mode characteristics of surface waves on various types of open waveguides. Of particular interest has been the utilization of such structures as surface wave antennas. A factor of prime importance in all surface wave applications is the efficient excitation of the desired mode on the guide. The excitation efficiency of a source is defined as the ratio of the power converted to the surface wave mode to the total power which is delivered by the source.

In order to determine the excitation efficiency of a source, one must solve the source form of Maxwell's equations which amounts to solving an inhomogeneous wave equation. The usual technique of solving the differential equation is to apply the method of integral transforms which yields the solution for the field in the form of a definite integral. The integral is evaluated by considering it as a contour integral in the plane of the complex propagation constant. The integrand has poles and branch points in the complex plane. Applying Cauchy's theorem to the contour integral, the integral becomes equal to the sum of the residues at the poles plus a branch cut integral. The poles correspond to the surface wave modes and the amplitude of a surface mode is given by the residue of the integrand at the pole. The branch cut integration yields the radiation field. Alternately, the radiation field is obtained from the asymptotic evaluation of the integral by means of a saddle point integration. This method of analysis yields the

amplitude of the radiation field and of the surface mode. One may then calculate the radiated power and surface wave power and determine the excitation efficiency of the source.

Cullen<sup>1</sup> calculated the efficiency of an infinitely long slot above a dielectric coated plane conductor. He also treated the slot above a corrugated surface and a source such as a gently flared horn. His theory predicted a maximum efficiency of 85 per cent for the slot above the coated conductor. Rich<sup>2</sup> attempted an experimental verification of Cullen's work and measured efficiencies less than 20 per cent for the slot above the coated conductor. Several factors may have contributed to the difference in results.<sup>3,4</sup>

Fernando and Barlow<sup>5</sup> considered a vertical dipole source above flat reactive surfaces. A maximum efficiency of about 80 per cent was predicted for a half-wave dipole above a coated or a corrugated surface. In order to estimate efficiency experimentally, they measured the amplitude of the radiation and surface wave fields and substituted into the theoretical field solutions to calculate the respective powers and efficiency. Good agreement was obtained between the theoretical launching efficiency and the efficiency calculated from the measured amplitude of the fields.

Roberts<sup>6,7</sup> investigated the single wire transmission line excited from a flanged coaxial cable. This source launches the transverse magnetic,  $E_{00}$  mode on the wire. He evaluated the input conductance of the coaxial line by assuming an infinitesimal gap between the wire and the outer conductor of the coax. The input conductance is the sum of the radiation conductance  $G_1$  and the characteristic conductance  $G_0$ . The excitation efficiency of the source may be calculated from  $G_1$  and  $G_0$ . Roberts' experimental work included measuring the input conductance of the coaxial line for a number of different

<sup>1</sup> A. L. Cullen, "The excitation of plane surface waves," *Proc. IEE*, vol. 101, pt. 4, pp. 225-234; August, 1954.

<sup>2</sup> G. J. Rich, "The launching of a plane surface wave," *Proc. IEE*, vol. 102, pt. B, pp. 237-246; March, 1955.

<sup>3</sup> A. L. Cullen, "Discussion on the launching of a plane surface wave," *Proc. IEE*, vol. 102, pt. B, pp. 824-825; November, 1955.

<sup>4</sup> R. H. DuHamel, "Discussion on the launching of a plane surface wave," *Proc. IEE*, vol. 103, pt. B, pp. 787-788; November, 1956.

<sup>5</sup> W. M. G. Fernando and H. E. M. Barlow, "An investigation of the properties of radial cylindrical surface waves launched over flat reactive surfaces," *Proc. IEE*, vol. 103, pt. B, pp. 307-318; May, 1956.

<sup>6</sup> T. E. Roberts, "Theory of the single wire transmission line," *J. Appl. Phys.*, vol. 24, pp. 57-67; January, 1953.

<sup>7</sup> T. E. Roberts, "An experimental investigation of the single wire transmission line," *TRANS. IRE*, vol. AP-2, pp. 46-56; April, 1954.

\* Manuscript received by the PGMTT, September 19, 1958. Revised manuscript received, December 3, 1958. The work described in this paper was supported by Wright Air Development Center under Contract No. AF33(616)-3220, and is extracted from a thesis submitted in partial fulfillment of the requirements for the Ph.D. degree, Dept. of Elec. Eng., University of Illinois, Urbana, Ill., 1958.

† Collins Radio Co., Cedar Rapids, Ia.

gap radii. The measured conductances were plotted on a graph and the curve was extrapolated to obtain the conductance of an infinitesimal gap, since it was impossible to measure such a source experimentally. The extrapolated value agreed quite closely with the conductance predicted from theory.

Most of the papers on excitation efficiency which have included experimental measurements have treated sources placed near infinite planar structures such as the dielectric coated conductor. Usually, it has not been feasible to measure efficiency for these structures. It seems worthwhile to apply the method of analysis to a problem which will permit direct experimental measurements of efficiency. The surface waveguide selected for the problem is the dielectric rod. The source, which has a simple physical realization, is the circular filament of magnetic current placed inside the rod and concentric with the longitudinal axis of the rod. One would expect the current ring to be an efficient exciter of the lowest order, transverse magnetic mode which can propagate on a dielectric rod. This mode is known as the  $E_{01}$  mode. The purpose of this investigation is to determine the efficiency with which the magnetic current ring excites the  $E_{01}$  mode and then to measure the efficiency experimentally. The excitation efficiency is readily measured using Deschamps' method for calibrating a two-port waveguide junction.

A similar problem has been treated by C. Jauquet,<sup>8,9</sup> who selected a magnetic current ring which was greater in diameter than the dielectric rod. In his papers, Jauquet obtains an integral solution for the field but does not present any calculations of excitation efficiency. His experimental measurements were concerned with the phase velocity and radial distribution of the surface wave mode.

### MATHEMATICAL FORMULATION

The problem to be investigated is illustrated in Fig. 1.

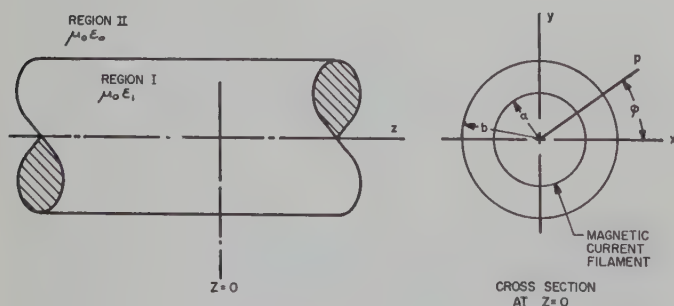


Fig. 1—Infinitely long dielectric rod excited by a circular filament of magnetic current located at  $z=0$ .

<sup>8</sup> C. Jauquet, "L'onde de surface sur un cylindre diélectrique le moyen de l'exciter—ses caractéristiques," *Rev. HF*, vol. 3, no. 8, pp. 283-296; 1956.

<sup>9</sup> C. Jauquet, "Excitation d'une onde de surface transverse magnétique se propageant sur un cylindre diélectrique," *Ann. Telecommun.*, vol. 12, pp. 217-233; June, 1957.

An infinitely long, dielectric rod of radius  $b$  is located such that its longitudinal axis corresponds to the  $z$  axis of circular cylinder coordinates  $(\rho, \phi, z)$ . The rod is considered lossless,  $\sigma=0$ , with a magnetic permeability  $\mu_0$  and permittivity  $\epsilon_1=\epsilon_r\epsilon_0$ , where  $\epsilon_r$  is the relative dielectric constant. The medium surrounding the rod and extending to infinity is free space, with constants  $\mu_0$  and  $\epsilon_0$ . The electromagnetic field source is a filamentary ring of magnetic current located at the plane  $z=0$ . The ring is of radius  $a$ , where  $0 < a < b$ , and is infinitesimally small in cross section. The source distribution is represented as a product of Dirac delta functions in the  $\rho$  and  $z$  coordinates as follows:

$$\bar{K} = \bar{\phi} \delta(\rho - a) \delta(z) \quad (1)$$

where  $\bar{\phi}$  is a unit vector in the  $\phi$  direction. The source distribution  $\bar{K}$  is independent of  $\phi$  and is a unit source such that

$$\iint \bar{K} \cdot \bar{\phi} da = \int_{-\Delta}^{+\Delta} \int_{0-\Delta}^{0+\Delta} \delta(\rho - a) \delta(z) dz d\rho = 1.$$

$\bar{K}$  has the dimensions of volts per square meter.

The electromagnetic field is a solution of Maxwell's equations. Written in differential form for  $e^{-i\omega t}$  time dependence, we have

$$\begin{aligned} \nabla \times \bar{E} &= i\omega\mu\bar{H} - \bar{K} \\ \nabla \times \bar{H} &= -i\omega\epsilon\bar{E}. \end{aligned} \quad (2)$$

Taking the curl of the second equation and then substituting the first relation for  $\nabla \times \bar{E}$  yields

$$-\nabla \times \nabla \times \bar{H} + \omega^2\mu\epsilon\bar{H} = -i\omega\epsilon\bar{K}. \quad (3)$$

The only non-zero component of  $\bar{K}$  is the coefficient of the unit vector  $\bar{\phi}$ . We may write the  $\phi$  component of the vector equation (3) and obtain the nonhomogeneous scalar equation

$$(-\nabla \times \nabla \times \bar{H})_\phi + \omega^2\mu\epsilon H_\phi = -i\omega\epsilon\delta(\rho - a)\delta(z)$$

where the  $\bar{\phi}$  component of the bracketed term is indicated.

The magnetic current filament generates a field having components  $H_\phi$ ,  $E_\rho$ , and  $E_z$ , while the components  $E_\phi$ ,  $H_\rho$ , and  $H_z$  are equal to zero. Due to the symmetry of the source, the field is independent of  $\phi$  and we note that all partial derivatives with respect to  $\phi$  must be zero. It is evident that the source produces a field which is circularly symmetric and transverse magnetic with respect to the  $z$  axis. Expanding the bracketed term in cylindrical coordinates, we obtain the partial differential equation relating  $H_\phi(\rho, z)$  to the source

$$\begin{aligned} \frac{\partial^2 H_\phi}{\partial \rho^2} + \frac{1}{\rho} \frac{\partial H_\phi}{\partial \rho} + \left(k^2 - \frac{1}{\rho^2}\right) H_\phi + \frac{\partial^2 H_\phi}{\partial z^2} \\ = -i\omega\epsilon\delta(\rho - a)\delta(z) \end{aligned} \quad (4)$$

where  $k^2 = \omega^2\mu\epsilon$ .



From  $\bar{E} = (1/-i\omega\epsilon)\nabla \times \bar{H}$ , it follows that

$$E_\rho(\rho, z) = \frac{1}{i\omega\epsilon} \frac{\partial H_\phi}{\partial z}$$

$$E_z(\rho, z) = \frac{1}{-i\omega\epsilon} \left( \frac{\partial H_\phi}{\partial \rho} + \frac{1}{\rho} H_\phi \right). \quad (5)$$

In order to solve (4) for  $H_\phi$ , we shall apply the method of integral transforms to reduce (4) to a nonhomogeneous, ordinary differential equation. We define the Fourier transform of  $H_\phi(\rho, z)$  as

$$h(\rho, \zeta) = \int_{-\infty}^{+\infty} H_\phi(\rho, z) e^{-i\zeta z} dz. \quad (6)$$

The inverse transform is given by

$$H_\phi(\rho, z) = \frac{1}{2\pi} \int_{-\infty}^{+\infty} h(\rho, \zeta) e^{i\zeta z} d\zeta. \quad (7)$$

Assuming that the transform of  $H_\phi(\rho, z)$  exists, we multiply each term of (4) by  $e^{-i\zeta z}$  and integrate over the infinite range with respect to  $z$  to obtain

$$\frac{d^2 h}{d\rho^2} + \frac{1}{\rho} \frac{dh}{d\rho} + \left( k^2 - \zeta^2 - \frac{1}{\rho^2} \right) h = -i\omega\epsilon \delta(\rho - a) \quad (8)$$

where the source variation  $\delta(z)$  is no longer present since

$$\int_{-\infty}^{+\infty} \delta(z) e^{-i\zeta z} dz = 1.$$

We may consider (8) as an ordinary differential equation in which  $\zeta$  is a parameter constant. The boundary conditions on  $h(\rho, \zeta)$  are obtained by taking the Fourier transform of the original boundary conditions on  $H_\phi(\rho, z)$  and  $\partial H_\phi/\partial \rho$ . The problem is one of solving (8) for  $h(\rho, \zeta)$  subject to the transformed boundary conditions.  $H_\phi(\rho, z)$  is then obtained by use of the inverse transform (7). The integral expression for  $H_\phi(\rho, z)$  is derived in the following section.

#### SOLUTION OF THE BOUNDARY VALUE PROBLEM

Consider the form of the nonhomogeneous differential equation (8). One could solve (8) using the Hankel transform; however, the definition of the delta function allows one to solve (8) in a simpler manner. The delta function is defined by the relations

$$\int_{a-\Delta}^{a+\Delta} \delta(\rho - a) d\rho = 1, \text{ and } \delta(\rho - a) = 0 \text{ for } \rho \neq a.$$

Consequently, for all  $\rho$  other than  $\rho = a$ , (8) reduces to the homogeneous differential equation

$$\frac{d^2 h}{d\rho^2} + \frac{1}{\rho} \frac{dh}{d\rho} + \left( k^2 - \zeta^2 - \frac{1}{\rho^2} \right) h = 0. \quad (9)$$

The delta function  $\delta(\rho - a)$  implies a boundary condition which  $h(\rho, \zeta)$  must satisfy at  $\rho = a$ . Multiplying each

term of (8) by  $d\rho$  and integrating over the interval  $2\Delta$  from  $\rho = a - \Delta$  to  $\rho = a + \Delta$ , one obtains

$$\frac{dh}{d\rho} \Big|_{a-\Delta}^{a+\Delta} + \int_{a-\Delta}^{a+\Delta} \frac{1}{\rho} \left( \frac{dh}{d\rho} \right) d\rho + (k^2 - \zeta^2) \int_{a-\Delta}^{a+\Delta} h d\rho$$

$$+ \frac{1}{\rho} h \Big|_{a-\Delta}^{a+\Delta} - \int_{a-\Delta}^{a+\Delta} \frac{1}{\rho} \left( \frac{dh}{d\rho} \right) d\rho = -i\omega\epsilon \int_{a-\Delta}^{a+\Delta} \delta(\rho - a) d\rho. \quad (10)$$

Assuming that  $h(\rho, \zeta)$  is continuous for all  $\rho$ , in the limit as  $\Delta \rightarrow 0$  and  $\rho \rightarrow a$ , (10) reduces to

$$\frac{dh}{d\rho} \Big|_{a+\Delta} - \frac{dh}{d\rho} \Big|_{a-\Delta} = -i\omega\epsilon. \quad (11)$$

We have shown that a continuous  $h(\rho, \zeta)$  which satisfies the homogeneous equation (9) and whose first derivative is discontinuous by  $-i\omega\epsilon$  at  $\rho = a$  is a solution of (8).

The remaining boundary conditions on  $h(\rho, \zeta)$  follow from the boundary conditions imposed on  $H_\phi(\rho, z)$  and  $E_z(\rho, z)$  by Maxwell's equations. Referring to Fig. 1, we denote the cross-sectional area of the rod as region I and the space outside the rod as region II. Since tangential  $\bar{H}$  is continuous at a magnetic current discontinuity, we see that  $H_\phi(\rho, z)$  is continuous at  $\rho = a$  for all  $z$  including the filament position  $z = 0$ . Since tangential  $\bar{E}$  and  $\bar{H}$  are continuous across a dielectric boundary, we note that  $H_\phi(\rho, z)$  and  $E_z(\rho, z)$  must be continuous at  $\rho = b$  for all  $z$ . The corresponding conditions on  $h(\rho, \zeta)$  are

1)  $H_\phi(\rho, z)$  continuous at  $\rho = a$  for all  $z$  implies that

$$h(\rho, \zeta) = \int_{-\infty}^{+\infty} H_\phi(\rho, z) e^{-i\zeta z} dz$$

must also be continuous at  $\rho = a$ , hence

$$h(\rho, \zeta) \Big|_{a-\Delta} = h(\rho, \zeta) \Big|_{a+\Delta}. \quad (12)$$

2) Similarly, since  $H_\phi(\rho, z)$  is continuous at  $\rho = b$  for all  $z$ ,

$$h(\rho, \zeta) \Big|_{b-\Delta} = h(\rho, \zeta) \Big|_{b+\Delta}. \quad (13)$$

3) From (5) we write

$$E_z(\rho, z) = \frac{1}{-i\omega\epsilon} \left( \frac{\partial H_\phi}{\partial \rho} + \frac{1}{\rho} H_\phi \right).$$

In region I, where  $0 \leq \rho \leq b$ , the permittivity  $\epsilon_1 = \epsilon_r \epsilon_0$ . In region II, where  $\rho > b$ ,  $\epsilon = \epsilon_0$ .  $E_z(\rho, z)$  continuous at  $\rho = b$  for all  $z$  requires

$$\frac{\partial H_\phi}{\partial \rho} + \frac{1}{\rho} H_\phi \Big|_{b-\Delta} = \epsilon_r \left( \frac{\partial H_\phi}{\partial \rho} + \frac{1}{\rho} H_\phi \right) \Big|_{b+\Delta}.$$

Taking the transform, we obtain

$$\epsilon_r \frac{dh}{d\rho} \Big|_{b+\Delta} - \frac{dh}{d\rho} \Big|_{b-\Delta} + (\epsilon_r - 1) \frac{1}{\rho} h \Big|_{b+\Delta} = 0 \quad (14)$$

by reason of (13).

In order to determine  $H_\phi(\rho, z)$  in region II, we must solve (8) for the corresponding  $h(\rho, \zeta)$ . Inside the dielectric rod, for all  $\rho$  except  $\rho = a$ , (8) becomes

$$\frac{d^2 h}{d\rho^2} + \frac{1}{\rho} \frac{dh}{d\rho} + \left(k_1^2 - \zeta^2 - \frac{1}{\rho^2}\right)h = 0 \quad (15)$$

where  $k_1^2 = \omega^2 \mu_0 \epsilon_1$ . Outside the dielectric rod and for all  $\rho$ , (8) becomes

$$\frac{d^2 h}{d\rho^2} + \frac{1}{\rho} \frac{dh}{d\rho} + \left(k_0^2 - \zeta^2 - \frac{1}{\rho^2}\right)h = 0 \quad (16)$$

where  $k_0^2 = \omega^2 \mu_0 \epsilon_0$ .

We proceed by writing general solutions  $h(\rho, \zeta)$  of (15) for the regions  $0 \leq \rho \leq a$ , and  $a \leq \rho \leq b$ . The discontinuity at  $\rho = a$  appears in the boundary condition (11). A general solution of (16) yields  $h(\rho, \zeta)$  for the region  $\rho \geq b$ . The three solutions possess six arbitrary constants. The constants are determined from the requirements that the field be finite at  $\rho = 0$ , that the field be regular at infinity and that it satisfy the radiation condition, and the four boundary conditions (11), (12), (13), and (14). Choosing the solution  $h(\rho, \zeta)$  for region II, the inverse transform (7) must then be evaluated to yield  $H_\phi(\rho, z)$  for  $\rho \geq b$ .

Eq. (15) is recognized as a form of Bessel's differential equation. It has the general solution

$$h(\rho, \zeta) = AJ_1(\nu_1 \rho) + PY_1(\nu_1 \rho)$$

where  $A$  and  $P$  are arbitrary constants,  $J_1(\nu_1 \rho)$  and  $Y_1(\nu_1 \rho)$  are Bessel functions of the first and second kind, respectively, and

$$\nu_1^2 = k_1^2 - \zeta^2.$$

Consider the region  $0 \leq \rho \leq a$ . Since  $H_\phi(\rho, z)$  and, therefore,  $h(\rho, \zeta)$  must be finite at  $\rho = 0$ , we determine that  $P = 0$ , since  $Y_1(\nu_1 \rho)$  is unbounded as  $\rho \rightarrow 0$ . Hence,

$$h(\rho, \zeta) = AJ_1(\nu_1 \rho) \quad (17)$$

where

$$\nu_1 = \sqrt{k_1^2 - \zeta^2}$$

$$0 \leq \rho \leq a.$$

For the region  $a \leq \rho \leq b$ , the  $Y_1$  function must be included, and we have

$$h(\rho, \zeta) = BJ_1(\nu_1 \rho) + CY_1(\nu_1 \rho). \quad (18)$$

A general solution of (16) is written in terms of Hankel functions of the first and second kind

$$h(\rho, \zeta) = DH_1^{(1)}(\nu_0 \rho) + QH_1^{(2)}(\nu_0 \rho)$$

where

$$\nu_0 = \sqrt{k_0^2 - \zeta^2}.$$

It will be seen later that, in general,  $\nu_0$  is complex; therefore we define the argument of  $\nu_0$  to be  $0 \leq \arg \nu_0 \leq \pi$ . As

$\rho \rightarrow \infty$ ,  $H_1^{(1)}(\nu_0 \rho)$  vanishes and  $H_1^{(2)}(\nu_0 \rho)$  is unbounded for the defined argument of  $\nu_0$ ; therefore,  $Q = 0$  and we obtain

$$h(\rho, \zeta) = DH_1^{(1)}(\nu_0 \rho) \quad (19)$$

where

$$\nu_0 = \sqrt{k_0^2 - \zeta^2}; \quad \begin{matrix} 0 \leq \arg \nu_0 \leq \pi \\ \rho \geq b \end{matrix}.$$

In order to solve for the arbitrary constants  $A$ ,  $B$ ,  $C$ , and  $D$ , we apply the boundary conditions (11), (12), (13), and (14) to the appropriate solutions (17), (18), and (19). Omitting the details, the following four equations are obtained:

$$-(\nu_1 b)AJ_1'(\nu_1 a) + (\nu_1 b)BJ_1'(\nu_1 a) + (\nu_1 b)CY_1'(\nu_1 a) = -i\omega\epsilon_1 b$$

$$AJ_1(\nu_1 a) - BJ_1(\nu_1 a) - CY_1(\nu_1 a) = 0$$

$$BJ_1(\nu_1 b) + CY_1(\nu_1 b) - DH_1^{(1)}(\nu_0 b) = 0$$

$$(\nu_1 b)BJ_1'(\nu_1 b) + (\nu_1 b)CY_1'(\nu_1 b)$$

$$- D[\epsilon_r(\nu_0 b)H_1^{(1)}(\nu_0 b) + (\epsilon_r - 1)H_1^{(1)}(\nu_0 b)] = 0. \quad (20)$$

This system of equations was solved by finding the inverse of the coefficient matrix. The constant  $D$  was determined to be

$$D = i\omega\epsilon_1 a \frac{J_1(\nu_1 a)}{(\nu_1 b)J_0(\nu_1 b)H_1^{(1)}(\nu_0 b) - \epsilon_r(\nu_0 b)J_1(\nu_1 b)H_0^{(1)}(\nu_0 b)}. \quad (21)$$

Substituting (21) into (19) we obtain  $h(\rho, \zeta)$  for the region  $\rho \geq b$ . The solution  $h(\rho, \zeta)$  is then substituted into the inverse transform (7) to yield the integral expression for  $H_\phi(\rho, z)$  in region II. This result is

$$H_\phi(\rho, z) = \frac{i\omega\epsilon_1 a}{2\pi} \int_{-\infty}^{+\infty} \frac{J_1(\nu_1 a)H_1^{(1)}(\nu_0 \rho)e^{i\zeta z}d\zeta}{(\nu_1 b)J_0(\nu_1 b)H_1^{(1)}(\nu_0 b) - \epsilon_r(\nu_0 b)J_1(\nu_1 b)H_0^{(1)}(\nu_0 b)} \quad (22)$$

where

$$\nu_1 = \sqrt{k_1^2 - \zeta^2}; \quad \nu_0 = \sqrt{k_0^2 - \zeta^2}$$

and

$$\rho \geq b.$$

#### SINGULARITIES OF THE INTEGRAND—SOLUTION OF THE MODE EQUATION

We wish to evaluate the real infinite integral (22). This is accomplished by considering it as a contour integral in the complex  $\zeta$  plane and applying Cauchy's residue theorem. The path of closure in the complex plane is selected to ensure convergence of the integral. Evaluation of the contour integral is treated in the following section. For the present we shall consider  $\zeta$  complex and determine the singularities of the integrand of (22).



### Branch Points

Consider the variable  $\nu_1$  which appears in the arguments of  $J_0$  and  $J_1$  in (22). Since  $\nu_1 = \sqrt{k_1^2 - \zeta^2}$ , then  $\nu_1$  is multiple-valued in any neighborhood of  $\zeta = \pm k_1$ . However, if one considers the power series expansions of  $J_0$  and  $J_1$ , one sees that the integrand is an even function of  $\nu_1$  so that the points  $\zeta = \pm k_1$  are not actually branch points. The Hankel function arguments contain the variable  $\nu_0 = \sqrt{k_0^2 - \zeta^2}$ . The Hankel function has a logarithmic singularity at  $\nu_0 = 0$ , and so is multiple-valued in any neighborhood of  $\zeta = \pm k_0$ . The points  $\pm k_0$  are, therefore, branch points of the integrand. We select branch cuts in the  $\zeta$  plane as shown in Fig. 2. We note that  $k^2 = \omega^2 \mu \epsilon$  is real. Thus, the points  $\pm k_1$  and the  $\pm k_0$  lie on the real axis with  $|k_1| > |k_0|$  since  $\epsilon_1 > \epsilon_0$ . The branch cuts are defined as  $\zeta = \pm k_0 + i \operatorname{Im} \zeta$ .

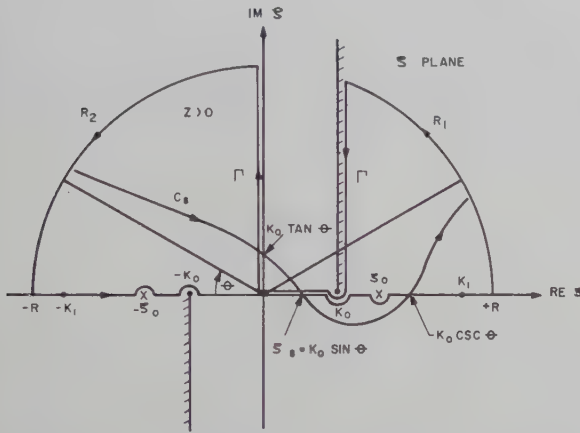


Fig. 2—Contour of integration in the  $\zeta$  plane.

### Poles

Before we investigate the integrand of (22) for poles, we shall discuss the significance of a pole in the physical problem. Assume that the point  $\zeta = \zeta_0$  is a pole of the integrand. When (22) is evaluated as a contour integral, a residue contribution at  $\zeta_0$  must be included. Thus,  $H_\phi(\rho, z)$  will have a term of the form

$$A H_1^{(1)}(\nu_0 \rho) e^{i \zeta_0 z}. \quad (23)$$

Since we assumed a lossless dielectric rod by taking  $k_1^2 = \omega^2 \mu_0 \epsilon_1$  real, we will expect (23) to represent a wave propagating without attenuation, which implies that  $\zeta_0$  is real. If  $\zeta_0$  is real and  $|\zeta_0| > |k_0|$ , then  $\nu_0$  is pure imaginary and  $H_1^{(1)}(\nu_0 \rho)$  reduces to the  $K_1$  Bessel function which decays exponentially with increasing argument. Under these conditions, (23) represents a surface wave of amplitude  $A$ , whose field distribution outside the dielectric rod is an exponential decay. The wave propagates in the positive  $z$  direction according to  $e^{-i(\omega t - \zeta_0 z)}$ . The poles of the integrand are those values of  $\zeta$  which cause the denominator of (22) to vanish. Equating the denominator of (22) to zero yields

$$(\nu_1 b) \frac{J_0(\nu_1 b)}{J_1(\nu_1 b)} = \epsilon_r (\nu_0 b) \frac{H_0^{(1)}(\nu_0 b)}{H_1^{(1)}(\nu_0 b)}. \quad (24)$$

For convenience of notation, let  $X_1 = \nu_1 b$  and  $X_0 = \nu_0 b$ ; then (24) may be written

$$X_1 \frac{J_0(X_1)}{J_1(X_1)} = \epsilon_r X_0 \frac{H_0^{(1)}(X_0)}{H_1^{(1)}(X_0)}. \quad (25)$$

It can be shown that the only values of real  $\zeta$  for which (25) can be satisfied are for  $\zeta$  in the range  $|k_0| < |\zeta| < |k_1|$ .<sup>10</sup> Recalling that  $\nu_1 = \sqrt{k_1^2 - \zeta^2}$  and  $\nu_0 = \sqrt{k_0^2 - \zeta^2}$ , where  $k_1^2 > k_0^2 > 0$ , consider  $\zeta$  real and  $|k_0| < |\zeta| < |k_1|$ . Then  $\nu_1$  is real and  $\nu_0$  is pure imaginary. It follows that  $X_1$  is real and  $X_0$  is pure imaginary. Let  $X_0 = i\xi$ , where  $\xi$  is positive real. Eq. (25) becomes

$$-X_1 \frac{J_0(X_1)}{J_1(X_1)} = \epsilon_r (-i\xi) \frac{H_0^{(1)}(i\xi)}{H_1^{(1)}(i\xi)} = \epsilon_r \xi \frac{K_0(\xi)}{K_1(\xi)} \quad (26)$$

where the  $K_n$  functions are modified Bessel functions of the second kind.

A graph of the functions  $-X_1[J_0(X_1)/J_1(X_1)]$  and  $\epsilon_r \xi[K_0(\xi)/K_1(\xi)]$  is presented in Fig. 3. The function  $-X_1[J_0(X_1)/J_1(X_1)]$  is discontinuous each time  $J_1(X_1)$  vanishes and so an infinity of branches occur for ever increasing  $X_1$ . It passes through zero each time  $J_0(X_1)$

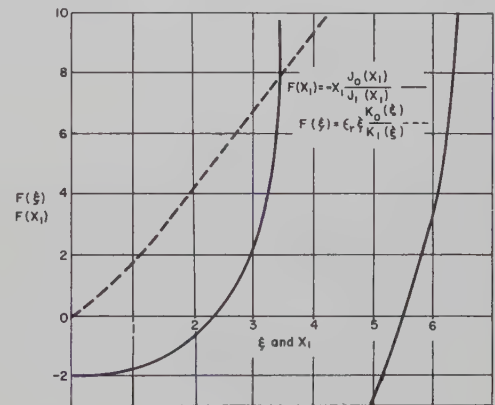


Fig. 3—Graph of the functions  $F(X_1)$  and  $F(\xi)$ . The transcendental mode equation is  $F(X_1) = F(\xi)$ .

has a zero. The function  $\epsilon_r \xi[K_0(\xi)/K_1(\xi)]$  approaches zero as  $\xi \rightarrow 0$  and increases positively for increasing  $\xi$ . It is evident in Fig. 3 that for every finite  $\xi$ , an infinity of values  $X_1$  exist which satisfy (26). In order to obtain a finite number of unique solutions of the mode equation, a second relation between  $X_1$  and  $\xi$  is needed. It follows from the definitions that

$$\begin{aligned} \nu_1^2 &= k_1^2 - \zeta^2 \\ \nu_0^2 &= k_0^2 - \zeta^2 \end{aligned}$$

where  $\zeta$  is identically the same in  $\nu_1$  and  $\nu_0$ . Elimination of  $\zeta^2$  yields

$$\nu_1^2 - \nu_0^2 = k_1^2 - k_0^2 = \left(\frac{2\pi}{\lambda_0}\right)^2 (\epsilon_r - 1)$$

<sup>10</sup> J. W. Duncan, "The Efficiency of Excitation of a Surface Wave on a Dielectric Cylinder," Antenna Lab., Elec. Eng. Res. Lab., Eng. Exper. Station, University of Illinois, Urbana, Ill., Tech. Rep. No. 32, pp. 20-22; May, 1958.

where  $\lambda_0$  is the free space wavelength corresponding to the source frequency. Multiplying by  $b^2$  yields

$$(\nu_0 b)^2 - (\nu_0 b)^2 = X_1^2 - X_0^2 = \left(\frac{2\pi b}{\lambda_0}\right)^2 (\epsilon_r - 1).$$

Since  $X_0 = i\xi$ , we obtain the second relation between  $X_1$  and  $\xi$ , which is

$$X_1^2 + \xi^2 = R^2 \quad (27)$$

where

$$R = \left(\frac{2\pi b}{\lambda_0}\right) \sqrt{\epsilon_r - 1} = k_0 b \sqrt{\epsilon_r - 1}.$$

The graphical solution of (26) is illustrated in Fig. 4, which includes curves of  $X_1$  as a function of  $\xi$  obtained from Fig. 3, and the relation (27). Note that (27) is the equation of a circle of radius  $R$  with center at the origin. The multiple solutions  $X_1$  for every  $\xi$  as discussed with Fig. 3 are evident in Fig. 4. The first branch of  $X_1$  starts at  $X_1 = 2.405$  for  $\xi = 0$  and approaches  $X_1 = 3.83$  asymptotically with increasing  $\xi$ .  $X_1 = 2.405$  is the first zero of  $J_0(X_1)$  and  $X_1 = 3.83$  is the first zero of  $J_1(X_1)$ . The second branch commences at 5.52 and approaches 7.02, which corresponds to the second zeros of  $J_0(X_1)$  and  $J_1(X_1)$ , respectively. An infinity of branches is thus established.

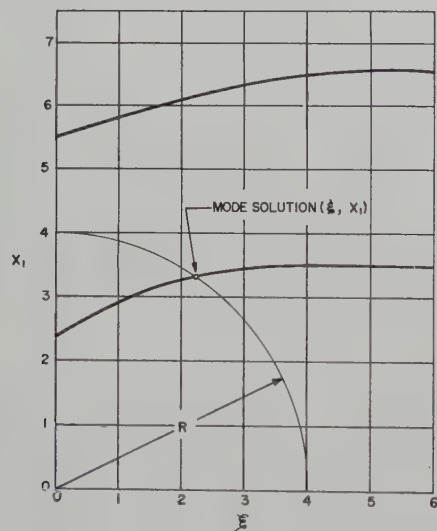


Fig. 4—Solution of the mode equation:  $X_1$  as a function of  $\xi$  which satisfies  $F(X_1) = F(\xi)$ , and the relation  $X_1^2 + \xi^2 = R^2$ .

Consider the case  $R < 2.405$ . Since  $X_1 = \sqrt{R^2 - \xi^2} < R$ , Fig. 3 shows that (26) cannot be satisfied for  $X_1 < 2.405$ , that is, no solution of the mode equation exists for  $R < 2.405$ . This is also evident in Fig. 4. Physically, this means that the dielectric rod waveguide is below cutoff and cannot propagate a surface wave of the transverse magnetic type.

Referring to Fig. 4, if  $2.405 < R < 5.52$ , a single, unique solution  $(\xi, X_1)$  of (26) and (27) results. Thus, (22) has poles at  $\zeta = \pm \zeta_0$ , where  $\zeta_0$  may be determined from the

solution  $(\xi, X_1)$ . The poles occur on the real axis in the region  $|k_0| < |\zeta| < |k_1|$ . We see that when  $R$  is restricted to the range  $2.405 < R < 5.52$ , the dielectric rod propagates a single surface wave which is the lowest order, circularly symmetric, transverse magnetic mode. It is known as the  $E_{01}$  mode and propagates as  $e^{i\zeta_0 z}$  for  $z > 0$  and  $e^{-i\zeta_0 z}$  for  $z < 0$ .

#### Solution of the Mode Equation

Specific solutions of (26) and (27) are required in order to calculate the power in the surface wave and excitation efficiency. A value of 2.56 was chosen for  $\epsilon_r$ , the relative dielectric constant of the rod.  $R$  was restricted to the range  $2.405 < R < 5.52$ . Eqs. (26) and (27) were solved by numerical methods on the University of Illinois digital computer.<sup>11</sup> Six solutions  $(\xi, X_1)$  were obtained for selected values of  $k_0 b$  equal to 2.2, 2.6, 3.0, 3.4, 3.8, and 4.2.

Table I presents  $\xi$ ,  $X_1$ , and the ratio  $\lambda_g/\lambda_0$  corresponding to each value of  $k_0 b$ .  $\lambda_g$  is the guide wavelength of the surface wave mode. The ratio  $\lambda_g/\lambda_0$  follows from the definition of  $\nu_0$ .

$$\frac{\lambda_g}{\lambda_0} = \frac{1}{\sqrt{1 + \left(\frac{\xi}{k_0 b}\right)^2}} \quad (28)$$

TABLE I

$k_0 b$	$\xi$	$X_1$	$\lambda_g/\lambda_0$
2.2	0.5603	2.6901	0.9691
2.6	1.2329	3.0043	0.9036
3.0	1.9353	3.2086	0.8403
3.4	2.6269	3.3366	0.7913
3.8	3.2905	3.4204	0.7560
4.2	3.9264	3.4788	0.7305

#### EVALUATION OF THE CONTOUR INTEGRAL

We evaluate the integral solution (22) by considering it as a contour integral in the complex  $\zeta$  plane. For convenience we write (22) in the form

$$H_\phi(\rho, z) = \int_{-\infty}^{+\infty} U(\zeta) d\zeta \quad (29)$$

where

$$U(\zeta) = \frac{i\omega\epsilon_1 a}{2\pi}$$

$$\frac{J_1(\nu_1 a) H_1^{(1)}(\nu_0 \rho) e^{i\zeta z}}{(\nu_1 b) J_0(\nu_1 b) H_1^{(1)}(\nu_0 b) - \epsilon_r (\nu_0 b) J_1(\nu_1 b) H_0^{(1)}(\nu_0 b)}$$

$$\nu_1 = \sqrt{k_1^2 - \zeta^2}$$

$$\nu_0 = \sqrt{k_0^2 - \zeta^2}.$$

To obtain (29) we select the closed contour shown in Fig. 2, which consists of the real axis from  $-R$  to  $+R$ , the circular arc  $R_1$  of radius  $R$ , the path  $\Gamma$  along the

<sup>11</sup> J. W. Duncan, *op. cit.*, pp. 83-105.



branch cut and imaginary axis, and the arc  $R_2$ . Applying Cauchy's residue theorem, we write

$$\int_{-R}^{+R} U(\zeta) d\zeta + \int_{R_1} + \int_{\Gamma} + \int_{R_2} = 2\pi i \text{ Residue } U(\zeta) \Big|_{\zeta_0}. \quad (30)$$

In the limit as  $R \rightarrow \infty$ , the integrand  $U(\zeta)$  vanishes along  $R_1$  and  $R_2$  so that (30) becomes

$$H_\phi(\rho, z) = \int_{-\infty}^{+\infty} U(\zeta) d\zeta = 2\pi i \text{ Residue } U(\zeta) \Big|_{\zeta_0} - \int_{\Gamma} U(\zeta) d\zeta. \quad (31)$$

The residue term of (31) is the surface wave field while the integration along  $\Gamma$  yields the radiation field. Evaluation of the line integral along  $\Gamma$  is extremely difficult. It is sufficient for our purposes to obtain an approximation to the far zone radiation field. Under these conditions the coordinates  $\rho$  and  $z$  in  $U(\zeta)$  are relatively large and the integral is of the type which may be evaluated

$$H_\phi(\rho, z) = \frac{i\omega\epsilon_1 a}{2\pi b} \int_{C_s} \frac{J_1(k_0 a w) H_1^{(1)}(k_0 \rho \cos \tau) e^{ik_0 z \sin \tau} \cos \tau d\tau}{w J_0(k_0 b w) H_1^{(1)}(k_0 b \cos \tau) - \epsilon_r \cos \tau J_1(k_0 b w) H_0^{(1)}(k_0 b \cos \tau)}. \quad (36)$$

by the saddle point method of integration.<sup>12</sup> Instead of integrating along the path  $\Gamma$  we deform  $\Gamma$  into the path of steepest descent  $C_s$  which passes through the saddle point of the integrand. The path  $C_s$ , which is directed in the reverse sense to  $\Gamma$ , is shown in Fig. 2. Thus, (31) may be replaced by

$$H_\phi(\rho, z) = 2\pi i \text{ Residue } U(\zeta) \Big|_{\zeta_0} + \int_{C_s} U(\zeta) d\zeta \quad (32)$$

$$H_\phi(r, \theta) = \frac{i\omega\epsilon_1 a}{2\pi b} e^{-i(3\pi/4)} \int_{C_s} F(\tau) \left[ \frac{2 \cos \tau}{\pi k_0 r \cos \theta} \right]^{1/2} e^{ik_0 r \cos(\tau-\theta)} d\tau \quad (37)$$

where

$$F(\tau) = \frac{J_1(k_0 a w)}{w J_0(k_0 b w) H_1^{(1)}(k_0 b \cos \tau) - \epsilon_r \cos \tau J_1(k_0 b w) H_0^{(1)}(k_0 b \cos \tau)}.$$

which is the desired form of the solution  $H_\phi(\rho, z)$  in region II.

### The Radiation Field

We shall now evaluate the integral  $\int_{C_s} U(\zeta) d\zeta$  by means of the saddle point method of integration. In applying this method it is convenient to introduce the transformation of variable

$$\zeta = k_0 \sin \tau \quad (33)$$

where

$$\tau = \psi + i\eta.$$

Now  $\tau = \sin^{-1}(\zeta/k_0)$  is a multiple-valued function of  $\zeta$  and the region of integration in the  $\zeta$  plane transforms into a strip in the  $\tau$  plane which is bound by two curved lines corresponding to the branch cuts in the  $\zeta$  plane. They are defined by

$$\sin \psi \cosh \eta = \pm 1. \quad (34)$$

The path of integration along the real axis in the  $\zeta$  plane transforms to the path  $C_1$  in the  $\tau$  plane as shown in Fig. 5. The branch points  $\zeta = \pm k_0$  transform to the points  $\tau = \pm \pi/2$  while the images of the poles  $\pm \zeta_0$  are the points  $\tau_0 = \pi/2 - i \cosh^{-1}(\zeta_0/k_0)$  and  $\tau_0 = -\pi/2 + i \cosh^{-1}(\zeta_0/k_0)$ . The transformation (33) yields

$$\begin{aligned} \nu_0 &= +k_0 \cos \tau \\ \nu_1 &= +k_0 \sqrt{\epsilon_r - \sin^2 \tau} = k_0 w \end{aligned} \quad (35)$$

where for convenience we let  $w$ , a function of  $\tau$ , represent the radical  $\sqrt{\epsilon_r - \sin^2 \tau}$ . Substituting (33) and (35) into the integral  $\int_{C_s} U(\zeta) d\zeta$ , one obtains

If  $\rho$  is large and  $k_0 \rho \cos \tau \neq 0$ , the Hankel function in the numerator of (36) may be replaced by its asymptotic representation. Furthermore, it is convenient to introduce the spherical coordinate system shown in Fig. 6, where the polar angle  $\theta$  is measured from the plane  $z=0$ . In this coordinate system we note that  $\rho = r \cos \theta$  and  $z = r \sin \theta$ . Substituting for  $\rho$  and  $z$  in (36) and replacing the Hankel function by its asymptotic formula yields

Integral (37) is valid for  $r$  large and  $k_0 r \cos \theta \neq 0$ . It is readily evaluated by the saddle point method. The saddle point is defined by the equation

$$\frac{d}{d\tau} \cos(\tau - \theta) = 0 \quad (38)$$

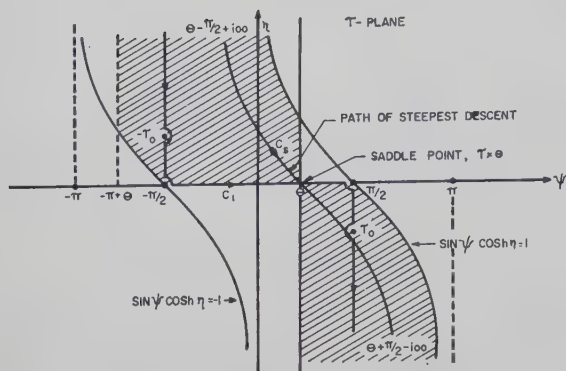
which yields

$$\tau = \theta. \quad (39)$$

Note that the saddle point corresponds to the polar angle  $\theta$ . In the  $\zeta$  plane the saddle point is

$$\zeta_s = k_0 \sin \theta. \quad (40)$$

<sup>12</sup> E. T. Copson, "Theory of Functions of a Complex Variable," Oxford University Press, London, Eng., pp. 330-331; 1955.

Fig. 5—Path of integration in the  $\tau$  plane.

The path of steepest descent  $C_s$  in the  $\tau$  plane is defined by the equation

$$\sin(\psi + \pi/2 - \theta) \cosh \eta = 1. \quad (41)$$

Fig. 6—Cylindrical coordinate system  $(\rho, \phi, z)$  and spherical coordinate system  $(r, \theta, \phi)$ .

Carrying out the evaluation of (44), one obtains

$$H_\phi^{II}(\rho, z) = A_{II} K_1(\xi \rho / b) e^{i \xi_0 z} \quad (45)$$

where

$$A_{II} = \frac{\omega \epsilon_1 \left( \frac{a}{b} \right) J_1 \left( \frac{k_0 a}{k_0 b} X_1 \right)}{\xi_0 b \left\{ \frac{2(R/\xi)^2}{X_1} J_0(X_1) K_1(\xi) + \left[ \epsilon_r \left( \frac{\xi}{X_1} \right) + \left( \frac{X_1}{\xi} \right) \right] J_0(X_1) K_0(\xi) + (\epsilon_r - 1) J_1(X_1) K_1(\xi) \right\}}$$

$$\xi_0 b = \sqrt{(k_0 b)^2 + \xi^2}$$

$$R^2 = X_1^2 + \xi^2.$$

The shaded area of Fig. 5 is the region of convergence of the integral (37) as  $\eta$  approaches  $\pm \infty$  on  $C_s$ .

Carrying out the evaluation of (37), one obtains

$$H_\phi(r, \theta) = -i \sqrt{\frac{\epsilon_0}{\mu_0}} \left( \frac{\epsilon_r a}{\pi b} \right) F(\theta) \frac{e^{i k_0 r}}{r} \quad (42)$$

where

$$F(\theta) = \frac{J_1(k_0 a w)}{w J_0(k_0 b w) H_1^{(1)}(k_0 b \cos \theta) - \epsilon_r \cos \theta J_1(k_0 b w) H_0^{(1)}(k_0 b \cos \theta)}.$$

It follows from Maxwell's equations that

$$E_\theta(r, \theta) = -i \left( \frac{\epsilon_r a}{\pi b} \right) F(\theta) \frac{e^{i k_0 r}}{r}. \quad (43)$$

#### The Surface Wave Field

Let  $H_\phi^{II}(\rho, z)$  represent the surface wave field in region II. It is given by

$$H_\phi^{II}(\rho, z) = 2\pi i \text{Residue } U(\xi) \Big|_{\xi_0} \quad (44)$$

where

$$\rho \geq b, \quad z > 0.$$

The pole  $\xi_0$  is a simple pole since the denominator of  $U(\xi)$  vanishes at  $\xi_0$  but its first derivative does not.

The other surface wave components in Regions I and II follow from Maxwell's equations. They are

$$E_\rho^{II}(\rho, z) = \left( \frac{\xi_0}{\omega \epsilon_0} \right) H_\phi^{II}(\rho, z)$$

$$H_\phi^I(\rho, z) = A_{II} \frac{K_1(\xi)}{J_1(X_1)} J_1(X_1 \rho / b) e^{i \xi_0 z}.$$

$$E_\rho^I(\rho, z) = \left( \frac{\xi_0}{\omega \epsilon_1} \right) H_\phi^I(\rho, z). \quad (46)$$

#### THE POWER INTEGRALS AND EXCITATION EFFICIENCY

The radiated power  $W^R$  is obtained by integrating the average Poynting vector over the surface of a large sphere of radius  $r$ . The radiation field, which has components  $E_\theta$  and  $H_\phi$ , is independent of  $\phi$  and is symmetrical about the plane  $\theta = 0$ . The integral for the radiated power is

$$W^R = \sqrt{\frac{\epsilon_0}{\mu_0}} \left( \frac{\epsilon_r a}{b} \right)^2 \frac{1}{\pi/2} \int_0^{\pi/2} \cos \theta |F(\theta)|^2 d\theta \quad (47)$$

where  $F(\theta)$  is defined in (42).

A discussion of the integrand of (47) is worthwhile at this point. We note that the magnitude of the radiation



field is proportional to  $|F(\theta)|$ . As  $\theta$  approaches  $\pi/2$ ,  $F(\theta)$  vanishes so the radiation pattern has a null along the axis of the dielectric rod. The influence of the source dimension ( $k_0a$ ) on the radiation field and  $W^R$  is contained in the function  $J_1(k_0aw)$  which is the numerator of  $F(\theta)$ . The dielectric rod parameter ( $k_0b$ ) appears only in the denominator. In order to obtain maximum excitation efficiency for any  $k_0b$ ,  $W^R$  should be a minimum.  $W^R$  will be a minimum if  $J_1(k_0aw)$  vanishes or is quite small as  $\theta$  ranges from zero to  $\pi/2$ ; this occurs when  $J_1(k_0aw)$  passes through a zero. Consider the function  $w = \sqrt{\epsilon_r - \sin^2 \theta}$  with  $\epsilon_r = 2.56$ . As  $\theta$  takes on values  $0 \leq \theta \leq \pi/2$ ,  $w$  has the range  $1.25 \leq w \leq 1.6$ . Assume an average value for  $w$ ,  $w_{av} = 1.42$ . We should expect the most efficient source to have the approximate dimension  $k_0a = 3.83/w_{av} = 2.7$ , where 3.83 is the first zero of the  $J_1$  function. This analysis is verified in the efficiency curves presented in the latter part of this section.

The integral (47) was evaluated numerically on the University of Illinois digital computer.  $W^R$  was computed as  $k_0a$  varied in discrete increments of 0.2 over the range  $0 < k_0a \leq k_0b$  for a particular value of  $k_0b$ . The results of these computations appear in the efficiency curves.

The surface wave power  $W^S$  is obtained by integrating the average Poynting vector over the surface of an infinite transverse plane normal to the  $z$  axis. Since the surface field components  $E_\rho$  and  $H_\phi$  are different for regions I and II, separate integrations are necessary for the regions  $0 \leq \rho \leq b$  and  $\rho \geq b$ . The resulting expression for the total surface wave power is

$$W^S = \sqrt{\frac{\epsilon_0}{\mu_0}} \left( \frac{\epsilon_r a}{b} \right)^2 N^S \quad (48)$$

where

$$N^S = \pi \frac{\lambda_g}{\lambda_0} \frac{\left\{ \frac{1}{\epsilon_r} \left[ \frac{K_1(\xi)}{J_1(X_1)} \right]^2 \left[ J_0^2(X_1) + J_1^2(X_1) - \frac{2}{X_1} J_0(X_1) J_1(X_1) \right] + \left[ K_0^2(\xi) - K_1^2(\xi) + \frac{2}{\xi} K_0(\xi) K_1(\xi) \right] \right\}}{\left\{ 2 \left[ \frac{\left( \frac{X_1}{\xi} \right)^2 + 1}{X_1} \right] J_0(X_1) K_1(\xi) + \left[ \epsilon_r \left( \frac{\xi}{X_1} \right) + \left( \frac{X_1}{\xi} \right) \right] J_0(X_1) K_0(\xi) + (\epsilon_r - 1) J_1(X_1) K_1(\xi) \right\}^2} J_1^2 \left( \frac{k_0 a}{k_0 b} X_1 \right).$$

Inspection of  $N^S$  shows that the source dimension ( $k_0a$ ) appears only in the argument of  $J_1^2[(k_0a/k_0b)X_1]$ . The remaining portion, which is rather formidable, is a function of  $\epsilon_r$  and the mode solution  $(\xi, X_1)$ . It has a constant value for any  $\epsilon_r$  and  $k_0b$ .  $N^S$  is a function of the source only by the term  $J_1^2[(k_0a/k_0b)X_1]$ . It should be noted, however, that  $a/b$  appears in the constant which multiplies  $N^S$  to give  $W^S$ . Selecting a value of  $k_0b$  with  $\epsilon_r = 2.56$ ,  $W^S$  was calculated according to (48) as a function of  $k_0a$  using values of  $\lambda_g/\lambda_0$ ,  $\xi$ , and  $X_1$  from Table I.

### Excitation Efficiency

The efficiency with which the source delivers power to the surface wave is called the excitation efficiency of the source. Denoting efficiency by the symbol  $\Upsilon$ , it is defined as

$$\Upsilon = \frac{W^S}{W^T} \quad (49)$$

where  $W^S$  is the surface wave power.

$W^T$  is the total power delivered by the source.

Goubau<sup>13</sup> has proved that, for lossless surface waveguides, the radiation and surface wave fields are orthogonal with regard to power considerations. In this case, the total energy delivered by the source is equal to the sum of the surface wave power and the radiated power. Since we are considering a lossless dielectric rod, the orthogonality condition holds and  $\Upsilon$  is given by

$$\Upsilon = \frac{W^S}{W^S + W^R} \quad (50)$$

where  $W^S$  is the surface wave power and  $W^R$  is the radiated power.

Efficiency was calculated according to (50) using computed values of  $W^S$  and  $W^R$ . Figs. 7 and 8 present curves of efficiency as a function of  $k_0a$  for the selected values of  $k_0b$ . Efficiencies greater than 90 per cent are predicted for  $k_0a$  approximately equal to 2.6.

### EXPERIMENTAL INVESTIGATION

The magnetic current ring was purposely chosen for the theoretical problem because it is a source which has a simple physical realization. Consider Fig. 1. By symmetry the magnetic current filament generates a field which has no electric component in the plane  $z=0$ . In the plane of the source the only non-zero component of  $\vec{E}$  is  $E_z$ , which is normal to the plane. Since tangential  $\vec{E}$  vanishes over the plane, an infinitely large metal sheet may be placed at the source position without disturbing the field. One may simulate the source by a very narrow annular slot in a large conducting sheet or ground plane.

Then, of course, the dielectric rod extends from the ground plane in only one direction. The annular slot may be illuminated using a circular or coaxial waveguide exciter. If the rod is terminated in a resistance card load which produces negligible reflection of the surface wave, then the finite rod excited by an annular slot in a ground plane simulates in a half space the theoretical problem of Fig. 1.

In order for the slot to be a good approximation of the filament, the slot width must be small compared to the wavelength and the electric field in the slot must be radial and uniform about the circumference. It is as-

<sup>13</sup> G. Goubau, "On the excitation of surface waves," PROC. IRE, vol. 40, pp. 865-868; July, 1952.

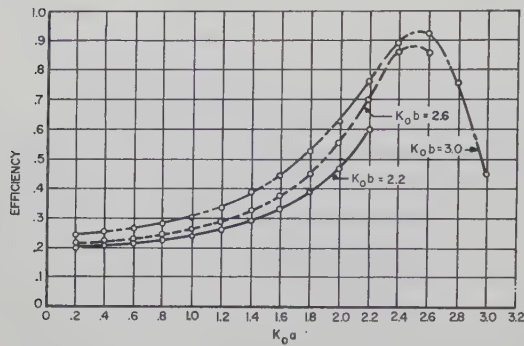


Fig. 7—Excitation efficiency as a function of the source dimension  $k_0 a$ .

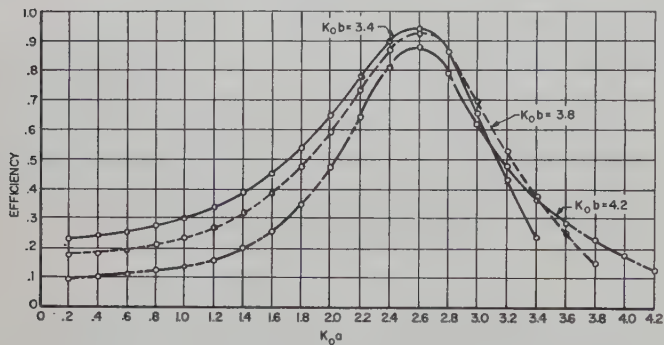


Fig. 8—Excitation efficiency as a function of the source dimension  $k_0 a$ .

sumed that the mean radius of the slot corresponds to the radius of the infinitesimal current filament. The slot may be illuminated from a circular waveguide propagating the  $TM_{01}$  mode, or from a coaxial line excited in the usual TEM mode. The coaxial line is preferable since the center conductor provides a convenient means of supporting the circular disc which is the ground plane within the annular slot.

The efficiency with which the slot excites the surface wave may be measured using Deschamps' method for determining the insertion loss of a waveguide junction.<sup>14,15</sup> The transition from the coaxial line to the dielectric rod waveguide is considered as a two-port waveguide junction. Assuming that the dielectric rod and coaxial line are lossless, then the dissipative attenuation of the junction results entirely from the power radiated into space by the slot. If all of the power delivered to the slot is converted to the surface wave, then no power is lost as stray radiation and the junction is 100 per cent efficient. This method has been used previously to measure the launching efficiency of sources placed on a dielectric image line.<sup>16</sup>

<sup>14</sup> G. A. Deschamps, "Determination of reflection coefficients and insertion loss of a waveguide junction," *J. Appl. Phys.*, vol. 24, pp. 1046-1050; August, 1953.

<sup>15</sup> H. F. Mathis, "Experimental procedures for determining the efficiency of four-terminal networks," *J. Appl. Phys.*, vol. 25, pp. 982-986; August, 1954.

<sup>16</sup> R. H. DuHamel and J. W. Duncan, "Launching efficiency of wires and slots for a dielectric rod waveguide," *TRANS. IRE*, vol. MTT-6, pp. 277-284; July, 1958.

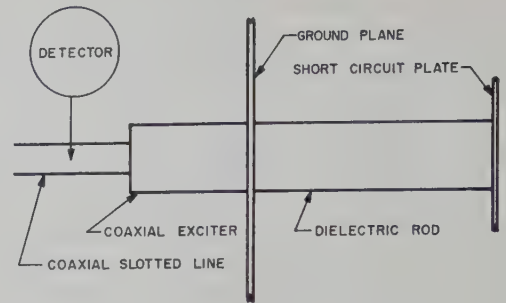


Fig. 9—Representation of the two-port junction.

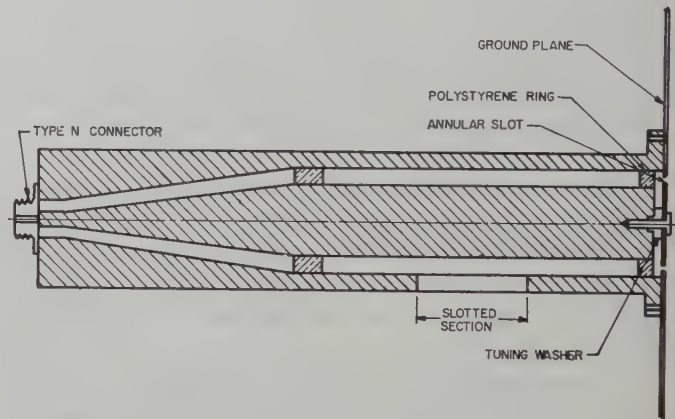


Fig. 10—Cross section of the coaxial exciter.

A schematic representation of the arrangement used to measure the efficiency of the junction is given in Fig. 9. The measurements were performed using a 2-inch diameter polystyrene rod mounted vertically on a 60-inch square ground plane. For most of the measurements the dielectric rod was 40 cm long, although in some instances, the length was increased to 134 cm.

Using Deschamps' method, one obtains the efficiency of the entire transition between the input reference plane and the output reference plane, that is, between the measuring probe and the short circuit termination. Since we are interested in measuring the dissipative attenuation of just the annular slot, it is essential that the rest of the transition shall introduce only negligible attenuation. For the present we shall ignore the dielectric rod loss since it is very small. It follows, then, that a low loss exciter must be constructed to illuminate the annular slot. The annular slot presents a very low conductance and capacitive susceptance to the exciting waveguide. Therefore, the feed waveguide must be a low impedance line with some means of tuning out the capacitive susceptance of the slot at the ground plane position.

Fig. 10 shows a cross sectional view of the low impedance coaxial line which was constructed for this purpose. The inner diameter of the outer wall of the coax was  $1\frac{7}{8}$  inches and the inner conductor diameter was  $1\frac{1}{4}$  inches, which yields a 24-ohm line. A two wavelength tapered section transformed the 24-ohm line to a standard 50 ohm, type N connector. Two polystyrene



rings centered the inner conductor within the cylinder. The ring at the ground plane position was a quarter-wavelength transformer which would match the 24-ohm line to a 9.5-ohm resistance load. A circular tuning disc or washer was placed on the end of the center conductor to provide a series inductive reactance to cancel the capacitive susceptance of the slot. The circular disc which formed the inner boundary of the annular slot was fixed to the tuning washer and the coax center conductor by a special mounting screw. Since the neighborhood of the annular slot and tuning washer is a resonant cavity, all parts were silver-plated to minimize losses.

A family of discs and rings were fabricated to permit varying the annular slot radius from  $\frac{1}{2}$ – $\frac{7}{8}$  inch while maintaining the slot width constant at  $\frac{1}{8}$  inch. The  $\frac{1}{8}$  inch slot width corresponds to  $.067 \lambda_0$  and  $.076 \lambda_0$  at  $k_0 b$  equal to 3.4 and 3.8, respectively. Recalling that the radius of the dielectric rod is 1 inch, it is convenient to express the slot radius in the normalized form  $a/b$ ; then the source dimension  $k_0 a$  for any  $k_0 b$  is given by  $k_0 b(a/b)$ . Six slots were constructed for the measurements. Table II gives the normalized slot radius  $a/b$ , and the corresponding dimension  $k_0 a$  at the two values of  $k_0 b$  which were used for the measurements.

TABLE II

Normalized Slot Radius $a/b$	$k_0 a$ When $k_0 b = 3.4$	$k_0 a$ When $k_0 b = 3.8$
0.50	1.70	1.90
0.625	2.12	2.38
0.687	2.34	2.61
0.75	2.55	2.85
0.812	2.76	3.08
0.875	2.98	3.32

A slot  $\frac{1}{8}$  inch wide and 2 inches long was milled in the side wall of the exciter so that the standing wave ratio in the exciter could be measured. After a particular slot was mounted on the exciter, various tuning washers were tested until one was found which reduced the VSWR in the exciter to less than 2 when the dielectric rod was terminated with a matched load. The image circle was determined from measurements made in a coaxial slotted line which was connected directly to the exciter through a type *N* elbow connector.

When efficiency was measured as shown in Fig. 9, the result obtained was not precisely the excitation efficiency of the annular slot; instead it was the efficiency of the entire transition between the measuring probe and the short circuit termination. Although the losses in the system were small, the measured efficiency was reduced somewhat by the dielectric rod attenuation and by the loss between the measuring probe and the ground plane. The system losses were measured approximately by means of Deschamps' method.<sup>17</sup> The measurements of slot launching efficiency were then corrected to account for the system losses.

<sup>17</sup> Duncan, *op. cit.*, pp. 66–72.

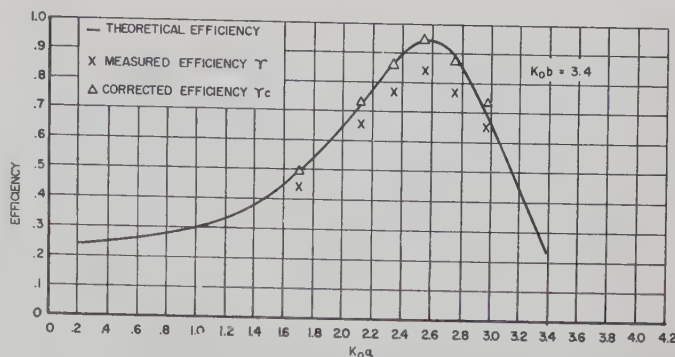


Fig. 11—Comparison of the theoretical and measured excitation efficiency.

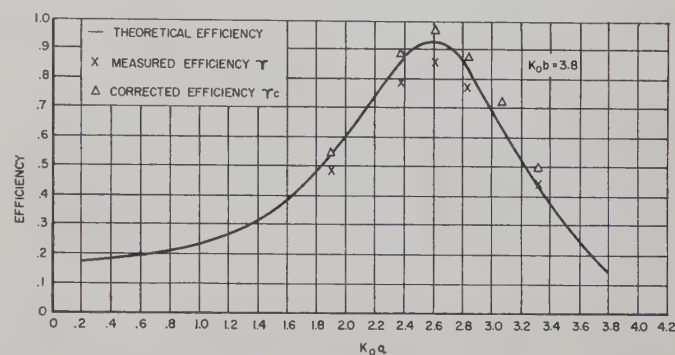


Fig. 12—Comparison of the theoretical and measured excitation efficiency.

Six slots were measured in the laboratory. Measurements were performed at frequencies of 6387 mc and 7138 mc which result in  $k_0 b$  equal to 3.4 and 3.8, respectively. The results are presented in Figs. 11 and 12 for comparison with the theoretical curves of efficiency. The data include the measured efficiency  $T$  and the corrected efficiency  $T_c$  for each source  $k_0 a$ . The very close agreement between the experimental points and the theoretical curve is evident. In all cases the measured efficiency  $T$ , which included the system losses, was within 10 per cent of the efficiency predicted by theory. The experimental measurements verify that an excitation efficiency of approximately 95 per cent may be obtained from an annular slot of dimension  $k_0 a = 2.6$ .

It should be emphasized that a good "matched" transition is necessary in order to realize the high efficiency of the annular slot. In the laboratory the predicted source efficiencies were not measured until the matched transition of the coaxial exciter was constructed. Of course, the efficiency of the annular slot is independent of the feed structure, but substantial coupling of power from the closed waveguide to the surface waveguide is obtained only when a good impedance match is provided at the aperture plane. Otherwise, a very high standing wave ratio exists in the vicinity of the aperture and most of the power delivered by the feed waveguide is reflected.

As a point of practical interest, the efficiency of the annular slot in the presence of a small ground plane was

determined. This effect was investigated by measuring slot efficiencies as the size of the ground plane was reduced. Surprisingly, the ground plane dimension had little effect on the efficiency. At least, this was the case at the two values of  $k_0b$  which were considered. The ground plane was reduced to a 10-inch diameter flange and no appreciable change in efficiency was noted. Consequently, the ground plane was removed so that the launching structure consisted of the dielectric rod mounted on the coaxial exciter. Efficiency was measured at  $k_0b$  equal to 3.4 and 3.8. The results are presented in Table III which includes, for comparison, the efficiency that was measured *with* the large ground plane. Note that these data have not been corrected to account for the system losses.

#### ACKNOWLEDGMENT

The author wishes to thank Prof. V. H. Rumsey who was his adviser at the beginning of the research and Dr. E. C. Jordan who was his adviser at its conclusion. He is indebted to Dr. R. H. DuHamel for several help-

TABLE III

$k_0b$	$k_0a$	Efficiency With Ground Plane	Efficiency No Ground Plane
3.4 ↓	1.70	0.44	0.428
	2.12	0.65	0.647
	2.34	0.76	0.779
	2.55	0.835	0.847
	2.76	0.77	0.829
	2.98	0.65	0.696
3.8 ↓	1.90	0.48	0.545
	2.38	0.775	0.776
	2.61	0.85	0.835
	2.85	0.77	0.776
	3.08	0.63	0.63
	3.32	0.44	0.413

ful suggestions and is particularly grateful to Dr. P. E. Mayes of the University of Illinois Antenna Laboratory for his counsel throughout the entire work.

The help of G. Berryman and K. Rosenberg, who performed most of the experimental measurements and numerical computations, is sincerely appreciated.

## Proposal for a Tunable Millimeter Wave Molecular Oscillator and Amplifier\*

J. R. SINGER†

**Summary**—An atomic beam apparatus suitable for a millimeter wave generator is theoretically discussed. The beam consists of atoms having a net magnetic moment. The upper and lower Zeeman levels of the atomic beam in a magnetic field are spatially separated by an inhomogeneous magnetic field. The upper state atoms enter a cavity where transitions occur at a frequency determined by a static magnetic field. The resonant frequency of the cavity is set at the transition frequency. The positive feedback of the cavity allows operation as an oscillator. Some of the more important parameters for oscillator operation are evaluated. The upper frequency limit is determined primarily by the resonant structure design.

#### INTRODUCTION

THE ammonia gas maser invented by Gordon, Zeiger and Townes<sup>1</sup> shows considerable promise as a frequency standard and as a narrow band amplifier. One limitation is the fixed frequency operation which is determined by the natural transition fre-

quencies of the  $\text{NH}_3$  molecule. An extension of the molecular beam technique which permits operation of a molecular oscillator amplifier in the mm wave region with a power output of the order of the ammonia maser is suggested in this paper.

The present scheme uses a Stern-Gerlach<sup>2</sup> type of molecular beam arrangement for achieving a polarized beam of atoms. The atoms in the lower energy state may be readily removed from the beam since they are spatially separated. The upper state atoms then adiabatically enter a homogeneous magnetic field region where they are subjected to an RF field polarized in the appropriate direction to induce atomic transitions. Induced transitions are always coherent in phase and amplification of RF is achieved if the rate of transitions times the energy from each transition exceeds the RF power input and the system losses. The system may be used as an oscillator since spontaneous emission will induce further transitions by use of a high  $Q$  structure

\* Manuscript received by the PGMTT, September 30, 1958; revised manuscript received, December 8, 1958. This work was supported by the Faculty Res. Com., University of California, and the U. S. Air Force under Contract No. AF 49(638)-102 monitored by the A. F. Office of Sci. Res., Air Res. and Dev. Command.

† Electronics Res. Lab., Univ. California, Berkeley, Calif.

<sup>1</sup> J. P. Gordon, H. J. Zeiger and C. H. Townes, "The maser," *Phys. Rev.*, vol. 99, pp. 1264-1274; August 15, 1955.

<sup>2</sup> W. Gerlach and O. Stern, "Der Experimentelle Nachweis des Magnetischen Moments des Silberatoms," *Zeit. Physik*, vol. 8, pp. 110-112; December, 1921.



giving positive feedback. The method of achieving a polarized atomic beam and the operation of the oscillator is discussed in the following sections. Some suggestions for use as an amplifier are given.

### POLARIZED ATOMIC BEAMS

Atoms in a magnetic field take up only  $2j+1$  orientations following the rules of space quantization. Here  $j$  is the vector sum of the orbital angular momentum ( $l$ ) and the spin ( $s$ ). If atoms in an  $S$  state (monatomic hydrogen, alkali metals, silver, etc., in their ground state) are utilized,  $l$  vanishes and  $s$  equals  $\frac{1}{2}$ . This provides only two orientations for the atoms: parallel and antiparallel to the field. The orientations may be described by an upper energy state (pointing up) and a lower energy state (pointing down). The difference in energy is the Zeeman splitting  $2\mu H$  where  $\mu$  is the magnetic moment of the atom (a Bohr magneton for most cases of interest) and  $H$  is the homogeneous portion of the magnetic field. The time  $t$  taken to achieve the quantized orientations is given by  $t \sim \hbar/2\mu H$  where  $\hbar$  is the Planck constant—this time is determined by the uncertainty principle and is much too short to measure under the usual circumstances.

If the magnetic atoms are subjected to an inhomogeneous magnetic field in the  $x$  direction, a force  $F$  is exerted on the atoms which is given by

$$F = \mu \frac{\partial |H_x|}{\partial x}. \quad (1)$$

Where the force is such that oppositely oriented magnetic moments are pulled in opposite directions as indicated schematically in Fig. 1. The average deflection  $d$  of each orientation depends upon the average time that an atom spends in the inhomogeneous field which may be expressed as

$$d = FL^2/2v^2M \quad (2)$$

where  $L$  is the length of path in the field,  $v$  is the average velocity of the atoms and  $M$  is the atomic mass. The average velocity squared, from kinetic theory is

$$v^2 = 4kT/M \quad (3)$$

where  $k$  is Boltzmann's constant, and  $T$  is the Kelvin temperature. By combining (1), (2), and (3) an expression for the deflection is obtained; that is,

$$d = \mu \frac{\partial |H_x|}{\partial x} L^2/8kT. \quad (4)$$

The separation of the oppositely pointing spins is twice the value of (4). If the beam separation desired is one cm, this can be readily accomplished with an inhomogeneous field of 5000 oersteds/cm, an atomic flight length of 100 cm, and a gas oven temperature of 500°K.

The atoms in the upper energy state will now enter a homogeneous magnetic field (see Fig. 1). The requirement that no transitions be induced in the course of a

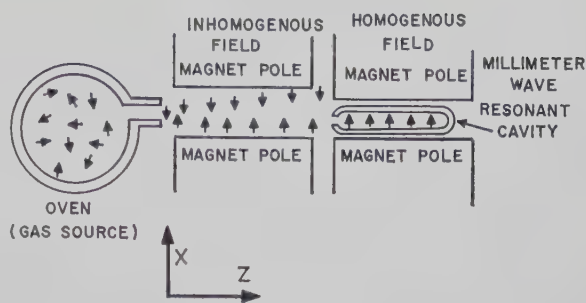


Fig. 1—A schematic of the Stern-Gerlach polarization scheme with oriented magnetic dipoles allowed access to the cavity for oscillation or amplification purposes.

change in field strength is such that the change in static field be at a rate that many precessions occur during the change; that is,

$$\frac{dH}{dt} \ll \gamma H^2 \quad (5)$$

where  $t$  is the time and  $\gamma$  is the gyromagnetic ratio. It is easy to satisfy (5) which implies that changes in energy are adiabatic in the Ehrenfest sense.

### OPERATIONAL CONSIDERATIONS

The portion of the beam entering the cavity is entirely in the upper energy state. The frequency  $\nu$  for transition to the lower state is determined by the magnetic field  $H$ , where

$$\nu = 2\mu H/h \quad (6)$$

and  $h$  is the Planck constant.

There is considerable freedom in choosing the parameter  $H$ , but as shall be described later, the range of operation is held within the bounds of the resonant cavity chosen. Consequently, if a wide tuning range is desired, provision must be made for tuning the cavity. Oscillator parameters which need further discussion are power output, and conditions for oscillation must occur. The important feature of an oscillator is its positive feedback. This feedback, in the case of a maser device, occurs in the following way. A few spontaneous emissions occur. The radiated fields are reflected by a high  $Q$  cavity. The reflected fields act on the rest of the atoms in the cavity causing induced emissions; the radiated field is reflected again and more induced emissions occur, etc. If the oscillation builds up as described, it soon reaches a maximum amplitude determined by the total number of excited atoms in the cavity available for emission. The major limitations to very high-frequency atomic beam oscillators are 1) the available beam intensities, and 2) the size of the cavities which can be constructed with a reasonably large  $Q$ .

### THE ATOMIC BEAM OSCILLATOR

The two possible states of an atom with spin  $\frac{1}{2}$  in a magnetic field may be described by,

$$\psi = a\psi_1 + b\psi_2 \quad (7)$$

where  $\psi_1$  is the lower state and  $\psi_2$  the upper state. If all the atoms enter the cavity in the upper state, then initially  $b$  is unity and  $a$  vanishes. If an RF field is coupled into the cavity and the frequency of this field is equal to the transition frequency given by (6) then the atomic perturbation is

$$-\mu H_1 \cos 2\pi\nu t \quad (8)$$

where  $H_1$  is the maximum RF magnetic field in the cavity depending upon the input RF power and the cavity  $Q$  and  $\nu$  is the RF frequency.

The probability that an atom will have made a transition downward and be found in the lower energy state after a time  $t$  is given by<sup>3</sup>

$$|a|^2 = \frac{(\bar{\mu}H_1/h)^2}{(\bar{\mu}H_1/h)^2 + (\Delta\nu)^2} \sin^2 \left\{ \pi t [(\bar{\mu}H_1/h)^2 + (\Delta\nu)^2]^{1/2} \right\} \quad (9)$$

where  $\Delta\nu$  is the frequency deviation from resonance and  $\bar{\mu}$  is the matrix element of the dipole transition. In the case under consideration here,  $\bar{\mu}^2 = \frac{1}{2}\mu^2$  where  $\mu$  is a Bohr magnetron.  $H_1$  is the RF field in the cavity, and  $t$  is the time spent in the perturbation field. The time  $t$  is the cavity length divided by the average velocity of the atoms.

In order that oscillation shall occur, losses in the resonant cavity must be equaled or exceeded by the power output of atomic transitions. The condition for equality is

$$\frac{1}{Q} = \frac{P}{2\pi\nu W} \quad (10)$$

where  $Q$  is  $2\pi$  times the energy stored in the cavity divided by the energy loss per cycle,  $P$  is the power of atomic emission, and  $W$  is the energy stored in the cavity. The emitted power  $P$  of (10) may be put into the form

$$P = Nh\nu |a|^2 \quad (11)$$

where  $N$  is the number of atoms available in the upper energy state per second.

At resonance  $\Delta\nu$  vanishes, and (9) becomes

$$|a|^2 = \sin^2(\pi\nu_1 t) \quad (12)$$

where  $\nu_1 = \bar{\mu}H_1/h$ . The value of  $\sin^2 \pi\nu_1 t$  is approximately  $(\pi\nu_1 t)^2$  for small values of  $\nu_1 t$ . This will be small as long as the stored energy in the cavity is small which is the physical situation of interest. Combining (8) and (10)–(12) and using our approximation, one obtains,

$$N = \frac{hV}{2(\pi\bar{\mu})^2 Q} \quad (13)$$

where  $\mu$  is the magnetic dipole moment of one Bohr magnetron,  $V$  is the volume of the cavity having the quality factor  $Q$ , and  $t$  is the time of flight of the atoms in the cavity as before.

Although the field in the cavity does not appear explicitly in (13) because of our approximation, the physical situation requires that the waveguide mode be such that the beam "sees" the RF magnetic field polarized in the proper direction for induced transitions. It is assumed that the beam is subjected to the average magnetic field in the cavity.

By using a cylindrical cavity of 12-cm length and 0.76-cm radius in the  $TE_{011}$  mode, one gets a theoretical  $Q$  of 17,800 according to Shimoda, Wang, and Townes.<sup>4</sup> This cavity was used by Townes and his group for the ammonia maser. The openings to admit passage of the beam were 0.4-inch diameter sections which were beyond cutoff for a 12.5-mm wavelength. Shimoda, *et al.*, have pointed out that this cavity is better suited for inducing magnetic transitions than the electric dipole transitions of the ammonia maser.

A beam input area of  $\frac{3}{4}$  cm<sup>2</sup> is provided with this cavity at an operating frequency of 12.5 mm. In order to push towards higher frequencies with the scheme presented here, one would like to improve the  $Q$ . This may be accomplished by cooling the cavity with liquid helium to pick up a factor of two or three in  $Q$ .

Operation at 12.5 mm is relatively easy. Assuming an atom with a low boiling point, such as Rb<sup>87</sup> and a  $Q$  of about 20,000 for the  $TE_{011}$  cavity described above, one requires an  $N$  of about  $10^{17}$  atoms/second/cm<sup>2</sup> in order to satisfy (13) and get continual oscillation. This flux is larger than any commonly used in conventional atomic beam work. A method for obtaining this flux will be discussed in a following section.

The value for  $N$  calculated above may be compared with the value used in the ammonia beam maser oscillator—about  $10^{18}$  molecules per second. The reason for the smaller value in ammonia masers is that the electric dipole moment is two orders of magnitude larger than the magnetic dipole used here. Beam intensities of  $10^{15}$  to  $10^{16}$  molecules/cm<sup>2</sup>/second have been utilized by NH<sub>3</sub> masers.<sup>5</sup> However, in the case of ammonia masers, only a fraction (6 per cent) of the beam is available for transitions at the desired frequency.<sup>5</sup> In the present case the large magnetic fields cause a Paschen-Back decoupling of the nuclear and electron spins, and the hyperfine structure splits the transition frequencies into  $2I+1$  levels. For isotopically pure Rb<sup>37</sup>,  $I=3/2$  and each electron transition is split into four levels. Consequently, about 25 per cent of the beam will have the desired transition frequency.<sup>6</sup>

The useful power output  $P_0$  from the oscillator is given by

$$P_0 = \frac{2\pi\nu W}{Q_c} \quad (14)$$

<sup>4</sup> K. Shimoda, T. C. Wang and C. H. Townes, "Further aspects of the theory of the maser," *Phys. Rev.*, vol. 192, pp. 1308–1321; June 1, 1956.

<sup>5</sup> J. C. Helmer, "Maser oscillations," *J. Appl. Phys.*, vol. 28, pp. 213–215; February, 1957.

<sup>6</sup> In second-order calculations, the electric quadrupole moment interaction will affect the frequency. However, this will only result in a broadening of the resonance line.

<sup>3</sup> L. I. Schiff, "Quantum Mechanics," McGraw-Hill Book Co., Inc., New York, N. Y., p. 191; 1949.



where  $Q_c$  is the coupling  $q$  to the output. Shimoda, *et al.*,<sup>4</sup> calculated that the optimum  $Q_c$  is twice the loaded  $Q$  of the cavity so that (14) becomes

$$P_0 = \frac{\pi \nu W}{Q} \quad (15)$$

which, for higher frequencies, should give higher output powers because of the linear dependence on frequency. It may be worth noting that the  $\text{NH}_3$  maser used as an oscillator at  $K$  band provides about  $10^{-10}$  watts.

#### OPERATION AS AN AMPLIFIER

The atomic beam amplifier has a low-noise figure just as in the case of the  $\text{NH}_3$  maser. One advantage of the present system is the feature of tunability. It may be possible to provide a cavity which can be tuned at the same time that the homogeneous magnetic field is varied. Both should be simultaneously set to a variable frequency  $\nu$  given by

$$\nu = 2\mu H/h. \quad (16)$$

This would permit sweeping a wide frequency range with a low-noise narrow-band amplifier. The power output must not be more than the order of millimicrowatts just as in the case of the  $\text{NH}_3$  maser. This limitation is set by the power saturation of the atomic beam; when the input power is greater than saturation as determined by the number of atoms per second available for an induced transition, then further amplification is not possible.

#### BEAM INTENSITY

Practical beams of the order of  $10^{15}$  atoms/second/cm<sup>2</sup> are easily obtained according to Silsbee.<sup>7</sup> However, to satisfy (13), the oscillation condition, another two orders of magnitude of flux are needed. To obtain such flux is an extremely difficult task, but is not impossible as the following discussion will show. Ramsey<sup>8</sup> discusses several methods of focusing which may be used to intensify the beam. One method which appears feasible is due to Rabi.<sup>9</sup> This scheme uses the analog of optical focusing and calculates the change of refractive index of a beam entering or leaving a magnetic field. One difficulty with this method is that many pole pieces of different shapes would be required to get a sufficiently dense beam since the bending is small at each change in refractive index.

A more convenient scheme of getting dense beams was invented by Stern<sup>10</sup> who called it the "multiplier." This consists of many converging beams each of which would be in an independent inhomogeneous field. Stern built such a device with 150 such converging beams.

The inhomogeneous fields consist of machined converging grooves in the pole pieces of the magnet used for separation of the upper and lower spin states. This provides an increase in flux density by a factor of 150 which is about the amount needed here. Further, this method may be extended to any number of channels. One ultimate limit is pressure broadening of the resonance line. The latter problem is not serious; even though atomic collisions may take place in the neighborhood of the cavity opening, the beam diverges once inside the cavity and the pressure is reduced. Consequently the collision probability is very small. Certainly operation at 12.5 mm will have no difficulties with pressure broadening. The major source of line broadening will be, as in the case of the ammonia maser, Doppler broadening.<sup>4</sup>

The beams which make a large angle with the central axis of the cavity could result in a somewhat reduced effect in starting oscillation. Thus a limitation to the number of useful beams appears. This may require careful design of the cavity so that the RF magnetic fields will act upon all of the diverging beam inside the cavity. By use of the symmetry of a rectangular cavity configuration somewhat more uniform transition fields may be possible. Further, the cavity may be designed with input and output slits so that the beams converge to a central region in the cavity and diverge towards an exit slit. Various cavity configurations have been thoroughly explored and calculated.<sup>4</sup> A cavity could be designed so as to contain the flux in about a 20° arc. This should permit the use of several hundred converging beams.

#### FURTHER CONSIDERATIONS

In order to get a long transit time in the cavity, it is desirable to use heavy atoms which are gaseous at low temperatures. However, this is not critical; any of the alkali metals would be satisfactory. As mentioned previously, the fields used here are large enough to observe the Paschen-Back effect between the nuclear and electron spins, consequently hyperfine-interaction will affect the frequency of electron transitions. It would be advantageous to use a low boiling point heavy metal such as Rb (696°C) in order to get low atomic velocities.  $\text{Ag}^{107}$  or  $\text{Ag}^{109}$  has the advantage of lower nuclear spin ( $\frac{1}{2}$ ), but the disadvantage of a high boiling point (2200°C). Rb<sup>87</sup> in isotopically pure form seems to be about the best choice. This is about 27 per cent of naturally occurring rubidium. With silver, the 107 and 109 isotopes are approximately 50 per cent each in nature. Use of silver may simplify the problem of securing the proper isotopes.

The discussion has generally slanted towards 12.5-mm operation. The reason for this is that the ammonia maser operates at that frequency. It is also advantageous to utilize a cavity design which has been well engineered.<sup>4</sup> Fundamentally, one has no limitation except the shrinking size of the cavity as one goes to shorter wavelengths.

<sup>7</sup> H. B. Silsbee, private communication.

<sup>8</sup> N. F. Ramsey, "Molecular Beams," Oxford University Press, New York, N. Y., chap. 16; 1956.

<sup>9</sup> I. I. Rabi, "Refraction of beams of molecules," *Nature*, vol. 123, p. 163; February 2, 1929.

<sup>10</sup> O. Stern, "Zur Methode der Molekularstrahlen I," *Zeit. Physik*, vol. 39, pp. 751-763; September, 1926.

However, the upper frequency limitation is also set by the difficulties of getting magnetic fields greater than 25,000 oersteds. This sets the limit at wavelengths of about 3 mm. Because of the associated cavity size and beam requirements, it is unlikely that the proposed system will be extended below 5 mm. Certainly there would be much to be gained by working at 1.25 cm initially where the  $\text{NH}_3$  maser can be used for a frequency reference.

For noise calculations, it would be difficult to improve upon the treatment given by Gordon and White<sup>11</sup> which applies to the  $\text{NH}_3$  maser, and scarcely any modification is needed to extend the treatment to magnetic dipole transitions. There is good reason to believe that a noise temperature of a few degrees Kelvin is attainable.

It may be well to point out that a solid-state system presents certain advantages over the proposal outlined

<sup>11</sup> J. P. Gordon and L. D. White, "Noise in maser amplifiers," *Proc. IRE*, vol. 46, pp. 1588-1594; September, 1958.

here.<sup>12</sup> The most important of these is a very much larger gain-bandwidth product. On the other hand, a continuously operating three-level solid-state maser requires a pump frequency higher than the operating frequency, and this is difficult to obtain at mm wavelengths. Also, a solid-state maser calls for very low temperatures in order to achieve long thermal relaxation times, while the gas beam maser has no such requirement.

#### ACKNOWLEDGMENT

It is a pleasure to thank H. B. Silsbee for an interesting discussion on molecular beams and for suggesting improvements in this manuscript. In addition, comments from C. H. Townes and S. Silver have proved profitable.

<sup>12</sup> Zacharias and A. Javan have been performing experiments related to the scheme proposed here. (Private communication from C. H. Townes.)

## High-Speed Microwave Switching of Semiconductors—II\*

ROBERT V. GARVER†

**Summary**—A relationship between low-power isolation and small-signal, low-frequency diode resistance is reported. A study of ambient heating indicates that with increasing temperature the diode characteristics tend to approach the line characteristic of the above relationship. Observed switching speeds of 1.5 to 3.0  $\mu\text{s}$  are reported. A theory is presented which agrees with the switching time data and predicts microwave switching times as low as 0.2 to 0.3  $\mu\text{s}$ . High speed switching is discussed with reference to significant parameters, e.g., hole storage, internal heating, and pulse reverse diode characteristics.

#### INTRODUCTION

IT has been shown in previous publications<sup>1-3</sup> that an  $n$ -type point contact germanium diode can be used to switch X-band microwaves. Placing the diode

across the center of the waveguide and impressing a reverse or forward voltage upon it will cause the diode to reflect or transmit the microwave power. The ratio of the microwave power past the diode in the reflecting state, to the incident microwave power, defines the isolation in db. The same ratio in the transmitting state, defines the insertion loss. Isolations of 25 to 35 db with constant insertion losses of 1 db were reported<sup>1</sup> over a 1000 mc band-width at 1 milliwatt incident microwave power. Using a 1N263, the only commercially available microwave germanium diode, rapid deterioration of isolation occurred for incident microwave peak powers greater than 5 milliwatts. Ambient heating showed constant insertion loss and only slight deterioration of isolation from 20°C to 150°C. It was shown<sup>2</sup> that decreasing the donor density of the germanium allowed the diode to switch up to 1 watt of incident microwave peak power. It was demonstrated by observing two pulses at succeeding closer intervals that there was essentially no dead time between switching events. The pulse time constants of the diode switch were found to be a function of germanium donor density and to be of the order of  $3 \times 10^{-9}$  to  $10 \times 10^{-9}$  seconds (3-10  $\mu\text{sec}$ ). Devices

\* Manuscript received by the PGMTT, October 31, 1958. Revised manuscript received, December 29, 1958.

† Diamond Ordnance Fuze Laboratories, Washington 25, D. C.

<sup>1</sup> M. A. Armistead, E. G. Spencer, and R. D. Hatcher, "Microwave semiconductor switch," *Proc. IRE*, vol. 44, p. 1875; December, 1956.

<sup>2</sup> R. V. Garver, E. G. Spencer, and R. C. LeCraw, "High speed microwave switching of semiconductors," *J. Appl. Phys.*, vol. 28, pp. 1336-1338; November, 1957.

<sup>3</sup> R. V. Garver, E. G. Spencer, and M. A. Harper, "Microwave semiconductor switching techniques," *IRE TRANS. ON MICROWAVE THEORY AND TECHNIQUES*, vol. MTT-6, pp. 378-383; October, 1958.



employing the principles of these diode switches are described.<sup>3</sup>

The crystal switch has proved useful in bench testing and has great potential uses in missiles and microwave computers. An understanding of the switching speed problem is of considerable importance, and was thus re-investigated. The details of the investigation are given so that application engineers may obtain a good understanding of the switching speed problem from the text, and to reinforce the point that the detector diode contributes most to the observed switching time and is a limiting factor in any microwave switching speed study.

Fabrication of higher power switches has provided a less delicate switch, but these cannot yet be mass produced with 1 db insertion loss. Despite intensive efforts in this laboratory to analyze the diodes, they defy the accepted laws of transistor physics. If point contact junctions of germanium and silicon are made in identical cartridges whose equivalent circuit is known for X-band, and the junction impedances are measured at X-band by varying the diode bias, the intrinsic impedances of the two junctions are quite different and neither junction behaves according to high frequency semiconductor theory; however, at 10 mc both diodes behave according to the theory. Quite simply, the modifications of semiconductor theory which describe microwave behavior of point contacts on germanium and silicon have not yet been found. In the design of semiconductor microwave devices in the past, the empirical approach, in the absence of theory, has proved fruitful. Thus, the empirical approach is used here to provide a test that may allow diode switches to be mass produced with 1 db insertion loss. A relationship between microwave attenuation and 10 mc small-signal junction resistance<sup>4</sup> has been determined, and it has been found to be supported by temperature and pulsing measurements. This relationship at the same time provides an understanding of the heating effects and reverse pulsing effects.

### ISOLATION

It was shown that for the isolation of the switch to be high for higher incident microwave peak powers, all parts of the microwave sine wave must cause little current to flow across the crystal junction.<sup>2</sup> This suggests the existence of a relationship between isolation and junction resistance. Measurements were made of 160 crystals, including some 1N263s, some pilot production high power models, and some hand made diode switches. The measurements consisted of 1) observing the maximum isolation and the minimum insertion loss of each switch for 1 milliwatt incident microwave peak power and 2) observing the junction resistance on a 10 mc bridge using the same applied voltages. Considerable scatter was observed but a consistent trend was evident. Fig. 1 shows the trend. For forward current through the

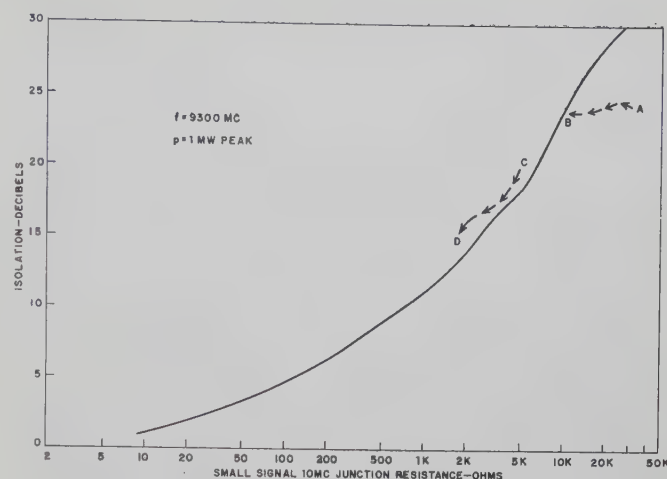


Fig. 1—Maximum small signal isolation as a function of small-signal 10-mc junction resistance for the same reverse bias. The arrow lines show two different effects observed in ambient heating. Lines either approach or lie within the proximity of the line characteristic of the function.

diode, a small signal resistance of 10 ohms gave about 1 db insertion loss. A reverse applied voltage giving  $10^4$  ohms small signal resistance gave about 24 db isolation. In many of the pilot production diodes the point contacts were near the edge of the germanium die and not near the crystal axis. These diodes were quite sensitive to rotation in the holder, giving radically different maximum isolations. This caused some of the scatter observed. Other contributing factors to the scatter may have been variation in area of contact, variation of hole injection characteristics, or some high frequency mechanism not yet known.

At different germanium donor densities the line above 20 db (Fig. 1) is not the same. The line characteristic of a diode having a high donor density ( $10^{18}/\text{cm}^3$ ) is moved slightly to the left, while the line for a diode with low donor density ( $10^{16}/\text{cm}^3$ ) is moved slightly to the right. Most of the data lie within  $\pm 1$  db of their characteristic line.

Fig. 1 is helpful in understanding the effect of ambient heating upon the isolation of the switch and may be useful in designing diode switches. This is explained in the following paragraph.

### AMBIENT HEATING

Earlier data<sup>1</sup> showed slight decrease in isolation with increase in ambient temperature. Later data on higher power diode switches revealed wide variations in change with ambient heating. Some few diodes improved with heating, while most others remained constant or showed the deterioration originally observed. The few diodes that improved showed some further improvement when returned to room temperature, and thereafter demonstrated the behavior of the others. These few diodes were probably welded during the thermal experiment to an improved characteristic. That is to say, they had not been welded enough in fabrication to have optimum characteristics.

<sup>4</sup> Junction resistance is defined as diode resistance at 10 mc.

Data from a higher power diode switch are shown in Fig. 2. At elevated ambient temperatures, the deterioration is greatest at higher powers, and deterioration exists at lower powers for this diode. A nondeteriorating diode gives the same line for higher ambient temperatures as for room temperature at low powers, while it drops off at higher powers for increasing temperature. Note that this diode, although deteriorating with temperature, gives greater than 20 db isolation for 50 milliwatt incident microwave peak power at a temperature greater than the melting point of the soft solder ( $180^{\circ}\text{C}$ ) used in making the diode. Upon returning this diode to room temperature, the isolation at low power returned to within  $\frac{1}{2}$  db of that observed at the beginning of the test. The deterioration at  $250^{\circ}\text{C}$  caused little permanent damage. Other diodes were heated only to  $150^{\circ}\text{C}$  to avoid melting the solder.

The reverse dc characteristics of an  $n$ -type point contact germanium diode of  $10^{16}$  donors/cm<sup>3</sup> are shown in Fig. 3. As ambient temperature is increased, the low voltage reverse resistance decreases, and breakdown occurs at lower reverse voltages. Referring to the solid line of Fig. 1, it should be expected that the isolation for lower power should decrease with increasing ambient temperature, and that due to the lowered voltage breakdown, higher power isolation should deteriorate rapidly. The question arises as to the behavior of the crystals that do not deteriorate at lower powers with increasing temperature. It is observed that those which do not deteriorate are represented by a horizontal progression on Fig. 1 as arrow line  $AB$ ; and that they lie to the right of their characteristic curve. Arrow line  $CD$  represents a crystal that deteriorated at low power with increasing ambient temperature. Note that it lies to the left of the characteristic curve. Thus the data from both diodes tend to approach or lie within the proximity of the characteristic curve. The fact that diodes away from the characteristic curve approach it when heated gives added support to the validity of the relationship. If the relationship of Fig. 1 is valid, then production techniques can be established which will give low 10 mc forward resistance and high 10 mc reverse resistance without changing the mechanical dimensions of the cartridge or whisker; hence, a better switch can be made. It has also been shown that the crystal switch can function well in a very high temperature environment.

#### SWITCHING SPEEDS

Switching speeds of 3 to 10  $\mu\text{secs}$  were reported,<sup>2</sup> and the mechanism causing those long response times was unknown. A different technique of pulsing has revealed observed switching speeds of 1.5 to 3.0  $\mu\text{secs}$ . An equivalent circuit has been established whose pulse response agrees with the data.

In measuring the pulse time constants by biasing the switch "off" and pulsing it "on,"<sup>2</sup> pulses which are too large cause the decay time to increase, while pulses which are too small give insertion loss greater than that

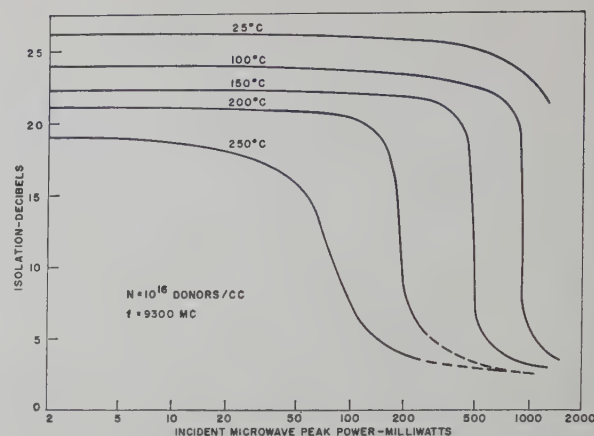


Fig. 2—Maximum isolation as a function of incident microwave peak power showing the effect of ambient heating. Upon cooling, the diodes returned to the curve characteristic of room temperature.

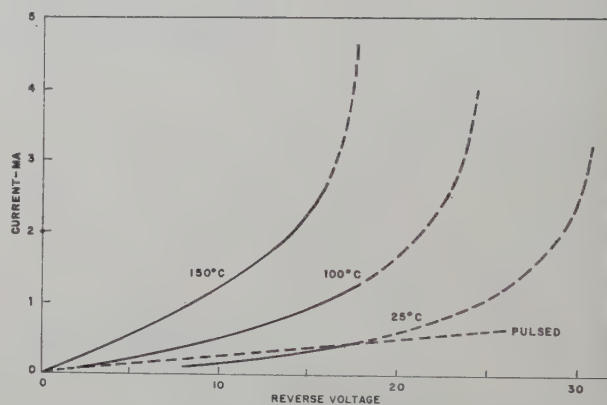


Fig. 3—Reverse characteristics of an  $n$ -type point-contact germanium diode. The curved lines are the dc reverse characteristics at various temperatures, while the straight line is characteristic of reverse pulsing from Bennett and Hunter.<sup>7</sup> The dashed lines are extrapolations.

observed at dc.<sup>5</sup> With higher power switches these factors must be balanced against each other. Using higher voltage pulses from a mercury switch pulse source, the trailing edge below the 30 per cent voltage level decays so slowly that it is easily mistaken for the 0.0 per cent level. To date, increases of decay time due to large pulses can be attributed to the increased amplitude of the trailing edge of the switching pulse. If there is time required for hole return, it is overshadowed by the effect of the trailing edge. For higher power switches the low dc insertion loss is due partially to heating resulting from current in the forward direction. For very short pulses, time is insufficient to permit heating; therefore, a higher voltage pulse is required, which will lower the resistance by greater hole injection.

To eliminate the difficulties encountered in pulsing the semiconductor microwave switch "on," the technique of pulsing the switch "off" is employed. Then too small a switching pulse voltage will not give maximum isolation, and too large a switching pulse voltage will

<sup>5</sup> DC switching of microwaves is distinguished from pulsed switching since there is a difference for pulses shorter than 0.5  $\mu\text{seconds}$ .



cause reverse current to flow with the occurrence of less than maximum isolation. The amplitude of the trailing edge is therefore kept to a minimum, and the optimum switching pulse amplitude is easily obtained. Fig. 4 shows the result of 200 milliwatts being pulsed "off" by a crystal switch of  $10^{16}$  donors/cm<sup>3</sup>.

The equivalent circuit for the switch pulsing network is shown in Fig. 5. To drive the crystal switch, a mercury switch pulser having output impedance of 50 ohms was employed. The 40-ohm and 10-ohm resistors are for matching the output impedance of the pulser. To bias the crystal "on" point  $B$  was connected to a dc voltage supply through a ferrite inductor. A  $0.01 \mu\text{f}$  capacitor was connected between points  $A$  and  $B$  to prevent the bias voltage from entering the pulser. A 4000-ohm resistor was connected between point  $A$  and ground to provide a dc return path for the pulser. These components have little effect upon the pulse shape, and therefore they are omitted from the diagram. Lead lengths were kept to a minimum.  $C_2$  is the capacitance of the detector crystal mount;  $C_1$  is the capacitance of the switching crystal mount.  $C_1$  is greater than  $C_2$  because attempts to lower  $C_1$  increased the insertion loss of the switch.  $L_1$  is the inductance of the switching diode whisker.  $R_x$  is the nonlinear resistance of the crystal switch. The contact voltage  $i_x R_x$  imparts the voltage pulse, by the diode switching action, to the microwaves, which are in turn detected to give  $V_d$ .  $V_d$  is the detected voltage of the detector with no load.  $R_{id}$  is the internal resistance of the detector.  $R_{id}$  was computed from measurements on loading of the detector with 100 mw peak microwave power incident and load resistors varied above and below 120 ohms.  $R_{id}$  is nonlinear but not enough so to affect the computations. The inductive reactance of the detector whisker at the highest frequency involved here is only  $0.07 R_{id}$ , and is therefore omitted. A traveling-wave oscilloscope having an input impedance of 120 ohms was used to view the pulses.

The inductance ( $L$ ) of the whiskers was computed from  $L = 0.00508l (\ln 4l/d - 1) \times 10^{-6}$  henries,<sup>6</sup> where  $l$  and  $d$  are in inches. It was assumed that the inductances of these bent wires are equal to the inductances they would have if they were straight. For the 1N263,  $L = 3.6 \times 10^{-9}$  henries. For the 1N23 type S-bend whisker,  $L = 5 \times 10^{-9}$  henries. For the switching speed study, the detector and all of the higher power switches were fabricated in the 1N23 type cartridge.

Because the diode of  $2 \times 10^{18}$  donors/cm<sup>3</sup> can control only low power microwaves, the trace observed on the oscilloscope was too small from which to obtain accurate information. Data from the other crystals is shown in Table I. By inserting attenuation between the switch and detector as the power incident to the switch is increased, the power incident to the detector is not allowed to exceed 100 milliwatt peak. This limits the

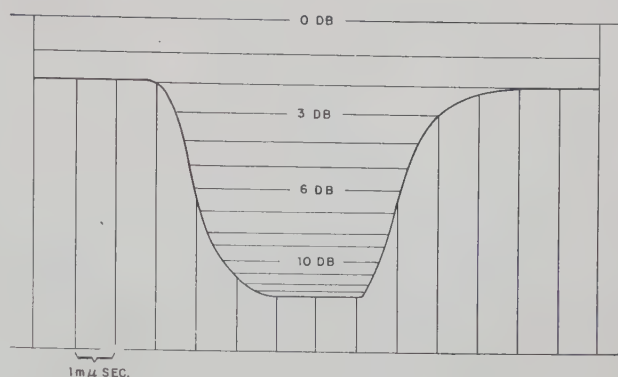


Fig. 4—Traveling wave scope display characteristic of pulsed "off" microwave switching using  $n$ -type germanium of  $10^{16}$  donors/cm<sup>3</sup>. 200 milliwatts of incident microwave peak power is being switched to 14 db isolation.

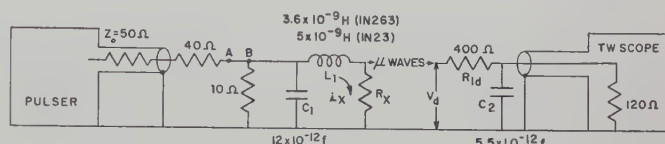


Fig. 5—Equivalent circuit for determining microwave pulsing time constants of the germanium diode switch with a silicon diode detector.

TABLE I  
EXPERIMENTAL AND THEORETICAL VALUES OF  
RISE TIME AND DECAY TIME

Donors (no./cm <sup>3</sup> )	Observed			Theoretical	
	3.5×10 <sup>16</sup>	1×10 <sup>16</sup>	3×10 <sup>15</sup>	Min.	Max.
Peak Power (watts)	0.05	0.20	1.50	—	—
Decay Time (μs)	1.6	1.5	2.2	1.5	2.4
Rise Time (μs)	1.8	1.9	3.0	1.4	3.4

cause of change in switching times to the switching diode. Pulse time constant is defined as the time elapsed between 10 per cent and 90 per cent of full pulse voltage amplitude. The minimum and maximum theoretical values shown in Table I were computed from the equivalent circuit of Fig. 4 on an analog computer. Taken into account in the computation were the non-linearity of  $R_x$ , the nonlinear relationship between  $i_x R_x$  and  $V_d$  (Fig. 6), the real shape of the switching pulse from the pulse source, and the traveling wave oscilloscope's rise time of 0.5  $\mu$ sec. The minimum value corresponds to low power diodes and the maximum value corresponds to high power diodes. The observed data lie between these maximum and minimum limits. The real pulse shape was obtained on the analog computer by changing parameters of a function generating circuit until a function was generated which, when put through the traveling wave oscilloscope analog, corresponded to the traveling wave oscilloscope's picture of the pulse. The nonlinearity of  $R_x$  was easily measured for each diode. The nonlinear relationship between  $i_x R_x$  and  $V_d$

<sup>6</sup> F. E. Terman, "Radio Engineer's Handbook," McGraw-Hill Book Co., Inc., New York, N. Y., p. 49; 1943.

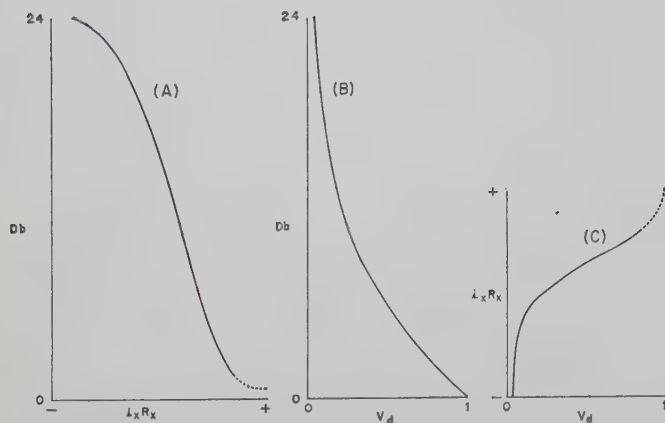


Fig. 6—Characteristics of the germanium diode switch and silicon diode detector for the purpose of determining their effect upon the pulsing time constant by limiting or heating.

may be obtained either as is shown in Fig. 6, or by direct measurement. Fig. 6 serves to show the difference between high- and low-power diodes as well as giving some meaning to microwave amplitudes at 10 per cent and 90 per cent voltage levels. Referring to Fig. 6, the solid line part of curve *A* is typical of higher power diode switches. Entering the dotted line region results in permanent damage to the crystal. However, for lower power diode switches the dotted line region is readily entered without damage. The lower insertion loss for the high-power diode switch is attained by lowering the diode resistance. This is accomplished by internally heating the junction with forward current. For lower power diode switches the resistivity of the germanium is low enough to give low forward diode resistance without generating internal heat. Curve *B* is characteristic of a 1N23B detector. Projecting curve *A* through curve *B* shows the limiting action of curve *C*.

It is observed in Fig. 4 that the pulsed isolation is only 14 db, while the dc isolation was 24 db. This lower pulsed isolation is typical of all germanium diode switches. It is suspected that this lowering of isolation is not caused by the return of stored injected holes, since their effect was not obvious in forward pulsing. The effect is probably due to the isothermal reverse characteristic differing from the dc characteristic. As was shown by Bennett and Hunter,<sup>7</sup> for pulses shorter than 500  $\mu$ sec the reverse characteristic is nearly a straight line from the origin, with a greater slope than the dc characteristic and extending beyond twice the breakdown voltage (see Fig. 3). The lower small-signal

resistance from the greater slope results in less isolation. It has also been observed that maximum pulsed isolation occurs at a much higher voltage than maximum dc isolation. This, too, is the result of the pulsing and dc characteristics being different.

From the analog computations it is predicted that, given a switching pulse voltage having 0  $\mu$ sec pulse time constant, the semiconductor microwave switch will impart pulse time constants to the microwave of 0.2 to 0.3  $\mu$ sec; and that, given a microwave pulse having 0  $\mu$ sec pulse time constant, the display will have a rise time of 1.3  $\mu$ sec and a decay time of 1.5  $\mu$ sec, due to the detector crystal and traveling wave oscilloscope. That is to say, the detector diode contributes most to the observed switching times and is a limiting factor in any microwave switching speed study.

### CONCLUSIONS

A consistent relationship has been observed between isolation and low-frequency small-signal junction resistance. The fact that diodes away from this characteristic line approach it when heated gives added support to the validity of the relationship. The establishment of this relationship should facilitate the fabrication of better diode switches.

Ambient heating results in little or no decrease in isolation at low powers and sudden rapid decrease in isolation at higher powers. This is explained in terms of the heating effect upon both the breakdown voltage and the slope of the dc reverse characteristics. It is concluded that the switch can function well in a very high-temperature environment.

Observations and calculations indicate the switch to be the highest speed microwave switch reported in the literature. The technique of pulsing the switch "on" results in increased decay time from the trailing edge of the switching voltage pulse, which obscures any evidence of the return of stored minority carriers. The technique of pulsing the switch "off" results in less than dc isolation due to the difference between dc reverse characteristics and short-pulse reverse characteristics. This investigation indicates that most of the observed switching time was due to the internal impedance of the diode detector and that it is a limiting factor in any switching speed study.

### ACKNOWLEDGMENT

The author should like to express his appreciation to E. G. Spencer and R. D. Hatcher for their continued interest; and to R. L. Wigington, J. T. Tippet, and K. L. Carroll of the National Security Agency for their help in the instrumentation for the switching time analysis.

<sup>7</sup> A. I. Bennett and L. P. Hunter, "Pulse measurement of the inverse voltage characteristics of germanium point contacts," *Phys. Rev.*, vol. 81, p. 152; January 1, 1951.



# A Logarithmic Transmission Line Chart\*

A. C. HUDSON†

**Summary**—A chart is presented which relates the real and imaginary components of the impedance at any position along a transmission line to the magnitude and location of the standing wave. In the present chart the ordinate is  $R/Z_0$  plotted logarithmically and the abscissa is a function of  $X/R$ . Thus a change in the reference impedance becomes a simple vertical translation of any point. An auxiliary chart permits the direct determination of the length and impedance of transmission line required to match a given impedance.

## INTRODUCTION

TRANSMISSION line impedance charts are well known.<sup>1</sup> There are, for example, the rectangular impedance chart and the circular or "Smith" chart,<sup>2</sup> which deal with a mismatched transmission line and relate the magnitude and position of the standing wave to the real and imaginary components of the impedance (or admittance) at any point along the transmission line.

The above description applies also to the present chart (Fig. 1). This chart has been designed for quick solution of problems in which the characteristic impedance of the transmission line varies discontinuously along its length. It is believed to be more convenient than the Smith chart for problems where successive lengths of line of varying impedance are connected in cascade and less convenient for certain other problems; for example, where shunt reactive stubs are connected along the line.

## REQUIREMENTS OF AN IMPEDANCE CHART

To achieve simplicity when the characteristic impedance of the transmission line is subject to discontinuous changes, a chart should be designed so that one of the axes represents some function of the phase angle  $\phi$ , where the impedance  $Z$  is written as  $|Z|\angle\phi$ . The simplest arrangement is to plot  $\phi$  itself on a linear scale. This has been done here; however, the  $\phi$  scale is not shown, rather the abscissa has been calibrated at even values of  $X/R$ .  $X/R$  is, of course,  $\tan^{-1}\phi$ ;  $X$  and  $R$  are the series reactance and resistance, respectively. The advantage of using  $\phi$  or some function of it for one rectangular axis is that a change of reference impedance represents a straight-line motion parallel to one axis since the phase angle  $\phi$  is independent of the reference impedance.

The other requirement of such a chart is that the other axis be  $\log |Z|$ , or  $\log R$ , or  $\log X$ . The second alternative,  $\log R$ , has been chosen here. Because of the logarithmic scale, a change of reference impedance represents the same amount of motion at any location on the chart. The choice of  $\log R$  rather than  $\log |Z|$ , and of  $X/R$  rather than  $\phi$ , was made for easy use of data in the  $R+jX$  form. This facilitates the interchange of data between the present chart and the Smith chart, for example. The rectangular form is also the most usual when using an impedance bridge. It is recognized that a  $\log |Z|$ ,  $\phi$  chart would be more elegant since it just represents the complex  $Z$  plane and would also be more useful when it is necessary to express the impedance in the polar form.

## RANGE OF THE CHART

Because the ordinate is a logarithmic scale, some limitation is necessary. Here, for convenience,  $R/Z_0$  has been limited to the range 0.1 to 10. To be consistent with this, the horizontal range has been chosen to include all points having a voltage standing wave ratio of 10 or less. Angles between  $80^\circ$  and  $90^\circ$  have not been included because in this region the two families of curved lines are too nearly parallel for convenient use. This difficulty would not arise with the  $\log Z$  chart.

## DESCRIPTION AND USE OF THE CHART

To be given the VSWR as a number greater than unity which will select one of the VSWR loci, seen to be roughly concentric with the center of the chart, and to be given the position of the voltage minimum, measured in electrical degrees from some reference point, is the most usual way to enter the chart. This position will select one of the radial lines marked in degrees toward the generator from the point of minimum impedance. Movement towards the generator will represent a counterclockwise motion on the chart.

The abscissa of the chart is drawn (but not calibrated) to represent, on a linear scale, the phase angle of the impedance; that is,  $\tan^{-1} X/R$ .  $X$  and  $R$  are the components of the impedance at the point in question. The range is  $-80^\circ$  to  $+80^\circ$ , angles between  $80^\circ$  and  $90^\circ$  being off the chart. The degrees scale is not shown; however, for convenience the abscissa is calibrated to the scale  $X/R$ .

It will be noted that  $X/R$  is independent of the reference characteristic impedance. Hence a change of impedance in the line will not change the abscissa, or in other words, reference impedance changes will be represented by vertical movements on the chart.

\* Manuscript received by the PGMTT, November 6, 1958; revised manuscript received, December 24, 1958.

† Nat. Res. Council of Canada, Radio and Elec. Eng. Div., Ottawa, Can.

<sup>1</sup> P. S. Carter, "Charts for transmission-line measurements and computations," *RCA Rev.*, vol. 3, pp. 355-368; January, 1939.

<sup>2</sup> P. H. Smith, "Transmission line calculator," *Electronics*, vol. 12, pp. 29-31; January, 1939.





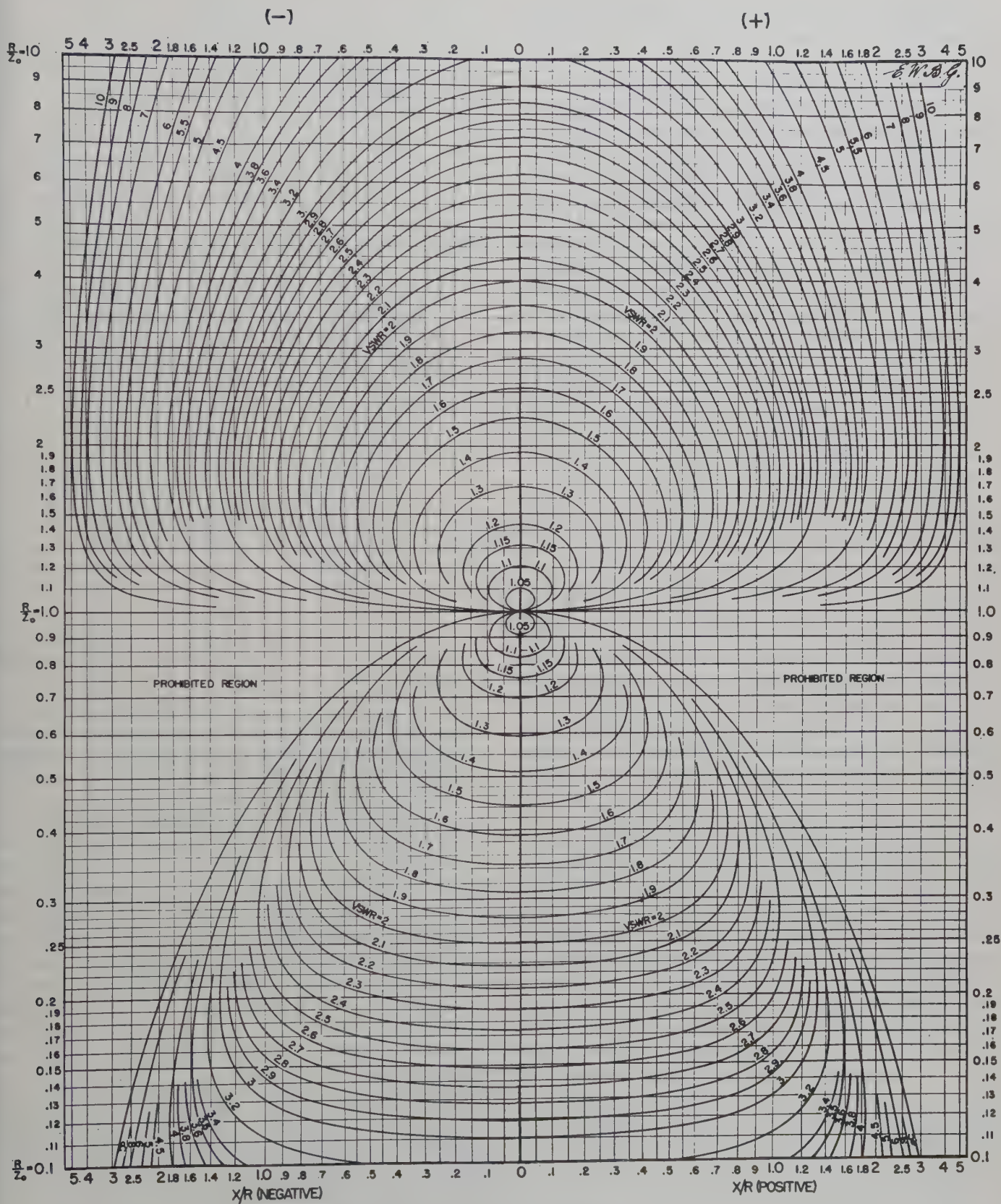


Fig. 2—Transposed logarithmic transmission line chart.

The ordinate of the chart is  $R/Z_0$ , where  $Z_0$  is the characteristic impedance of the transmission line. Because of the logarithmic scale, a change in reference impedance of a certain ratio will represent the same amount of vertical movement anywhere on the chart.

Consider a point plotted to a reference impedance of, say, 50 ohms. Assume that we wish to move along a 50-ohm line  $\frac{1}{8}$  wavelength toward the generator. We follow the VSWR locus in a counterclockwise direction, counting off  $45^\circ$  on the degrees scale. Now assume that the transmission line changes at this point to one having a characteristic impedance of 75 ohms.  $R/Z_0$  will be reduced to  $50/75$  of its former value. Thus we move vertically down on the chart, the distance moved being found by setting a pair of dividers on the ordinate scale between any two points which are in the ratio 50:75, for example, 0.5 and 0.75. We may now move along the new standing-wave ratio locus counterclockwise for the number of electrical degrees corresponding to the length of the section of 75-ohm line. To return now to the original 50-ohm reference, the point is moved vertically upwards by the same divider setting.

The use of the chart for a typical broad-band matching problem will be discussed later, but first the transposed chart, Fig. 2, will be described.

#### TRANSPosed CHART

The purpose of Fig. 2 is to answer the question, "What length of line of what impedance will match a given impedance?" To put the question in a more practical form, "Of those transmission lines which are available, which impedance is the best, and what length should be used?" Conventional charts do not answer this question explicitly. The present chart (Fig. 1) is somewhat better, but one trial-and-error operation with a pair of dividers is still necessary.

Suppose for example that we wish to match an impedance represented by point  $A$  [Fig. 3(a)] point  $A$  being referred to the impedance of the standard transmission line which is in use. Note that Fig. 3(a) is a representation of Fig. 1. We transform from point  $A$  to  $B$ ; in other words, a transmission line which is lower in impedance by the ratio represented by the distance  $AB$  is used. We now move counterclockwise along the constant VSWR locus to point  $C$ , the point of zero reactance. The length of the lower-impedance line is given by the difference in the degree readings at the points  $B$  and  $C$ . The transformation back to the standard impedance is represented by the downward move  $CD$ . For a perfect match, we wish point  $D$  to coincide with  $O$ . Thus, in terms of Fig. 1, to match point  $A$  (Fig. 3), such a VSWR locus that  $AB=CO$  is sought; this is a trial-and-error procedure.

But suppose that the VSWR locus shown on Fig. 3(a) is the correct locus to match point  $A$ ; in other words, suppose that  $AB=CO$ . Now suppose also that the VSWR locus is moved bodily downward until it is tangent to the  $R/Z_0=1$  axis, as indicated in Fig. 3(b). Dis-

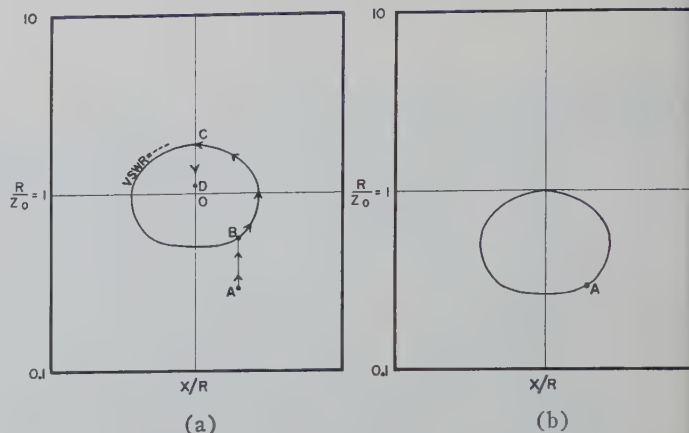


Fig. 3—(a) Diagrammatic representation of the chart of Fig. 1 with only one VSWR locus shown. If this locus is the correct one to match point  $A$ , then point  $D$  will coincide with  $O$ . (b) Transposed version of (a). Here the locus in (a) has been moved bodily downward. If it is the correct locus, it will pass through  $A$ .

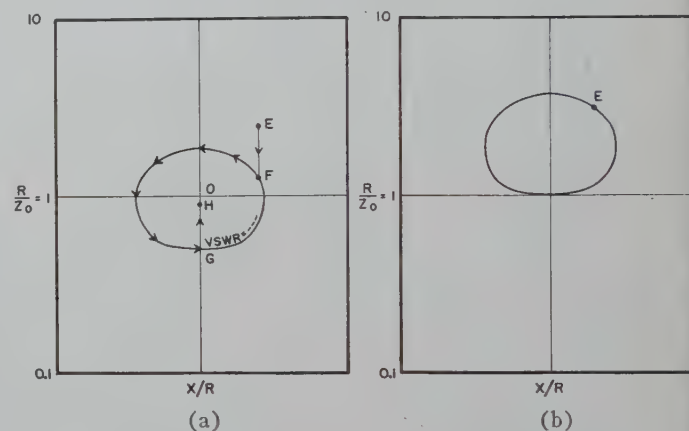


Fig. 4—(a) Diagrammatic representation of the chart of Fig. 1 with only one VSWR locus shown. If this locus is the correct one to match point  $E$ , then point  $H$  will coincide with  $O$ . (b) Transposed version of (a). Here the locus in (a) has been moved bodily upward. If it is the correct locus, it will pass through  $E$ .

tance  $CO$  will collapse to zero and since  $AB=CO$ ,  $AB$  will collapse to zero also. Thus the transposed locus will pass through point  $A$ . Suppose finally that all of the VSWR loci in Fig. 1 are translated downward until they are tangent to the  $R/Z_0=1$  axis, then the VSWR locus now passing through any point  $A$  is the correct one to use for matching the impedance represented by point  $A$ . It will be noted that the impedance transformation ratio for a correct match is always equal to  $V$ , the VSWR on the matching section. The lower half of Fig. 2 has been prepared by sliding the VSWR loci in the manner described above.

Now, Fig. 3 deals with an impedance whose normalized resistive component,  $R/Z_0$ , is less than unity and requires a lower impedance line for matching. If, on the other hand, the value of  $R/Z_0$  is greater than unity, we refer to Fig. 4. In Fig. 4(a) it is assumed that we wish to match point  $E$ . In an exactly analogous manner we move down to point  $F$ , then counterclockwise to  $G$ , and up to  $H$ . Thus by sliding all the VSWR loci upward, as has been done in the upper half of Fig. 2, the correct VSWR may be read directly.



One way of presenting the data of Fig. 2 would be to superimpose it on Fig. 1; however, in the absence of two-color printing, Fig. 1 would become difficult to read. Figs. 1 and 2 are the same size however, so a point from Fig. 1 may be conveniently transferred to Fig. 2 with dividers or compass.

### USE OF THE TRANSPOSED CHART

For greater clarity, the use of Fig. 2 will now be described without any references to the method of formation of the chart. Given an impedance normalized to  $Z_0$ , and represented by some point on Fig. 1, it is required to find the length and impedance of a section of transmission line which will match the given impedance to a line of characteristic impedance  $Z_0$ .

- 1) Transfer the point geometrically to Fig. 2.
- 2) Read the value of VSWR indicated on this chart. Let us assume that the value found is  $V$ . No more use is made of Fig. 2.
- 3) Draw a line vertically<sup>3</sup> from the original point on Fig. 1 to intersect the VSWR curve of value  $V$ .
- 4) Note that the impedance transformation ratio represented by the length of this line is exactly  $V$ , and in fact, best accuracy in the previous step is obtained by setting a pair of dividers at this ratio, as determined by the ordinate scale.
- 5) a) If the original point is in the lower half plane, the characteristic impedance of the matching section is  $Z_0$  decreased in the above ratio  $V$ . b) If the original point is in the upper half plane, the impedance of the matching section is  $Z_0$  increased in the ratio  $V$ .
- 6) To find the length of the matching section, move from the intersection on curve  $V$  (see step 3) counterclockwise to the first zero reactance point which is in the opposite half plane (vertically) to the original point.
- 7) The number of degrees passed in this motion gives the length of the matching line.

It may be seen from Fig. 4 that all points in the upper half-plane may be matched, but matching of some impedances which have  $R/Z_0 < 1$  is impossible. For comparison, one may refer to published analytical expressions<sup>4</sup> for the length and impedance of the matching section.

<sup>3</sup> The following rules will define which of the two possible intersections is used: 1) if the original point is in the upper half-plane the motion is downward and vice versa; 2) the first intersection encountered is the correct one.

<sup>4</sup> "Very High-Frequency Techniques," Radio Res. Lab., Harvard Univ., McGraw-Hill Book Co., Inc., New York, N. Y., and London, Eng. (first ed.), vol. 1, p. 60; 1947.

### A TYPICAL BROAD-BAND MATCHING PROBLEM

This problem will be described very briefly. A model of an antenna for use with a 50-ohm system was measured with a standing-wave line, eight points being measured in the band 96 to 300 mc. (These were model-testing frequencies; the actual antenna was to operate at frequencies lower by a factor of 48.) The points were plotted on a chart similar to Fig. 1, using the VSWR and position of the minimum to locate the points. The resultant curve made several excursions over the chart and reached some values of VSWR as high as 12. The position of the curve, mainly in the upper half-plane, suggested the use of a matching section of higher impedance. So as a first trial a 97-ohm line, having an electrical length of  $10^\circ$  at 100 mc, was tried. This line was thought of as having a length of  $1^\circ$  per 10 mc. Using one divider setting of the ratio 97 to 50, the points were moved down, then around counterclockwise, increasing the angle reading by an appropriate amount for each frequency, for example, a  $17.5^\circ$  increase at 175 mc. Then, with the same divider setting, the points were moved vertically upward, thus giving the final VSWR. No writing was done on the chart itself, one point being treated at a time and the final VSWR being plotted on a linear scale of VSWR vs frequency. One single setting of a slide rule gave the electrical length for all frequencies. The final choice was a 75-ohm line of length  $2^\circ$  per 10 mc, which matched the antenna to within a VSWR of 3.5. This provided a very economical matching device since it was necessary only to replace 17.3 feet of 50-ohm cable with 75-ohm cable (17.3 feet in the actual antenna, not the scale model). This type of problem, where the final match requirement is not severe, is often amenable to this kind of matching. The time required to plot each VSWR vs frequency curve was about six minutes.

### USE OF THE CHART FOR ADMITTANCE

As with the conventional impedance charts, the present chart may be used to represent admittance instead of impedance, the abscissa scale then being  $B/G$ , and the ordinate scale  $G/Y_0$ . The right-hand (positive) side of the chart which is inductive for the impedance chart becomes capacitive when the chart is used as an admittance chart and vice versa. To change from impedance to admittance the point is moved  $90^\circ$  in either direction along a line of constant VSWR.

### ACKNOWLEDGMENT

Plotting of the digital computer data and the layout were done by E. J. Stevens, and the charts were drawn by E. W. B. Goffin.

# The Far Fields Excited by a Point Source in a Passive Dissipationless Anisotropic Uniform Waveguide\*

A. D. BRESLER†

**Summary**—The direction of the net power flow associated with a propagating mode of an arbitrary passive dissipationless anisotropic uniform waveguide may be opposite to its direction of (phase) propagation. It is shown that when a point source is introduced into a waveguide in which this is the case, such propagating modes contribute to the fields excited by this source only in that direction for which their power flow is directed away from the source. In addition it is shown that the nonpropagating modes contribute to the total field only in that direction in which they decay with increasing distance away from the source so that the far fields are given by a superposition of propagating modes only. The proof given makes use of the known properties of the frequency dependence of the physical parameters of any linear passive system in which the causality restriction is satisfied.

## INTRODUCTION

THE motivation for the study reported here becomes evident when one attempts to formulate the solutions to discontinuity problems involving waveguides containing anisotropic media. For example, let us consider the discontinuity problem posed by the introduction of a perfectly conducting transverse obstacle into a perfectly conducting rectangular waveguide which is either empty or, as in Fig. 1, partially filled with a dissipationless anisotropic ferrite. In either case, the formulation of the solution to the problem involves replacing the obstacle by a distribution of induced currents [1] and, for all  $z \neq z'$ , expressing the total field in the waveguide as the sum of the specified excitation plus the fields excited by the induced sources. Thus, to solve these problems requires a knowledge of the fields excited by a point source located at  $z = z'$  in the uniform waveguide with the discontinuity removed, *i.e.*, the Green's function for the uniform waveguide. Although we have argued from a specific example, it is well known that the conclusion can be generalized to the statement that the solution to any discontinuity problem requires that, in one guise or another, we introduce the Green's function for the uniform waveguide as an integrating factor. In the following we are concerned with the modal descriptions for such Green's functions. In this discussion we employ the term "mode" in a somewhat different sense from the conventional usage and we therefore first digress to clarify this point.

\* Manuscript received by the PGMTT, November 10, 1958. The investigation reported herein has been made possible by the support of the U. S. Air Force under Contract No. AF-19(604)-2031. This paper is based on a portion of a dissertation "On the discontinuity problem at the input to an anisotropic waveguide," submitted in partial fulfillment of the requirements for the D.E.E. degree at the Polytechnic Inst. of Brooklyn, Brooklyn, N. Y. This dissertation will also be issued as Rep. R-716-59 of the Microwave Res. Inst.

† Microwave Res. Inst., Polytechnic Inst. of Brooklyn, Brooklyn, N. Y.

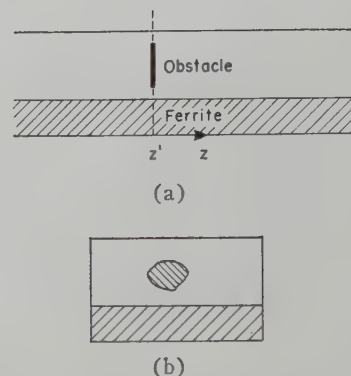


Fig. 1—Obstacle in a partially filled rectangular waveguide. (a) Longitudinal section. (b) Cross section at  $z = z'$ .

The modes of a uniform waveguide are taken to be those combinations of electric and magnetic fields which, together, comprise admissible solutions to the homogeneous time-independent Maxwell equations. These equations constitute an eigenvalue problem for the determination of the modes and of their associated propagation constants, or eigenvalues,  $\kappa$  [2]–[4]. Isotropic uniform waveguides are reflection symmetric; *i.e.*, they are invariant to a reflection through any plane transverse to  $z$ , and therefore if  $\kappa$  is an eigenvalue then  $-\kappa$  must also be an eigenvalue. The manner in which we have defined a mode implies that we must distinguish between the modes associated with  $\pm\kappa$ . In isotropic waveguides the mode associated with  $-\kappa$  may be obtained from that for  $+\kappa$  by simply reversing the direction of the transverse magnetic field. Thus, for example, we describe an empty rectangular waveguide propagating only the  $TE_{10}$  mode as one which supports two propagating modes which propagate in opposite directions with equal magnitude propagation constants. The time and  $z$  dependence of a mode are taken as  $\exp i(\kappa z - \omega t)$  so that the propagating modes are associated with real propagation constants.

In the discussion which follows we contrast certain properties of "conventional" and "anisotropic" waveguides. We define a "conventional" waveguide as a uniform waveguide completely filled with a passive dissipationless isotropic homogeneous medium and bounded (if at all) by electric walls. By an "anisotropic" waveguide we mean a uniform waveguide containing passive anisotropic media and bounded (if at all) by a combination of electric, magnetic, and other reactive walls. Uniform waveguides which are both dissipationless and "anisotropic" comprise the entire class of passive dissipationless uniform waveguides [2], [3].



The modal description for the fields produced in a conventional waveguide by a point source at  $z=z'$  distinguishes between the two regions  $z \geq z'$  as follows. In each of these two regions the total field is described in terms of only those cut-off modes which decay in the direction away from the source and those propagating modes which propagate away from the source, not in terms of all the modes. In conventional waveguides the direction of the net power flow associated with a propagating mode coincides with its direction of (phase) propagation. Thus, for  $z \geq z'$ , the far fields at  $|z-z'| \rightarrow \infty$  consist of superpositions of propagating modes which, individually, propagate and transport energy in the direction away from the source. The cut-off modes of a conventional waveguide are characterized by purely imaginary  $\kappa$ . Thus they are properly described as non-propagating and one is not surprised to find that, considered individually, there is no net power flow associated with these modes.

In dissipationless anisotropic waveguides the cut-off modes need no longer be characterized by imaginary  $\kappa$  only, but may be associated with complex  $\kappa$  which must occur in complex conjugate pairs. The cut-off modes associated with complex  $\kappa$  are, strictly speaking, no longer describable as nonpropagating modes. Despite this it can be shown that, taken individually, there is no net power flow associated with these modes [2], [4]. Since the cut-off modes again contribute only to the energy stored in the waveguide, we expect (and will prove) that only those cut-off modes are excited which decay exponentially in the direction away from the source. Thus the far fields at  $|z-z'| \rightarrow \infty$  will again consist of a superposition of propagating modes only.

For a dissipationless anisotropic waveguide which is not reflection symmetric<sup>1</sup> the real eigenvalues associated with the propagating modes need not occur in positive and negative pairs. In an extreme case, one might find that all the propagating modes have positive propagation constants. It does not seem likely that all these modes will contribute only for  $z > z'$  and that the far field for  $z < z'$  will vanish. Indeed, with this assumption, an ideal system can be constructed which violates basic thermodynamic principles [5]. The key to the riddle is supplied by the recognition that, in anisotropic waveguides, the direction of the net power flow associated with a propagating mode may be opposite to its direction of (phase) propagation. Now, while it must certainly be true that the net power flow associated with the total far fields must always be directed outward from the source, this alone does not automatically imply that each propagating mode which contributes to the far field must, individually, carry power away from the source. However, it appears intuitively obvious (at least to the author) that it must be the direction of energy trans-

port, not propagation, which is significant in determining the direction in which a given propagating mode contributes. In the following we prove that this is indeed the case; *i.e.*, when a point source is introduced into a passive dissipationless anisotropic waveguide, the far fields in either direction away from the source consist of only those propagating modes which transport energy in that direction.

#### THE GREEN'S FUNCTION FOR AN ARBITRARY UNIFORM WAVEGUIDE

The steady-state Maxwell equations are written here in terms of linear operators  $\mathcal{L}$  and  $\Gamma_z$ , in a form which displays explicitly the dependence on the longitudinal coordinate  $z$  only, as follows [2], [3]:

$$\left( \mathcal{L} - \frac{1}{i} \frac{\partial}{\partial z} \Gamma_z \right) \Psi(z) = -i\Phi(z) \quad (1)$$

where

$$\mathcal{L} = \omega W - \Gamma_{pt} \rightarrow \omega \begin{pmatrix} \epsilon & 0 \\ 0 & \mu \end{pmatrix} - \begin{pmatrix} 0 & \nabla_t \times 1 \\ \nabla_t \times 1 & 0 \end{pmatrix}, \quad (2)$$

$$\Gamma_z \rightarrow \begin{pmatrix} 0 & iz_0 \times 1 \\ iz_0 \times 1 & 0 \end{pmatrix}, \quad (3)$$

$$\Psi(z) \rightarrow \begin{pmatrix} \mathbf{E}(z) \\ i\mathbf{H}(z) \end{pmatrix}, \quad \Phi(z) \rightarrow \begin{pmatrix} \mathbf{J}(z) \\ i\mathbf{M}(z) \end{pmatrix}, \quad (4)$$

where  $\mathbf{E}(z)$  and  $\mathbf{H}(z)$  are the steady-state electric and magnetic fields, respectively;  $\mathbf{J}(z)$  and  $\mathbf{M}(z)$  represent the distributions of electric and magnetic current sources, respectively;  $\mu$  and  $\epsilon$  are, respectively, the ( $z$ -independent) permeability and permittivity dyadics for the media filling the guide;  $\nabla_t$  is the transverse gradient operator;  $1$  is the unit dyadic; and  $\mathbf{z}_0$  is the unit vector in the longitudinal direction. In (2)–(4) an arrow is used to indicate that the matrices constitute representations of abstract elements and operators in a properly defined space. The rules for operation of operators on elements or for the sequential operation of two operators consist of the normal rules of matrix algebra with the understanding that the dot product is implied for products of dyadics and vectors or of two dyadics.

The steady-state Maxwell equations (1) provide a unique specification for  $\Psi(z)$  only when we specify the boundary conditions on  $\Psi(z)$  at the waveguide walls. By the same token,  $\mathcal{L}$  is not uniquely defined unless we associate with its (formal) definition (2) a statement of the boundary conditions to be satisfied at the waveguide walls by all elements  $\Psi$  on which  $\mathcal{L}$  is to operate. This statement of boundary conditions constitutes a specification of a "domain" for  $\mathcal{L}$  and serves to distinguish a particular  $\mathcal{L}$  from all other operators  $\mathcal{L}$  with the same (formal) matrix representation [3].

To effect the reduction of the inhomogeneous Maxwell equations (1) to an equivalent point source excitation problem, we introduce an operator Green's function  $g(z, z')$  via the requirement

<sup>1</sup> Waveguides containing media with purely transverse anisotropy (*e.g.*, gyrotropic media magnetized parallel to the waveguide axis) retain the reflection symmetry property [4].

$$\Psi(z) = -i \int_{-\infty}^{\infty} \mathcal{G}(z, z') \Phi(z') dz'. \quad (5)$$

Assuming the validity of the required interchange of differentiation and integration operations, etc., it is evident that substitution from (5) into (1) yields:

$$\left( \mathcal{L} - \frac{1}{i} \frac{\partial}{\partial z} \Gamma_z \right) \mathcal{G}(z, z') = I \delta(z - z') \quad (6)$$

as the equation which  $\mathcal{G}(z, z')$  must satisfy. In this equation  $\delta(z - z')$  is the unit impulse function and  $I$  is the unit operator in the space of all coordinates still held abstract. For our purposes it is not necessary to exhibit any details of the inner structure of the (operator) Green's functions. The interested reader will find these details given in another report [3].

Thus far we have dealt with  $z$ -dependent problems. For an infinite uniform waveguide the  $z$  dependence may be eliminated by the introduction of Fourier integral representations for all  $z$ -dependent quantities. In particular, we represent  $\mathcal{G}(z, z')$  as follows:

$$\mathcal{G}(z, z') = \frac{1}{2\pi} \int_{-\infty}^{\infty} \mathcal{G}(\kappa) e^{i\kappa(z-z')} d\kappa \quad (\text{Im } \kappa = 0). \quad (7)$$

Again assuming the validity of the required interchanges of differentiation and integration operations, we substitute from (7) into (6) to obtain:

$$(\mathcal{L} - \kappa \Gamma_z) \mathcal{G}(\kappa) = I \quad (8)$$

as the equation which  $\mathcal{G}(\kappa)$  must satisfy. Thus,  $\mathcal{G}(\kappa)$  is seen to be the "resolvent operator" or "characteristic Green's function" for the operator  $\mathcal{L}$ . As such it can be shown [6] that  $\mathcal{G}(\kappa)$  is analytic almost everywhere in the complex  $\kappa$  plane. The singularities of  $\mathcal{G}(\kappa)$  are found to be poles<sup>2</sup> located at points in the complex  $\kappa$  plane corresponding to the eigenvalues of  $\mathcal{L}$  [6]. Thus, in dissipationless waveguides,  $\mathcal{G}(\kappa)$  may have poles on the real  $\kappa$  axis. When such real poles occur, the integral in (7) is not well defined. In this case, to insure the uniqueness of the transform relation, we introduce the usual "small loss approximation" by allowing  $\omega$  to take on a small positive imaginary part (*i.e.*,  $1 \gg \text{Im } \omega > 0$ ). When this is done, all real eigenvalues are displaced off the real axis and the integral in (7) provides a unique specification for  $\mathcal{G}(z, z')$ .

#### THE FAR FIELDS EXCITED BY A POINT SOURCE

In the discussion which follows we confine our attention to passive dissipationless uniform waveguides. We assume that all the eigenvalues of the operator  $\mathcal{L}$  associated with a waveguide of this type are known and

<sup>2</sup> For waveguides with open cross sections one also finds branch point singularities. These imply the necessity of introducing branch cuts to define a unique  $\mathcal{G}(\kappa)$  satisfying appropriate restrictions on the behavior of the fields in the transverse plane. Points on the branch cut correspond to eigenvalues of a continuous spectrum. For our purposes it is sufficient to view such a branch cut as a coalescence of a dense set of poles [6].

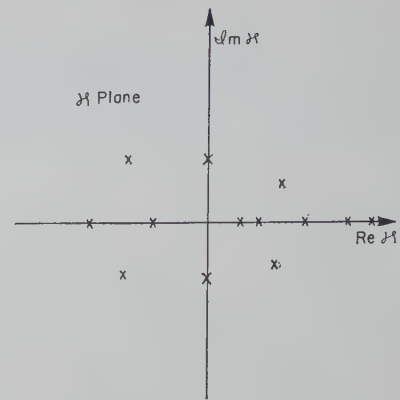


Fig. 2—Locations of poles of  $\mathcal{G}(\kappa)$  when  $\text{Im } \omega = 0$ .

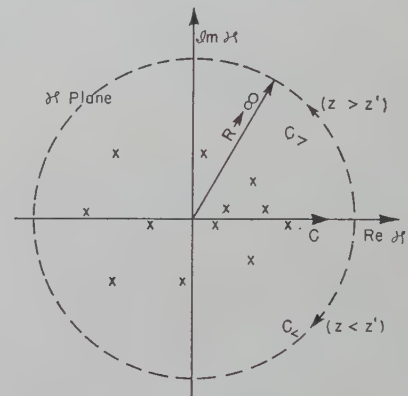


Fig. 3—Integration paths used in evaluating  $\mathcal{G}(z, z')$  when  $1 \gg \text{Im } \omega > 0$ .

that these are located in the complex  $\kappa$  plane as indicated in Fig. 2. The disposition shown for the real propagation constants is appropriate to a waveguide which is not reflection symmetric. Only a few of the infinity of complex eigenvalues corresponding to the cut-off modes are shown in Fig. 2. These are shown to occur in complex conjugate pairs as is appropriate for a dissipationless waveguide. When we allow  $\omega$  to take on a small positive imaginary part, the real eigenvalues are displaced off the real axis as indicated in Fig. 3. The complex eigenvalues are also shifted slightly. However, for sufficiently small  $\text{Im } \omega$ , these remain in that half plane (above and below the real axis) in which they were located with  $\text{Im } \omega = 0$ .

An expression for  $\mathcal{G}(z, z')$  in terms of residues at the poles of  $\mathcal{G}(\kappa)$  is obtained by recognizing that  $\int \mathcal{G}(\kappa) \exp i\kappa(z-z') d\kappa$  taken over the path  $C$  (see Fig. 3) is identical with the closed contour integral over either  $C + C_{\infty}$  according as  $z \geq z'$ . This is so because the behavior of  $\mathcal{G}(\kappa)$  as  $\kappa \rightarrow \infty$  is such that the specified integral vanishes over  $C_{\infty}$  according as  $z \geq z'$  [6]. Therefore, contributions to  $\mathcal{G}(z, z')$  for  $z \geq z'$  arise only from the residues at poles for which  $\text{Im } \kappa \geq 0$ . The residue series for  $\mathcal{G}(z, z')$  is, for all  $z \neq z'$ , equivalent to a modal representation for this operator [6]. It therefore follows that, in each of the two regions  $z \geq z'$ ,  $\mathcal{G}(z, z')$  is completely specified by a superposition of only those modes which



decay in the direction away from the source. This establishes that, in the limit as  $\text{Im } \omega \rightarrow 0$ , the far fields excited by a point source will consist of superpositions of propagating modes only.

There still remains the question of determining whether a particular propagating mode contributes to the field for  $z > z'$  or  $z < z'$ . To answer this question we must determine whether a particular propagation constant  $\kappa_\alpha$  which is real for  $\text{Im } \omega = 0$  has a positive or a negative imaginary part when  $\text{Im } \omega > 0$ . This in turn requires information concerning the frequency derivative of a real propagation constant since, for  $1 \gg \text{Im } \omega > 0$ , we may approximate the shifted value of  $\kappa_\alpha$  by:<sup>3</sup>

$$\kappa_\alpha(\omega \neq \omega^*) = \kappa_\alpha(\omega = \omega^*) + i \frac{d\kappa_\alpha(\omega = \omega^*)}{d\omega} \text{Im } \omega + \dots \quad (9)$$

Thus, for small positive  $\text{Im } \omega$ ,  $\text{Im } \kappa_\alpha \geq 0$  according as

$$\frac{d\kappa_\alpha(\omega = \omega^*)}{d\omega} \geq 0.$$

This result obtains in any dissipationless waveguide. In the next section we demonstrate that, for waveguides which are both passive and dissipationless,

$$\frac{d\kappa_\alpha(\omega = \omega^*)}{d\omega}$$

is positive or negative according as the power flow associated with the corresponding propagating mode is positive or negative. This will complete the proof for the statement that in any passive dissipationless waveguide a propagating mode contributes to the field of a point source only in that direction for which the transport of energy is outward from the source.

#### ON THE FREQUENCY DERIVATIVE OF A REAL PROPAGATION CONSTANT

To establish a connection between the power flow associated with a propagating mode and the frequency derivative of its propagation constant, we deal with the eigenvalue problem:

$$(\mathcal{L} - \kappa_\alpha \Gamma_z) \Psi_\alpha = 0 \quad (10)$$

which determines the  $z$ -independent mode function  $\Psi_\alpha \equiv \Psi(\kappa_\alpha)$  associated with the eigenvalue  $\kappa_\alpha$ . The eigenvalue problem (10) is obtained from (1) by setting  $\Phi(z) = 0$ , taking the  $z$  dependence of  $\Psi(z)$  as  $\exp i\kappa_\alpha z$  and eliminating the  $z$  dependence. In this section we have occasion to deal with both  $z$ -dependent and  $z$ -independent elements. The dependence on  $z$  will be explicitly indicated for the former.

To obtain the results we are seeking, it is necessary to exploit certain properties of  $\mathcal{L}$  and  $\Gamma_z$  which become evident only after we have introduced an adjointness con-

cept for operators. For this purpose we define the (hermitian) inner product [3] of two elements via:

$$(\Psi_\beta, \Psi_\alpha) = \iint_S [E_\beta^* \cdot E_\alpha + (iH_\beta)^* \cdot (iH_\alpha)] dS. \quad (11)$$

This definition requires an integration over the cross section,  $S$ , of the waveguide in addition to the operations usually required to obtain the (hermitian) inner product of column matrices. Based on this inner product there is associated with a given operator, *e.g.*,  $\mathcal{L}$ , an adjoint operator  $\mathcal{L}^+$  via the adjointness relation [3]:

$$(\Psi^+, \mathcal{L}\Psi) - (\mathcal{L}^+\Psi^+, \Psi) = 0. \quad (12)$$

As it stands, this relation provides only the formal definition (matrix representation) for  $\mathcal{L}^+$ . As was the case with  $\mathcal{L}$ ,  $\mathcal{L}^+$  is not uniquely defined without a specification of its domain. This is provided by choosing the domain of  $\mathcal{L}^+$  as the set of all elements  $\Psi^+$  so that (12) is satisfied for all elements  $\Psi$  in the domain of  $\mathcal{L}$ .

$\mathcal{L}$  is hermitian, *i.e.*,  $\mathcal{L} = \mathcal{L}^+$ , when the matrix representations and the domains of  $\mathcal{L}$  and  $\mathcal{L}^+$  are identical. It is evident from (11) and (12) that the inner product  $(\Psi, \mathcal{L}\Psi)$  is real when  $\mathcal{L}$  is hermitian, imaginary when  $\mathcal{L}$  is skew hermitian ( $\mathcal{L} = -\mathcal{L}^+$ ). It therefore follows that any operator may be expressed as the sum of hermitian and skew hermitian parts by writing, *e.g.*,  $\mathcal{L} = \mathcal{L}_1 + i\mathcal{L}_2$  with  $\mathcal{L}_{1,2} = \mathcal{L}_{1,2}^+$ .  $\mathcal{L}^+$  is then given by  $\mathcal{L}^+ = \mathcal{L}_1 - i\mathcal{L}_2$  and it is therefore appropriate to designate  $\mathcal{L}_1 = \text{Re } \mathcal{L}$  and  $\mathcal{L}_2 = \text{Im } \mathcal{L}$ . A positive hermitian operator,  $\mathcal{L} = \mathcal{L}^+ > 0$ , is defined as one for which  $(\Psi, \mathcal{L}\Psi) > 0$  for every  $\Psi \neq 0$  in the domain of  $\mathcal{L}$ .

We turn now to a consideration of the properties of the operators  $\mathcal{L} = \omega W - \Gamma_{pt}$  and  $\Gamma_z$ . It is evident that  $\mathcal{L}^+ = \omega^* W^+ - \Gamma_{pt}^+$  and therefore, in considering  $\mathcal{L}$ , we examine the properties of  $W$  and  $\Gamma_{pt}$  separately. Since the matrix representations in (2) and (3) for  $W$  and  $\Gamma_z$ , respectively, contain no differentiation operations, the domains of these operators need not be artificially restricted and it follows from (12) that the matrix representations for  $W^+$  and  $\Gamma_z^+$  are simply the conjugate transpose of those for  $W$  and  $\Gamma_z$ , respectively. It is further evident from ordinary matrix considerations that  $\Gamma_z = \Gamma_z^+$ . For an arbitrary electromagnetic field (element)  $\Psi$  we find, on substitution from (3) and (4) into (12), that:

$$(\Psi, \Gamma_z \Psi) = 2 \text{Re} \iint_S z_0 \cdot E \times H^* dS = 2P \quad (13)$$

where  $P$  is the net power flow along  $+z$  associated with the electromagnetic field. For an arbitrary  $z$ -dependent element  $\Psi(z)$  we find, on substitution from (2) and (4) into (12), that:

$$\begin{aligned} & \int_{z_1}^{z_2} (\Psi(z), W\Psi(z)) dz \\ &= \int_{z_1}^{z_2} \iint_S [E^*(z) \cdot \epsilon \cdot E(z) + H^*(z) \cdot \mu \cdot H(z)] dS dz. \end{aligned} \quad (14)$$

<sup>3</sup> To write this equation it must be assumed that  $\kappa_\alpha$  is an analytic function of  $\omega$  in a suitable neighborhood of the real  $\omega$  axis. This assumption is justified by the results obtained in the next section.

The imaginary part of the integral on the right represents the energy/cycle dissipated in the waveguide between the two transverse planes at  $z_1$  and  $z_2$  and it must therefore be zero for passive dissipationless media, positive when dissipation is present. Since this must be true for any arbitrary  $z$  dependence in  $\Psi(z)$  it follows that passive dissipationless media are characterized by  $W = W^+$ . For passive media, dissipationless or not, we must have  $\text{Re } -i\omega W \geq 0$ . It is pertinent to remark that  $\text{Re } -i\omega W$  is a measure of the power dissipated in the waveguide.

To evaluate  $\Gamma_{pt}^+$  we examine

$$\begin{aligned} (\Psi^+, \Gamma_{pt}\Psi) - (\Gamma_{pt}\Psi^+, \Psi) \\ = i \iint_S [E^{+*} \cdot \nabla_t \times H - H \cdot \nabla_t \times E^{+*} \\ - H^{+*} \cdot \nabla_t \times E + E \cdot \nabla_t \times H^{+*}] dS \end{aligned} \quad (15)$$

where  $\Psi$  is in the domain of  $\Gamma_{pt}$ . By application of the appropriate Green's identity we replace the surface integral by a line integral to obtain

$$\begin{aligned} (\Psi^+, \Gamma_{pt}\Psi) - (\Gamma_{pt}\Psi^+, \Psi) \\ = -i \oint \mathbf{v} \cdot [E \times H^{+*} + E^{+*} \times H] ds \end{aligned} \quad (16)$$

where  $\mathbf{v}$  is the unit outward normal at the waveguide walls and  $s$  is the coordinate along the periphery of the waveguide cross section (see Fig. 4).

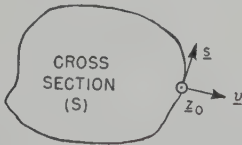


Fig. 4—Coordinates on the waveguide walls.

This last result makes evident that  $\Gamma_{pt}$  and  $\Gamma_{pt}^+$  have the same matrix representations provided that the domain of  $\Gamma_{pt}^+$  is chosen so that the boundary integral on the right vanishes identically. For complete generality we assume that  $E$  and  $H$  satisfy an impedance boundary condition at the waveguide walls.

Thus, we prescribe:

$$E = Z \cdot H \times \mathbf{v} \quad (\text{on boundaries}) \quad (17)$$

where  $Z$  is a dyadic with components in the  $sz$  plane only. When this boundary condition is introduced into (16) it becomes evident that the domain of  $\Gamma_{pt}^+$  is defined by the boundary condition  $E^+ = \tilde{Z} \cdot H \times \mathbf{v}$  with  $\tilde{Z} = -Z^*$ ; i.e.,  $\tilde{Z}$  is the negative of the conjugate transpose of  $Z$ . Therefore,  $\Gamma_{pt} = \Gamma_{pt}^+$  when  $Z = -\tilde{Z}^*$ , i.e., when the waveguide is bounded by a combination of reactive walls. The limiting cases of electric walls ( $Z=0$ ) and magnetic walls ( $Z^{-1}=0$ ) are obviously included within the class of reactive walls.

For our purposes it is significant to point out that:

$$\begin{aligned} \int_{z_1}^{z_2} \oint \mathbf{v} \cdot E(z) \times H^*(z) ds dz \\ = \text{Re} \int_{z_1}^{z_2} \oint H^*(z) \times \mathbf{v} \cdot Z \cdot H(z) \times \mathbf{v} ds dz \end{aligned} \quad (18)$$

represents the power flow into the section of the waveguide walls lying between  $z_1$  and  $z_2$ . The boundary integral on the right may obviously be expressed in terms of an inner product definition similar to that in (11). In this sense, we shall understand  $\text{Re } Z$  and  $\text{Im } Z$  to imply the hermitian and skew hermitian parts of  $Z$ , respectively. Then, arguing as we did in connection with (14), we recognize that  $\text{Re } Z \geq 0$  for passive boundaries with  $\text{Re } Z = 0$  for reactive (i.e., passive dissipationless) boundaries. Since  $\text{Re } Z = 0$  is equivalent to  $Z = -\tilde{Z}^* = -Z^+$ , it follows that  $\Gamma_{pt}$  is hermitian for waveguides bounded by passive dissipationless walls. When we add to this the fact that  $W = W^+$  for passive dissipationless media, it becomes evident that, for real  $\omega$ , passive dissipationless waveguides are characterized by  $\mathcal{L} = \mathcal{L}^+$ .

We are now in possession of all the tools we require to establish a connection between the power flow ( $P_\alpha$ ) associated with a propagating mode ( $\Psi_\alpha$ ) of a passive dissipationless waveguide and the frequency derivative of its real propagation constant ( $\kappa_\alpha$ ). We first show that, in general, the product  $\kappa_\alpha P_\alpha$  need not be positive. To do this we form the inner product of (10) with  $\Psi_\alpha$  to obtain:<sup>4</sup>

$$\kappa_\alpha = \frac{(\Psi_\alpha, \mathcal{L}\Psi_\alpha)}{(\Psi_\alpha, \Gamma_z\Psi_\alpha)} = \frac{(\Psi_\alpha, \mathcal{L}\Psi_\alpha)}{2P_\alpha}. \quad (19)$$

Thus  $\kappa_\alpha$  and  $P_\alpha$  must have the same sign, i.e., the directions of propagation and of energy transport must coincide, only when  $\mathcal{L} > 0$ . In general,  $\mathcal{L}$  is not positive and therefore  $\kappa_\alpha P_\alpha$  is not necessarily positive. To obtain an expression for the derivative of  $\kappa_\alpha$  we first differentiate (10) to obtain:

$$(\mathcal{L}' - \kappa_\alpha' \Gamma_z) \Psi_\alpha + (\mathcal{L} - \kappa_\alpha \Gamma_z) \Psi_\alpha' = 0 \quad (20)$$

where the prime superscript indicates differentiation with respect to real  $\omega$ . Forming the inner product of this equation with  $\Psi_\alpha$  we obtain

$$\kappa_\alpha' = \frac{(\Psi_\alpha, \mathcal{L}'\Psi_\alpha) + (\Psi_\alpha, \mathcal{L}\Psi_\alpha') - \kappa_\alpha (\Psi_\alpha, \Gamma_z\Psi_\alpha')}{2P_\alpha}. \quad (21)$$

Since the domain of  $\mathcal{L}$  is defined by the boundary condition (17), the boundary condition satisfied by  $\Psi_\alpha'$  is:

$$E_\alpha' = Z \cdot H_\alpha' \times \mathbf{v} + Z' \cdot H_\alpha \times \mathbf{v} \quad (22)$$

so that  $\Psi_\alpha'$  does not lie in the domain of  $\mathcal{L}$  unless  $Z' = 0$ .

<sup>4</sup> Since  $\mathcal{L}$  and  $\Gamma_z$  are both hermitian,  $\kappa_\alpha$  is given here as the ratio of two real numbers. This expression must, however, be valid for all  $\kappa_\alpha$ , real or complex. This apparent contradiction is resolved by recognizing that, for  $\text{Im } \kappa_\alpha \neq 0$ , both numerator and denominator are equal to zero [2], [4].



Since  $\mathcal{L} = \mathcal{L}^+$ ,  $\Gamma_z = \Gamma_z^+$ , and  $\kappa_\alpha = \kappa_\alpha^*$  it follows that, for  $Z' = 0$ , i.e., for frequency independent boundary conditions:

$$(\Psi_\alpha, \mathcal{L}\Psi_\alpha') = (\mathcal{L}\Psi_\alpha, \Psi_\alpha') = \kappa_\alpha(\Psi_\alpha, \Gamma_z\Psi_\alpha') \quad (23)$$

so that the last two terms in the numerator of (21) cancel each other. When  $Z' \neq 0$ , the properties  $W = W^+$  and  $Z = -Z^+$  still obtain. These may then be employed, together with (16), (17), and (22), to establish that:

$$(\Psi_\alpha, \mathcal{L}\Psi_\alpha') - (\mathcal{L}\Psi_\alpha, \Psi_\alpha') = \oint H_\alpha^* \times \mathbf{v} \cdot iZ' \cdot H_\alpha \times \mathbf{v} ds. \quad (24)$$

Therefore, in general, the expression for  $\kappa_\alpha'$  in (21) becomes:

$$2P_\alpha\kappa_\alpha' = (\Psi_\alpha, \mathcal{L}\Psi_\alpha') + \oint H_\alpha^* \times \mathbf{v} \cdot iZ' \cdot H_\alpha \times \mathbf{v} ds. \quad (25)$$

To establish that  $P_\alpha\kappa_\alpha' > 0$  we must now show that  $\mathcal{L}' > 0$  and  $iZ' > 0$ . Since  $\Gamma_p$  is independent of  $\omega$ , the requirement  $\mathcal{L}' > 0$  is equivalent to  $(\omega W)' > 0$ .

To complete our proof we will invoke results established by Wu [7], Toll [8], and Youla [9]. These authors have studied the properties of "impedance operators"  $Z(\omega)$  associated with linear passive systems which satisfy the causality restriction and in which a real excitation gives rise to a real response. In essence, to qualify as an "impedance operator,"  $Z(\omega)$  must be a linear operator which determines the response of such a system and, for real  $\omega$ , the real (hermitian) part of  $Z(\omega)$  must be a measure of the dissipation of the system so that  $\text{Re } Z(\omega) \geq 0$  for all  $\omega = \omega^*$ . The authors cited above have shown that: 1)  $Z(\omega)$  is analytic and  $\text{Re } Z(\omega) \geq 0$  in the upper half plane ( $\text{Im } \omega > 0$ ); 2) the limit of  $Z(\omega)$  as  $\text{Im } \omega \rightarrow 0$  exists from above almost everywhere on the real  $\omega$  axis; and 3)  $Z(\omega) = Z^+(\omega)$  for  $\omega = -\omega^*$ . In addition, Youla [9] has shown that when  $Z(\omega) = -Z^+(\omega)$  for  $\omega = \omega^*$ , the derivative of  $\text{Im } Z(\omega)$  on the real  $\omega$  axis is always negative.<sup>5</sup> Now, it follows from the identifications based on (14) and (18) that both  $-i\omega W$  and  $Z$  qualify as impedance operators and, in the dissipationless case, both are skew hermitian for real  $\omega$ . Therefore  $(\omega W)' > 0$  and  $iZ' > 0$  so that:

$$\kappa_\alpha' P_\alpha > 0. \quad (26)$$

<sup>5</sup> This statement ignores the possibility that  $Z(\omega)$  may represent the impedance of, e.g., a "short circuit" so that the derivative of  $\text{Im } Z(\omega)$  on the real  $\omega$  axis is equal to zero for all real  $\omega$ .

This completes the proof for the statement that in any passive dissipationless waveguide a propagating mode contributes to the field excited by a point source only in that direction for which the power flow is directed outward from the source.

It is of interest to note that it follows from (26) that  $\kappa_\alpha'$  cannot equal zero unless  $P_\alpha$  is infinite. We therefore do not expect to find maximum or minimum points of  $\kappa_\alpha(\omega)$  at any finite value of  $\kappa_\alpha$ . This interpretation also applies to modes of the continuous spectrum of a waveguide with open cross section. In this case both numerator and denominator of (21) are proportional to delta functions so that  $\kappa_\alpha'$  cannot be zero unless  $P_\alpha$  has a higher order infinity, i.e., unless the coefficient of the delta function in  $P_\alpha$  is itself infinite. It is reasonable to expect that this will not occur at a finite  $\kappa_\alpha$ .

#### ACKNOWLEDGMENT

The author is pleased to acknowledge his indebtedness to his thesis adviser, Prof. N. Marcuvitz, for his helpful criticism and pertinent suggestions.

#### BIBLIOGRAPHY

- [1] N. Marcuvitz and J. Schwinger, "On the representation of the electric and magnetic fields produced by currents and discontinuities in waveguides," *J. Appl. Phys.*, vol. 22, pp. 806-819; June, 1951.
- [2] A. D. Bresler, G. H. Joshi, and N. Marcuvitz, "Orthogonality properties for modes in active and passive uniform waveguides," *J. Appl. Phys.*, vol. 29, pp. 794-799; May, 1958.
- [3] A. D. Bresler and N. Marcuvitz, "Operator Methods in Electromagnetic Field Theory; I: Abstract Operator Formulation for the Maxwell Equations," *Microwave Res. Inst., Polytechnic Inst. of Brooklyn, Brooklyn, N. Y.*, Rep. R-495-56; May, 1956.
- [4] A. D. Bresler and N. Marcuvitz, "Operator Methods in Electromagnetic Field Theory; II: Guided Modes in Uniform Cylindrical Waveguide Regions," *Microwave Res. Inst., Polytechnic Inst. of Brooklyn, Brooklyn, N. Y.*, Rep. R-565-57; March, 1957.
- [5] B. Lax, "Combined panel session on propagation in doubly-refracting media and future directions for research in electromagnetic wave theory in modern physics," *IRE TRANS. ON ANTENNAS AND PROPAGATION*, vol. AP-4, pp. 573-576; July, 1956. This reference contains a discussion of a thermodynamic paradox which, while similar to the one to which we allude here, is based on the presumed existence of a waveguide which supports a single propagating mode in one direction only.
- [6] N. Marcuvitz, "Field representations in spherically stratified regions," *Commun. Pure Appl. Math.*, vol. 4, pp. 263-315; August, 1951. Also published in "Theory of Electromagnetic Wave: A Symposium," Interscience Publishers, Inc., New York, N. Y.; 1951.
- [7] T. T. Wu, "Causality and Frequency Response Functions," *Cruft Lab., Harvard University, Cambridge, Mass.*, Tech. Rep. No. 223; April 1, 1955.
- [8] J. S. Toll, "Causality and the dispersion relation: logical foundations," *Phys. Rev.*, vol. 104, pp. 1760-1770; December 15, 1956.
- [9] D. C. Youla, "Representation Theory of Linear Passive Networks," *Microwave Res. Inst., Polytechnic Inst. of Brooklyn, Brooklyn, N. Y.*, Rep. R-655-58; April, 1958.

# Analysis of a Negative Conductance Amplifier Operated with a Nonideal Circulator\*

E. W. SARD†

**Summary**—Negative conductance amplifiers are usually operated with a circulator in order to achieve greater gain-bandwidth products and stable operation. Typical circulators differ from ideal circulators in that the forward loss between ports is not zero, and the reverse isolation between ports is not infinite. The main effects of noninfinite isolation are shown to be a modified gain-bandwidth product and a change in output admittance of the circulator output port. These effects result principally from the finite isolation between the output and amplifier ports. The main effect of incidental dissipation has previously been shown to be an increase in system noise figure.

This paper considers only the effects caused by noninfinite isolation. A model of a lossless three-port circulator with noninfinite isolation is set up, and a negative conductance amplifier is considered to be connected to one port of this circulator. The magnitude of negative conductance is assumed to be limited to ensure a positive output conductance at the output port of the circulator (that is, the combination of negative conductance amplifier and nonideal circulator is assumed to be open-circuit stable). Subject to this assumption, the combination of negative conductance amplifier and nonideal circulator is then analyzed for its output admittance, available power gain, and effective input noise temperature.

## INTRODUCTION

THE gain-bandwidth product of a one-port negative conductance amplifier (such as a maser or reactance amplifier) is greatly increased by operation with a nonreciprocal device, in particular an ideal circulator. In addition, constancy of output admittance is also greatly increased. The question arises, what is the effect on operation if the circulator is not ideal, that is, the forward loss between ports is not zero and the reverse isolation between ports is not infinite? The main effects of noninfinite isolation will be shown to be a modified gain-bandwidth product and a change in output admittance of the circulator output port. These effects result principally from the finite isolation between the output and amplifier ports. The main effect of incidental dissipation has previously been shown to be an increase in system noise figure.<sup>1</sup>

This paper considers only the effects caused by noninfinite isolation. More complete models of a nonideal circulator can be formulated, if desired, by using an analysis similar to that presented here. It is believed, however, that the inclusion of small forward loss will have a direct effect only on the system noise figure while not appreciably affecting the output admittance or available power gain.

A three-port circulator is considered here, with the direction of power flow from port 1 (input) to port 2 (connected to the negative conductance amplifier) to port 3 (output). Specifically, a noninfinite isolation is assumed to exist between ports 3 and 2. No other departures from ideal characteristics are assumed except those resulting from the assumption of the circulator being lossless. Some workers<sup>1,2</sup> analyze the effect of this noninfinite isolation by a combination of Friis's classical treatment of the over-all noise figure of cascaded networks<sup>3</sup> and a consideration that noise power radiates back from the input terminals of the second stage to be amplified in the first stage. This is really not a rigorous application of Friis's work. Consider the following two possible cases.

The first possibility is that the first stage consisting of the negative conductance amplifier and the nonideal circulator has a positive output conductance (that is, the first stage is open-circuit stable). Then, as discussed by Friis, both the available power gain and the effective input noise temperature<sup>4</sup> of the first stage can be calculated for a particular generator admittance without specifying any characteristics of the second stage. The noise emanating from the input terminals of the second stage, if any, will affect only the effective input noise temperature of the second stage, which must be measured using a source admittance equal to the output admittance of the first stage. For this case, the over-all effective input noise temperature  $T$  can be expressed in terms of the first stage effective input noise temperature  $T_1$ , the first stage available power gain  $K_1$ , and the second stage effective input noise temperature  $T_2$  by the relation,  $T = T_1 + T_2/K_1$ . This assumes that subsequent stages do not contribute to the value of  $T$ . If they do, and if each subsequent stage has a positive output conductance, terms of the form  $T_n/K_1K_2 \cdots K_{n-1}$ , where  $n$  denotes the stage number, can be added to the relation for  $T$ .

The second possibility is that the first stage, consisting of the negative conductance amplifier and the nonideal circulator, has a negative output conductance. Then, to avoid oscillations, the input conductance of the second stage must be sufficiently positive to make the net conductance positive at the junction of the first and second stages. This possibility is actually more likely to

\* Manuscript received by the PGMTT, November 17, 1958. Revised manuscript received, December 29, 1958. Work for this paper was performed under Signal Corps Contract No. DA-36-039-sc-78161.

† Airborne Instruments Lab., div. Cutler-Hammer, Inc., Mineola, N. Y.

<sup>1</sup> F. R. Arams and G. Kray, "Design considerations for circulator maser systems," *PROC. IRE*, vol. 46, pp. 912-913; May, 1958.

<sup>2</sup> A. E. Siegman, "Gain bandwidth and noise in maser amplifiers," *Proc. IRE*, vol. 45, pp. 1737-1738; December, 1957.

<sup>3</sup> H. T. Friis, "Noise figures of radio receivers," *Proc. IRE*, vol. 32, pp. 419-422; July, 1944.

<sup>4</sup> Friis uses noise figure rather than effective input noise temperature, but this does not affect the argument, since the two quantities are directly related.



occur when operating a negative conductance amplifier without a nonreciprocal device. Here, very definitely, Friis's definitions do not directly apply since his concepts of available signal and noise power outputs are meaningless. In this case, it does seem reasonable to think of the noise from the input terminals of the second stage radiating back to the first stage to be amplified. Now, however, the characteristics of the second stage must be specified to describe the performance of the first stage. Furthermore, how does one calculate simply the contribution of the second stage to the over-all effective input noise temperature? The usual expedient is to assume that the first stage gain (not available gain) is so large that the second stage contribution is negligible. This may not be a good assumption in practice, however, when dealing with an extremely low noise first stage or with a second stage whose noisiness is critically dependent on its source admittance. In any case, from a theoretical standpoint it is desirable to have a rigorous method of calculating the contributions of the second stage and subsequent stages to the over-all effective input noise temperature. Only in this way can the importance of these contributions be quantitatively assessed.

Returning now to the approach taken in this paper, it seemed desirable to apply the classical treatment of Friis to the new situation of a negative conductance amplifier. This, clearly, can be done for the combination of the negative conductance amplifier and the nonideal circulator if the assumption is made that the output conductance is positive. This is a reasonable assumption if the circulator is well made and the gain is not too high. The inequality following (17) gives the quantitative condition required to satisfy this assumption.

It is then shown, using standard network analysis, that the finite isolation of the circulator principally affects the output admittance and available power gain of the combination of negative conductance amplifier and circulator. The effective input noise temperature, however, is but slightly affected.

#### ADMITTANCE MATRIX OF NONIDEAL THREE-PORT CIRCULATOR

The first step in the analysis is to determine the admittance matrix of the assumed model of a nonideal three-port circulator. A convenient way to do this is to make use of the scattering matrix concept.<sup>5</sup> Thus, a scattering matrix of a lossless three-port circulator with insertion power gain  $\epsilon^2$  between ports 3 and 2 is

$$S = \begin{bmatrix} j\epsilon & 0 & \sqrt{1-\epsilon^2} \\ \sqrt{1-\epsilon^2} & 0 & j\epsilon \\ 0 & 1 & 0 \end{bmatrix}. \quad (1)$$

Some discussion of (1) is in order. In general, the insertion power gain between ports  $m$  and  $n$  of a network is  $|s_{n,m}|^2$  (note the interchange in order of subscripts). Thus, having  $s_{23}=j\epsilon$  in (1) provides an insertion power gain  $\epsilon^2$  between ports 3 and 2, as desired. The assumed phase of  $s_{23}$ , as well as the particular nonideal values of  $s_{11}$ ,  $s_{13}$ , and  $s_{21}$ , seem to be the simplest way of maintaining the assumed lossless character of the circulator, the condition for which is  $[S^{*T}][S]=E$ , where  $[S^{*T}]$  is the matrix transpose of the complex conjugate of  $S$ , and  $E$  is the identity matrix.

If the currents and voltages at all three ports are normalized to the same conductance  $G_0$ , the admittance matrix is then

$$Y = G_0[E + S]^{-1}[E - S]. \quad (2)$$

Finally, substitution of (1) into (2) gives, for the admittance matrix of the nonideal three-port circulator,

$$Y = G_0 \begin{bmatrix} -j\epsilon & \sqrt{1-\epsilon^2} & -\sqrt{1-\epsilon^2} \\ -\sqrt{1-\epsilon^2} & j\epsilon & 1-j\epsilon \\ \sqrt{1-\epsilon^2} & -(1+j\epsilon) & j\epsilon \end{bmatrix} \quad (3)$$

$$= \begin{bmatrix} Y_{11} & Y_{12} & Y_{13} \\ Y_{21} & Y_{22} & Y_{23} \\ Y_{31} & Y_{32} & Y_{33} \end{bmatrix}.$$

As a sidelight, substitution of  $\epsilon=0$  in (3) gives the admittance matrix of an ideal three-port circulator;

$$[Y]_{\text{ideal}} = G_0 \begin{bmatrix} 0 & 1 & -1 \\ -1 & 0 & 1 \\ 1 & -1 & 0 \end{bmatrix}. \quad (4)$$

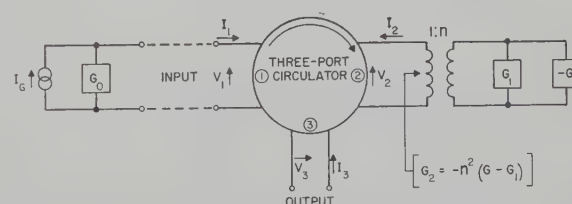


Fig. 1—Small-signal circuit of negative conductance amplifier-circulator combination.

#### OUTPUT ADMITTANCE OF NEGATIVE CONDUCTANCE AMPLIFIER WITH NONIDEAL CIRCULATOR

Fig. 1 shows the circuit of the negative conductance amplifier-circulator combination. The negative conductance amplifier is represented by a negative conductance  $-G$ , a circuit loss  $G_1$ , and an ideal transformer of turns ratio  $1:n$ . Also included are a current generator  $I_G$  and its associated conductance  $G_0$ . It is seen that this is a midband representation of the negative conductance amplifier, since no susceptances are shown.

The terminal currents and voltages at the three ports of the circulator are related by

<sup>5</sup> H. J. Carlin, "The scattering matrix in network theory," IRE TRANSACTIONS ON CIRCUIT THEORY, vol. CT-3, pp. 88-97; June, 1956.

$$\begin{aligned} I_1 &= Y_{11}V_1 + Y_{12}V_2 + Y_{13}V_3 \\ I_2 &= Y_{21}V_1 + Y_{22}V_2 + Y_{23}V_3 \\ I_3 &= Y_{31}V_1 + Y_{32}V_2 + Y_{33}V_3 \end{aligned} \quad (5)$$

where the nine  $Y$ -values are given by (3). Also, the current and voltage at port 2 are related by

$$I_2 = -G_2V_2 \quad (6)$$

where

$$G_2 = -n^2(G - G_1).$$

Substitution of (6) in (5) gives the equations of the two-port combination of negative conductance amplifier and nonideal circulator,

$$\begin{aligned} I_1 &= Y_{11}'V_1 + Y_{13}'V_3 \\ I_3 &= Y_{31}'V_1 + Y_{33}'V_3 \end{aligned} \quad (7)$$

where

$$\begin{aligned} Y_{11}' &= Y_{11} - \frac{Y_{12}Y_{21}}{Y_{22} + G_2} \\ Y_{13}' &= Y_{13} - \frac{Y_{12}Y_{23}}{Y_{22} + G_2} \\ Y_{31}' &= Y_{31} - \frac{Y_{21}Y_{32}}{Y_{22} + G_2} \\ Y_{33}' &= Y_{33} - \frac{Y_{23}Y_{32}}{Y_{22} + G_2}. \end{aligned}$$

Substitution of (3) into (7) gives the normalized admittances,

$$\begin{aligned} y_{11}' &= \frac{Y_{11}'}{G_0} = \frac{1 - j\epsilon g_2}{g_2 + j\epsilon} \\ y_{13}' &= \frac{Y_{13}'}{G_0} = \frac{-(1 + g_2)\sqrt{1 - \epsilon^2}}{g_2 + j\epsilon} \\ y_{31}' &= \frac{Y_{31}'}{G_0} = \frac{-(1 - g_2)\sqrt{1 - \epsilon^2}}{g_2 + j\epsilon} \\ y_{33}' &= \frac{Y_{33}'}{G_0} = \frac{1 + j\epsilon g_2}{g_2 + j\epsilon} \end{aligned} \quad (8)$$

where  $g_2 = G_2/G_0$ . The normalized output admittance is then

$$\begin{aligned} v_{out} &= \frac{Y_{out}}{G_0} = y_{33}' - \frac{y_{13}'y_{31}'}{y_{11}' + 1} \\ &= \frac{1}{G_0} [G_{out} + jB_{out}]. \end{aligned} \quad (9)$$

Finally, substitution of (8) into (9) gives the normalized output conductance and susceptance

$$g_{out} = \frac{G_{out}}{G_0} = \frac{1 - \epsilon^2 \left( \frac{1 - g_2}{1 + g_2} \right)^2}{1 + \epsilon^2 \left( \frac{1 - g_2}{1 + g_2} \right)^2} \quad (10a)$$

$$b_{out} = \frac{B_{out}}{G_0} = \frac{-2\epsilon \left( \frac{1 - g_2}{1 + g_2} \right)}{1 + \epsilon^2 \left( \frac{1 - g_2}{1 + g_2} \right)^2}. \quad (10b)$$

Note that, since a positive value of  $G_{out}$  is assumed,  $|g_2| < (1 - \epsilon)/(1 + \epsilon)$ . Furthermore, the magnitude of output admittance is constant and equal to  $G_0$ . In terms of the normalized conductance and susceptance,  $g_{out}^2 + b_{out}^2 = 1$ . Further discussion of the variations of  $g_{out}$  and  $b_{out}$  with the value of  $\epsilon$  will be postponed until the available power gain is calculated.

#### AVAILABLE POWER GAIN OF NEGATIVE CONDUCTANCE AMPLIFIER WITH NONIDEAL CIRCULATOR

The available power output (that is, the power that would be delivered to a conjugate load,  $G_{out} - jB_{out}$ ) is

$$[P_3]_{av} = \frac{|I_3|_{V_3=0}^2}{4G_{out}} \quad (11a)$$

where  $[I_3]_{V_3=0}$  is the current that would flow from the output port if it were short-circuited; and similarly, the available power input is

$$[P_G]_{av} = \frac{|I_G|^2}{4G_0}. \quad (11b)$$

The quotient of (11a) and (11b) gives the available power gain

$$K_{av} = \frac{[P_3]_{av}}{[P_G]_{av}} = \frac{1}{g_{out}} \left| \frac{I_3}{I_G} \right|_{V_3=0}^2. \quad (12)$$

Substitution of the terminal conditions,  $I_1 = I_G - G_0V_1$  and  $V_3 = 0$ , into (7) gives the ratio of short-circuit output current to generator current

$$\left[ \frac{I_3}{I_G} \right]_{V_3=0} = \frac{Y_{31}'}{Y_{11}' + G_0} = \frac{y_{31}'}{y_{11}' + 1}. \quad (13)$$

Finally, substitution of (13), (8), and (10a) into (12) gives, for the available power gain,

$$K_{av} = \frac{(1 - \epsilon^2) \left( \frac{1 - g_2}{1 + g_2} \right)^2}{1 - \epsilon^2 \left( \frac{1 - g_2}{1 + g_2} \right)^2}. \quad (14)$$

From (14), if an ideal circulator were used ( $\epsilon = 0$ ), the available power gain would be

$$K_{av}' = \left[ \frac{1 - g_2}{1 + g_2} \right]^2. \quad (15)$$



To see the effect of  $\epsilon$  on the available power gain, substitution of (15) into (14) gives the ratio of available power gains with nonideal and ideal circulators:

$$\frac{K_{av}}{K_{av}'} = \frac{1 - \epsilon^2}{1 - \epsilon^2 K_{av}'} \approx \frac{1}{1 - \epsilon^2 K_{av}'}, \quad \epsilon^2 \ll 1. \quad (16)$$

This is an interesting result; the available power gain is increased by noninfinite isolation between ports 3 and 2 of the circulator. Note that, neglecting any bandwidth restriction at port 3, the bandwidths are the same for these two gains, since  $G_2$ , the net negative conductance connected to port 2, is held fixed for the comparison of gains. Eq. (16) is plotted in Fig. 2, with parameter  $\epsilon^2 K_{av}'$  as the abscissa.

With the help of the above expressions involving available power gains, (10) for the normalized output conductance and susceptance can be interpreted more readily. Substitution of (15) into (10) gives, for the magnitudes of the normalized output conductance and susceptance,

$$g_{out} = \frac{1 - \epsilon^2 K_{av}'}{1 + \epsilon^2 K_{av}'} \quad (17a)$$

$$|b_{out}| = \frac{2\sqrt{\epsilon^2 K_{av}'}}{1 + \epsilon^2 K_{av}'} \quad (17b)$$

[The negative sign of  $b_{out}$  in (10b) has no particular significance, arising as it does from the assumed positive sign of  $\epsilon$  in (1).] It is seen that the output conductance decreases, and the output susceptance increases, as  $\epsilon$  increases. Furthermore, the assumption of  $G_{out} > 0$  requires  $\epsilon^2 K_{av}' < 1$ . Eqs. (17) are also plotted in Fig. 2.

It may be more convenient to have the normalized output conductance and susceptance related directly to the available power gain, rather than to have these three quantities each related to the available power gain if the circulator were ideal. Substitution of  $K_{av}'$  from (16) into (17) gives, for the magnitudes of the normalized output conductance and susceptance, in terms of the available power gain,

$$g_{out} = \frac{1 - \epsilon^2}{1 - \epsilon^2 + 2\epsilon^2 K_{av}} \approx \frac{1}{1 + 2\epsilon^2 K_{av}}, \quad \epsilon^2 \ll 1 \quad (18a)$$

$$|b_{out}| = \frac{2\sqrt{\epsilon^2 K_{av}(1 - \epsilon^2 + \epsilon^2 K_{av})}}{1 - \epsilon^2 + 2\epsilon^2 K_{av}} \approx \frac{2\sqrt{\epsilon^2 K_{av}(1 + \epsilon^2 K_{av})}}{1 + 2\epsilon^2 K_{av}}, \quad \epsilon^2 \ll 1. \quad (18b)$$

Eqs. (18) are plotted in Fig. 3, with parameter  $\epsilon^2 K_{av}$  as the abscissa.

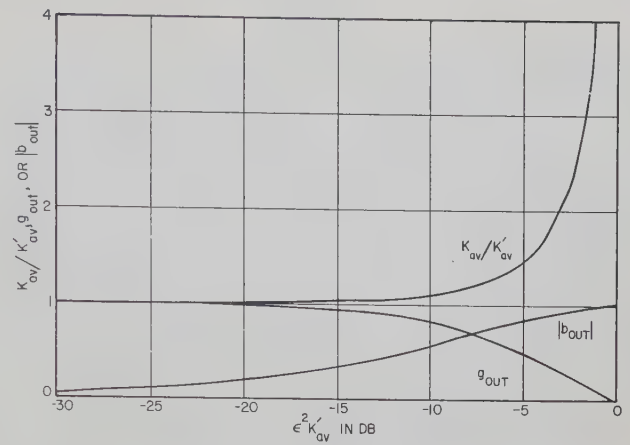


Fig. 2—Normalized gain and output admittance of negative conductance amplifier with nonideal circulator vs parameter  $\epsilon^2 K_{av}'$ .

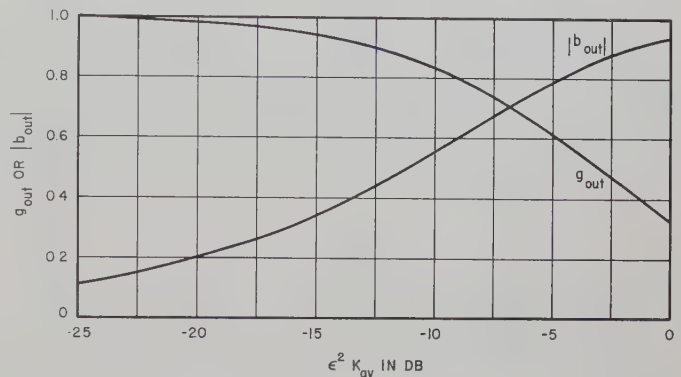


Fig. 3—Normalized output admittance of negative conductance amplifier with nonideal circulator vs parameter  $\epsilon^2 K_{av}$ .

An alternative way of describing the output admittance is in terms of the reflection coefficient and standing-wave ratio, using  $G_0$  as the reference conductance. Thus, from (10) and (17) the output reflection coefficient is

$$\Gamma = \frac{1 - y_{out}}{1 + y_{out}} = -j\sqrt{\epsilon^2 K_{av}'}, \quad (19a)$$

and the output standing-wave ratio is

$$SWR = \frac{1 + |\Gamma|}{1 - |\Gamma|} = \frac{1 + \sqrt{\epsilon^2 K_{av}'}}{1 - \sqrt{\epsilon^2 K_{av}'}}. \quad (19b)$$

Eqs. (19) can also be expressed in terms of the actual available power gain ( $K_{av}$ ) by substitution of  $K_{av}'$  from (16);

$$\Gamma = -j\sqrt{\frac{\epsilon^2 K_{av}}{1 - \epsilon^2 + \epsilon^2 K_{av}}} \approx -j\sqrt{\frac{\epsilon^2 K_{av}}{1 + \epsilon^2 K_{av}}}, \quad \epsilon^2 \ll 1, \quad (20a)$$

$$SWR = \frac{[\sqrt{1 - \epsilon^2 + \epsilon^2 K_{av}} + \sqrt{\epsilon^2 K_{av}}]^2}{1 - \epsilon^2} \approx [\sqrt{1 + \epsilon^2 K_{av}} + \sqrt{\epsilon^2 K_{av}}]^2, \quad \epsilon \ll 1. \quad (20b)$$

To summarize, when the product of the reverse insertion power gain from port 3 to port 2 of the actual circulator ( $\epsilon^2$ ) and the available power gain if the circulator were ideal ( $K_{av}'$ ) is not very small, compared to unity, both the available power gain and the output admittance of the negative conductance amplifier-circulator combination are greatly affected. That this product should affect operation when it is not very small compared to unity is not really surprising. The situation resembles an amplifier with positive feedback whose  $\mu\beta$  product is not very small compared to unity.

#### EFFECTIVE INPUT NOISE TEMPERATURE OF NEGATIVE CONDUCTANCE AMPLIFIER WITH NONIDEAL CIRCULATOR

For calculating the effective input noise temperature, the only source of noise considered in the negative conductance amplifier is that due to loss conductance  $G_1$  (see Fig. 1). (There is no source of noise in the circulator since it is assumed lossless.) The value of the associated mean square noise current generator, as transformed through the ideal transformer to port 2 of the circulator, is

$$\overline{i_1^2} = 4n^2G_1kT_1B \quad (21)$$

where  $k$ =Boltzmann's constant,  $T_1$ =absolute temperature of  $G_1$ , and  $B$ =spot bandwidth for which calculation is made. Consideration of this one noise source will enable a determination to be made of the effect, if any, of the nonideal circulator.

It can be shown that the effective input noise temperature is, in general, given by

$$T_e = (F - 1)T_0 = \frac{[N_0 - K_{av}kT_0B]}{K_{av}kB} \quad (22)$$

where  $F$ =noise figure,  $T_0$ =reference temperature of generator=290°K, and  $N_0$ =available noise output power. The available noise output power exclusive of the generator contribution is

$$[N_0 - K_{av}kT_0B] = \frac{[\overline{i_{out}^2}]_{V_3=0}}{4G_{out}} \quad (23)$$

where  $[\overline{i_{out}^2}]_{V_3=0}$  is the short-circuit mean square noise current at the output port due to loss conductance  $G_1$ . The value of  $[\overline{i_{out}^2}]_{V_3=0}$  is

$$[\overline{i_{out}^2}]_{V_3=0} = \overline{i_1^2} \left| \frac{I_3}{I_{G2}} \right|_{V_3=0}^2 \quad (24)$$

where  $[I_3/I_{G2}]_{V_3=0}$  is the ratio of short-circuit current at the output port (port 3 of the circulator) to a current generator  $I_{G2}$  connected to port 2 of the circulator. Substitution of (23), (24), and (21) into (22) gives, for the effective input noise temperature,

$$T_e = \left[ \frac{1}{g_{out}} \right] \left[ \frac{1}{K_{av}} \right] \left| \frac{I_3}{I_{G2}} \right|_{V_3=0}^2 \left[ \frac{n^2G_1}{G_0} \right] T_1. \quad (25)$$

The ratio  $[I_3/I_{G2}]_{V_3=0}$  can be evaluated by substituting the terminal conditions  $I_1 = -G_0V_1$ ,  $I_2 = I_{G2} - G_2V_2$ , and  $V_3 = 0$  into (5). Then,

$$\left[ \frac{I_3}{I_{G2}} \right]_{V_3=0} = \frac{Y_{32}(Y_{11} + G_0) - Y_{12}Y_{31}}{(Y_{11} + G_0)(Y_{22} + G_2) - Y_{12}Y_{21}}. \quad (26)$$

After substitution of the  $Y$ -values from (3), (26) reduces to

$$\left[ \frac{I_3}{I_{G2}} \right]_{V_3=0} = - \left[ \frac{2}{1 + g_2} \right] \left[ \frac{1}{1 + j\epsilon \left( \frac{1 - g_2}{1 + g_2} \right)} \right]. \quad (27)$$

Finally, substitution of (10a), (14), and (27) into (25) gives

$$T_e = \left[ \frac{1}{1 - \epsilon^2} \right] \left[ \frac{2}{1 - g_2} \right]^2 \left[ \frac{n^2G_1}{G_0} \right] T_1. \quad (28)$$

It is seen that the last two factors of (28) represent the effective input noise temperature of the negative conductance amplifier alone. Thus the first two factors, since they are always greater than unity, represent a degradation factor due to use of the circulator. Unlike the available power gain and output admittance, however, the effective input noise temperature is approximately the same with ideal or nonideal circulators, if  $\epsilon^2 \ll 1$ .

To further interpret (28), substitution of  $g_2$  from (15) gives for the degradation factor,

$$\left[ \frac{1}{1 - \epsilon^2} \right] \left[ \frac{2}{1 - g_2} \right]^2 = \left[ \frac{1}{1 - \epsilon^2} \right] \left[ 1 + \frac{1}{\sqrt{K_{av}'}} \right]^2. \quad (29a)$$

Alternatively, substitution of  $K_{av}'$  from (16) into (29a) gives

$$\begin{aligned} \left[ \frac{1}{1 - \epsilon^2} \right] \left[ \frac{2}{1 - g_2} \right]^2 &= \left[ \frac{1}{1 - \epsilon^2} \right] \left[ 1 + \sqrt{\epsilon^2 + \frac{1 - \epsilon^2}{K_{av}}} \right]^2. \end{aligned} \quad (29b)$$

Eq. (29b) shows that, for the case of high available power gain and low reverse insertion gain, the degradation factor is but slightly greater than unity.

#### PERFORMANCE OF OVER-ALL AMPLIFIER

It has been shown that noninfinite isolation of the circulator affects the characteristics of the combination of a negative conductance amplifier and a circulator. The output admittance ( $Y_{out}$ ) and the available power gain ( $K_{av}$ ) can be greatly affected, whereas the effective input noise temperature ( $T_e$ ) is usually but slightly affected. The above amplifier, being a low-noise amplifier, would naturally be used as the first stage of an amplifying system. What, then, will be the effect of the above



changes in characteristics of such a first stage on the effective input noise temperature of the over-all amplifier? In the introduction it was pointed out that the over-all effective input noise temperature could be expressed in terms of the characteristics of the first and second stages by the relation  $T = T_1 + T_2/K_1$ , where  $T_1$  and  $K_1$  are identified as  $T_o$  and  $K_{av}$  of the main text. The apparent effect of the nonideal circulator is then to increase  $K_1$  and probably also to increase  $T_2$ , while leaving  $T_1$  essentially unchanged. The increase in  $T_2$  arises if it is assumed, as is usual, that the second stage has been designed for optimum noise performance with a  $G_o$ -generator. Without specifying how  $T_2$  changes with the source admittance seen by the second stage ( $Y_{out}$  of the first stage), it is not clear how the quantity  $T_2/K_1$ , and thus  $T$ , is affected. In any case, conceptually,  $T_2$  can be restored to optimum by inserting a lossless transformer between the first and second stages to provide the correct source admittance for the second stage. The result should be to restore the over-all effective input noise temperature to that obtainable if the circulator were ideal. In fact, the increased value of  $K_1$  may even significantly lower the value of  $T_2/K_1$ , to give an even lower value of  $T$ .

## CONCLUSIONS

An analysis of the operation of a negative conductance amplifier with a nonideal circulator, using an admittedly greatly simplified model of the circulator, has shown that the output admittance, available power gain, and effective input noise temperature are all affected by the circulator being nonideal. This effect is most pronounced on the first two characteristics, for which it is determined by the product of the reverse insertion power gain (isolation) from ports 3 to 2 of the circulator and the available power gain of the negative conductance amplifier if connected to an ideal circulator. For large products, a transformer may be required at the output port of the circulator to avoid degrading the performance of the second stage.

## ACKNOWLEDGMENT

Many persons at Airborne Instruments Laboratory were of help to the author, in particular W. D. White who determined the scattering matrix of the assumed circulator model; B. Salzberg and J. C. Greene, who made many useful suggestions; and R. Gardner who checked the paper including the equations.

# Correspondence

## Propagation Constants in Rectangular Waveguide Partially Filled with Dielectric\*

There is considerable current interest in the production of guided electromagnetic waves having phase velocities equal to or less than the speed of light in free space (for example, in the design of traveling-wave slot antennas and of devices involving electron traveling-wave interactions). Such phase velocities can be obtained conveniently by partially loading a rectangular waveguide with dielectric material. In antenna work particularly, because of the field configurations, it is usually desirable to place the dielectric interface so that it is parallel to the broad face of the waveguide, as indicated in Fig. 1. The calculation of phase velocities in such a waveguide has been considered in the literature,<sup>1-3</sup> and there is published information on some of the cutoff frequencies,<sup>3</sup> but (since in this case there is no convenient relationship between the cutoff frequencies and the propagation constants) there has been little detailed information available concerning the phase velocities as a function of waveguide proportions and dielectric material. Thus a compilation has been made of such information for the dominant (hybrid) mode.

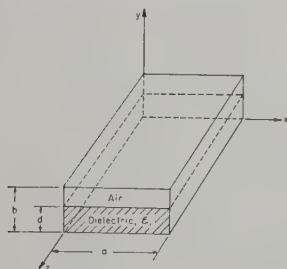


Fig. 1—Partially dielectric filled waveguide with dimension designations and coordinate system.

It can be shown<sup>4</sup> that the exact solution of Maxwell's equations, assuming perfect materials in the waveguide geometry indicated in Fig. 1, leads to the following transcendental equation for the propagation constants:

$$(k_{y1}/\epsilon_1) \tanh k_{y1}d = (k_{y2}/\epsilon_2) \tanh k_{y2}(d-b) \quad (1)$$

where  $k_{y1}$  and  $k_{y2}$  are the transverse propagation constants related by

$$k_{y2}^2 = k_{y1}^2 + (2\pi/\lambda)^2(\epsilon_r - 1). \quad (2)$$

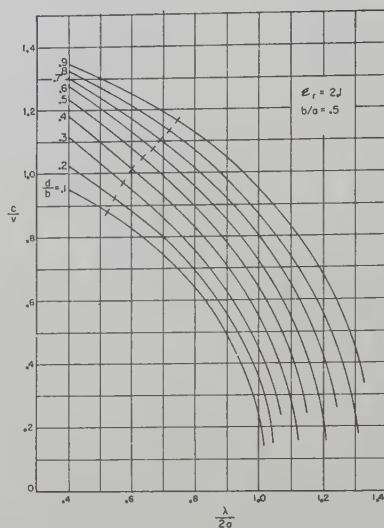


Fig. 2—Phase velocity of the dominant mode in the waveguide of Fig. 1, with permittivity 2.1 and aspect ratio of 0.5. Dashes across the curves indicate the region of cutoff of the next higher order mode.

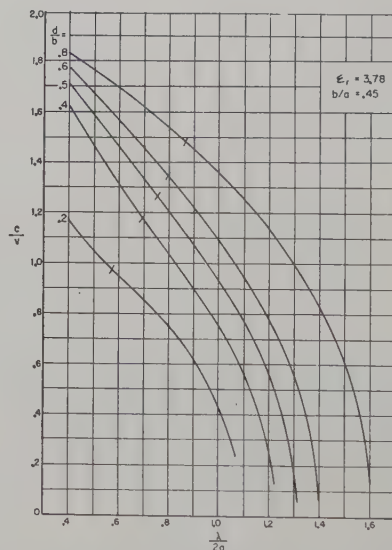


Fig. 3—Phase velocity of the dominant mode in the waveguide of Fig. 1, with permittivity 3.78 and aspect ratio of 0.45. Dashes across the curves indicate the region of cutoff of the next higher order mode.

The ratio of free space velocity,  $c$ , to the phase velocity in the waveguide,  $v$ , can be found from

$$c/v = \left[ \epsilon_r - \left( \frac{n\lambda}{2a} \right)^2 + (k_{y1}\lambda/2\pi)^2 \right]^{1/2} \quad (3)$$

where  $\lambda$  is the free space wavelength,  $\epsilon_r = \epsilon_1/\epsilon_2$ .

The computational difficulty lies in the fact that the quantities  $k_{y1}$  and  $k_{y2}$  depend upon the parameters  $\epsilon_r$ ,  $b$ , and  $d$  in such a way that a change in any one of these requires a new numerical solution of the transcendental equation (1). Thus, any ex-

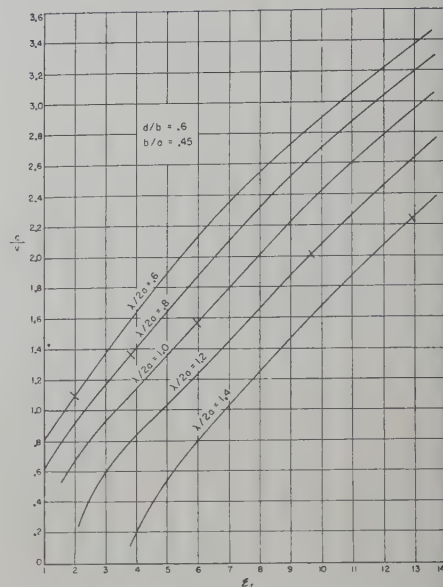


Fig. 4—Phase velocity ratio of the dominant mode in the waveguide of Fig. 1, as a function of permittivity, with 60 per cent filling and aspect ratio of 0.45. Cross lines indicate the region of cutoff of the next higher order mode.

tensive tabulation of results makes the use of a high-speed computing machine almost imperative. At the University of Illinois a digital computer was employed, first to solve the transcendental equation, and then to calculate the  $(c/v)$  ratios. A detailed graphical and tabular presentation of the results is available in a technical report for limited distribution.<sup>4</sup> In this report, results can be found which pertain to seven of the common solid dielectric materials (dielectric constants 1.6, 2.1, 2.54, 3.78, 5.75, 10, and 13.7), with fillings ( $d/b$ ) ranging from 10 to 90 per cent, and aspect ratios ( $b/a$ ) ranging from 0.25 to 1. The report also includes tables of values to facilitate calculations in which more accuracy is required than can be obtained from the graphs.

For economy, this note includes only sample graphs of the type mentioned above. Figs. 2 and 3 show the variation of the phase velocity ratio  $(c/v)$  for waveguides having the proportions indicated, with dielectric constants 2.1 and 3.78, respectively. The dashes across the curves indicate the region of cutoff for whichever of the higher order modes has the lower cutoff frequency. The curves for the special cases of no filling and complete filling are of course the circles centered at the origin ( $c/v = \lambda/2a = 0$ ) which have radii of unity and  $\epsilon_r^{1/2}$  (in units of  $\lambda/2a$ ), respectively. Fig. 4 indicates another type of information which can be assembled from the data which are available. It exhibits the variation of  $c/v$  as a function of dielectric constant, for the particular waveguide proportions indicated.

W. L. WEEKS  
University of Illinois  
Urbana, Ill.

\* Received by the PGM-TT, October 7, 1958.

<sup>1</sup> L. Pincherle, "Electromagnetic waves in metal tubes filled longitudinally with two dielectrics," *Phys. Rev.*, vol. 66, pp. 118-130; September, 1944.

<sup>2</sup> N. Marcuvitz, "Waveguide Handbook," McGraw-Hill Book Co., Inc., New York, N. Y., pp. 391-393; 1950.

<sup>3</sup> J. Van Bladel and T. J. Higgins, "Cut-off frequency in two-dielectric layered rectangular waveguide," *J. Appl. Phys.*, vol. 22, pp. 329-334; March, 1951.

<sup>4</sup> W. L. Weeks, "Propagation Constants in Rectangular Waveguides Partially Filled with Dielectric," Antenna Lab., Elec. Eng. Res. Lab., University of Illinois, Urbana, Tech. Rep. No. 28; December, 1957.



## A Short Rugged Ferrite Half-Wave Plate for a Single-Sideband Modulator\*

One type of microwave phase shifter consists of two quarter-wave plates between which is placed a half-wave plate whose principal axis is rotatable.<sup>1</sup> The phase shift introduced is directly proportional to the angular displacement of the principal axis of the half-wave plate. Continuous rotation of the principal axis causes continuous advancement or retardation of the phase of the signal traversing the phase shifter. This causes a frequency shift of the signal and the device can thus be used as a single-sideband modulator.<sup>2</sup>

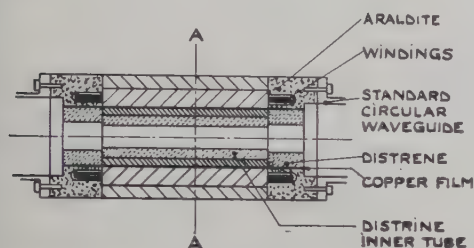


Fig. 1—Cross section of ferrite half-wave plate.

A certain amount of work has been carried out using a tube of ferrite in reduced guide. The ferrite used was an experimental ferrite Type MM3 supplied by Marconi's Wireless Telegraph Company, Ltd. The dimensions of the tube are 0.7 inch O.D.  $\times$  0.5 inch I.D.  $\times$  2 inches long. The ferrite tube was loaded with distrene tubes of 0.5 inch O.D. and various I.D. dimensions. The final half-wave plate arrangement is shown in Fig. 1.

Fig. 2 shows a typical phase shift characteristic obtained. The kinks associated with the ordinary wave phase characteristic are a function of the ferrite tube dielectric loading and the input matching arrangement. The input circuit consisted of a single

SECTION A-A

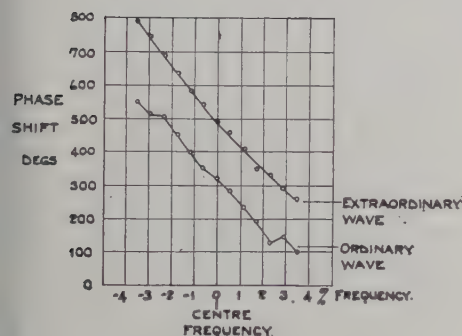


Fig. 2—Phase shift vs frequency characteristic of ordinary and extraordinary wave propagation.

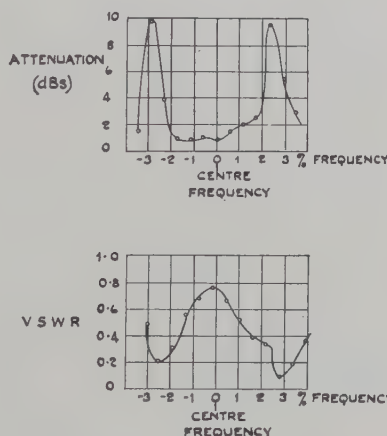


Fig. 3—Attenuation and VSWR vs frequency characteristic of the ferrite half wave plate.

A ferrite half-wave plate in reduced guide has been described by Karayianis and Cacheris.<sup>3</sup> The direction of the applied transverse magnetic field forms the principal axis of the half-wave plate. The advantage of working in reduced guide is that since the guide is more dispersive, a higher differential phase shift per applied field can be obtained. The major disadvantage is the increased difficulties associated with matching the ferrite loaded reduced guide to the normal waveguide run. Matching was attempted by Cacheris and Karayianis by using two 2-inch dielectric tapers. These are difficult to manufacture and are lengthy for some applications.

\* Received by the PGMTT, October 9, 1958.

<sup>1</sup> A. G. Fox, "An adjustable wave-guide phase changer," *Proc. IRE*, vol. 35, pp. 1489-1498; December, 1947.

<sup>2</sup> J. Cacheris, "Microwave single-sideband modulator using ferrites," *Proc. IRE*, vol. 42, pp. 1242-1247; August, 1954.

<sup>3</sup> N. Karayianis and J. Cacheris, "Birefringence of ferrites in circular waveguide," *Proc. IRE*, vol. 44, pp. 1414-1421; October, 1956.

The author wishes to thank the manager, The English Electric Company, Ltd., Luton, for permission to publish this note and Dr. Benzie of Marconi's Wireless Telegraph Company, Ltd., for supplying the ferrite tubes.

H. I. GLASS

Control Dept.

The English Electric Co., Ltd.  
Luton, Bedfordshire, Eng.

## A Technique for Minimizing Hysteresis in a 35-DB Ferrite Variable Attenuator\*

A requirement arose for a low-power microwave transmitter, the output power of which could be controlled over 40 db with a reset accuracy of 0.5 db for single frequency operation.

The experimental arrangement used is shown in Fig. 1.

The electronically variable short circuit is shown in Fig. 2. This has been described by Scharfman.<sup>1</sup>

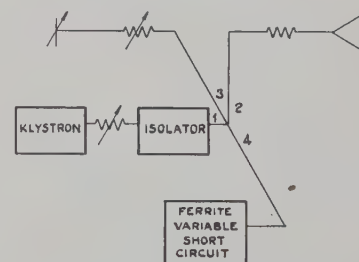


Fig. 1—Variable attenuator.

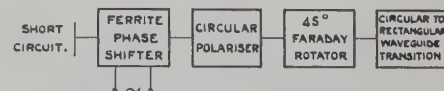


Fig. 2—Electronically variable short circuit.

"quarter wavelength" transformer, which was a distrene tube of 0.70 inch O.D. and the I.D. was determined experimentally for any particular frequency range. A typical value was 0.312 inch I.D. The minimum length of the transformer is determined by the winding overlay (Fig. 1). A typical performance curve for this transformer is shown in Fig. 3. It is evident that the insertion loss of the half-wave plate is extremely mismatch sensitive. Where the mismatch is small the insertion loss is approximately 1 db. An impedance plot of this arrangement would not yield a simple theoretical broadband match.

The over-all length of the half-wave plate and matching assembly is less than 3 inches. It could be useful in a single-sideband modulator where a rugged and compact design is desirable, and where narrow band operation is satisfactory.

For one sense of circular polarization the slope of the phase shift vs field curve becomes zero as the ferrite saturates, but for the other sense this is not so marked. This is shown in Fig. 3. Fig. 4 shows the attenuation between arms 1 and 2 vs relative phase difference between arms 3 and 4 of the magic T. It can be seen that the slope of the attenuation vs relative phase shift characteristic curve is extremely steep at the maximum attenuation point. Consider a negatively circularly polarized wave fed into a ferrite loaded section which is subjected to a field sufficiently large to saturate the ferrite. This corresponds to the point P in Fig. 3. The attenuator and short circuit in arm 3 can now be adjusted to give maximum attenuation between arms 1 and 2. This

\* Received by the PGMTT, October 9, 1958.

<sup>1</sup> H. Scharfman, "Three new ferrite phase shifters," *Proc. IRE*, vol. 44, pp. 1456-1459; October, 1956.

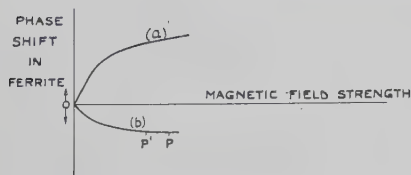


Fig. 3—Phase shift vs applied field. (a) Positively polarized wave. (b) Negatively polarized wave.

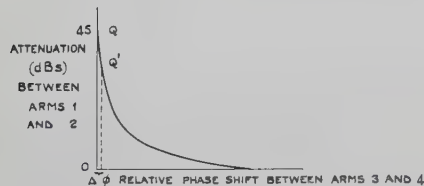


Fig. 4—Attenuation vs relative phase shift.

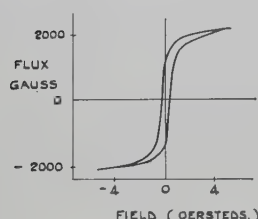


Fig. 5—Hysteresis loop of typical microwave ferrite.

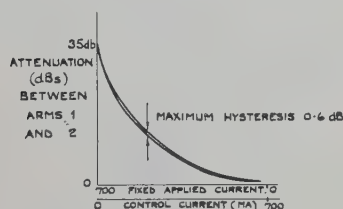


Fig. 6—Attenuator characteristic.

corresponds to the point  $Q$  in Fig. 4. If the magnetic field on the ferrite is now changed by a relatively large amount (to point  $P'$  in Fig. 3), the actual change in phase in arm 4 is quite small. This results in a small relative phase shift between arms 3 and 4 and this in turn causes the attenuation between arms 1 and 2 to change to the amount corresponding to  $Q'$  (Fig. 4). Thus it is obvious that on plotting a curve of attenuation between arms 1 and 2 vs magnetic field applied to the ferrite, a characteristic is obtained whose slope near the maximum attenuation point  $Q$  is considerably less steep than that of the curve of Fig. 4. This is shown in Fig. 6.

Since hysteresis is very small near saturation its effect near the steep part of the characteristic of Fig. 6 is very small. Below saturation the hysteresis of the ferrite is more marked (Fig. 5), but since the slope of the characteristic of Fig. 6 is much smaller when the applied field decreases, the effect of this increase in hysteresis is minimized. The final curve for the attenuator is shown in Fig. 6 where it can be seen that the maximum hysteresis measured corresponds to 0.6 db.

The author wishes to thank the manager, the English Electric Company, Ltd., Luton, for permission to publish this note.

H. I. GLASS

Control Dept.

The English Electric Co., Ltd.  
Luton, Bedfordshire, Eng.

## Quarter-Wave Compensation of Resonant Discontinuities\*

### INTRODUCTION

In designing RF transmission line components it is often necessary to place a short-circuited quarter-wavelength stub in parallel with the line or an open-circuited quarter-wavelength stub in series with the line. The stub can be broadbanded by merely changing the characteristic impedance of the line on either side of the stub for a distance of one quarter wavelength.

### BROAD-BAND STUB

It is not generally recognized how broadband a simple stub with quarter-wave transformers can be made. Previous investigators<sup>1</sup> have merely adjusted the transformer impedance for perfect match at two frequencies which depart somewhat from the resonant frequency of the stub without regard for the reflection in the pass band. The following analysis tries to correlate the bandwidth with the allowable reflection in the pass band.

A coaxial broad-band stub is shown in Fig. 1. On each side of the stub the center conductor is enlarged for a length of  $\lambda_0/4$  at the center frequency. In these quarter-wave transformers the characteristic impedance is  $Z_1$ . The stub is  $\lambda_0/4$  long and its characteristic impedance is  $Z_2$ . The characteristic impedance of the line is taken as 1 ohm in what follows so that  $Z_1$  and  $Z_2$  are multiples of the characteristic impedance.

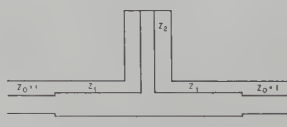


Fig. 1—Coaxial broad-band stub.

The  $ABCD$  matrix of the stub plus transformers is

$$\begin{bmatrix} \cos \theta & jZ_1 \sin \theta \\ j(1/Z_1) \sin \theta & \cos \theta \end{bmatrix} \begin{bmatrix} 1 & 0 \\ -j(1/Z_2) \tan \theta & 1 \end{bmatrix} \begin{bmatrix} \cos \theta & jZ_1 \sin \theta \\ j(1/Z_1) \sin \theta & \cos \theta \end{bmatrix}$$

where  $\theta$  is electrical length of each quarter-wave transformer and the stub. If we let

\* Received by the PGMTT, October 27, 1958. The research in this document was supported jointly by the Army, Navy, and Air Force under contract with Mass. Inst. Tech.  
<sup>1</sup> G. L. Ragan, "Microwave Transmission Circuits," M.I.T. Rad. Lab. Ser., McGraw-Hill Book Co., Inc., New York, N. Y., vol. 9, pp. 173-176; 1948.

$\theta = \pi/2 + \phi$ , the over-all matrix becomes

$$\begin{bmatrix} -\sin \phi & jZ_1 \cos \phi \\ j(1/Z_1) \cos \phi & -\sin \phi \end{bmatrix} \begin{bmatrix} 1 & 0 \\ -j(1/Z_2) \tan \phi & 1 \end{bmatrix} \begin{bmatrix} -\sin \phi & jZ_1 \cos \phi \\ j(1/Z_1) \cos \phi & -\sin \phi \end{bmatrix}$$

which when multiplied gives

$$\begin{bmatrix} \sin^2 \phi - \cos^2 \phi + (Z_1/Z_2) \sin^2 \phi & -jZ_1 \sin \phi \cos \phi (2 + Z_1/Z_2) \\ -j(1/Z_1) \sin \phi \cos \phi (2 - Z_1/Z_2 \tan^2 \phi) & \sin^2 \phi - \cos^2 \phi + (Z_1/Z_2) \sin^2 \phi \end{bmatrix}$$

The insertion loss is given by<sup>2</sup>

$$L = 10 \log_{10} \{1 + 1/4[(A-D)^2 - (B-C)^2]\} \\ = 10 \log_{10} \{1 + 1/4[(2/Z_1 - 2Z_1 - Z_1^2/Z_2 + 1/Z_2) \sin \phi \cos \phi - 1/Z_2 \tan^2 \phi]^2\} \\ = 10 \log_{10} (1 + m^2/4) \quad (1)$$

where

$$mZ_2 = R \sin \phi \cos \phi - \tan \phi \quad (2)$$

$$R = 2Z_2/Z_1 - 2Z_1Z_2 - Z_1^2 + 1. \quad (3)$$

A graph of the magnitude of  $|m|Z_2$  is shown in Fig. 2.

$R=1$  gives the maximally flat case with a zero derivative at the origin.

For  $R$  greater than 1, a triple peaked response is obtained.

Using some simple trigonometric substitutions it can be shown that  $\phi_2 = 2\phi_1$ ; also,

$$m_1Z_2 = \tan \phi_2 \left( \frac{1 - \cos \phi_2}{1 + \cos \phi_2} \right) \quad (4)$$

and

$$R = \frac{2}{\cos^2 \phi_2 + \cos \phi_2} \quad (5)$$

where  $\phi_1$  is the value of  $\phi$  for worst reflections in the pass band,  $\phi_2$  is the band edge, and  $m_1$  is the worst value of  $m$  in the pass band.

The quantity  $m_1$  is related to the worst voltage standing wave ratio  $S$  by

$$m_1 = \frac{S-1}{\sqrt{S}} \quad (6)$$

and the bandwidth is given by

$$BW = 2\phi_2/90. \quad (7)$$

A graph of  $m_1Z_2$  as a function of bandwidth is shown in Fig. 3.

As an example, suppose it is desired to design a stub support for a coaxial line to have a standing wave ratio of no greater than 1.05 over as wide a frequency band as possible. Because of voltage breakdown considerations it is decided that the largest value  $Z_2$  may have is one. Then from (6),  $m_1 = 0.0488$ , and from Fig. 3 the bandwidth is 70.4 per cent or a frequency ratio of 2.09:1.  $R$  is determined from (5), and  $Z_1$  from (3).

The required value of  $Z_1$  for various values of  $Z_2$  is plotted as a function of bandwidth in Fig. 4. This graph shows that the diameter of the quarter-wave transformers is rather critical. The desired  $Z_1$  is only slightly smaller than the zero bandwidth case.

<sup>2</sup> R. M. Fano and A. W. Lawson, "Microwave Transmission Circuits," M.I.T. Rad. Lab. Ser., McGraw-Hill Book Co., Inc., New York, N. Y., vol. 9, ch. 9 and 10; 1948.



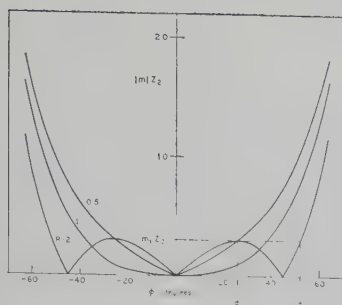


Fig. 2—Variation of  $m$  with  $\phi$  for various values of  $R$ .

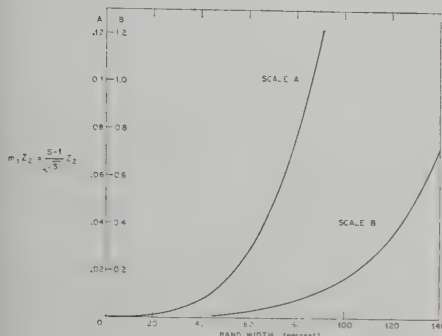


Fig. 3—Variation of  $m_1 Z_2$  with bandwidth.

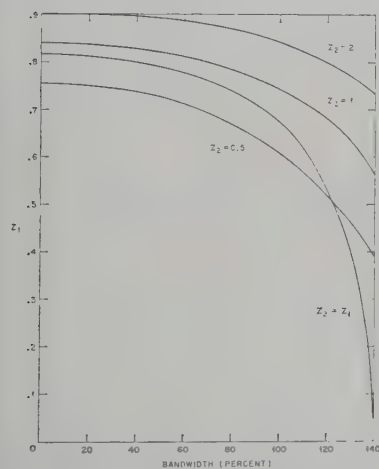


Fig. 4— $Z_1$  as a function of bandwidth for various stub impedances.

Although the above analysis assumed a coaxial stub it is obvious that the analysis can be applied to other TEM transmission lines and to waveguides. In particular it may be applied to the problem of making an extremely broad-band T junction for a branched duplexer.

#### AN EXTREMELY BROAD-BAND ROTARY JOINT

Electrically a choke type rotary joint consists of an open-circuited quarter-wavelength stub in series with a transmission line. A comparison with the broad-band stub of the previous section, which is a short-circuited quarter-wavelength stub in parallel with the line, suggests that an analysis of the choke type rotary joint on an admittance

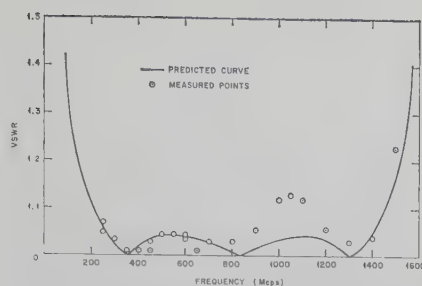


Fig. 5—Predicted and measured VSWR of broad-band rotary joint.

basis may give a result similar to the above analysis. This indeed is the case. If  $Z_1$  and  $Z_2$  in (1) through (7) are replaced by  $Y_1$  and  $Y_2$ , respectively, these equations will give the response of a choke type rotary joint and at the same time will point out a method of broadbanding such a rotary joint. Broadbanding may be achieved by reducing the characteristic admittance of the transmission line by the proper amount for a quarter wavelength on either side of the chokes. Physically, this may be accomplished by decreasing the radius of the inner conductor or increasing the radius of the outer conductor of a coaxial line rotary joint.

A broad-band rotary joint using the above theory has been built and tested in three and one-eighth inch coaxial line. The predicted and measured results are shown in Fig. 5. The measured results agree quite well with the theory except in the region near 1100 mc. This can be explained by the lack of the theory in accounting for the capacitive discontinuity at the end of the series choke in the inner conductor and the effect of the short-circuited high impedance quarter-wave section at the end of the series choke in the outer conductor.

The sum of the characteristic impedances of the inner and outer chokes was 3.3 ohms and the main line had an impedance of 50 ohms. The rotary joint was designed to have a VSWR less than 1.04 over a 135 per cent bandwidth. For the same VSWR with no compensation the bandwidth would have been 70 per cent.

In conclusion the above analysis may be used to broadband any quarter-wavelength choke or stub type discontinuity and accurately predict its performance.

C. E. MUEHE  
Lincoln Lab.  
Mass. Inst. Tech.  
Lexington, Mass

given in my paper<sup>2</sup> and the restatement of it that is given and proven in the Appendix. If we define  $l$  to be the degree, the maximum of the degrees of the numerator and the denominator, of the rational function  $Z(p)$ , and  $r$  to be the number of line sections in the impedance transformer, then in the first statement of the theorem,  $l$  is unspecified and  $n=r$  while in the second statement  $l=n$  and  $r$  is unspecified. Now the second theorem is correct, even in view of Ozaki's comments, and accordingly is adequate for a proof of the physical realizability of the allowed insertion loss functions. The first theorem, however, is incorrectly stated as Ozaki's example has shown.

Ozaki's third condition, "Assuming that the numerator and denominator of  $Z(p)$  in (1) are prime to each other, the degrees of both the numerator and denominator must be equal to  $n$ ," correctly requires that  $l=n$  and adds the restriction that the numerator and denominator of  $Z(p)$  contain no common factors.

The requirement that the degree of the numerator of  $Z(p)$  equal the degree of the denominator is a salient feature of the theory. My failure to define  $l=n$ , which has this consequence when taken with condition 2, in the first statement of the theorem, was simply an oversight. I permitted the removal of common factors<sup>3</sup> in the second statement of the theorem by not specifying  $r$ , since it is readily shown that the removal of a common factor from the numerator and denominator of a  $Z(p)$ , satisfying condition 2, results in a  $Z'(p)$  which again satisfies this condition.

Ozaki's third condition permits the proof of a sharper theorem than my application required, namely one in which  $l=n=r$ . His condition, however, is unnecessarily restrictive since the relative primeness of the numerator and denominator is not a necessary condition for the truth of this class of theorem. For example, if the terminating resistance,  $R$ , is preceded by a section of line of characteristic impedance,  $R$ , then the numerator and denominator of  $Z(p)$  contain the common factor,  $p+1$ . In fact it is readily demonstrated that the only common factors permitted by condition 2 are products of  $p+1$  and  $p-1$ . The first can be realized while the occurrence of the latter would result in the indeterminacy of  $Z(1)$ .

A more general theorem of this type can be stated:

The necessary and sufficient conditions that a rational function of  $p$ , determinant for  $p=1$ , with real coefficients, of degree at most  $n$  in numerator or denominator written in the form

$$Z(p) = \frac{m_1(p) + n_1(p)}{m_2(p) + n_2(p)}$$

with  $m_1$  and  $m_2$  odd or even and  $n_1$  and  $n_2$  even or odd, be the input impedance of a cascade of  $n$  equal-length transmission line sections terminated in a resistance are:

#### Comments on Ozaki's Comments\*

Ozaki's<sup>1</sup> comments have drawn my attention to the fact that there is a significant difference between "The Synthesis Theorem"

\* Received by the PGMTT, October 30, 1958.

<sup>1</sup> H. Ozaki, "On Riblet's theorem," IRE TRANS. ON MICROWAVE THEORY AND TECHNIQUES, vol. MTT-6, pp. 331-332, July, 1958.

<sup>2</sup> H. J. Riblet, "General synthesis of quarter-wave impedance transformers," IRE TRANS. ON MICROWAVE THEORY AND TECHNIQUES, vol. MTT-5, pp. 36-43, January, 1957.

<sup>3</sup> For example, the well-known result that a positive real function of  $p$  is a quotient of two Hurwitz polynomials is true in general only if the removal of common factors from numerator and denominator is permitted.

- 1)  $Z(p)$  must be a positive real function of  $p$ ;
- 2)  $m_1(p)m_2(p) - n_1(p)n_2(p) = C(p^2 - 1)^n$ .

Condition 2 implies that both numerator and denominator are of degree  $n$  and it is readily argued that an impedance function formed by terminating a section of transmission line in an indeterminate impedance function will remain indeterminate. Furthermore if  $Z(p)$  is normalized so that the coefficient of  $p^2$  in its denominator is unity then  $C$  equals the terminating resistance.

HENRY J. RIBLET  
Microwave Dev. Labs., Inc.  
Wellesley, Mass.

(1) it is convenient to express, e.g., the  $\epsilon$  dyadic as

$$\epsilon \rightarrow \begin{bmatrix} \epsilon_t & \epsilon_{tz} \\ \epsilon_{zt} & \epsilon_z \end{bmatrix} \quad (3)$$

where  $\epsilon_t$  is a transverse dyadic,  $\epsilon_{tz}$  and  $\epsilon_{zt}$  are vectors, and  $\epsilon_z$  is a scalar; i.e.,

$$\epsilon = \epsilon_t + \epsilon_z \mathbf{1}_z + \epsilon_{zt} \mathbf{z}_0 + \epsilon_{tz} \mathbf{z}_0. \quad (4)$$

A similar representation is chosen for the  $\mu$  dyadic. It can then be shown that the (independent) transverse field components satisfy the following pair of (coupled) second-order differential equations (transverse vector eigenvalue problem):

$$\begin{bmatrix} \left( \omega \epsilon_t - \frac{1}{\omega} \nabla_t \times \mathbf{z}_0 \frac{1}{\mu_z} \mathbf{z}_0 \times \nabla_t - \frac{\omega}{\epsilon_z} \epsilon_{tz} \epsilon_{zt} \right) & \left( \frac{\epsilon_{tz}}{\epsilon_z} \mathbf{z}_0 \times \nabla_t + \nabla_t \times \mathbf{z}_0 \frac{\mu_{zt}}{\mu_z} - i k \mathbf{z}_0 \times \mathbf{1}_t \right) \\ \left( \frac{\mu_{tz}}{\mu_z} \mathbf{z}_0 \times \nabla_t + \nabla_t \times \mathbf{z}_0 \frac{\epsilon_{zt}}{\epsilon_z} - i k \mathbf{z}_0 \times \mathbf{1}_t \right) & \left( \omega \mu_t - \frac{1}{\omega} \nabla_t \times \mathbf{z}_0 \frac{1}{\epsilon_z} \mathbf{z}_0 \times \nabla_t - \frac{\omega}{\mu_z} \mu_{tz} \mu_{zt} \right) \end{bmatrix} \begin{bmatrix} E_t \\ i H_t \end{bmatrix} = 0. \quad (5)$$

Once solutions to (5) are obtained, the corresponding longitudinal field components can be determined from a knowledge of the transverse components via

$$\begin{bmatrix} E_z \\ i H_z \end{bmatrix} = \begin{bmatrix} -\frac{1}{\epsilon_z} \epsilon_{zt} & \frac{1}{\omega \epsilon_z} \mathbf{z}_0 \times \nabla_t \\ \frac{1}{\omega \mu_z} \mathbf{z}_0 \times \nabla_t & -\frac{1}{\mu_z} \mu_{zt} \end{bmatrix} \begin{bmatrix} E_t \\ i H_t \end{bmatrix} \quad (6)$$

In general, to obtain solutions to the transverse vector eigenvalue problem (5) is a formidable task. We recall that even in the case of isotropic waveguides such solutions are usually obtained by replacing the vector eigenvalue problem by a pair of scalar eigenvalue problems whose eigenfunctions are (except in the case of TEM modes) proportional to the longitudinal field components. A similar technique may be employed in the general anisotropic situation under consideration here. It can be shown that the transverse field components are derivable from the longitudinal field components via

$$D(\kappa) \begin{bmatrix} E_t \\ i H_t \end{bmatrix} = \mathfrak{A} \mathfrak{B} \begin{bmatrix} E_z \\ i H_z \end{bmatrix} \quad (7)$$

where

$$D(\kappa) = \kappa^4 + \omega^2 \kappa^2 \text{Tr}(\mathbf{z}_0 \times \mu_t \cdot \mathbf{z}_0 \times \epsilon_t) + \omega^4 \Delta_\epsilon \Delta_\mu, \quad (8)$$

$$\mathfrak{A} = k^2 \Delta_\epsilon \Delta_\mu \begin{bmatrix} \omega \epsilon_t^{-1} & i k \epsilon_t^{-1} \cdot \mathbf{z}_0 \times \mu_t^{-1} \\ i k \mu_t^{-1} \cdot \mathbf{z}_0 \times \epsilon_t^{-1} & \omega \mu_t^{-1} \end{bmatrix} + \kappa^2 \begin{bmatrix} \omega \mathbf{z}_0 \times \mu_t \times \mathbf{z}_0 & -i k \mathbf{z}_0 \times \mathbf{1}_t \\ -i k \mathbf{z}_0 \times \mathbf{1}_t & \omega \mathbf{z}_0 \times \epsilon_t \times \mathbf{z}_0 \end{bmatrix}, \quad (9)$$

$$\mathfrak{B} = \begin{bmatrix} -\omega \epsilon_{tz} & \nabla_t \times \mathbf{z}_0 \\ \nabla_t \times \mathbf{z}_0 & -\omega \mu_{tz} \end{bmatrix}, \quad (10)$$

$\Delta_\epsilon$  and  $\Delta_\mu$  are the determinants of (the matrix representations of) the  $\epsilon_t$  and  $\mu_t$  dyadics, respectively, and  $\text{Tr}(\mathbf{z}_0 \times \mu_t \cdot \mathbf{z}_0 \times \epsilon_t)$  is the trace of (the matrix representation for) the dyadic  $\mathbf{z}_0 \times \mu_t \cdot \mathbf{z}_0 \times \epsilon_t$ . Further, it can be shown that the longitudinal field components satisfy the following pair of (coupled) second-order differential equations (scalar eigenvalue problem):

$$\begin{bmatrix} \epsilon_z E_z \\ i \mu_z H_z \end{bmatrix} = \hat{\mathfrak{B}} \frac{\mathfrak{A}}{D(\kappa)} \mathfrak{B} \begin{bmatrix} E_z \\ i H_z \end{bmatrix} \quad (11)$$

where  $D(\kappa)$ ,  $\mathfrak{A}$ ,  $\mathfrak{B}$  are defined in (7)–(9) and:

$$\hat{\mathfrak{B}} = \begin{bmatrix} -\omega \epsilon_{zt} & \mathbf{z}_0 \times \nabla_t \\ \mathbf{z}_0 \times \nabla_t & -\omega \mu_{zt} \end{bmatrix}. \quad (12)$$

Note that, in general,  $1/D(\kappa)$  does not commute with either  $\mathfrak{B}$  or  $\hat{\mathfrak{B}}$  since these contain differentiation operations. The reader may verify that the result in (11) reduces to the equation given by Kales<sup>2</sup> for the special case of an axially magnetized gyromagnetic medium (i.e., where  $\epsilon$  is a scalar and  $\mu_{tz} = \mu_{zt} = 0$ ).

Any solution  $E_z$ ,  $H_z$  to (11) yields, via (7), an eigenfunction (mode) of the transverse vector eigenvalue problem (5). This

## Vector Formulations for the Field Equations in Anisotropic Waveguides\*

In the following we will exhibit vector formulations for the equations determining the different components of the electromagnetic field in a source-free uniform waveguide. All results will be stated without proof. The derivations are given elsewhere.<sup>1</sup> The vector formulations given below are applicable to uniform waveguides containing anisotropic media restricted only by the requirement that the permittivity ( $\epsilon$ ) and permeability ( $\mu$ ) dyadics be independent of the axial coordinate  $z$ . For uniform waveguides (with the indicated restriction on  $\mu$  and  $\epsilon$ ) we consider solutions to the Maxwell equations which display characteristic time and  $z$  dependence of the form  $\exp i(\kappa z - \omega t)$ . This assumption permits us to eliminate the  $z$  and  $t$  dependence from the Maxwell equations and rewrite these as:

$$\begin{bmatrix} \omega \epsilon & -\nabla_t \times \mathbf{1} - i k \mathbf{z}_0 \times \mathbf{1}_t \\ -\nabla_t \times \mathbf{1} - i k \mathbf{z}_0 \times \mathbf{1}_t & \omega \mu \end{bmatrix} \cdot \begin{bmatrix} E \\ i H \end{bmatrix} = 0. \quad (1)$$

Here, as in all the matrix equations which follow, dot product multiplication is to be understood for the products of dyadics and vectors. In (1),  $E$  and  $H$  are, respectively, the steady-state electric and magnetic fields;  $\nabla_t$  is the transverse gradient operator;  $\mathbf{z}_0$  is the unit vector in the axial direction;  $\mathbf{1}$  is the unit dyadic; and  $\mathbf{1}_t$  is the unit transverse dyadic:

$$\mathbf{1}_t = \mathbf{1} - \mathbf{1}_z = \mathbf{1} - \mathbf{z}_0 \mathbf{z}_0. \quad (2)$$

It is well known that the transverse field components,  $E_t$  and  $H_t$ , constitute the independent field components. To eliminate the dependent longitudinal components from

\* Received by the PGMTT, October 31, 1958. This note is based on a study undertaken pursuant to Contract AF-19(604)-2301 with the AF Cambridge Res. Center.

<sup>1</sup> A. D. Bresler, "Vector Formulations for the Electromagnetic Field Equations in Uniform Waveguides Containing Anisotropic Media," Microwave Res. Inst., Polytechnic Inst. of Brooklyn, Brooklyn, N. Y., Rep. R-676-58; September, 1958.

procedure is manifestly not valid when  $D(\kappa) = 0$ . Therefore, the set of vector eigenfunctions obtained from all the solutions to (11) becomes complete only when we add such vector eigenfunctions of (5) which are admitted when  $D(\kappa) = 0$ . That these additional eigenfunctions are the analogs of the TEM modes in the anisotropic case is evident from the fact that  $D(\kappa) = (\omega^2 \mu \epsilon - \kappa^2)^2$  for an isotropic medium with scalar  $\mu$  and  $\epsilon$ . The analogy to TEM modes indicated here should not be taken to imply any TEM-like properties of these eigenfunctions in the anisotropic case.

A. D. BRESLER  
Microwave Res. Inst.  
Polytechnic Inst. of Brooklyn  
Brooklyn, N.Y.

<sup>2</sup> M. L. Kales, "Modes in waveguides that contain ferrites," *J. Appl. Phys.*, vol. 24, pp. 604–608; May, 1953.

## An Extension of the Reflection Coefficient Chart to Include Active Networks\*

### INTRODUCTION

At a single frequency, a two-port can be represented by the scattering matrix [1], [5]

$$[b] = [S][a] \quad (1a)$$

$$b_1 = s_{11}a_1 + s_{12}a_2 \quad (1b)$$

$$b_1 = s_{21}a_1 + s_{22}a_2 \quad (1c)$$

where  $s_{12} = s_{21}$  in the reciprocal two-port. If one defines an input reflection coefficient  $\Gamma_{in} = b_1/a_1$  and a load reflection coefficient  $\Gamma_L = a_2/b_2$  one can form

$$\Gamma_{in} = \frac{(s_{12}^2 - s_{11}s_{22})\Gamma_L + s_{11}}{1 - s_{22}\Gamma_L}. \quad (2)$$

Eq. (2) can be considered as a mapping of the  $\Gamma_L$  plane into the  $\Gamma_{in}$  plane. Since this is a bilinear transformation, angles between

\* Received by the PGMTT, November 17, 1958.



intersecting lines are preserved and circles will transform into other circles. The load reflection coefficient can be written as  $|\Gamma_L|e^{j\arg\Gamma_L}$ , where for a passive load  $|\Gamma_L| \leq 1$ . At some output reference plane, the insertion of varying amounts of matched lossless line will vary the angle of  $\Gamma_L$  so that the locus of  $\Gamma_L$  will be a circle centered at the origin and with a radius of  $|\Gamma_L|$ . The locus of the input reflection coefficient will also be a circle which will not in general be centered at the origin of the  $\Gamma_{in}$  plane. If  $|\Gamma_L| = 1$ , the  $\Gamma_{in}$  circle can be used to measure [2], [3] the scattering coefficients of the two-port. This circle may be referred to as the loss circle of the two-port. It is noted that if the load is dissipative (*i.e.*,  $|\Gamma_L| < 1$ ), the  $\Gamma_L$  circles will be concentric with the unity circle and will have smaller radii. The  $\Gamma_{in}$  circles will lie within the transformed unity circle, although the centers of the circles will not coincide but lie [4] on a straight line connecting the iconcenter and the origin of the  $\Gamma_{in}$  plane. If the angle of  $\Gamma_L$  is held constant (modulo  $\pi$ ), this will describe a diameter of the unity circle in the  $\Gamma_L$  plane. This will map into the  $\Gamma_{in}$  plane as arcs of circles orthogonal to transformed constant  $|\Gamma_L|$  circles. Since all of the diameters in the  $\Gamma_L$  plane intersected at the origin, all of the arcs in the  $\Gamma_{in}$  plane will intersect at the iconcenter.

#### ACTIVE NETWORKS AS LOADS

If the restriction that the  $|\Gamma_L| \leq 1$  is removed, corresponding to a source of power or negative resistance at the output, the extension of the theory follows logically. If  $|\Gamma_L|$  is a constant and greater than unity, the locus will be a circle with a radius greater than unity (*i.e.*, outside the Smith Chart). It will be mapped into a circle which may or may not be all or in part outside the Smith Chart. If no part of the circle is outside the unity circle, an observer at the input port could not tell that there was an active element at the output. If part (or all) of the circle is outside of the chart the observer might (or would) see power coming out of the two-port's input, depending on the phase angle of  $\Gamma_L$ . If the angle of  $\Gamma_L$  is held constant (modulo  $\pi$ ), the extension of the diameter in the  $\Gamma_L$  plane will map into the complete orthogonal circle as the magnitude of  $\Gamma_L$  varies from zero to infinity. It should be noted that the radii of the orthogonal circles will vary and one will have an infinite radius (a straight line). For every phase angle of  $\Gamma_L$  there will be a maximum  $|\Gamma_{in}|$ . Examining (2) it can be seen that if  $s_{22}\Gamma_L = 1$  the input reflection coefficient will become infinite. Since  $b_1/a_1$  is infinite and  $a_1$  is presumed to be finite,  $b_1$  is infinite or infinite power is coming out of the input of the two-port. The value of  $\Gamma_L$  equal to the reciprocal of  $s_{22}$  for infinite power can also be obtained from (1b) as the power at the output becomes infinite. It is noted that letting  $\Gamma_L$  approach infinity will not represent infinite power except when  $s_{22} = 0$ .

#### ACTIVE NETWORKS IN THE TWO-PORT

Returning to the passive load, it might appear that if  $|s_{22}|$  was equal to unity there was the possibility of obtaining infinite power from a passive two-port. From the

conservation of energy in the passive two-port  $|s_{12}|^2 + |s_{22}|^2 \leq 1$ . Therefore  $s_{12} = 0$ . Similarly, it can be shown by taking the equality<sup>1</sup> again  $|s_{11}| = 1$ . When these values are substituted in (2),  $\Gamma_{in} = s_{11}$ . The two-port has been broken into two disjoint one-ports (no transmission between the two).

If the two-port contained some active elements the scattering coefficients could have any value. It is probable that the active elements will alter the reciprocity relationship  $s_{12} = s_{21}$ . However an equivalent reciprocal<sup>2</sup>  $s_{12}'$  could be determined by the Deschamps method  $s_{12}' = \sqrt{s_{12}s_{21}}$ . Therefore it is clear that active elements can be handled whether they appear in the load or the two-port.

#### REPRESENTATION OF MICROWAVE CIRCUITS

The bilinear transformation may be written as  $\Gamma_{in} = T(\Gamma_L)$  where  $\Gamma_{in}$  and  $\Gamma_L$  represent the input and the output of the two-port, while the transformation  $T$  describes the two-port uniquely. Any  $\Gamma_{in}$  circle can be obtained from an infinite combination of  $T$ 's and  $\Gamma_L$ 's. The transformations  $T$  can be considered as belonging to three distinct types of transformations depending on whether  $|\Gamma_L|$  is greater than, equal to, or less than unity. For a given loss circle a set of scattering coefficients can be determined. Only if  $|\Gamma_L| = 1$ , the determined scattering coefficients will be the actual coefficients of the network. However, an observer at the input is unable to distinguish how the given loss circle is obtained and he can represent the two-port and the load as an "equivalent" two-port with a purely reactive load. If the load is purely reactive the "equivalent" network becomes the actual network.

If the other two parameters,  $\Gamma_L$  and  $T$ , are held constant (separately), added information may be found out about the behavior of microwave circuits. If the transformation  $T$  is held constant, the two-port is invariant, and the previous discussion regarding the transformation of  $\Gamma_L$  circles to  $\Gamma_{in}$  circles is applicable. The converse of the previous statement is also true since inverse transformation is also bilinear. If the load reflection circle is held constant, varying  $\Gamma_{in}$  will determine the transformation or the network.

Therefore it can be seen by the extension of the reflection coefficient chart that it is possible to represent any two-port and load at the input by another two-port with a purely reactive termination. Therefore a prescription of the  $\Gamma_{in}$  and  $\Gamma_L$  circles will determine a network. This description reduces to that of Deschamps when the  $\Gamma_L$  circle is the unit circle. The graphical method gives a clear geometric picture of the behavior of a given two-port in terms of input and output reflection coefficient loci.

L. J. KAPLAN  
D. J. R. STOCK  
Elec. Eng. Dept.  
New York University  
New York, N. Y.

#### BIBLIOGRAPHY

- [1] C. G. Montgomery, R. H. Dicke, and E. M. Purcell, "Principles of Microwave Circuits," McGraw-Hill Book Co., Inc., New York, N. Y.; 1948.
- [2] G. Deschamps, "Determination of reflection coefficients and insertion loss of a waveguide junction," *J. Appl. Phys.*, vol. 24, pp. 1046-1050; August, 1953.
- [3] J. E. Storer, L. S. Sheingold, and S. Stein, "A simple graphical analysis of a two-port waveguide junction," *Proc. IRE*, vol. 41, pp. 1004-1013; August, 1953.
- [4] H. F. Mathis, "Some properties of image circles," *IRE TRANS. ON MICROWAVE THEORY AND TECHNIQUES*, vol. MTT-4, pp. 48-50; January, 1956.
- [5] E. L. Ginzton, "Microwave Measurements," McGraw-Hill Book Co., Inc., New York, N. Y.; 1957.
- [6] L. R. Ford, "Automorphic Functions," McGraw-Hill Book Co., Inc., New York, N. Y.; 1929.

#### Characteristics of a Ferrite-Loaded Rectangular Waveguide Twist\*

The Faraday effect in a straight rectangular waveguide, a section of which is completely filled with a ferrite material subjected to an axial magnetic field, has been described by Du Pré,<sup>1</sup> who states that, owing to the presence of a medium of dielectric constant and permeability greater than those of air, modes other than the usual  $TE_{10}$  mode may be propagated in the ferrite-filled section. In particular, the  $TE_{01}$  mode whose electric vector is perpendicular to the narrow dimension of the guide may be supported. If, owing to Faraday rotation, the  $TE_{10}$  mode is converted to the  $TE_{01}$  mode, propagation cannot take place beyond the ferrite-filled section. Experimentally this was confirmed by Du Pré who observed a minimum of transmitted power for 90° rotation. Similar results were obtained in this laboratory with a straight rectangular guide loaded with a cylindrical ferrite specimen the ends of which were tapered for matching purposes as shown in Fig. 1(a). For a given axial magnetic field the reduction of transmitted power was largest with the specimen in the center of the guide, but, as might have been expected, no nonreciprocal effects were observed. A twisted rectangular waveguide section, however, loaded with the same specimen, exhibited nonreciprocal characteristics. In the experiment the sample was mounted centrally midway between the flanges of a 90° commercial 0.4×0.9 inch twist and an axial magnetic field was applied as shown in Fig. 1(b).

For constant incident power the transmitted power varied with both the magnitude and the direction of the magnetic field. With the particular nickel-cobalt ferrite used, nonreciprocal behavior was most pronounced at around 8900 mc where, at the optimum value of field current, reversal of the magnetic field caused a reduction of

\* Received by the PGM-TT, November 24, 1958. This work was carried out under AEC Contract AT(30-1)-1909.

<sup>1</sup> F. K. Du Pré, "Experiments on the microwave Faraday and Cotton-Mouton effects," *Proc. Symp. on Modern Advances in Microwave Techniques*, New York, N. Y., pp. 205-213; November, 1954.

<sup>1</sup> If  $|s_{12}|^2 + |s_{22}|^2 < 1$ , it would be impossible for  $|s_{22}|$  to be unity and therefore  $|s_{22}\Gamma_L| < 1$ .

<sup>2</sup> Only as far as an observer at the input is concerned.

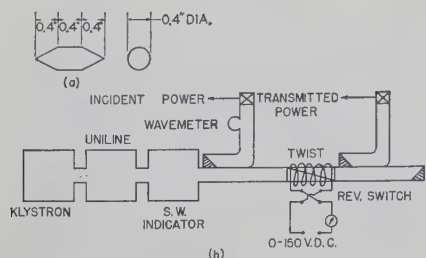


Fig. 1—(a) Tapered cylindrical ferrite specimen; (b) block diagram of experimental equipment.

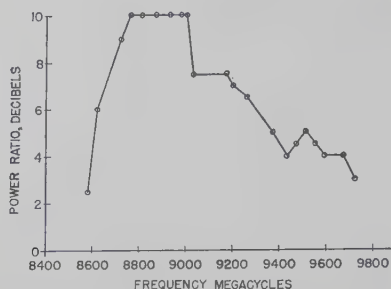


Fig. 2—Transmitted power ratio on reversal of magnetic field at constant magnetizing current ( $H = 160$  oersteds).

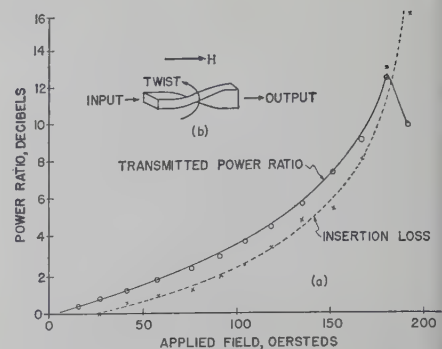


Fig. 3—(a) Transmitted power ratio and insertion loss at constant frequency ( $f = 8900$  mc); (b) conditions for attenuation in forward direction.

the transmitted power by more than 10 db. The power ratio on reversal of the magnetic field is shown in Fig. 2 at a constant value of magnetizing current for the frequency range of 8600–9700 mc and in Fig. 3(a) at a constant frequency of 8900 mc with the magnetizing current variable. The insertion loss was approximately equal to the power ratio over the range investigated. Conditions for attenuation in the forward direction are shown schematically in Fig. 3(b).

The voltage standing wave ratio of the ferrite-loaded twist was about 2.5 and was

not affected appreciably by changes of frequency or magnetic field. The corresponding reduction of incident power of approximately 1 db was taken into account in plotting the above data.

The field configuration in the loaded rectangular twist does not lend itself to simple analysis, particularly since higher modes are likely to be excited, because of the discontinuity presented by the ferrite specimen. However, it is conceivable that a combination of  $TE_{10}$  and  $TE_{01}$  modes could result in

a circularly polarized component which in conjunction with the axial magnetic field causes the effects described.

Thanks are due to Dr. C. L. Hogan for his interest in these experiments and for the supply of ferrite material.

A. E. BARRINGTON  
Cambridge Electron Accelerator  
Harvard University  
Cambridge, Mass.

## Contributors

Helmut M. Altschuler (S'47-A'49-M'54-SM'55) was born in Germany in 1922. He received the B.S. and M.S. degrees from



H. M. ALTSCHULER

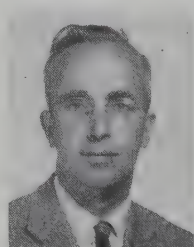
the Polytechnic Institute of Brooklyn, N. Y., in 1947 and 1949, respectively, both in electrical engineering. At the present time, he is continuing his graduate studies at P.I.B.

During 1947 and 1948 Mr. Altschuler held a Research Fellowship at the Microwave Research Institute of P.I.B., and since then has been employed there, presently in the capacity of research associate.

His work has been chiefly concerned with the development of impedance meters, microwave measurement techniques, and equivalent network representations.

Mr. Altschuler is a member of Sigma Xi and Eta Kappa Nu.

Bert A. Auld (S'49-A'53-M'58) was born on November 4, 1922, in Wei-Hwei-fu, China. He received the B.S. degree in electrical engineering from the University of British Columbia, Vancouver, B. C., Can., in 1946.



B. A. AULD

From 1946 to 1948 he was employed by the National Research Council, Ottawa, Can. In 1949 he received the M.S. degree, and in 1952, the Ph.D. degree in electrical engineering from Stanford University, Stanford, Calif. During the following year he worked at the Stanford Microwave Laboratory on VHF and UHF antennas. From 1953 to 1955 he was employed by Electrical and Musical Industries Ltd., Hayes, Middlesex, England, where he worked on the stagger-tuning of multicavity klystrons. Since 1955 he has conducted research on

microwave ferrite devices and has taught applied electromagnetic theory at the University of British Columbia.



Carroll M. Barrack (S'49-A'50-M'56) was born in Baltimore, Md., on March 15, 1927. He received the B.S. and Ph.D. degrees in electrical engineering in 1950 and 1956, respectively, from The Johns Hopkins University, Baltimore, Md.



C. M. BARRACK

In 1954, he became associated with Aircraft Armaments, Inc., Cockeysville, Md., where he worked on video and pulse circuitry, precision test equipment, radar systems, data handling equipment, and weapons systems evaluation. In



1957 he joined Electronics Communications, Inc., Timonium, Md., as a research engineer concerned with the development of microwave ferrite devices. He is presently an electronics department manager at Miller Research Laboratories, Baltimore, Md.

Dr. Barrack is a member of Tau Beta Pi, Sigma Xi, and an associate member of the AIEE.



Aaron D. Bresler (S'43-A'46-M'55-SM'59) was born in New York, N. Y., on June 20, 1924. He received the B.E.E. degree

from the College of the City of New York in 1944. From 1944 to 1947 he served with the U. S. Army Signal Corps., attaining the rank of first lieutenant. In the year following his discharge, Mr. Bresler was employed as a telephone engineer with the armed services in Austria. From

1948 to 1951, and again from 1953-1955, he was an instructor in the Electrical Engineering Department of C.C.N.Y. In 1951 he received the M.E.E. degree from the Polytechnic Institute of Brooklyn and joined the staff of its Microwave Research Institute where, for two years, he engaged in development work on microwave components. Since rejoining the staff of the Microwave Research Institute in 1955 he has been engaged in analytical studies of propagation and diffraction phenomena in anisotropic waveguides.

Mr. Bresler is a member of Tau Beta Pi, Eta Kappa Nu, and Sigma Xi.



Marvin Cohn (S'49-A'51-M'57) was born in Chicago, Ill., on September 25, 1928. He received the B.S.E.E. degree in 1950 and the M.S.E.E. degree in 1953, both from the Illinois Institute of Technology, Chicago.

From 1951 to 1952, he was employed by the Glenn L. Martin Company, Baltimore, Md.; he was with the Radiation Laboratory of The Johns Hopkins University, Baltimore, from 1952 until he entered the U. S. Army Signal Corps in 1953. He was stationed at White Sands Proving Grounds where he worked on the analysis of missile tracking systems.

In 1955 he returned to the Radiation Laboratory, where he has done research and development work on broad-band and super-heterodyne receivers and surface-wave transmission lines. He is head of the Millimeter Wave Techniques Group of the Radiation Laboratory.

Mr. Cohn is a member of Eta Kappa Nu, Tau Beta Pi, and Sigma Xi.



William Culshaw (SM'57) was born in Lancashire, England, on February 5, 1914. He received the B.Sc. degree in physics from



W. CULSHAW

the University of Sheffield in 1941, the B.Sc. degree in mathematics and the Ph.D. degree both from the University of London in 1947 and 1952, respectively. From 1942 to 1954 he was a staff member of the Telecommunications Research Establishment, Malvern, England, where he was with the microwave receiver and millimeter wave divisions. From 1954 to 1956 he was a member of the Radio Physics Laboratory, Ottawa, Canada, where he worked on scattering, and antenna problems.

Since 1956, he has been a member of the Microwave Physics Section of the National Bureau of Standards, Boulder Laboratories, Boulder, Colo., where his primary interests are in millimeter wave research, and microwave optics.

Dr. Culshaw is a member of the Scientific Research Society of America.



James W. Duncan (A'53-SM'59) was born in Decatur, Ill., on September 15, 1926. From 1944-1946 he served as an electronic



J. W. DUNCAN

technician with the U. S. Navy. He attended Millikin University, Decatur, from 1946-1948, and in 1950 received the B.S. degree in electrical engineering from the University of Colorado, Boulder. From 1950-1953 he was a development engineer at the Sandia Corporation, Albuquerque, N. M. During the years 1953-1958, he was on the staff of the Electrical Engineering Department of the University of Illinois, Urbana, where he was a research assistant and later associate in the Antenna Laboratory, performing research on surface wave launchers and antennas.

Dr. Duncan received the M.S. and Ph.D. degrees in electrical engineering in 1955 and 1958, respectively, from the University of Illinois. In September, 1958, he joined the antenna group at Collins Radio Company, Cedar Rapids, Ia.

He is a member of Sigma Xi, Tau Beta Pi, Eta Kappa Nu, Sigma Tau, and Pi Mu Epsilon.

Robert V. Garver, for a photo and biography, see p. 458 of the October, 1958 issue of these TRANSACTIONS.



Leonard O. Goldstone (M'51-SM'55) was born in Ogdensburg, N. Y., on February 15, 1922. He received the B.S. degree from



L. O. GOLDSTONE

Clarkson College of Technology, Potsdam, N. Y., in 1947, and the M.S. and Ph.D. degrees from the Polytechnic Institute of Brooklyn, Brooklyn, N. Y., in 1950 and 1957, respectively, all in electrical engineering. From 1947 to 1954 he was an instructor,

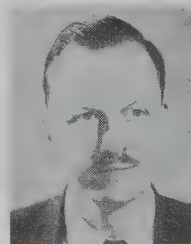
and then assistant professor in the Electrical Engineering Department of P.I.B.

From 1954 to 1957 he was a research associate at the Microwave Research Institute of P.I.B. where he was engaged in research on propagation in unconventional waveguides with applications to traveling wave antennas. In 1957, he returned to the Faculty of P.I.B. as assistant professor of electrical engineering. He is also presently serving as a research consultant to Kahn Research Laboratories, Inc.

Dr. Goldstone is a member of Eta Kappa Nu and Sigma Xi.



Arthur C. Hudson (M'53) was born on May 4, 1919, in Toronto, Ont., Can. He received the degree of B.A.Sc. in electrical engineering from the University of Toronto in 1941.



A. C. HUDSON

From 1941 to 1945, he was engaged in quality control of cathode-ray tube manufacture at Research Enterprises Limited, in Toronto. Since then he has been employed in the Radio and Electrical Engineering Division of the National Research Council of Canada in Ottawa, where he has been engaged in various aspects of microwave radar.

Mr. Hudson is a professional engineer in the Province of Ontario.



C. M. Johnson, for a photo and biography, please see p. 183 of the January, 1959 issue of these TRANSACTIONS.

Takeshi Kawahashi was born on February 21, 1921, in Heijo, Japan. He received the B.E. degree in electrical engineering from the University of Tokyo in 1943.



T. KAWAHASHI

He then became associated with the Nippon Electric Co., where, during World War II, he was engaged in laboratory research on radar equipment. Since then he has been associated with the development of supermultichannel microwave relay systems at the Development and Research Section, Radio Department, where he is an acting chief of the microwave group.

Mr. Kawahashi is a member of the Institute of Electrical Communication Engineers of Japan.

❖

D. D. King, for a photo and biography, please see p. 336 of the July, 1958 issue of these TRANSACTIONS.

❖

Katsu Matsumaru (A'55) was born on May 30, 1913, in Tokyo, Japan. He was graduated from Tokyo University with the B.S. degree in 1939.



K. MATSUMARU

From 1940 to 1943, he served as an assistant at Tokyo University and later, from 1944-1951, he served in the same capacity at the Tokyo Institute of Technology.

In 1951, Mr. Matsumaru joined the Radio Development Section of the Electrical Communication Laboratory, Nippon Telegraph and Telephone Public Corporation in Tokyo, Japan, where he has participated in the microwave research program.

❖

Eugene W. Sard (A'49-M'55) was born in Brooklyn, N. Y., on December 21, 1923. He received the B.S. and M.S. degrees in electrical engineering in 1944 and 1948, respectively, from the Massachusetts Institute of Technology, Cambridge, Mass.



E. W. SARD

From 1944 to 1946, he served in the USNR as a radar officer. From 1946 to 1948, he was a research assistant in the Center of Analysis and the Servo-

mechanisms Laboratory at M.I.T., working on digital computers.

Since 1948, he has been with Airborne Instruments Laboratory, Mineola, N. Y., working at first in the Radar Department and more recently in the Applied Electronics Department. For the past two years he has been working on the application of semiconductor diodes to various fields including fast switching, harmonic generation, and low-noise amplification.

Mr. Sard is a member of Sigma Xi.

❖

Jerome R. Singer (S'55-M'57) was born October 16, 1921, in Cleveland, Ohio. After four years at sea as a navigator, he received the B.S. degree in mathematics from the University of Illinois, Urbana, and the M.S. and Ph.D. degrees in physics from Northwestern University, Evanston, Ill., and the University of Connecticut, Storrs, respectively.



J. R. SINGER

He has been a member of the engineering staff of Sperry Gyroscope Co. and Boeing Airplane Co. He was a solid-state physicist at the Naval Ordnance Laboratory, White Oak, Md., and chief staff physicist of the National Scientific Laboratories, Inc., Washington, D. C. He is presently an associate professor in the electrical engineering division at the University of California, Berkeley.

His interests are in solid-state physics, particularly magnetic materials, masers, and electronic systems.

Dr. Singer is a member of the Physical Society, Sigma Xi, AAAS, Physical Society of Great Britain, Optical Society of America, and Acoustical Society of America.

❖

Charles C. H. Tang was born on September 27, 1924, in Shanghai, China. He received the B.S. degree in physics in 1946 from the University of Shanghai. He taught in the physics department of the University from 1946 to 1949; from 1950 to 1951 he was chief accountant at the Universal Textile Co., Ltd., Hongkong.



C. C. H. TANG

In 1952, he received the M.S. degree in electrical engineering from Oklahoma State University, Stillwater, and then entered Harvard University, Cam-

bridge, Mass., on a Gordon McKay Scholarship, where in 1956 he received the Ph.D. degree in applied physics. After remaining at Harvard for a year as a Research Fellow he joined the University of California, Berkeley, where from 1957 to 1958 he was an assistant professor in electrical engineering. Currently he is an associate professor in physics at Tunghai University, Taichung, Taiwan.

Dr. Tang is a member of Sigma Xi and Phi Kappa Phi.

❖

Teiji Uchida was born on December 17, 1931, at Morioka, Iwateken, Japan.

In 1954, he received the B.E. degree in electrical engineering from the University of Tokyo.



T. UCHIDA

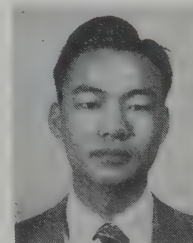
After his graduation, he joined the Nippon Electric Co., and since that time, has been engaged in the development of supermultichannel microwave relay systems at the Development and Research Section, Radio De-

partment, where he is a member of the engineering staff.

Mr. Uchida is a member of the Institute of Electrical Communication Engineers of Japan and of the Institute of Electrical Engineers of Japan.

❖

Omar Wing (S'50-A'53-M'58) was born in Detroit, Mich., on March 2, 1928. He received the B.S. degree in electrical engineering from the University of Tennessee, Knoxville, Tenn., in 1950, and the M.S. degree from the Massachusetts Institute of Technology, Cambridge, Mass., in 1952.



O. WING

He then joined Bell Telephone Laboratories as a member of the technical staff. Since 1956, on

leave from Bell Laboratories, he has been an instructor in electrical engineering at Columbia University, New York, N. Y.

Mr. Wing is a member of Tau Beta Pi, Eta Kappa Nu, Phi Kappa Phi, Sigma Xi, and the AIEE.

❖

Leo Young, for a photo and biography, please see p. 186 of the January, 1959 issue of these TRANSACTIONS.



# 1959 PGMTT National Symposium

The 1959 PGMTT National Symposium sponsored by the IRE Professional Group on Microwave Theory and Techniques, in co-operation with the Division of Applied Physics, Harvard University, will be held at Paine Hall, Harvard University, Cambridge, Mass., June 1-3, 1959.

The Technical Program Committee Chairman is Henry Riblet. Other members of the Committee are: Carl Faflick, Irving Goldstein, Victor Jones, John Reed, Peter Rizzi, and Karl Willenbrock.

Advance registration is urged. Free parking stickers are reserved for advanced registrants. Registration fees are \$3.00 for IRE members and \$5.00 for nonmembers; there is no fee for students. The price of the banquet is \$6.00 and luncheons are \$0.95 per person. Parking stickers for large registrants will be available for \$1.00 if any are left. Advance registration should be addressed to W. H. From, Ewen-Knight Corporation, 206 A St., Needham, Mass., and checks should be payable to W. H. From, Treasurer. A ladies program will include a tour of historic Boston on June 1, a tea and tour of the Art Museum on June 2, and a luncheon on Wednesday, June 3.

## PROGRAM

### REGISTRATION

Mon. 8:00-8:45 A.M.

### SESSION 1

Mon. 8:45 A.M.-NOON

#### FILTERS AND COMPONENTS

Chairman: R. W. P. KING, *Harvard University, Cambridge, Mass.*

#### Opening Addresses

W. L. PRITCHARD, *Symposium Chairman, Raytheon Mfg. Co., Wayland, Mass.*

T. S. SAAD, *Chairman, PGMTT, Sage Labs., Wellesley, Mass.*

MCGEORGE BUNDY, *Dean of the Faculty of Arts and Sciences, Harvard University, Cambridge, Mass.*

#### Directional Couplers—An Example of Microwave Developments

HAROLD A. WHEELER, *Wheeler Labs., Inc., Great Neck, N. Y.*

#### A Constant Resistance Microwave Filter

J. REED, J. CHILD, AND H. THOMAS, *Raytheon Mfg. Co., Wayland, Mass.*

#### The Design and Measurement of Two Broad-band Coaxial Phase Shifters

C. F. AUGUSTINE AND J. CHEAL, *Bendix Aviation Corp., Detroit, Mich.*

#### Microwave Phase Shifters

DAVID L. FYE, *Electromagnetic Rad. Lab., Air Res. and Dev. Command, Bedford, Mass.*

#### Dissipation Effects in Microwave Filters

SEYMOUR B. COHN, *Stanford Res. Inst., Menlo Park, Calif.*

#### Wide-Stop-Band Waveguide Filters

B. SCHIFFMAN, *Varian Associates, and S. B. COHN, Stanford Res. Inst., Menlo Park, Calif.*

#### Tunable Microwave Filters

E. TORGOW AND D. JACENKO, *Polytechnic Inst. of Brooklyn, Brooklyn, N. Y.*

#### A Transmission Line Backward Wave Filter

M. E. HINES AND E. T. HARKLESS, *Bell Telephone Labs., Murray Hill, N. J.*

### SESSION 2

Mon. 2:00-5:00 P.M.

#### MICROWAVES I

Chairman: KIYO TOMIYASU, *G.E. Microwave Lab., Palo Alto, Calif.*

#### A Survey of the Microwave Research in Japan in 1958

ISAO SOMEYA, *Secretary, Tokyo Chapter, PGMTT*

#### Determination of Some Electrical Properties of a Gas Detonation by Microwave Techniques

BERNARD HAYES, *Los Alamos Sci. Lab.,*

*University of California, Los Alamos, N. M.*

#### Microphony in Waveguide

I. GOLDSTEIN AND S. SOORSOORIAN, *Raytheon Mfg. Co., Bedford, Mass.*

#### Tunable Spherical Cavity Resonators

E. RICHTER, *Ewen Knight Corp., Needham, Mass., and A. E. O'BRIEN, JR., Raytheon Mfg. Co., Bedford, Mass.*

#### Use of Partially-Filled Dielectric Coaxial Lines in Nonreciprocal Devices

G. S. HELLER AND J. S. COE, *M.I.T. Lincoln Lab., Lexington, Mass.*

#### Coupling of Multiple Cavity Systems

G. S. KINO AND M. A. ALLEN, *Stanford University, Stanford, Calif.*

#### Dielectric Loading and Tapered Field Effects in Ferrite Devices Using Perturbation Methods

R. F. SOOHOO, *M.I.T. Lincoln Lab., Lexington, Mass.*

#### Theoretical Limitations of Ferrite Amplifier Performance

R. W. DAMON AND J. R. ESHBACH, *G.E. Res. Lab., Schenectady, N. Y.*

#### TE<sub>10</sub> Shuttle Pulse Measurements in Multimode Circular Waveguide

W. D. WARTERS AND H. E. ROWE, *Bell Telephone Labs., Inc., Holmdel, N. J.*

#### Pulse Responses of Some TEM Transmission-line Components

W. J. GETSINGER, *Stanford Res. Inst., Menlo Park, Calif.*

### SESSION 3

Mon. 8:00-10:00 P.M.

#### CAMBRIDGE ELECTRON ACCELERATOR

#### Radio Frequency Systems of the Cambridge Electron Accelerator

K. W. ROBINSON, *C.E.A., Cambridge, Mass.*



1959 PGMTT National Symposium Committee: (left to right) P. Crandell, National Co.; P. Rizzi, Ewen Knight; W. From, Finance, Ewen Knight; I. Goldstein, Raytheon; K. Willenbrock, Harvard University; H. Riblet, Technical Program, Microwave Development Labs.; W. Pritchard, Symposium Committee Chairman, Raytheon; R. Rivers, Publicity, Aircom; Mrs. W. Pritchard, Ladies Program; Mrs. T. Saad; T. Saad, Local Arrangements, Sage Labs.

### Model Studies of a Strongly Coupled Synchrotron RF System

J. DEKLAVA, A. E. BARRINGTON, AND J. R. REES, *C.E.A., Cambridge, Mass.*

### Visit to the Cambridge Electron Accelerator

## SESSION 4

Tues. 8:45 A.M.—NOON

### MASER TECHNIQUES

*Chairman:* M. T. WEISS, *Bell Telephone Labs., Inc., Holmdel, N. J.*

### Physical Principles of Solid-State Masers

N. BLOEMBERGEN, *Harvard University, Cambridge, Mass.*

### Relaxation Effects in Maser Materials

S. SHAPIRO, *Harvard University, Cambridge, Mass.*

### An L-Band and Y-Junction Circulator

L. DAVIS, JR., U. MILANO, AND J. SAUNDERS, *Raytheon Mfg. Co., Waltham, Mass.*

### Low-Temperature Germanium Microwave Switch

R. H. KINGSTON AND S. H. AUTLER, *M.I.T., Lincoln Lab., Lexington, Mass.*

### Quantum Mechanical Amplifiers: Present Performance Status

M. W. P. STRANDBERG, *M.I.T., Cambridge, Mass.*

### The Design of Large Gain Bandwidth Product Masers

W. FROM, *Ewen Knight Corp., Needham, Mass.*

### Packaged Tunable L-Band Maser System

F. R. ARAMS AND S. OKWIT, *Airborne Instrument Lab., Mineola, N. Y.*

## SESSION 5

Tues. 2:00—5:00 P.M.

### MICROWAVES II

*Chairman:* EUGENE FUBINI, *Airborne Instruments Lab., Mineola, N. Y.*

### Survey of Noise Figure Problems

P. STRUM, *Granger Associates, Palo Alto, Calif.*

### Analysis of Cascaded Microwave Network by Means of Signal Flow Graphs

K. HUNTON, *Hewlett-Packard Co., Palo Alto, Calif.*

### Measurement of Bandwidth of Microwave Resonator by Phase Shift of Signal Modulation

D. S. LERNER AND H. A. WHEELER, *Wheeler Labs., Inc., Great Neck, N. Y.*

### A Double-Sweep Comparator for Microwave Ferrite Device Measurements

J. A. WEISS AND R. W. JUDKINS, *Bell Telephone Labs., Inc., Murray Hill, N. J.*

### Comparison of Deviations from Square Law for RF Crystal Diodes and Barretters

G. U. SORGER AND B. O. WEINSCHEL, *Weinschel Engineering Co., Inc., Kensington, Md.*

### The Accumulation of Small Errors in Extended Periodic Structures

M. C. PEASE, *Sylvania Electric Products, Inc., Mountain View, Calif.*

### Theory of the Germanium Diode Microwave Switch

R. V. GARVER, J. A. ROSADO, AND E. F. TURNER, *Diamond Ordnance Fuze Labs., Washington 25, D. C.*

### Single-Pole Double-Throw Wide-Band Microwave Switch

M. BLOOM, *Sylvania Electronic Systems, Waltham, Mass.*

### Diodes in Multiple Switches and Time Varying Dielectrics

J. GALEJS, *Sylvania Electronic Systems, Waltham, Mass.*

## SYMPOSIUM BANQUET

*Place*—Harkness Commons, Harvard University, Cambridge, Mass.

*Time*—Cocktail Hour: 6:00–7:00 P.M. Dinner: 7:00 P.M., June 2, 1959.

*Toastmaster*—W. L. Pritchard, Symposium Committee Chairman.

*Opening Remarks*—Prof. Harvey Brooks, Harvard University.

*Microwave Prize*—Awarded by T. Saad, Chairman, PGMTT Administrative Committee.

*Banquet Address*—Prof. E. M. Purcell, Harvard University.

## SESSION 6

Wed. 8:45 A.M.—NOON

### FERRITES

*Chairman:* E. STRUMWASSER, *Hughes Aircraft Co., Culver City, Calif.*

### Recent Advances in Materials for Microwave Ferrite Devices

V. JONES, *Harvard University, Cambridge, Mass.*

### L-Band Ferromagnetic Resonance Experiments at High Peak Power Levels

J. H. SAUNDERS, E. SCHLÖMANN, AND M. H. SIRVETZ, *Raytheon Mfg. Co., Waltham, Mass.*

### High-Power Ferromagnetic Resonance at X-Band in Polycrystalline Garnets

J. J. GREEN, *Gordon McKay Lab., Harvard University, Cambridge, Mass.* and E. SCHLÖMANN, *Raytheon Mfg. Co., Waltham, Mass.*

### Use of Demagnetizing Fields to Minimize Temperature Effects in Ferrite Devices

W. H. VONAULOCK, *Bell Telephone Labs., Inc., Whippany, N. J.*

### Some New Ferrite Design Forms

HAROLD SEIDEL, *Bell Telephone Labs., Inc., Murray Hill, N. J.*

### The Design and Operations of Two Types of Medium Power Microwave Ferrimagnetic Limiters

E. N. SKOMAL AND M. A. MEDINA, *Sylvania Electric Products, Inc., Mountain View, Calif.*

### Ferrite Multimode High-Power Signal Suppressor

W. C. HEITHAUS, S. C. SLOAN, B. J. DUNCAN, and L. SWERN, *Sperry Microwave Electronics Co., Clearwater, Fla.*

### A New Approach to the Design of Low-Frequency, Ferrite Phase Shifters

R. L. FOGEL, *Hughes Aircraft Co., Culver City, Calif.*

### Broad-Band Ridge Waveguide Ferrite Devices

E. S. GRIMES, JR., D. D. BARTHOLOMEW, D. C. SCOTT, AND S. C. SLOAN, *Sperry Microwave Electronics Co., Clearwater, Fla.*

## SESSION 7

Wed. 2:00—5:00 P.M.

### VARIABLE REACTANCE DEVICES

*Chairman:* H. MAUS, *M.I.T., Cambridge, Mass.*

### Progress Report on Variable Capacitance Diodes

A. UHLIR, *Microwave Associates, Burlington, Mass.*

### RF Logic Circuits Using Subharmonic Oscillators

F. STERZER, *Radio Corp. of America, Princeton, N. J.*

### A Variable Reactance Diode Phase Shifter

E. STERN, *G.E. Co., Syracuse, N. Y.*

### Theory of Filter-Type Parametric Amplifiers

P. PARZEN, *Radio Corp. of America.*

### Parametric Amplifiers: State of the Art

R. S. ENGELBRECHT, *Bell Telephone Labs., Inc., Whippany, N. J.*

### Performance of Low-Noise Tunable- Cavity and Traveling-Wave Parametric Amplifiers

E. M. T. JONES, R. C. HONEY, AND J. S. HONDA, *Stanford Res. Inst., Menlo Park, Calif.*

### Design and Field Test of Two Different Types of Reactance Amplifiers

J. POPPE AND H. J. PEPPIATT, *G.E. Co., Syracuse, N. Y.*

### Some Considerations of Four-Frequency Parametric Circuits

DAVID ADAMS, *University of Michigan Res. Inst., Ann Arbor, Mich.*



# AVAILABLE BACK ISSUES OF IRE TRANSACTIONS ON MICROWAVE THEORY AND TECHNIQUES

PUBLICATION	PRICES		
	Group Members	IRE Members	Non- Members
Vol. MTT-2, No. 3, Sept., 1954	\$1.10	\$1.65	\$3.30
Vol. MTT-3, No. 1, Jan., 1955	\$1.50	\$2.25	\$4.50
Vol. MTT-3, No. 4, July, 1955	\$1.60	\$2.40	\$4.80
Vol. MTT-4, No. 1, Jan., 1956	\$1.65	\$2.45	\$4.95
Vol. MTT-4, No. 3, July, 1956	\$1.25	\$1.85	\$3.75
Vol. MTT-4, No. 4, Oct., 1956	\$1.85	\$2.75	\$5.55
Vol. MTT-5, No. 2, April, 1957	\$1.90	\$2.85	\$5.70
Vol. MTT-5, No. 3, July, 1957	\$1.15	\$1.70	\$3.45
Vol. MTT-5, No. 4, Oct., 1957	\$1.20	\$1.80	\$3.60
Vol. MTT-6, No. 1, Jan., 1958	\$2.65	\$3.95	\$7.95
Vol. MTT-6, No. 2, April, 1958	\$2.50	\$3.75	\$7.50
Vol. MTT-6, No. 3, July, 1958	\$2.00	\$3.00	\$6.00
Vol. MTT-6, No. 1, Oct., 1958	\$2.50	\$3.75	\$7.50
Vol. MTT-7, No. 1, Jan., 1959	\$3.75	\$5.60	\$11.25

\*Colleges, Universities, Subscription Agencies, and All Libraries may purchase at IRE Member rate.

## MICROWAVE ENGINEERS

Stanford Research Institute offers unique and professionally challenging employment in the advancement of microwave theory and techniques.

Attractive salaries for experienced professional personnel with degrees in Electrical Engineering or Physics to participate in research involving:

- **MICROWAVE FILTERS and STRIP-LINE COMPONENTS**
- **PARAMETRIC AMPLIFIERS**
- **FERRITE DEVICES**
- **MICROWAVE ANTENNAS**

*Write to:*

Professional Employment Manager

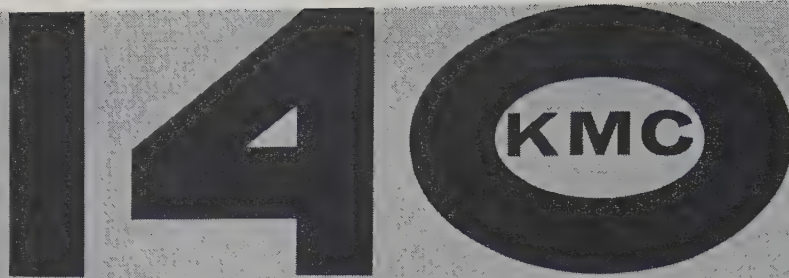
**STANFORD  
RESEARCH  
INSTITUTE**

Menlo Park, California

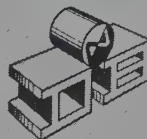
## NOTICE TO ADVERTISERS

•

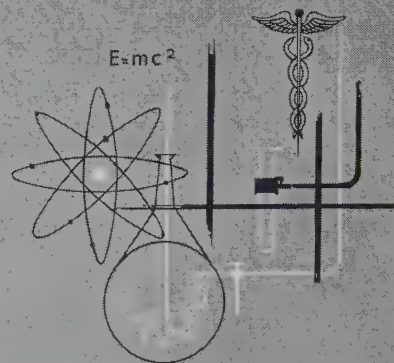
Effective immediately the IRE TRANSACTIONS ON MICROWAVE THEORY AND TECHNIQUES will accept display advertising. For full details contact Tore N. Anderson, Advertising Editor, PGMTT TRANSACTIONS, 1539 Deer Path, Mountainside, N.J.



# ULTRAMICROWAVE\* EQUIPMENT BY



*-it works - it's accurate - it's available*



These millimeter wave units can greatly enlarge your scope of microwave activity. Research previously considered impractical at 140 KMC can now be carried on successfully.

De Mornay-Bonardi manufactures cavity wave-meters, crystal multipliers, crystal mounts, E-H tuners, and standing wave detectors specifically for use at 140 KMC. They work—we've been using these units effectively in our own laboratories for developing other items. These instruments are accurate—functionally as accurate as De Mornay-Bonardi equipment used at 90 KMC. You can order these units now—we're currently filling orders on 140 KMC instruments.

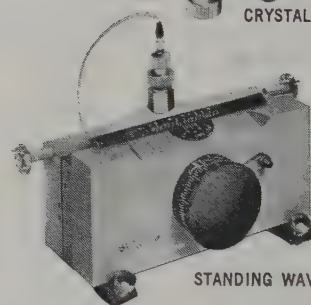
*Write for complete data*



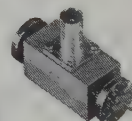
**DE MORNAY-BONARDI**  
780 SOUTH ARROYO PARKWAY • PASADENA, CALIF.



CRYSTAL MULTIPLIERS



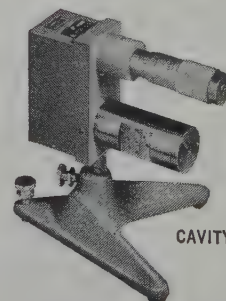
STANDING WAVE DETECTORS



CRYSTAL MOUNTS



E-H TUNERS



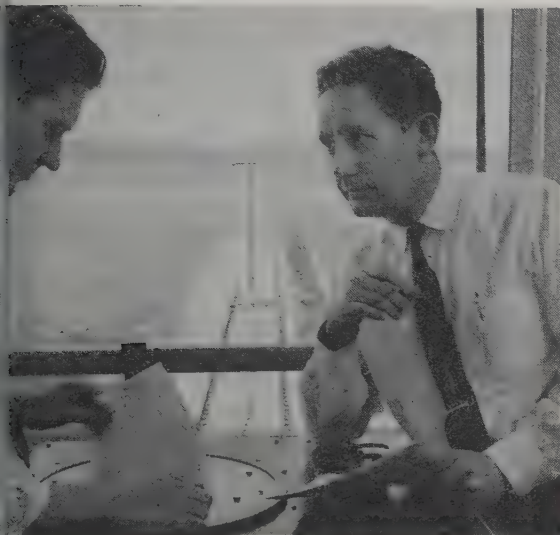
CAVITY WAVEMETERS

\*TRADE MARK DE MORNAY-BONARDI



(right) Lockheed Q-5 target missile features telemetry that registers miss-distance and theoretical hits in testing accuracy of other missiles.

## ANTENNA— TELEMETRY

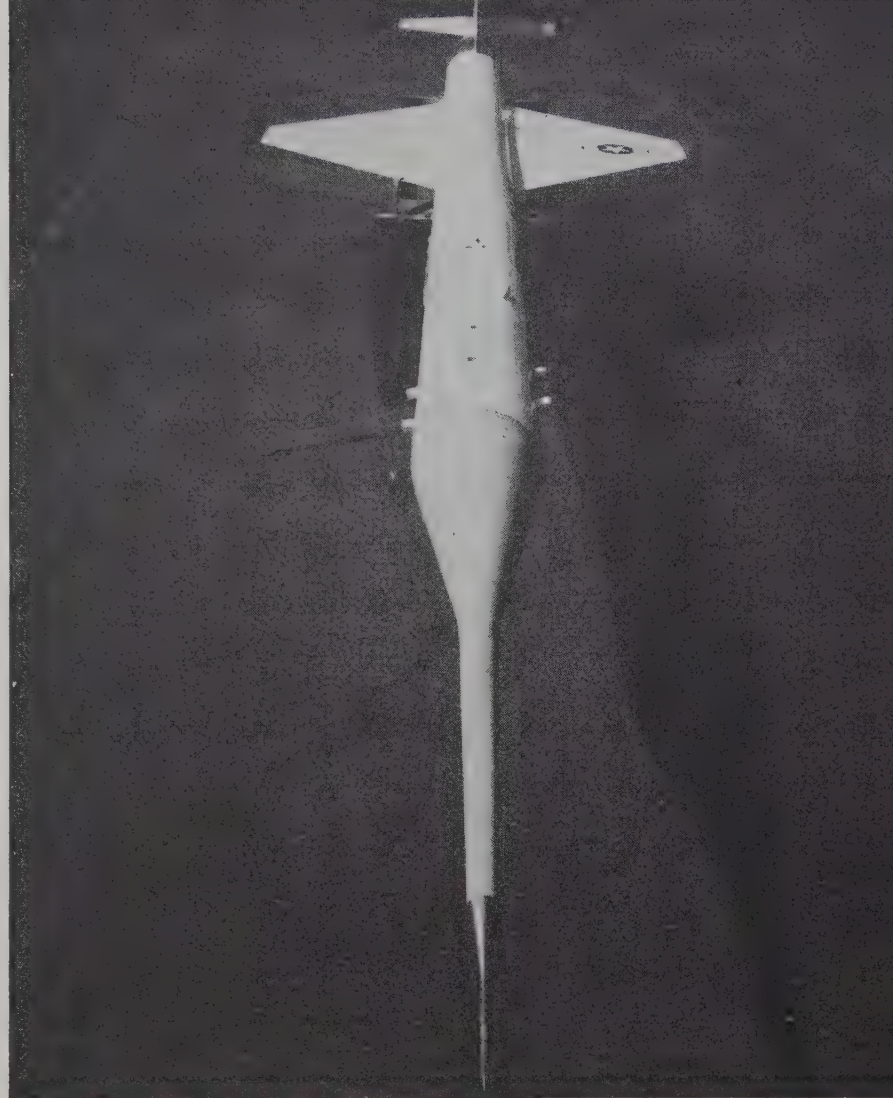


Studying results of antenna pattern measurements — part of the activity of the Space Communications laboratory.

# Lockheed

**MISSILES AND SPACE  
DIVISION**

SUNNYVALE, PALO ALTO, VAN NUYS,  
SANTA CRUZ, SANTA MARIA, CALIFORNIA  
CAPE CANAVERAL, FLORIDA • ALAMOGORDO, NEW MEXICO



## Expanding the Frontiers of Space Technology

Lockheed maintains extensive research capabilities for the development of antennas and telemetering systems and spacecraft applications.

Laboratory studies in antennas and electromagnetic propagation include the application of solid state materials to microwave transmission line components; the design of antennas to survive the rigors of space flight; the effects of space on radio signals and radar detection; and the scattering from missile shapes and space vehicles. Research is also being conducted in the application of ferrites and MASERS; on problems of radio transmission between space vehicles and Earth, re-entry scattering and diffraction by man-made objects and ionized gases; and development of antennas for data link systems between satellites and ground stations.

Telemetering has been brought to a high degree of successful application in the integration of circuits and components into high-performance systems. A completely sub-miniaturized FM-FM system has been developed, along with a complete PAM-FM system characterized by highly efficient band-width utilization, low power consumption and economy of size and weight. This represents a significant achievement in the field of high capacity telemetry.

Scientists and engineers of outstanding talent and inquiring mind are invited to join us in the nation's most interesting and challenging basic research and development programs. Write: Research and Development Staff, Dept. D-56, 962 W. El Camino Real, Sunnyvale, California.

*"The organization that contributed most in the past year to the advancement of the art of missiles and astronautics."*

NATIONAL MISSILE INDUSTRY CONFERENCE AWARD











## INSTITUTIONAL LISTINGS

The IRE Professional Group on Microwave Theory and Techniques is grateful for the assistance given by the firms listed below, and invites application for Institutional Listing from other firms interested in the Microwave field.

AIRTRON, INC., 1101 W. Elizabeth Ave., Linden, N. J.

Designers and Producers of Complete Line of Microwave, Electronic and Aircraft Components

COLLINS RADIO CO., Cedar Rapids, Iowa

Complete Industrial Microwave, Communication, Navigation and Flight Control Systems

LITTON INDUSTRIES, Electron Tube Div., 960 Industrial Rd., San Carlos, Calif.

Magnetron, Klystrons, Carcinotrons, TWT's, Backward Wave Oscillators, Gas Discharge Tubes, Noise Sources

MICROWAVE CHEMICALS LABORATORY, INC., 282 Seventh Ave., New York 1, N.Y.

Single Crystals and Polycrystalline Y.I.G. and Related Ferrites Designed for Your Devices

MICROWAVE DEVELOPMENT LABS., INC., 92 Broad St., Babson Park 57, Mass.

Designers, Developers and Producers of Microwave Components and Assemblies, 400 mc to 70 kmc

SAGE LABORATORIES, INC., 159 Linden St., Wellesley 81, Mass.

Microwave Engineering Specialists

WEINSCHEL ENGINEERING CO., INC., Kensington, Md.

Attenuation Standards, Coaxial Attenuators and Insertion Loss Test Sets

WHEELER LABORATORIES, INC., 122 Cutter Mill Road, Great Neck, N.Y.

Consulting Services, Research & Development, Microwave Antennas & Waveguide Components

The charge for an Institutional Listing is \$50.00 per issue or \$140.00 for four consecutive issues. Applications for Institutional Listings and checks (made out to the Institute of Radio Engineers) should be sent to Tore N. Anderson, PGMTT Advertising Editor, 1539 Deer Path, Mountainside, N.J.

### NOTICE TO ADVERTISERS

Effective immediately the IRE TRANSACTIONS ON MICROWAVE THEORY AND TECHNIQUES will accept display advertising. For full details contact Tore N. Anderson, Advertising Editor, PGMTT TRANSACTIONS, 1539 Deer Path, Mountainside, N. J.



see the newcomer among FXR's extensive line of

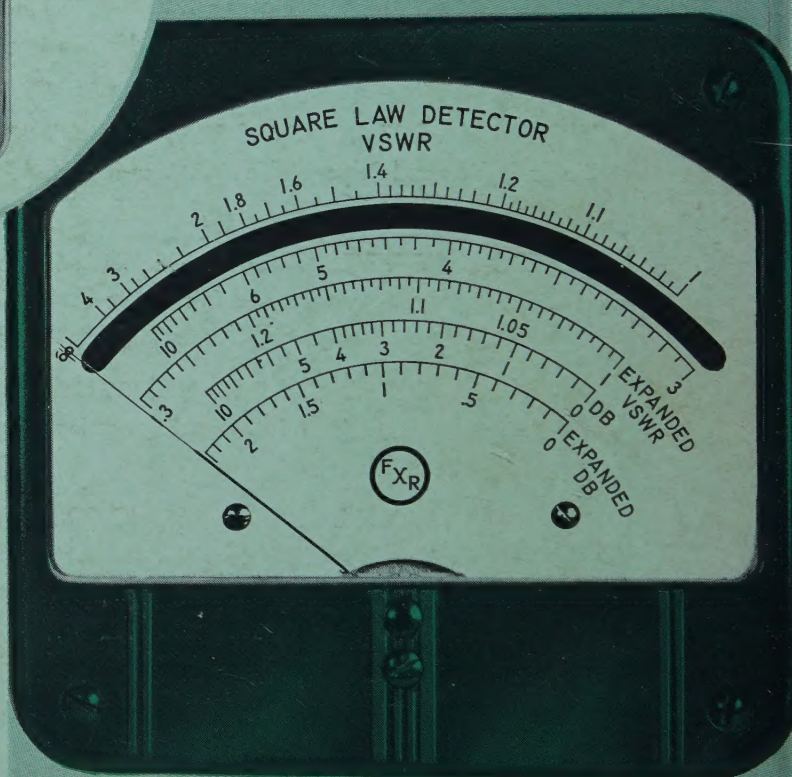
# PRECISION MICROWAVE EQUIPMENT



Model  
B 812 A

## INNOVATIONS where they are most effective

- Oversized 5-inch mirror-backed meter, with 1% linearity, provides high resolution and accuracy. It can be tilted for even greater ease of reading than its oversize affords.
- The meter is also *REMOVABLE* for convenient placement and it is equipped with a vernier attenuator for remote adjustment over a 3 DB range.
- A filter, tunable between 950 and 1050 CPS, permits exact alignment of the instrument with the output frequency of the signal source.
- Range, 70 DB; expanded scale for VSWR and DB; panel switch shifts the meter reading —5 DB to move it to an area of the scale more easily read.
- Gain automatically maintained when readings are switched from normal to expanded scale.
- Low microphonic, subminiature tube in input circuit increases usable sensitivity.
- Full scale sensitivity, 0.1  $\mu$ V; signal to noise ratio, 3:1.



## STANDING WAVE AMPLIFIER

**FXR, Inc.**  
formerly F-R MACHINE WORKS, Inc.



PRECISION  
MICROWAVE  
EQUIPMENT  
•  
HIGH POWER  
MODULATORS  
•  
RADAR  
COMPONENTS  
•  
ELECTRONIC  
TEST  
EQUIPMENT

DESIGN • DEVELOPMENT • MANUFACTURE  
26-12 BOROUGH PLACE, WOODSIDE 77, NEW YORK